A FULLY SCALED SHORT DURATION TURBINE EXPERIMENT

by

GERALD ROGER GUENETTE, JR

S.B., Massachusetts Institute of Technology
(1968)

S.M., Massachusetts Institute of Technology
(1970)

Submitted to the Department of Aeronautics
and Astronautics in Partial Fulfillment of
the Requirements for the Degree of

DOCTOR OF SCIENCE

at the

MASSACHUSETTS INSTITUTE OF TECHNOLOGY

September 1985

Signature of Author _____
Dept. of Aeronautics and Astronautics 26 August 1985

Certified by _____
Professor Alan H. Epstein Thesis Supervisor

Certified by _____
Professor Edward M. Greitzer

Certified by _____
Professor Eugene E. Covert

Certified by _____
Professor Jack L. Kerrebrock

Accepted by _____
Professor Harold Y. Wachman Chairman, Departmental
Graduate Committee

A FULLY SCALED SHORT DURATION TURBINE EXPERIMENT

by

GERALD ROGER GUENETTE, JR

Submitted to the Department of Aeronautics and Astronautics on 26 August 1985 in partial fulfillment of the requirements for the Degree of Doctor of Science in Aeronautics and Astronautics.

Abstract

Short duration experiments were conducted on a transonic high pressure turbine stage in a facility specifically developed to provide rigorous simulation of the operational environment of both present and future generation engines. These tests demonstrated the feasibility of conducting fully scaled, short duration experiments on a rotating turbine stage and provided time resolved data on the rotor tip casing flow. In particular, unique high frequency heat flux data was obtained with a newly developed gauge which yields direct surface heat flux measurements on unmodified warm turbine rig components. Time resolved measurements of the tip casing flow revealed the influence of rotor enthalpy extraction and tip leakage flow upon the end wall heat load distribution. These tests not only provided data on an important problem for which little full scale quantitative data existed but also demonstrated the unique capabilities of the short duration test facility and heat flux instrumentation to provide fundamental data on turbine flow phenomena.

Acknowledgements

TABLE OF CONTENTS

LIST OF TABLES

CHAPTER 1

INTRODUCTION

As the performance required of aircraft high pressure turbines continues to advance, there is an increasing need to explore many of the fundamental aspects of turbine fluid physics which have hitherto received little or no attention. Some of these, especially during the earlier stages of turbine technical development, were probably of second order, while others, although critical to performance, were simply just too difficult to attack with the technical tools and resources available. Some three dimensional effects perhaps fell into the first category, while unsteady heat transfer, rotor/wake interactions, cooling, and end wall phenomena belong in the latter.

The study of any of these problems in the actual engine would be an extraodinarily complex, if not impossible, task, with the harsh operating environment making fine-resolution instrumentation very difficult. This problem is further aggravated by access restrictions to the turbine flow path. Parametric studies are limited, not only by the operating point and safety restrictions, but also by the high running and maintainance costs of full scale engines. These all conspire to significantly limit both instrumentation flexibility and parametric range, especially for fundamental studies.

There is, therefore, a crucial need for research facilities which can simulate the important high pressure turbine parameters, but in a more benign environment and at much lower cost. Fundamental experiments are well suited to the use of short duration facilities since, for turbines,

most high speed aerodynamic and heat transfer phenomena occur on blade passing time scales. Investigators could tailor the test environment to simulate both present and future operating regimes and utilize the full benefits of the highest instrumentation technology available to perform detailed, time and spatially resolved measurements.

Several such facilities are now in use or under construction, including light isentropic piston cascade tunnels, blowdown cascades, and a small shock tunnel driven turbine. With the exception of the latter, these are stationary cascades designed primarily for airfoil heat transfer and aerodynamic studies. Although each has its benefits, none of these facilities provides a fully scaled test environment for full size rotating hardware, under conditions which allow for complete, time resolved aerodynamic and heat transfer surveys.

The goal of this project, therefore, was to obtain time resolved measurements on a full, rotating, high pressure turbine stage under rigorously scaled operating conditions. To this end, a short duration test facility was designed, constructed, and demonstrated which provides a suitable testing environment, as outlined above. To fully utilize the capabilities of this facility, this research also included the development of new, high response, heat flux sensor technology, which is generally applicable to all stationary and rotating warm rig turbine components, including cooled rotor blades.

To prove the facility concept, tests were initially performed to verify its capability to provide a faithful simulation of all the important dimensionless performance and flow field parameters. Initial heat flux tests were performed upon the stationary rotor tip casing and nozzle guide vanes to verify the overall performance capabilities of the new sensor

technology. Unique, high resolution pressure and heat flux measurements were then obtained upon the stationary rotor tip end wall, providing new information on this important aspect of high pressure turbine flow.

CHAPTER 2

DESIGN OF THE EXPERIMENTAL FACILITY

2.1 Facility Design Requirements

A goal of this project was to design, build and utilize a short duration turbine test facility benefiting from the experience gained from past turbine efforts and from the the MIT Blowdown Compressor Facility. The philosophy which directed this effort is summed up in the following design requirements:

1. The full scale turbine operating environment must be rigorously simulated including all non-dimensional parameters which characterize operating point and the detailed internal flow phenomena;
2. A complete stage, nozzle guide vanes and rotor, must be tested;
3. The turbine should be as large as possible to facilitate instrumentation;
4. The test times must be sufficiently long for full aerodynamic surveys;
5. The test hardware must provide for ease and flexibility of instrumentation access; and
6. The construction and operating cost must be of academic scale.

2.2 Facility Scaling

Scaling the turbine operating environment requires an understanding of the basic physical forces that govern the flow of momentum and energy within the machine. Non-dimensional formulation of the governing equations shows that it is the ratios of forces, fluxes and states that determine the flow field. Therefore, only the relevant non-dimensional parameters and boundary conditions, not the actual running conditions, need be matched for a faithful experimental simulation.

The component performance of a gas turbine depends upon both the machine and its working fluid. The working fluid generally behaves as a

calorifically perfect gas at the pressures and temperatures typical of high pressure turbines, thereby facilitating the simulation. Total temperature ratio is the relevant variable quantifying the non-dimensional work output and the overall stage performance takes the functional form,

$$\frac{\dot{m}\sqrt{RT_T}}{P_T D^2} \quad , \quad \tau_t = f\left\{\pi_t \; , \; \frac{ND}{\sqrt{RT_T}} \; , \; \frac{\dot{m}}{\mu D} \; , \; \gamma\right\}$$

where the dependent parameters, here chosen to be the corrected mass flow and total temperature ratio, are functions of the pressure ratio, corrected speed, Reynolds number, and specific heat ratio. This expression defines the turbine characteristics and provides the basis for scaling the operating point.

In addition to the quantities specified above, several others are required to properly model the thermal and aerodynamic boundary layer development within the machine and, consequently, the heat flux distribution and the other internal phenomena (such as wake interaction effects and tip clearance flows) which significantly influence overall performance. The most inportant are the gas to wall temperature ratio, Prandtl and Reynolds numbers. Free stream turbulence intensity also has a significant influence upon transition and heat flux. For cooled turbines, an additional set of dimensionless quantities must be considered, including the coolant to free stream mass flux and temperature ratios.

It is important to note here the advantages of short duration testing for turbine heat flux simulation. These result from the observation that operational surface temperature variations are usually a small fraction of the driving gas to wall temperature difference. The same will be true for a short duration test. With proper selection of the initial gas to mean

metal temperature ratio, excellent test time similarity can be obtained, and with appropriate instrumentation, heat flux may be directly measured for these known boundary conditions.

The scaling equations are written as follows, with a prime denoting the scaled conditions.

Temperature Ratios:

$$\frac{T'_g}{T'_m} = \frac{T_g}{T_m} \tag{2.1}$$

$$\frac{T'_c}{T'_m} = \frac{T_c}{T_m} \tag{2.2}$$

The subscripts g, m, and c refer to the main gas flow, the metal, and the coolant gas respectively.

Compressibility:

$$\gamma' = \gamma \tag{2.3}$$

$$\frac{M'}{M} = \frac{U'}{U}\sqrt{\frac{\mathbf{m}'}{\mathbf{m}}\frac{T_g}{T'_g}}$$

Reynolds Number:

$$\frac{Re'}{Re} = \frac{\rho' U' D' \mu}{\rho U D \mu'} \tag{2.4}$$

For Re' = Re and M' = M, Eq. (2.4) can be written as

$$\frac{P'}{P} = \frac{\mu'}{\mu}\sqrt{\frac{\mathbf{m}}{\mathbf{m}'}\frac{T'}{T}}\frac{D}{D'} \tag{2.5}$$

where P is the total pressure and $\mathbf{m}$ is the molecular weight. The rotational effects may be scaled either as Rossby number or corrected speed. Here we have chosen corrected speed.

$$\frac{N'D'}{\sqrt{\gamma' T'/\mathbf{m}'}} = \frac{ND}{\sqrt{\gamma T/\mathbf{m}}} \tag{2.6}$$

for $\gamma' = \gamma$, Eq. (2.6) becomes

$$\frac{N'}{N} = \frac{T'}{T}\sqrt{\frac{m}{m'}}\,\frac{D}{D'} \tag{2.7}$$

Buoyancy effects due to rotation scale as the Rayleigh number, Ra

$$Ra = \frac{r}{D}\,\frac{Re^2}{Ro^2}\,P_r\,\frac{\Delta T}{T} \tag{2.8}$$

where r/D is the same with geometry scaling. Thus, the above equations imply that buoyancy effects are properly modelled so long as

$$Pr' = Pr \tag{2.9}$$

The key scaling is that of temperature ratio. It is primarily the very high temperature of the full scale turbine which renders investigations both difficult and expensive. By reducing the absolute level of temperature while maintaining the proper gas/metal temperature ratios (Eqs. 2.1 and 2.2), the fluid mechanics and heat transfer can be accurately simulated (so far as we know) under relatively benign conditions. Note that, by reducing the absolute gas temperature, the pressure required for Reynolds No. matching (Eq. 2.5) is reduced, thus reducing the facility construction and operating costs. Also, the mechanical rotating speed of the turbine is decreased (Eq. 2.7), thus reducing rotational stresses and simplifying the mechanical design and rotating system instrumentation. The decrease in rotational speed also reduces the frequency response required of fixed frame instrumentation for a given rotational frame resolution.

At low speeds, fluid flow is not strongly affected by variations of the ratio of specific heats, γ. For transonic and supersonic turbines, however, γ matching may not be simply ignored. At a given temperature, γ is a function primarily of gas composition. The test gas γ can be adjusted

through an appropriate combination of high and low γ molecules, i.e., monatomic and large molecular weight gases. Through judicious selection of the constituents for a selected γ, the molecular weight of the gas mixture can be increased as compared to that of air which is normally used in test facilities, although not simulating the engine γ. Maximizing the molecular weight has the advantages of: a) decreasing the pressure level required at constant Reynolds No. (thus reducing construction costs); and b) decreasing the speed of sound of the gas (thus reducing the turbine rotational speed with the benefits listed above). The heaviest monatomic gas whose price is consistent with large volume consumption is Argon.

The properties of several argon-refrigerant mixtures at typical scaled conditions are presented in Table 2.1. For the main flow, the 75% Argon-25% Freon-12 mole fraction mixture is the composition of choice because of Freon-12's low cost ($2 per Kg) compared to the heavier mixtures. The film coolant flow must be at low temperature (~200°K). This requires a saturation temperature lower than that of Freon-12; thus Freon-14 is selected for the coolant.

The scaling laws were applied to a typical modern turbine design with the results illustrated in Table 2.2. Given the choice of gas species, the desired γ sets the mixture ratios. The metal temperature selection sets the inflow and coolant temperatures. Reynolds number similarity then determines the pressure. The Prandtl number is not a free variable. Fortuitously in this case, the Prandtl number of the mixture is quite close to that for high temperature air. The mechanical rotational speed is set to keep the corrected speed constant. Note that the rotating system stresses have been reduced by a factor of four and the required instrumentation bandwidth by a factor of two. The mass flow is down from

full scale by a factor of three, while the power produced (and thus the size required of the power absorber) is reduced by a factor of 24.

Using the scaled inlet conditions in Table 2.2, it can be seen that, for a typical high pressure turbine with a 4 to 1 pressure ratio, the turbine outflow is at approximately standard pressure and temperature, further simplifying the instrumentation task.

Clearly, the scaling has enormously reduced the resources required for turbine testing while preserving the important fluid physics.

2.3 Facility Configuration

Many facility configurations were examined which could meet most, if not all, of the scaling criteria enunciated in the preceding section. All were based on transient testing techniques, both to reduce the construction and operating costs and to exploit many of the transient heat transfer and fluid dynamic testing techniques developed over the last 20 years. Since the predominant source of unsteadiness in turbines is rotor-stator interaction, a test time on the order of 1,000 to 10,000 blade passings (0.1 to 1.0 seconds) should suffice for most studies.

Four configurations were studied in some detail, either because they seemed particularly simple, utilized equipment on hand, or built upon previous experience.

The first configuration consisted of high pressure storage tanks (100 to 200 atmospheres) feeding a flow heater in line with the turbine (Fig. 2.1a). A large flywheel could absorb the turbine power produced. The advantage here is that, with the heater and fast acting regulators in the flow path, constant turbine inlet pressure and temperature can be maintained. The principal disadvantage is that the high pressure gas storage precludes the use of a heavy gas mixture (the heavy gases condense at the

high pressure).

The second configuration is a variation on the first in which the high pressure gas storage is replaced by a room pressure expulsion bladder so that a heavy gas mixture can be used. The bladder would be contained in a pre-heated shell since little pressure drop would be available for an inline flow heater. The scheme has the disadvantage of failing to maintain full Reynolds number similarity. Also, the technology required for a $10m^3$ 500°K expulsion bladder appears risky.

The third configuration considered was the original concept which motivated this project. In this scheme, the turbine is directly coupled to a compressor whose inlet is the turbine's outlet. Thus, the turbine and compressor turn at the same mechanical speed and share the same flowpath. Since a choked turbine produces power proportional to the tip Mach No. squared and a centrifugal compressor does work as the square of the tip Mach No., the turbine-compressor pair are matched over a considerable range and operate at constant corrected speed without the need of a control system. The corrected weight flow is constant so long as any orifice in the flow path remains choked. If we now place the turbine-compressor test section between two tanks, the upstream supply tank filled with the gas mixture at appropriate conditions and the downstream dump tank evacuated to full vacuum, the facility is complete with the addition of a valve or diaphragm between the supply tank and test section.

The design of such a blowdown tunnel was carried out in some detail. A compressor was chosen in this design over a flywheel for two reasons. The first is that the compressor can maintain a closer match in corrected speed compared to the flywheel since, with the flywheel, the turbine mechanical speed must always increase (if only a small amount), while with the

compressor, the turbine speed can slow to match the drop in inlet temperature that is inherent to a blowdown from a fixed volume tank. Thus, the flywheel may be appropriate for constant inlet condition schemes such as the two discussed above but an energy absorber is really required for a blowdown. The second reason is that the large power output of a transonic turbine requires a very massive flywheel, complicating the mechanical design.

The compressor design proved to be troublesome, however. The problem is that the very high work output of a large transonic turbine is considerably greater than any existing single centrifugal compressor stage can absorb. Since the turbine and compressor are constrained to turn at the same mechanical speed (excluding gearing), the only way to increase the power absorption is to increase the compressor diameter. The power scales with the square of the compressor diameter but the moment of inertia scales as the fourth power of diameter. Thus, the compressor grows into an enormous flywheel whose aerodynamic characteristics are of secondary importance.

As the compressor diameter passed one meter in the design, it was clear that a safe mechanical design of the rotating system would be very difficult. (Note that the aerodynamic design is not so difficult since the compressor efficiency does not effect the power absorption, only the pressure rise. The pressure rise does, however, determine the volume of the dump tank required. The principal aerodynamic design consideration for the compressor is that the weight flow vs. speed characteristic match that of the turbine.)

Various compressor designs were then attempted, including multiple centrifugals, a supersonic axial compressor, and the adaptation of a multistage aircraft engine high pressure compressor. These schemes did not seem

to offer much in reducing either the mechanical complexity or the technical risk of the project.

Another configuration investigated replaced the compressor with an eddy current brake. An eddy brake consists of a moving conductor (metal disk or drum) in an imposed magnetic field. The motion induces secondary currents (eddy currents) in the conductor which opposes the applied field, thus generating a braking force. The power is dissipated as heat in the conductor. The eddy brake is attractive because the braking torque is proportional to the square of the rotational speed. Thus, an eddy brake coupled to turbine will, as the compressor, match the turbine characteristic without the need of a control system. The eddy brake offered the advantage of a high power density design, simplifying packaging and rig layout. Unlike a mechanical friction brake, the eddy brake has no moving parts other than the conductor and thus relatively few mechanical and dynamic design problems.

Due to the above potential advantages of the eddy current brake and also due to the investigators' expertise in compressor design and ignorance of eddy current brakes, the eddy brake configuration was chosen for the blowdown turbine.

At this point, a turbine stage was selected about which to size the facility. Instrumentation considerations dictated as large a turbine as possible. In fact, even the largest production high pressure turbines have typical blade spans of only 6 cm. Large size means large mass flow, however, and it is mass flow which drives the facility costs. Since a turbine from a 50,000 lb. thrust engine was beyond the resources of this program, a 0.55 meter (22 inch) diameter turbine size was selected. This choice was consistent with the resources in hand, comparable in size to

that in the NASA High Pressure Facility, and has 2/3 the span of the largest high pressure turbines.

Although the goal of the blowdown turbine project is the exploration of phenomena not readily studied in other facilities, it is desirable to verify early in the program that turbine performance in the blowdown tunnel is the same as in more conventional facilities. Thus, an existing, conventionally tested turbine was selected for the tunnel, both to provide a baseline for performance comparisons and to reduce program costs. The turbine selected is of Rolls-Royce Limited design and manufacture. It is a high work, transonic design of the late 1970's. The inlet conditions are those listed as full scale in Table 2.2. Additional design parameters of interest include:

Turbine Loading, $\Delta H/U^2$ - 2.3

Total Pressure Ratio - 4.5

Specific Output, $C_p \Delta T/T$ - 0.29 kJ/kg °K

Cooled and uncooled blading is available for both the rotor and the nozzle guide vanes (NGV's).

A calculation of the blowdown tunnel performance was used to demonstrate the overall concept and to facilitate tank sizing. A mathematical model of the turbine blowdown process with eddy brake can be found in Appendix A. The results of the model are shown in the following figures. Figure (2.2) illustrates that, although the rotational speed changes during the test, the corrected speed is calculated as constant to better than 1% over 200 ms, as are the pressure ratio and thus the corrected weight flow (Fig. 2.3). The calculated torque balance is shown in Fig. (2.4).

The size of the downstream dump tank is set by the overall run time desired at a particular turbine pressure ratio. The supply tank size is

set by the allowable change in temperature ratio during the test time (<1%). The coolant flow is fed from a supply tank separate from that for the main flow. Its size is set so that its volume ratio with the supply tanks equals that of the flow rates. Thus, the blowing ratio across the film cooling holes is maintained constant over the test time.

TABLE 2.1
COMPOSITION AND THERMOPHYSICAL PROPERTIES

γ_{MIX} = 1.28, T = 400°F, P = 14.7 psia

Refrigerant			Argon - Refrigerant Mixtures						
	Mass%	Mole%	M_{MIX} $\left(\frac{lbm}{lbm\text{-}mole}\right)$	C_{PMIX} $\left(\frac{BTU}{lbm\text{-}°R}\right)$	R_{MIX} $\left(\frac{BTU}{lbm\text{-}°R}\right)$	γ_{MIX}	μ_{MIX} $\left(\frac{BTU}{sec\text{-}ft}\right)$	κ_{MIX} $\left(\frac{BTU}{sec\text{-}ft\text{-}°F}\right)$	$P_{r_{MIX}}$
R-12	50.94	25.54	60.63	0.1500	3.276×10^{-2}	1.279	1.785×10^{-5}	3.548×10^{-6}	0.755
R-13	49.58	27.32	57.58	0.1579	3.449×10^{-2}	1.279			
R13B1	57.84	26.90	69.26	0.1313	2.867×10^{-2}	1.279	1.939×10^{-5}	3.515×10^{-6}	0.724
R-14	47.80	29.36	54.06	0.1682	3.674×10^{-2}	1.279	1.994×10^{-5}	4.222×10^{-6}	0.794
R-22	52.55	33.84	55.69	0.1633	3.566×10^{-2}	1.279	1.761×10^{-5}	3.648×10^{-6}	0.788
R-115	39.97	14.69	56.76	0.1602	3.498×10^{-2}	1.279	1.925×10^{-5}	3.935×10^{-6}	0.783
Air at 1780° 14.696 psia			28.97	0.3066	6.856×10^{-2}	1.289	3.892×10^{-5}	15.86×10^{-6}	0.752

TABLE 2.2
MIT BLOWDOWN TURBINE SCALING

	Full Scale	MIT Blowdown
Fluid	Air	Ar-R12
Ratio Specific Heats	1.27	1.27
Mean Metal Temperature, T_m	1118°K (1550°F)	295°K (72°F)
Metal/Gas Temperature Ratio, T_m/T_g	0.63	0.63
Inlet Total Temperature, T_g	1780°K (2750°F)	478°K (400°F)
Cooling Air Temperature	790°K (960°F)	212°K (-77°F)
Airfoil Cooling Air Flow	12.5%	12.5%
True NGV Chord	8.0 cm	5.9 cm
Reynolds Number*	2.7×10^6	2.7×10^6
Inlet Total Pressure, atm (psia)	19.6 (289)	4.3 (64)
Outlet Total Pressure, atm (psia)	4.5 (66)	1.0 (14.7)
Outlet Total Temperature	1280°K (1844°F)	343°K (160°F)
Prandtl Number	0.752	0.755
Rotor Speed, RPM	12,734	6,190
Mass Flow, kg/sec	49.00	16.55
Power, watts	24,880,000	1,078,000
Test Time	Cont.	0.2 sec.

*Based on NGV chord and isentropic exit conditions.

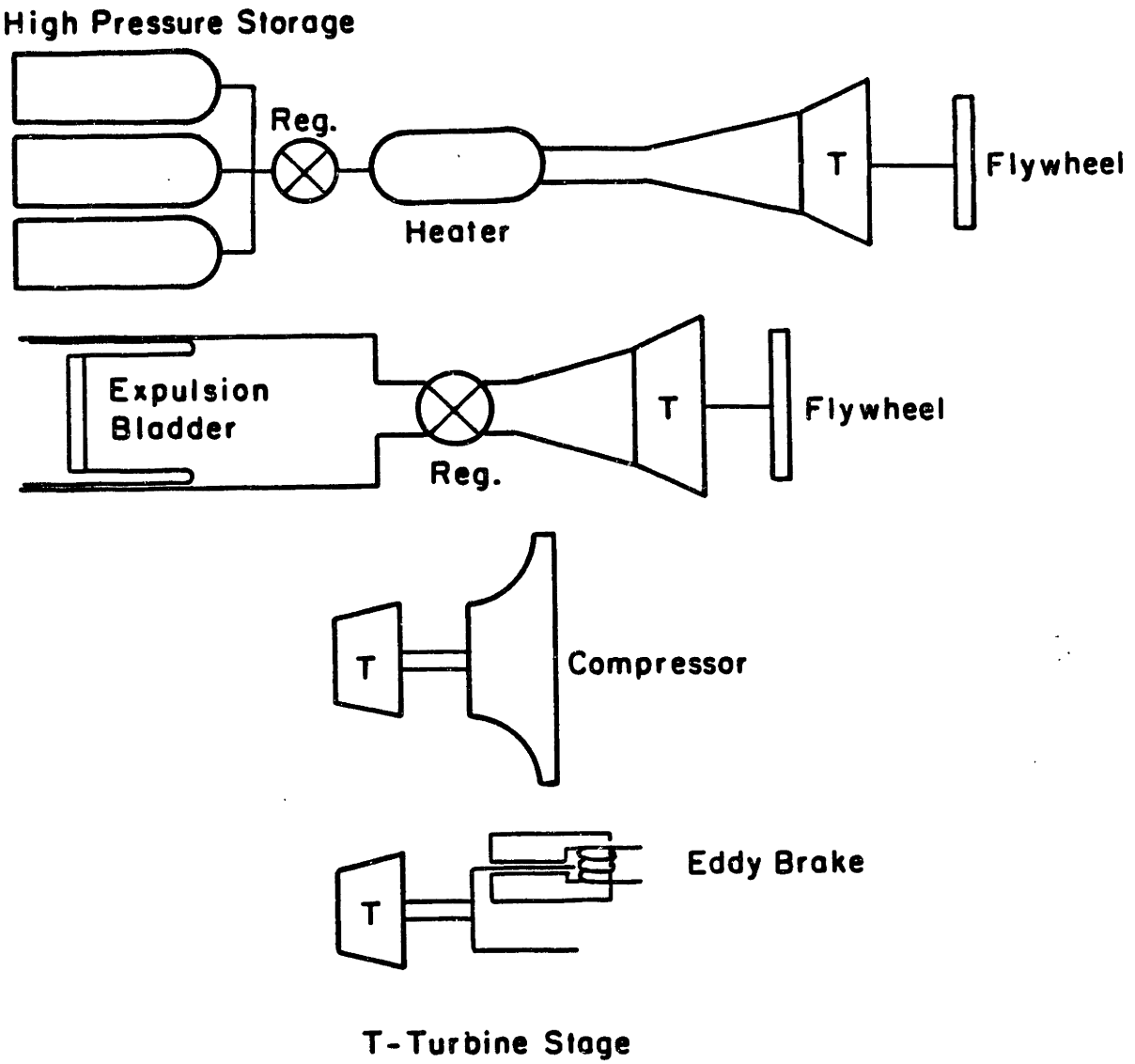

FIGURE 2.1: CANDIDATE FACILITY CONFIGURATIONS

(A) 150 ATM GAS STORAGE WITH FLOW HEATER AND FLYWHEEL

(B) ROOM PRESSURE EXPULSION BLADDER AND FLYWHEEL

(C) BLOWDOWN WITH COMPRESSOR POWER ABSORBER

(D) BLOWDOWN WITH EDDY BRAKE POWER ABSORBER

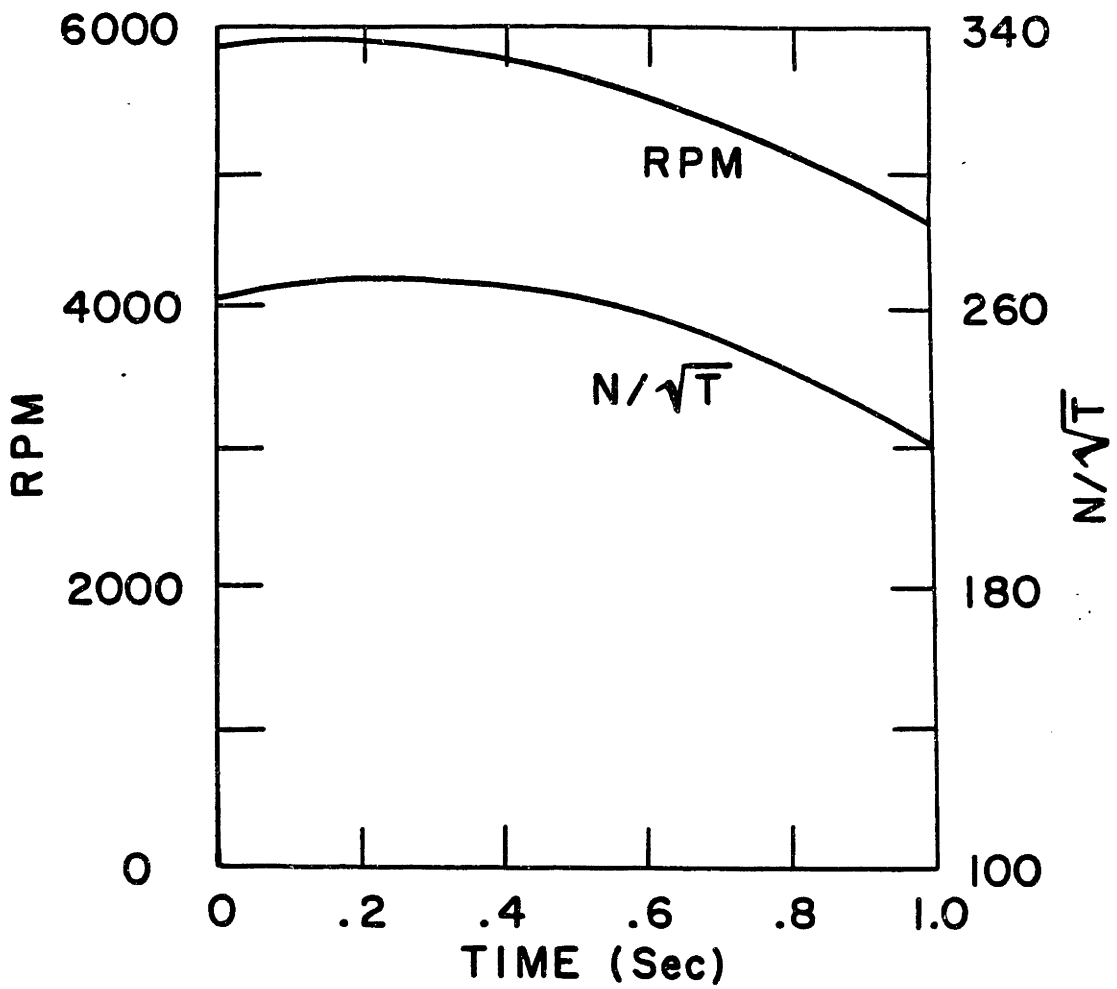

FIGURE 2.2: TYPICAL PREDICTED BLOWDOWN TURBINE MECHANICAL AND CORRECTED SPEED VARIATION

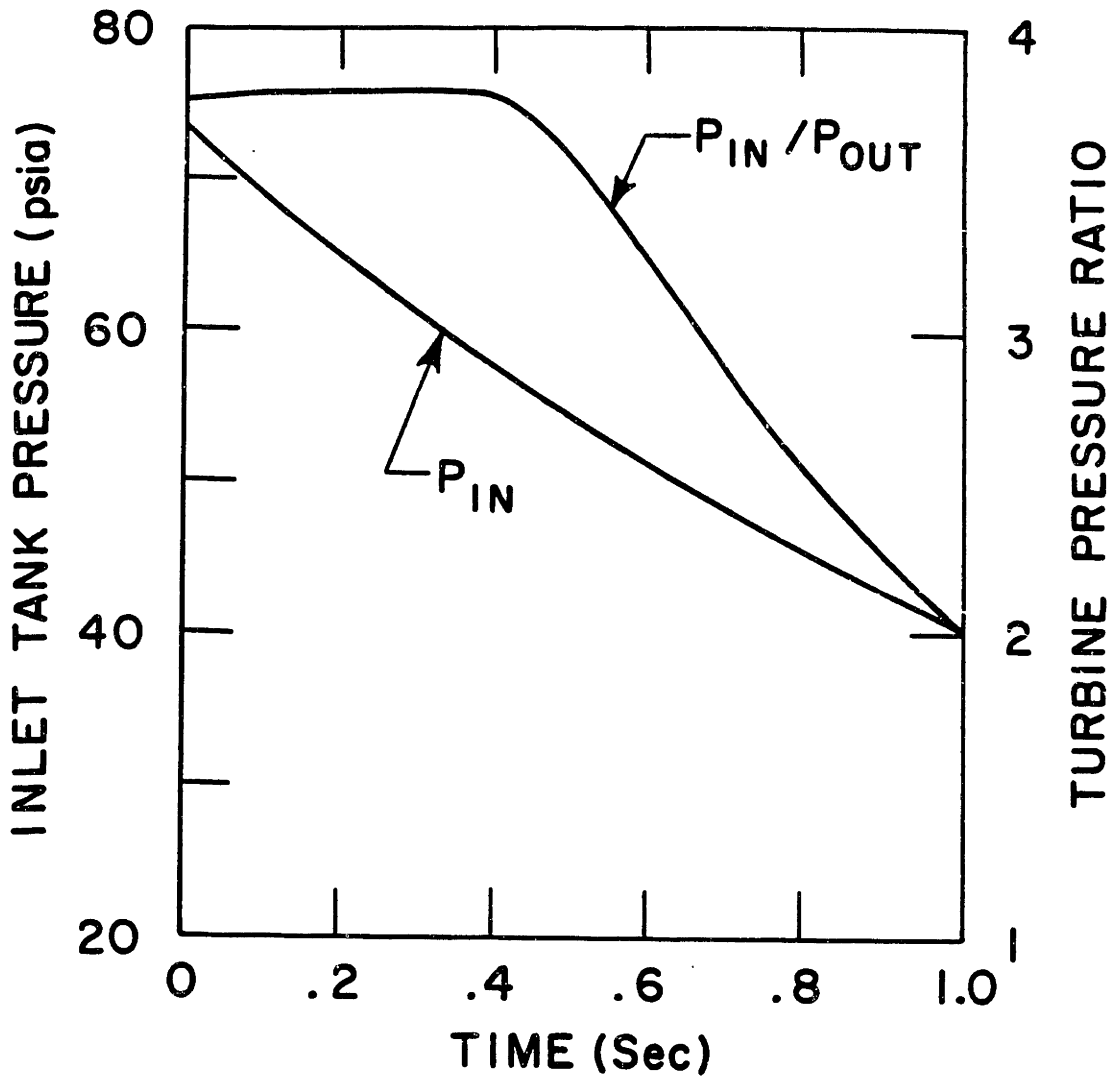

FIGURE 2.3: TYPICAL PREDICTED BLOWDOWN INLET PRESSURE AND TURBINE PRESSURE RATIO HISTORY

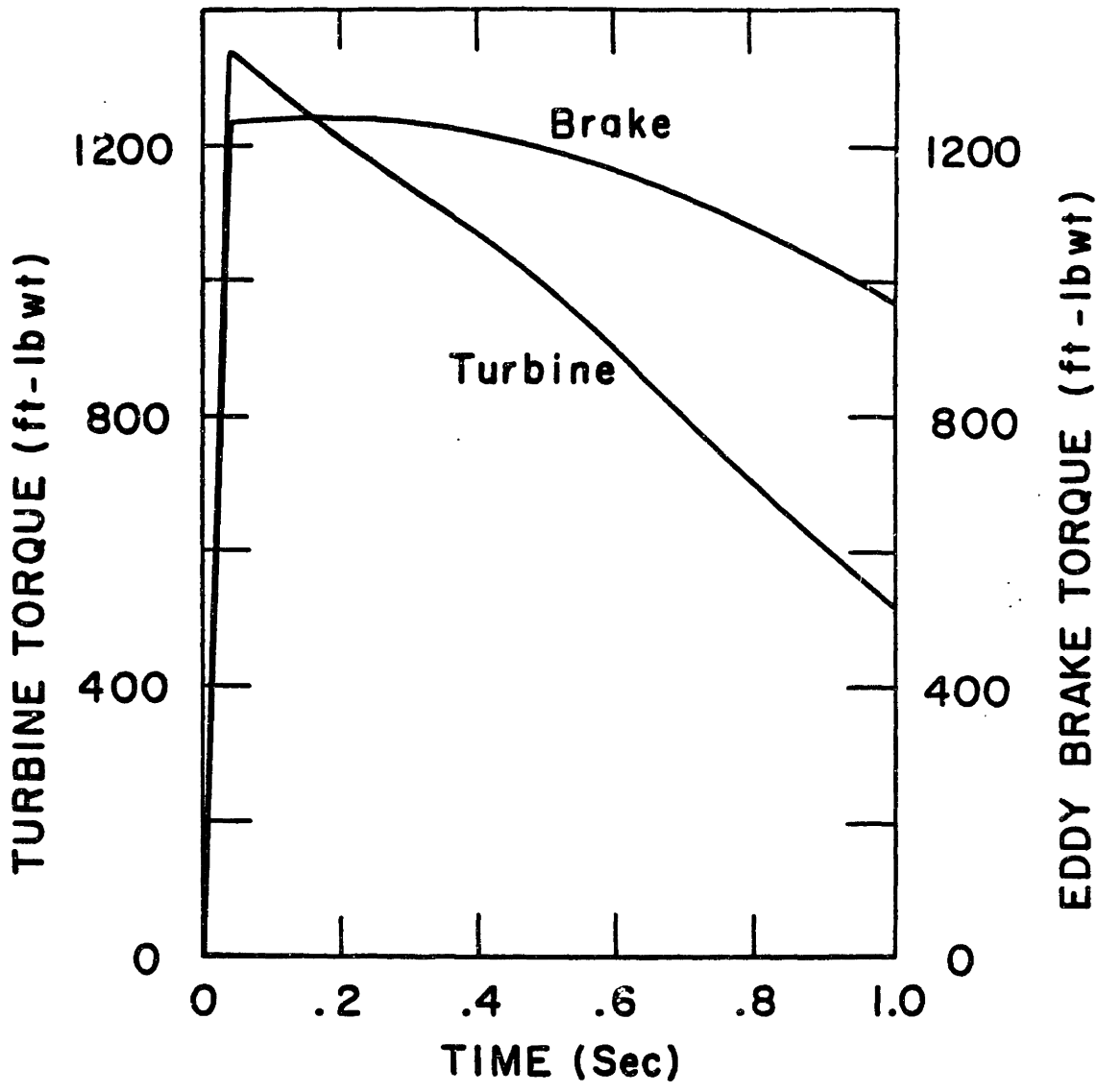

FIGURE 2.4: PREDICTED VARIATION IN TURBINE TORQUE PRODUCED AND EDDY BRAKE TORQUE ABSORBED

CHAPTER 3

DETAILED FACILITY DESCRIPTION

The MIT Blowdown Turbine Facility (Fig. 3.1) consists of a supply tank separated by a large, fast-acting valve from the test section containing the turbine stage which discharges into a vacuum dump tank. Prior to a test, the entire facility is evacuated (0.1 torr) by a mechanical vacuum pump. The supply tank and valve are then heated by oil circulating in a jacket around the tank. After the desired temperature is reached, the fast-acting valve is closed and the supply tank pressurized with the appropriate gas mixture. The turbine, which is still in vacuum, is brought to operating speed by a small electric motor. The test is initiated by simultaneously opening the valve and energizing the eddy brake magnets. The steady test time starts about 200 ms after the valve actuation begins and lasts for 200-300 ms until the downstream throttle unchokes.

The facility has been sized to allow testing at twice design Reynolds No. ($2x(3x10^6)$) in argon-freon, or at design Re in air. The facility design inlet total pressure of 10 atm in the laboratory corresponds to 40 atm at engine conditions. The maximum facility inlet total temperature is 533°K (500°F), thus facilitating carbon steel construction and the use of elastomer seals. This corresponds to a scaled engine temperature of 2300°K (3680°F) assuming a 1250°K (1790°F) metal temperature or a 2500°K (4040°F) for a 1350°K (1970°F) metal temperature. Thus, the facility operating envelope, shown in Fig. (3.2), includes the full range of present and proposed engine designs.

The following sections describe the facility hardware: the main valve, the test section, the eddy current brake, the tanks and auxiliary

systems, the data acquisition system, and the flow instrumentation.

3.1 Main Valve

The main valve separates the supply tank from the test section. The valve must seal the 10 atm supply tank pressure against the test section vacuum at temperatures up to 530°K (500°F), open fully in 50 ms, and provide a disturbance-free inflow to the test section. These are challenging requirements and the valve design and manufacture developed into a major engineering effort.

Several classes of valves were reviewed, including explosively or mechanically ruptured diaphragms (as used on the MIT Blowdown Compressor Tunnel), small diameter valves followed by expansions and flow straighteners, and large diameter valves with integral flow contraction. The last type was chosen because it seemed to offer both the minimum flow establishment time and smoothest inflow profile, although at the expense of increased size of the moving parts.

An annular plug design was selected, as conceptually illustrated in Fig. (3.3). In the closed position, the 0.9m diameter cone-shaped plug seals against the inner and outer annuli of the flow path. To open, the cone slides forward along its shaft to form a smooth annular contraction from the supply tank into the test section. The valve flowpath is contoured to provide a smooth and continuous area contraction to keep the boundary layers thin.

Since the high temperature operating requirement precludes the use of aluminum for the moving parts, the entire valve is constructed of mild steel and, therefore, is fairly massive (100 Kg). This requires that large forces (10,000-20,000 lbf) be applied to accelerate and decelerate the slider in a 50 ms time period. Conventional very high pressure hydraulic

technology could be used, but the high temperature operation and geometrical constraints considerably complicate the application. Thus, in the interests of mechanical simplicity, a pneumatic pilot-operated design was selected in which the gas pressure in the supply tank provides most of the force required for acceleration and deceleration.

The valve operation proceeds as follows (with reference to Fig. 3.4). Initially, the slider is closed, the supply tank (A) is pressurized, and both the downstream flowpath (B) and the damping chamber (C) in the slider (D) are evacuated (the damping chamber is connected to the dump tank via three 2.54 cm diameter lines in one of the shaft support struts (G)). To start the opening sequence, the 10 cm diameter pneumatic pilot cylinder (H) on the valve centerline is actuated from a small high pressure argon cylinder (I) by a solenoid valve (J). The pilot cylinder accelerates the slider forward, breaking O ring seals (K) and (L). The downstream flowpath now fills with gas since the nozzle guide vanes act as a downstream orifice. The damping chamber is also filling but at a very low rate since the area of the gap formed by the orifice plate (E) and the power cylinder (M) is very small, 0.5 mm. Thus, a pressure difference is developed across the conical slider surface, which provides the force necessary to accelerate the slider. This is the acceleration period (Fig. 3.5). Once the slider moves sufficiently far so that the power cylinder is no longer over the orifice plate, the damping chamber rapidly fills to supply tank pressure through the annular gap, reducing the net force on the slider to zero. This is the coast period. The slider motion next carries the damping cylinder (N) over the seal plate, closing down the gap from the damping chamber to the supply tank. Further slider motion now compresses the gas in the damping chamber, decelerating the slider smoothly to a stop.

Excessive bouncing of the slider is reduced by the small leakage through the seal plate-damping cylinder gap, by leakage through the vacuum lines in the shaft, by non-adiabatic effects, and by residual pressure in the pilot cylinder. Any residual mechanical energy in the system is absorbed by springs (O) and a crane damper (P).

A fairly detailed mathematical model of the system's dynamics and fluid mechanics was constructed to aid both in the conceptual and detailed design of the valve and in its initial testing. The valve was designed with the aid of a fairly detailed mathematical model of the system's fluid mechanics and dynamics. The variables considered include slider mass, orifice areas and discharge coefficients, power and damper cylinder lengths, friction, leakage, damper and spring dynamics, and pilot pressures and volumes as shown in Fig. (3.6). All fluid flow is assumed one-dimensional and adiabatic. Because the valve represented a substantial fraction of the overall facility investment, extensive design trade and sensitivity studies were performed upon those parameters, especially the orifice discharge coefficients, which were hard to quantify initially. Upon delivery, the orifice areas and discharge coefficients were first calibrated by monitoring the damping chamber pressure while moving the slider with the pilot cylinder alone and then fitting the computer model to the data. The predicted pressure, force, velocity, and position behavior is shown in Fig. (3.7) for a full-scale blowdown run at room temperature. A comparison of the calculated versus measured performance (Fig. 3.8) shows good agreement (slightly more bounce in the actual valve than predicted), thus confirming the fidelity of the model and the proper operation of the valve. Note that the valve is full open (full open is defined as the minimum position in which the smallest valve area is equal

to the largest downstream area) 50 ms after the main seal breaks.

Several mechanical design features of the valve are worth noting. The slider is carried on graphite rings (Q) which slide on the main shaft (R). The shaft surface is carbonized to a hardness of Rockwell 55C to eliminate wear. The main slider seals against a self-aligning (elastomer mounted) seating ring (S), thus reducing the manufacturing tolerances required. To insure controlled thermal growth and reduce facility setup time, the main frame, shaft, and slider are oil heated. The slider position is monitored by a fiberoptic array in the shaft. The bifurcated fiberoptic bundles are brought through a pressure/vacuum seal to externally mounted illuminators and sensors. The chamber pressure is measured with a high temperature pressure transducer mounted on the seal plate.

The valve dynamics are not independent of supply tank pressure and gas composition. Damping, in particular, is sensitive to the operating conditions. If operation considerably off the design point conditions is required, the dynamics can be fine tuned with an external throttle valve on the vacuum line from the damping chamber to the dump tank. Coarser adjustment must be done by altering the lengths of the power and damping cylinders.

The main valve has been tested at room temperature in air, carbon dioxide, and an argon-Freon mixture, and at several supply tank pressures in order to further verify that the computer model accurately simulates the valve dynamics, as well as at design temperature and pressure (400°F at 65 psia). Performance has been completely satisfactory and very close to prediction.

3.2 Test Section

The test section contains the inlet section, nozzle guide vanes,

rotating assembly (including the turbine rotor and eddy brake), the exhaust channel, and the throttle. Figure (3.9) shows the rig flow path while the test section is detailed in Fig. (3.10). MIT was responsible for the preliminary design of the test section while Rolls-Royce Inc. was responsible for the detailed design and construction.

The test section is designed to operate at room temperature. A silicone rubber thermal barrier is used at the upstream mating plane with the main valve to restrict heat flow from the hot valve. Water circulation in small manifolds on the inner and outer annulus walls helps maintain room temperature conditions in the test section. Three struts support the upstream inner annulus and carry the inner boundary layer bleed, the coolant flow, and instrumentation wiring. These struts mate with the three struts in the main valve.

Immediately downstream of the struts are boundary layer bleeds on the inner and outer annulus walls which are sized to remove up to 30% of the total mass flow in order to insure clean inflow to the turbine. The bleeds are manifolded together and discharge to the dump tank. There is sufficient space at this station to permit the later addition of turbulence generation grids. The boundary layer bleed is followed by a rapid flow path contraction to the nozzle guide vanes (NGV's), thus duplicating the geometry in the Rolls-Royce Limited rig in which this stage was originally tested.

The rotor flow exits into a constant area duct which in turn discharges radially into the dump tank. A sleeve throttle on the annular discharge is used to adjust the downstream flow and thus set the stage pressure ratio. The rotor cooling air path is isolated from the main flow path by standard knife edge seals.

The rotating assembly is supported by two 100 mm diameter, high-speed angular contact ball bearings with the rotor and eddy brake drum overhung from either end. The bearings are operated in vacuum and are lightly grease lubricated to avoid problems with oil contamination. The short run times preclude the need for bearing cooling. Vibrometers are located on each bearing mount to monitor the rotating system condition. The rotational power is provided by a 10 KW d.c. drive motor.

The turbine rotor hub contains a mounting can for rotating system electronics. A 50 channel slip ring assembly is mounted to this can through a flexible coupling. A 732 count per revolution (12 per blade) optical encoder monitors the rotor angular position and speed. The encoder, slip rings, and drive motor operate in the laboratory environment (STP air) and are isolated by carbon face seals from the test section environment (vacuum to 10 atm).

The rotating system has been tested to 150% of design speed without the rotor mounted and at 125% speed as a complete unit. No vibratory problems have been encountered. One per rev movement at the bearing housing as inferred from accelerometer measurements is 5 μm (0.2 mil) during a full pressure test.

The eddy brake consists of a thin wall (6 mm), 1/4 meter diameter Inconel 718 drum rotating in the magnetic field of 10 U-core magnets. The magnet assembly can be mounted on load cells (as indicated in Fig. 3.10) which would then act as the turbine torque meter. The construction of the torque meter has been deferred, however, in favor of attempting to calibrate the eddy brake torque vs. speed characteristics to the 0.5% level, thus obviating the need for a separate torque meter. The eddy brake is described in more detail in the following section.

What happens if the brake fails to actuate? Turbine rotor runaway is a concern in all turbine rigs, not just the blowdown turbine facility. The solution adopted in this case has been to design the maximum safe rotational speed to be equal to the calculated peak runaway speed. This has been estimated at 12,000 rpm (twice the normal operating speed) by assuming that all the potential energy in the supply tank is converted to rotational energy, a conservative over-estimate. The rotating system design was greatly simplified by the fact that 12,000 rpm is the operating speed for which this particular rotor was designed for conventional rig testing at Rolls-Royce Limited.

Instrumentation and optical access is provided by three 13 cm wide windows spaced 120° apart around the outer case. These windows extend from upstream of the NGV's to 11 cm downstream of the rotor. The NGV's, whose coolant originally entered from the tip, have been modified to a hub feed configuration in order to provide unobstructed access for instrumentation and optical studies.

The rotating system bearings and shaft have been sized to carry the additional load of a rotating system probe-traversing mechanism mounted immediately behind the rotor.

3.3 Eddy Brake

Although simple in concept, the eddy current brake proved to be a challenging design problem. An eddy current brake is basically an electrical generator. The motion of a conductor through an applied magnetic field induces a current in the conductor which results in a (Lorentz) force in opposition to the motion. This force (or torque in rotating geometry) provides the braking. The power absorbed appears as the resistive heating from the induced current circulating in the moving

conductor. When the induced magnetic field is small compared to the applied magnetic field, the braking force is linearly proportional to the velocity past the magnet poles. As the the velocity is increased, the induced field strength grows relative to that of the applied field and the induced field begins to exclude the applied field from the conductor. This reduces the incremental rise of breaking force with speed (i.e., reduces the slope of force versus speed curve) until the critical speed is reached, at which point the induced field strength equals that of the applied field and the braking force begins to decrease with increasing speed. A detailed analysis of the brake can be found in Appendix B.

A simple model of the basic eddy current brake torque versus speed characteristic is the induction motor model which closely approximates the brake behavior up to the critical speed, ω_o:

$$T = kB_o^2 \frac{\omega}{1+(\omega/\omega_o)^2} \tag{3.1}$$

where T is the torque; k, a constant established by geometry and material properties; B_o, the applied magnetic field strength; ω, the angular velocity; and ω_o, the critical velocity at which the induced field strength equals that of the applied field. This relation is plotted in Fig. (3.11). At speeds low compared to ω_o, the torque versus speed relationship is linear. Clearly, we wish to design the brake so that the brake critical speed, ω_o, is well above the turbine operating speed and would prefer to be on the linear part of the curve.

The critical speed is a function of geometry and material properties,

$$\omega_o = \frac{\pi(2g/\tau)}{\mu\sigma\Delta r} \tag{3.2}$$

where μ is the permeativity of free space; σ, the conductivity of the

conductor material; 2g the gap between adjacent poles of the magnet; τ, the pole pitch of the magnets; r, the radius from the center of rotation; and Δ, the thickness of the conductor.

The geometric design parameter, k, can be written as

$$k = nA_p\sigma_{eff}\Delta r^2 M \tag{3.3}$$

where A_p is the cross-sectional area of the magnetic pole face normal to the direction of the applied field; n, the number of poles; and M, an empirical field fringing parameter approximately 1.2 to 1.7 ($M \sim A_g/A_p$ where A_g is area of the applied field on the drum, per pole).

The simplest design is one in which the moving conductor serves as a heat sink for the resistive dissipation. It is uncooled during the test with its temperature rising as power is absorbed. The principal design problem arises from the high rotational speed required by the turbine compared to other applications more typical of eddy brakes. This forces the conductor radius (r) and thickness (Δ) to be small (Eq. 3.2) in order to keep the critical speed high, which in turn reduces the conductor volume and thus the amount of mass available as a heat sink.

Two design solutions were adopted which enhanced the viability of the eddy brake concept. The first was to use a drum rather than a disk configuration. With the drum geometry, the conductor moves at a uniform linear velocity past the magnet poles, while for the disk, the velocity varies with radius. The drum thus reduces the peak velocity for a given average velocity and power absorption. Another substantial advantage is that the analysis of the drum configuration is considerably simpler than that for the disk with a concomitant reduction in design uncertainty.

The second design decision was to optimize the choice of drum

material. Non-magnetic stainless steels are used in eddy brakes because of their high resistance, high strength at temperature, and ready availability. A comparison with aerospace nickel alloys in Table 3.1 shows that a substantial advantage can be realized in both resistivity and strength at temperature by using the more exotic materials. A suitable forging of Inconel 718 just happened to be available and was therefore chosen for the drum.

TABLE 3.1
COMPARISON OF EDDY BRAKE DRUM MATERIALS

Alloy	Resistivity (σ) $10^6 \cdot (\Omega \cdot cm)$	Yield Strength (0.2%) 20°C	550°C (ksi)
314 S.S.	76.8	50	30
321 S.S.	71.8	30	22
347 S.S.	72.8	35	24
A-286	91.0	105	88
Inconel 625	129.0	71	59
Inconel 718	124.0	172	154

A cantilever drum design was adopted for reasons of simplicity. This imposes a limit on the drum length to diameter ratio due to structural dynamical stability considerations. (The drum is mechanically excited at its rotational frequency times the number of magnet poles.) The drum structural dynamics were analysed by Rolls-Royce Inc. and the 15 cm drum length selected has proved free from dynamic problems. The calculated temperature rise in the drum, ignoring conduction at the end, is 340°C (600°F) at the design Reynolds number (3×10^6) for the ACE turbine presently installed and would be twice that at the maximum facility inlet pressure condition. The design geometry of the eddy current brake is summarized in Table 3.2.

TABLE 3.2
EDDY CURRENT BRAKE CONFIGURATION SUMMARY

Nominal Operating Point----ACE Turbine design point at scaled test conditions

Power	P = 1,078,000 watts
Speed	N = 6190 RPM

Machine Configuration------Cylindrical electrically conducting "loss" drum attached to main shaft, excited by circumferential array of alternating d.c. electromagnets.

Loss Drum

Material	Inconel 718		
Physical properties			
Magnetic permeability	μ =	$4\pi \times 10^{-7}$ H/m	
Electrical conductivity	σ =	0.801×10^{6} $(\Omega\text{-m})^{-1}$	
Density	ρ =	8.19 g/cc	
Specific heat	C_p =	427 J/kg-K	
Configuration			
Mean radius	r =	0.1619	m (1.00 in)
Thickness	Δ =	6.35×10^{-3}	m (0.25 in)
Axial length (min. active)	w =	0.1524	m (6.0 in)

Excitation Magnets

Cores			
Material	Grade M-6 transformer stock and ingot iron		
Saturation limit	Approx. 20,000 Gauss		
Number of poles	n =	20	
Pole width (circumferential)	2a =	0.0254	m (1.00 in)
Pole length (axial)	2b =	0.1524	m (6.00 in)
Pole pitch	τ =	0.0509	m (2.003 in)
Mechanical airgap	l_g =	0.0127	m (0.50 in)
Coils			
Turns	N =	444 turns per coil #23AWG magnet wire	
Resistance	R_c =	~12 ohms per coil	
Inductance	L_c =	~0.12 henrys per coil	
Power dissipation	P_c =	2700 watts per coil @ 15A excitation	

Machine Characteristics

Magnet time constant	τ_c =	0.010 sec
Drum effective conductivity	σ_{eff} =	0.721×10^{-6} $(\Omega\text{-m})^{-1}$
Drum axial resistance	R_D =	3.27×10^{-5} Ω
Induced current (equivalent axial)	i_{eg} =	175,000 amps @ 1 MW dissipation
Drum heating	ΔT =	290°C per 10^6 joules absorbed

The eddy brake magnets are required to provide a 0.7 tesla magnetic field across the 1.25 cm gap, rise from zero to full field strength in 50ms, and provide a constant strength field for periods up to one second. Brake critical speed considerations discussed above dictated 20 magnet poles. Initially, an induction motor-like design consisting of 20 poles on a common circular yoke (Fig. 3.12) was considered. This was rejected in favor f a 10 U-core configuration for reasons of manufacturing cost and uncertainty in the electro-dynamic design of the drum. The cores are laminated from 0.38 mm thick transformer steel (M6) in order to reduce the rise time of the magnetic field. A magnetic return path inside the eddy drum is laminated from the same material.

The U-core arrangement permits ready adjustment of the magnet gap, g, which could be used to change the brake critical speed, ω_o, should the initial calculation have proved in error. However, the manufacturing costs of the U-core were not substantially less than the induction motor design would have been; the brake dynamics closely followed prediction so that magnetic gap adjustment was not required, and the U-core design had a flux leakage problem not initially appreciated. Thus, in retrospect, the induction motor design would now be the arrangement of choice.

The magnet coils were initially designed with 444 turns of 20 AWG copper wire on a 4.5 cm high core. The magnets in this configuration did not behave as designed, however, and produced a field across the drum only 75% of that required for full scale facility operation. The measured torque versus magnet current characteristic indicated that the magnet cores were saturating at relatively low gap field strength. Re-analysis of the magnet design revealed a serious field leakage problem between the arms of the U-cores. Basically, the arms of each core and its neighbors form

additional gaps in parallel with the gap across the drum. Since these magnetic gaps behave much as parallel resistors, the field through the drum gap is considerably reduced, by a factor of three in this case. A relatively simple solution was adopted which consisted of (a) the fabrication of new coils wound from smaller wire (23 AWG) to reduce the coil length to 2 cm, (b) positioning the coils at the tips of the magnet arms, and (c) inserting an ingot iron filler in the U-shaped space between the tops of the coils and the top of the U-core. Figure 3.13 shows both the old and new configurations. The net effect of modification is to reduce the leakage by 75%. Reduction of the coil wire diameter increases the power dissipated in the coils to 60 KW and therefore increases the coil temperature rise to approximately 25°C in one second.

The magnet field must be switched on rapidly so that the eddy brake turn on time is comparable to the 50 ms opening time of the main valve, and must then be automatically turned off to prevent overheating and coil burnup. A simple switching circuit (Fig. 3.14) is used to turn on the current.

The power source for the magnets is a 250hp D.C. motor-generator set rated at 250V, 600A continuous service. This generator was never intended to come up to load in 10ms, therefore a water cooled 0.4 ohm ballast resistor is used to initially establish the operating point on the generator load line. A vacuum contactor rated at 50 kV, 150A continuous service is used to switch the magnet coils in parallel with the ballast resistor. Starting from a high load condition, the generator is then able to handle the additional load of the coils with negligible transients.

During brake operation, 800 amps at 200V is drawn from the generator, which has sufficient inertia to provide this overload of current for one

second. The magnets are de-energized by switching off the shunt field excitation to the generator and allowing the current to decay. This prevents the high voltage arcing problems associated with the opening of a large inductive circuit. The generator is protected by both fuses and a fast acting D.C. circuit breaker. The magnet coils are also fused with a 2 to 4 second time constant. One kilojoule varistors are included to protect the switch and magnet coils. Isolation amplifiers are used to protect the data acquisition system channels monitoring the brake currents and voltages from high voltage transients.

The ballast resistor consists of four 2-meter lengths of 0.476 cm (3/16 inch) diameter 0.04 cm (0.016 inch) wall thickness type 316 stainless steel tubing. Forty liters/min of water are pumped through the tubing at 12 atm pressure by a 3 hp gear pump. At this flow rate and pressure, the tube wall heat transfer coefficient, 20 kW/m^2 (750,000 BTU/ft^2 hr), is sufficient for the resistor to absorb 200 KW. Interlock circuitry provides a warning and can shut off the generator field should the resistor cooling flow be lost.

The performance of the power system is illustrated in Fig. 3.15, which shows the total current drawn from the generator, the current through the magnet coils, and the voltage across the magnet coils as a function of time. The magnets are switched on at time zero and the generator field switched off at 1.1 sec. The small droop in coil current (and thus magnetic field strenth) is due to the overloading of the generator. This is advantageous because it extends the turbine constant corrected operating speed period since the fraction of the brake power absorption attributable to stored rotational energy (moment of inertia) decreases with the square of the rotational speed of the turbine. This can be inferred from Fig.

2.2.

The performance of the eddy current brake was measured by energizing the magnets while the turbine was rotating in vacuum. Thus, the brake is absorbing only the stored rotational energy and the torque can be calculated from the change in rotational speed. Tests were performed with and without the turbine disk-blade assembly mounted to the shaft in order to provide two levels of stored energy (moments of inertia). The moment of inertia was measured using a torsion spring assembly and the absolute accuracy of the brake power absorption is constrained by the accuracy of the moment of inertia measurement. The accuracy was sufficient to obtain corrected speed control to better than one percent during operational runs of the facility. Brake calibration was conducted, however, with the original magnet configuration. Further work is planned, with the new magnets, to determine if the absolute accuracy of brake calibration is sufficient to allow its use as a turbine torque meter.

A measured power versus speed curve is shown in Fig. 3.16, from which a critical speed of ω_o = 770 radians/sec can be inferred.

3.4 Tanks and Auxiliary Systems

Although physically large, the dump and supply tanks are relatively minor facility cost items. The supply tank volume is set by the requirement for a small inlet total temperature drop over the test time, while the dump tank volume controls the time to unchoking of the turbine outlet throttle and thus the run time at constant corrected flow. The volumes are $10m^3$ (364 ft^3) and $16m^3$ (570 ft^3) respectively. The supply tank is double-walled with a 1.6 cm (5/8 inch) gap between walls for oil circulation. The tank is trunnion-mounted on a wheeled carriage to eliminate thermal growth problems. The tank is rated at 10 atm. working pressure.

The oil system is based on a commercial unit consisting of an 80 KW electric heater, 212 l/m (55 gpm) pump, expansion tank, and controls, Fig. 3.17. The joints in the system are welded and connections to the supply tank and valve are by way of flexible metal hose. The heat transfer fluid is a commercial oil (Dowtherm G) rated to 288°C (550°F). The oil can be valved to a pressurized water-cooled heat exchanger to cool down the facility after a test, if required for disassembly.

The tanks are evacuated with a 255 m^3/hr (150 cfm), mechanical vacuum pump through appropriate valves and piping. The dump tank and test section can be evacuated to 70 μm of Hg. A water-cooled heat exchanger in the pump inlet line allows the tunnel to be pumped down immediately after a test to facilitate rapid turnaround.

The argon and freon test gas is metered and mixed as the supply tank is filled. A 15 KW electric heater provides the power to vaporize the freon and warm the argon which is supplied from a tank farm located elsewhere in the building, Fig. 3.18.

Power for the rotor drive is provided by a 12 KW motor generator welding set. A preset digital tachometer initiates the start of the test as the commanded rotor speed is reached.

The auxiliary facility equipment is sized for a 2-3 hour tunnel setup time. The actual cycle time is governed more by instrumentation respotting and data review times than by mechanical considerations.

3.5 Data Acquisition System

The specification of the data acquisition system (DAS) is principally determined by the requirements for detailed examination of the time resolved heat transfer and fluid flow in the high speed turbine. The 6 kHz blade passing frequency and relatively thin NGV wakes (1/5 to 1/10 of the

blade spacing) dictates an analogue bandwidth of 30 to 100 KHz for each channel. The need for simultaneous heat transfer and pressure measurement along the airfoil surfaces requires a large number of channels, 25 to 100. Thus, 5 to 20 million samples per second are required for the 0.1 to 0.4 second test time (considering sampling theorem restrictions), thus producing 1 to 8 million total samples.

The total number of samples that need be taken during a test can be reduced by noting that the data acquisition system need not run at the highest data rate during all parts of the blowdown. Information during the initial startup transient and during post-test flow sloshing is of use principally for tracking transducer drifts, and thus can be taken at relatively modest data rates. The variable data rate requirement can be met with a programmable multispeed clock.

The commercially available data acquisition system which comes closest to meeting these requirements is a CAMAC-based transient acquisition system with local internal memory for each 4-channel cluster. The CAMAC system met most of the blowdown tunnel system requirements but was weak in several important areas. The first was that the 10-bit resolution, but 8-bit accuracy, of the units is marginal for the heat transfer gauges, not because 1 part in 256 is insufficient heat flux resolution, but because of the need to track transducer signals over a wide pretest to post-test range. The second weakness was the maximum of 32,000 samples of memory per channel. The third was the very high memory cost.

As an alternative to the commercial system, a custom designed DAS was considered. This was attractive since the system could be tailored to this application, and it was affordable because a large high-speed memory was available at no increment cost to the experimental portion of the program.

This is the random access memory (RAM) required by the companion computational fluid dynamic (CFD) effort. The preliminary design of the system was done at MIT while the final design and construction was performed by an outside vendor. Not including the cost of the memory, the system is 40% less expensive than the commercial system in its initial configuration and would be 80% less in a fully expanded version.

The DAS is designed for 100 high speed, 12-bit channels with 200 KHz per channel maximum sampling rate. Up to 128 lower speed channels, organized into 8 groups of 16, are multiplexed onto 8 of the high speed channels. The high speed channels are used for the heat transfer gauges and high frequency pressure transducers which record the blade to blade flow, while the low speed channels are used for overall facility monitoring, pitot rakes, etc. The sampling rate is controlled by four programmable multispeed clocks (20 Hz to 200 KHz) which are individually set with a sampling rate and number of samples prior to a test. The data is stored in 32 M byte solid state (RAM) memory for post-test readout to a host computer. The present configuration consists of 45 high speed channels, four 16-channel multiplexers, and a 64-bit wide digital input stream.

The data acquisition system is organized as illustrated in Fig. 3.19. The analogue front end, digital sequencer, and control microprocessor is located adjacent to the blowdown facility. The digitized data is transmitted as parallel 32-bit words to the computer room 200 feet distant. A first in first out (FIFO) buffer smooths the data flow into the semiconductor memory (to allow for memory refresh). The maximum digital data rate is 8.4 M words/sec. or 34 M bytes/sec. The memory is interfaced to a Perkin-Elmer 3242 computer which, along with its attached array processor,

is dedicated to the companion CFD effort, and to a Digital Equipment Corp. PDP 11/70 computer, which is used for the data reduction. The DAS is locally controlled by a Rockwell AIM-65 (6502 μP) microcomputer, which is used to preset the test conditions. The AIM-65 is connected to the PDP-11/70 by an RS-232C serial data link, Fig. 3.19. The AIM-65 program resides in read only memory (ROM) or can be downline loaded from the host.

The overall test sequence is controlled by the PDP-11/70, which instructs the AIM-65 to set the sampling rates and burst lengths and then requests the exclusive use of the 32 M byte memory from the P-E. The DAS can then be armed and placed under the control of the digital sequencer used to operate the tunnel. After a test is complete, the data is read from the memory by the PDP-11/70 for storage on disk and later analysis.

A typical time sequence would run the high speed channels at 20 kHz/ch from the start of test (t = 0) to the start of the matched test time (t = 250 ms), at 200 kHz during the test time (t = 250 ms to t = 550 ms), at 20 kHz to the first tank "slosh" (t = 2 sec), and at 20 Hz for the next 60 seconds as the entire facility comes to equilibrium.

As the data is stored in the PDP-11/70, it is organized into a form compatible with the data-based management system developed for the Blowdown Compressor Facility. The organization has been modified to account for the much larger size of the data stream from the blowdown turbine (Fig. 3.20).

3.5.1 Analogue Front End Characteristics

The 12-bit high speed channels are organized five to a printed circuit card. Each card also contains two 1-bit digital input channels and two party bits. The card output is arranged into two 32-bit words, which are sequentially read onto the 32-bit data bus (Motorola VMEBUS) for transmission to the memory.

Each high speed channel consists of a band limited input pre-amplifier, sample and hold amplifier, and 12-bit 200 kHz analogue to digital converter. The input pre-amplifier span and offset can be changed by jumpers on the P.C. card to ±0.5, ±5V, 0-1V, 0-10V. Channel specifications are listed in Table 3.3.

Signals not requiring the full bandwidth of the high speed channel are input to one of the eight 16-channel, low speed multiplexers (MUX). Each of the 16 multiplexer channels are sequentially switched to a high speed channel input. If all 16 channels of a multiplexer are not required, the microprocessor may select a smaller number (1 to 16) during the pretest setup. Each multiplexer can be individually set. The number of high speed channel groups can be preset at the same time.

3.5.2 Channel Setup and Checkout

Effective operation of a short duration test facility requires that each input signal be checked before each test. With up to 216 separate channels, conventional plugging and unplugging of cables for connection to oscilloscopes or voltmeters can be both tedious and likely to induce errors. To facilitate pretest transducer checkout, the DAS was equipped with a numerical display which can function as a digital voltmeter and an analogue output (12-bit D/A converter) for connection to an oscilloscope. Thus, using the input keyboard, individual high speed and multiplexer channels can be sequentially called up for pretest checkout without the need to disturb the cabling.

The entire system can also be run by the host computer (PDP-11/70) as a data logger, with the output of as many as 40 channels displayed on the screen simultaneously, updated at a rate of about 3 Hz. This data can also be stored for later analysis. This mode is commonly used for transducer

checkout and calibration.

TABLE 3.3
DATA ACQUISITION SYSTEM SPECIFICATIONS

Input Impedance	1 MΩ
Input Range	±0.5V, ±5V, 0-1V, 0-10V
Resolution	12 bits
Linearity	0.012%
Absolute Accuracy	0.1%
Aperture Uncertainty	100 ps
Max Sampling Rate	200 kHz/channel
Max No. of Channels:	
High Speed	100
Low Speed	96
Max Number of Samples	20,000,000

3.6 Flow Instrumentation

Flow instrumentation for the Blowdown Turbine closely resembles that used on the MIT Blowdown Compressor Facility. It consists of time resolved instrumentation including: traversing probes to measure total and static pressures and air angles, wall static transducers on the outer casing wall and NGV and rotor blade surfaces, and a total temperature-total pressure probe. Low frequency response pitot instrumentation can be used where the flow is quasi-steady, as in the annulus upstream of the NGV's.

3.6.1 High Frequency Response Measurement

There are four traversing probes which are initially intended for traversing behind the rotor or the NGV's with the rotor removed. The four-way probe (Fig. 3.21) consists of four semiconductor strain gauge pressure transducers mounted around a 3 mm diameter cylinder. The transducers are arranged such that the probe can simultaneously measure total and static pressure and azimuthal and radial angles (±20°). Data reduction is done with the aid of calibrations performed as a function of Mach

number. (These calibrations have only been carried out to Mach 0.9, however, and will be extended for turbine operation.) The probe is water cooled (or heated) to increase thermal stability. Frequency response is determined by the cylinder size and rolls off above 12 kHz, which is probably marginal for the rotor outflow. The four-way probe is the only instrument small enough to traverse between the NGV's and the rotor, although interference and blockage effects must be determined.

Total pressure can be measured independently using a cobra head impact probe with a transducer mounted one diameter in from the conical probe entrance (Fig. 3.22). This probe is smaller in diameter (2 mm) and thus has higher frequency response than the 4-way probe. It has also proved to have better d.c. stability. Another version of this probe is under construction, incorporating a smaller transducer so that the probe diameter is only 1.4 mm. This class of transducer has poor d.c. stability, however, so that only a.c. information will be available.

Rotor outflow total temperature may be surveyed using a dual wire aspirating probe (Fig. 3.23), which can simultaneously measure total temperature and pressure with a frequency response of d.c. to 20 kHz. This probe was developed for a compressor loss study. The probe's d.c. accuracy is 1%, while its resolution is 0.3%. We are considering attempting to manufacture a 1/2 scale model of the probe (1.5 mm diameter) for future use in the blowdown turbine.

Wall static pressures will be measured on the casing above the rotor and on the NGV and rotor blades. At present, four transducers are being flush mounted on the NGV suction side toward the rear of the blade, at locations previously instrumented at Rolls-Royce Limited. These will serve both as a proof test and a measure of the unsteady rotor influence on the

NGV loading. One transducer is to be mounted on the rotor blade close to the leading edge. This is primarily a test article (although a transducer has been operated on a compressor blade at similar stress levels with satisfactory results). The transducers on the blades must be permanently mounted. Because of their high cost ($1000 per mounted transducer), a cautious approach has been adopted.

Drift and stability are always an important consideration when using high frequency response instrumentation. Development of semiconductor strain gauge transducers over the last 15 years has brought the performance of the best units to a level equal to that of typical conventional transducers (0.04%/°C). Conventional scanning valve pressure recording systems rely as much on continuous on-line calibrations as they do on transducer stability for measurement absolute accuracy. In the blowdown turbine, a similar scheme can be used for traversing probes. The probes reside in a cavity in the tunnel wall, along with a stable reference transducer, so that a reference pressure is known immediately preceding and following the traverse. Thus, it is only the drift during the short traverse time (15 to 200 ms) which can influence the measurements. Also, since the transducers are in vacuum immediately preceding the test and at a stable pressure a few seconds following the test, transducer sensitivity can be absolutely established. The net absolute accuracy of the measurement is about 1% for the more stable probes (total pressure). In general, the pressure transducers agree to within ±0.5% after the test. The static pressure transducers to be mounted on the blades cannot be dynamically calibrated by this technique and their absolute accuracy has yet to be established.

3.6.2 Low Frequency Response Measurement

The steady test time of the facility is long enough to permit the use

of carefully designed pneumatic instrumentation. This is to be used either for comparison with similar measurements taken at Rolls-Royce Limited or as a lower cost scheme for measurements in regions of essentially steady flow.

The comparison studies use conventional Kiel probes four chords downstream of the rotor exit, duplicating measurements taken at Rolls-Royce Limited. These will then be compared with the high frequency total pressure probe results.

Static taps will be used around the NGV chord to record "tube averaged" airfoil static pressure distributions. The advantage of the pneumatic over the high frequency measurements is simply one of cost and time. A dense array of pressure taps (20 per blade) can be installed, but all need not be connected to transducers during each run since the external transducers can be moved. Faulty transducers can be readily replaced. Also, the transducer is in a more benign environment than when surface mounted. The magnitude of the errors induced by the "tube" averaging will be inferred from comparison with the high frequency flush mounted transducers at similar chordwise locations.

3.6.3 Traversing Mechanisms

Two traversers have been designed to permit survey of the rotor outflow with the high frequency response probes. One is for use in the stationary frame which mounts to an instrumentation access window, and the other is designed to be mounted on the rotating assembly directly behind the rotor.

The stationary traverser is designed to make radial traverses at four circumferential locations in 100 ms (see Fig. 3.24). The radial motion is driven by a stepping motor-cam system. Radial position versus time is linearized electronically in the motor drive circuitry. The circumferen-

tial travel, powered by a hydraulic/pneumatic blowdown actuator, is designed to move the unit at constant velocity along a tangent to the test section outer case. (A linear motor drive was considered for its finer speed vs. position control, but rejected due to high cost.) The distance covered is 7 cm, allowing the outflow from 2-1/2 NGV passages to be surveyed. The radial and azimuthal probe positions are monitored by linear differential variable transformer (LDVT) transducers.

The rotating traverser is still in design. A typical configuration is illustrated in Fig. 3.25. The probe and a diametrically opposed dummy balance probe traverse a single radially outward scan powered by the centrifugal load. The probes are mounted on cross-connected hydraulic pistons to insure balance and to control the scan velocity. The probe release is activated through a swash plate mechanism from the stationary frame. Construction of the rotating traverser has been deferred due to overall facility workload.

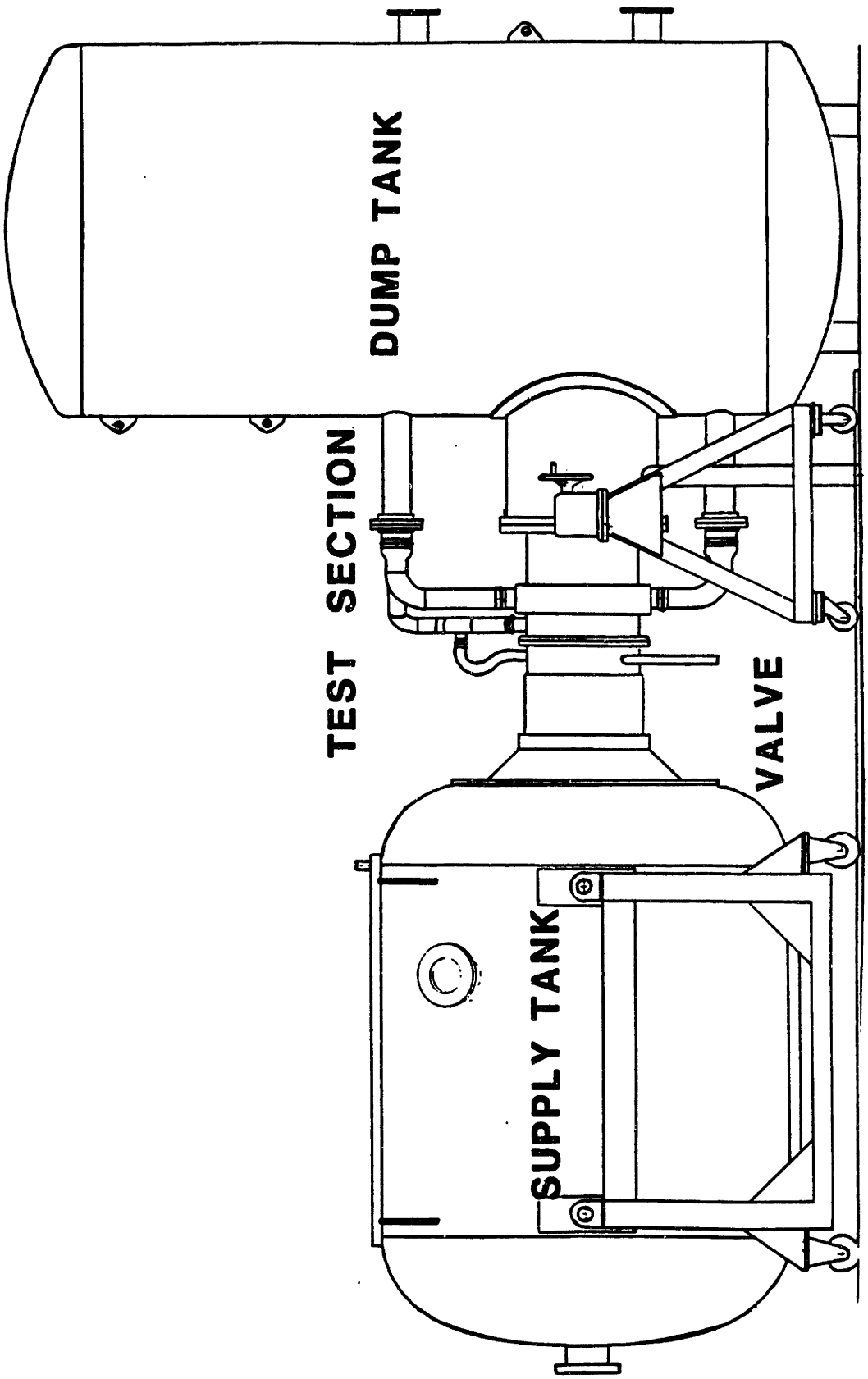

FIGURE 3.1: BLOWDOWN TURBINE FACILITY EXTERNAL VIEW

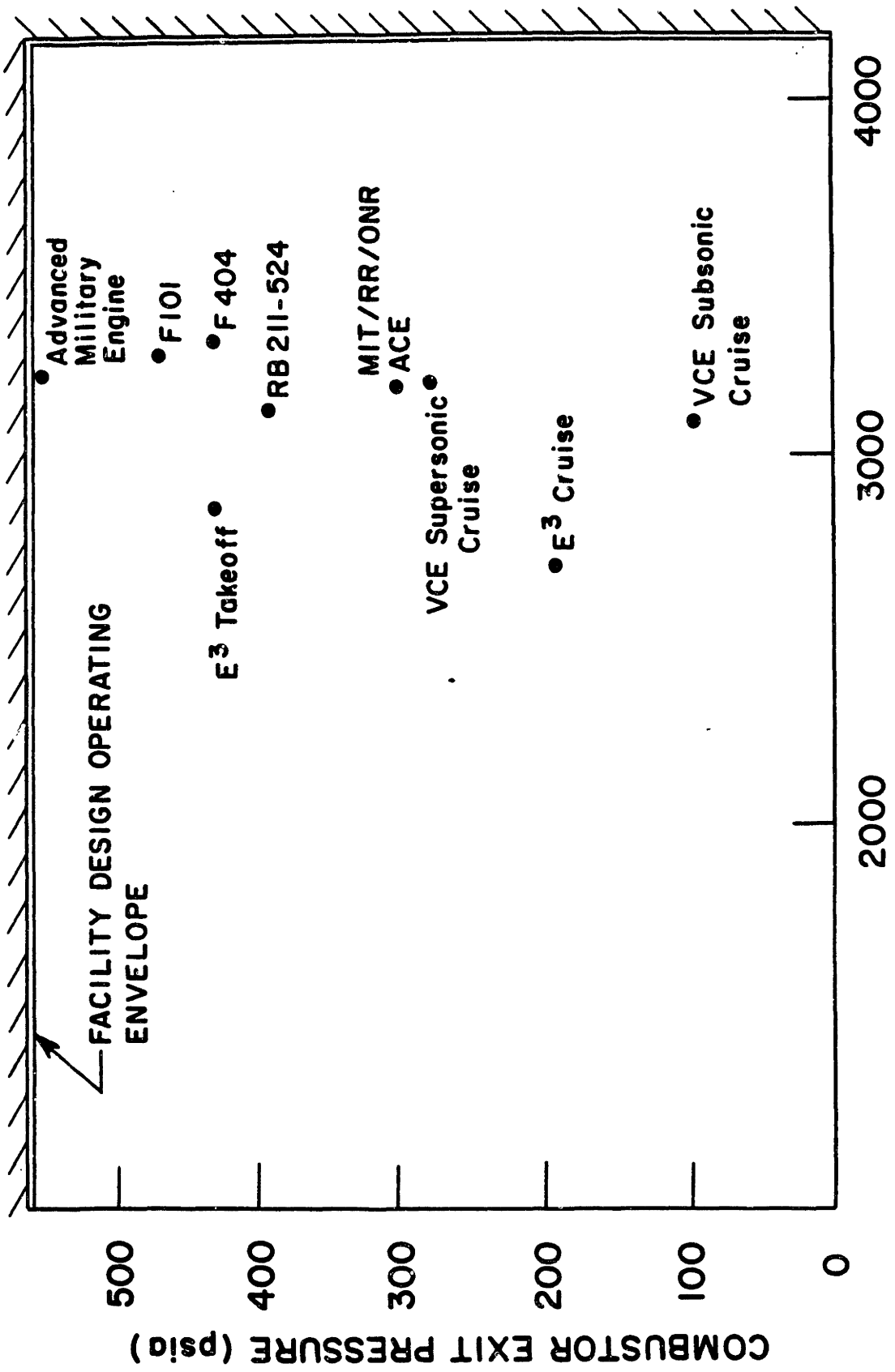

FIGURE 3.2: BLOWDOWN FACILITY SIMULATION CAPABILITY

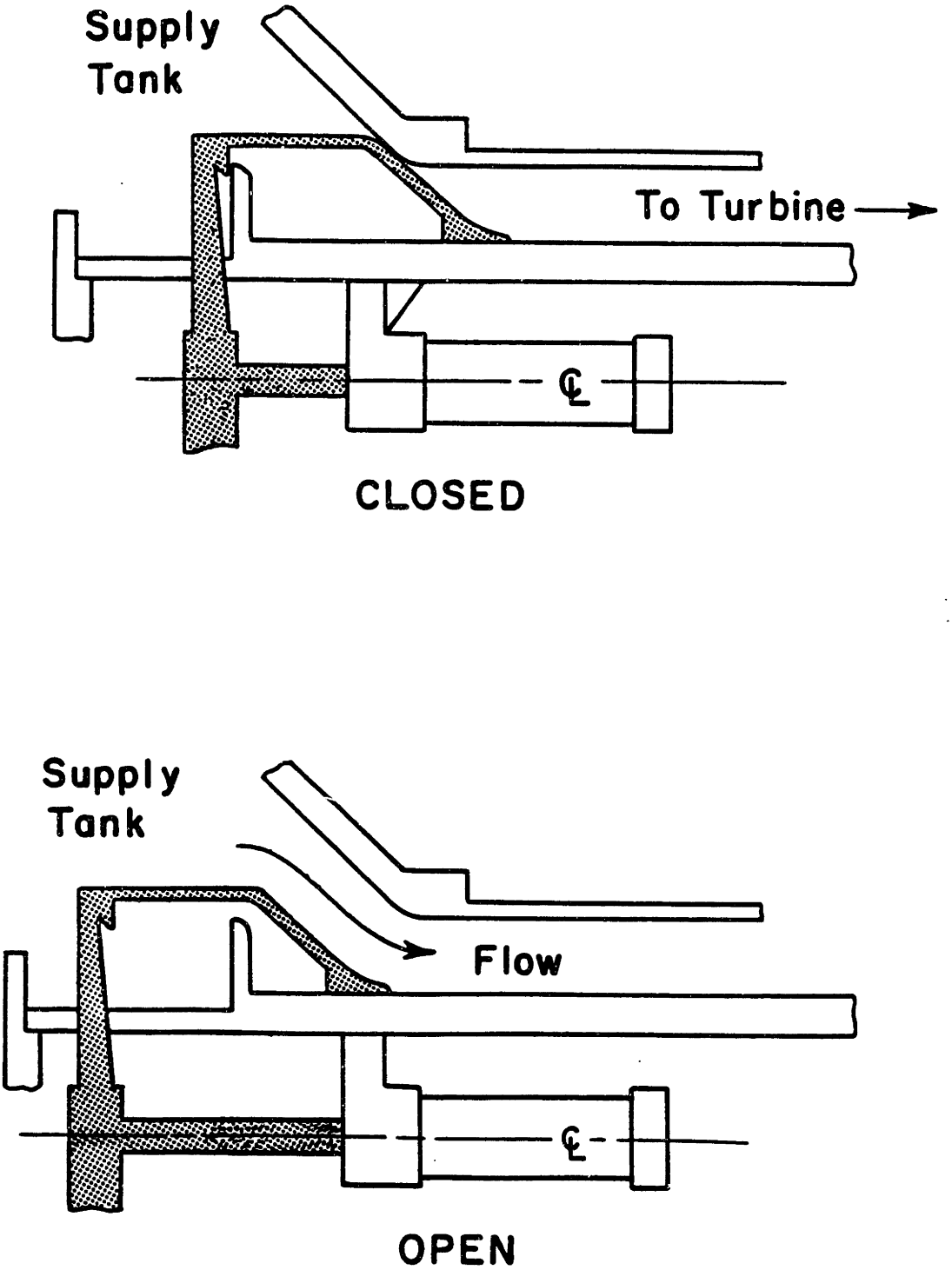

FIGURE 3.3: MAIN ANNULAR PLUG VALVE SCHEME

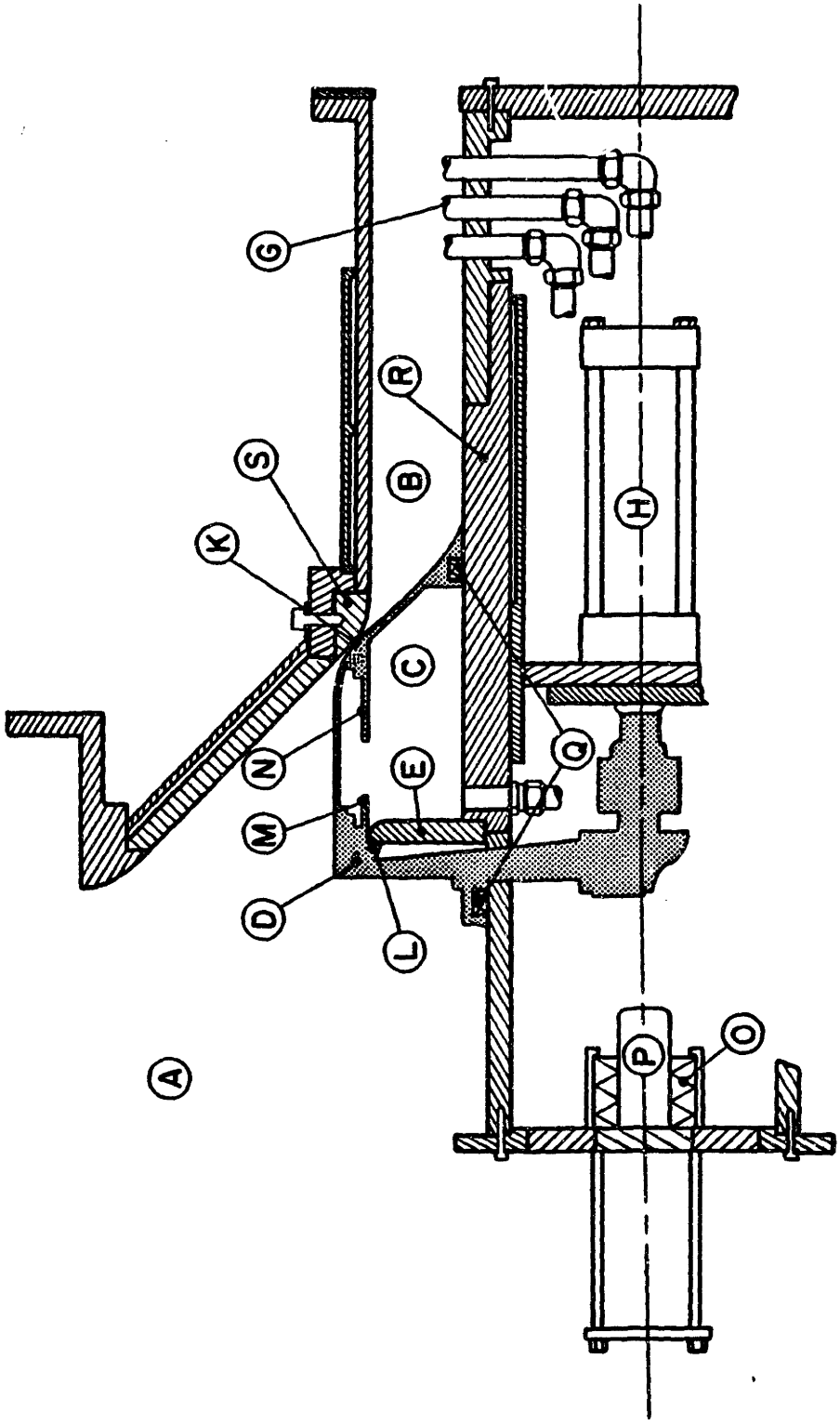

FIGURE 3.4: MAIN VALVE CONSTRUCTION DETAIL

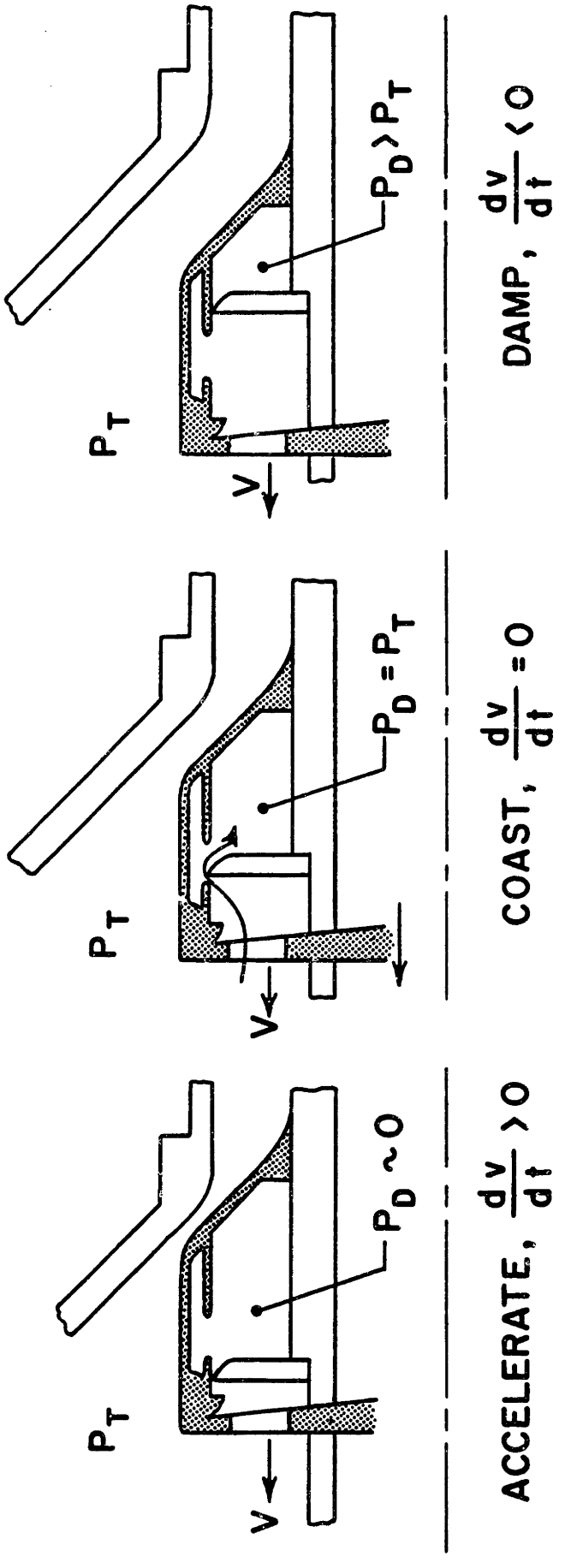

FIGURE 3.5: VALVE ACTUATION SEQUENCE

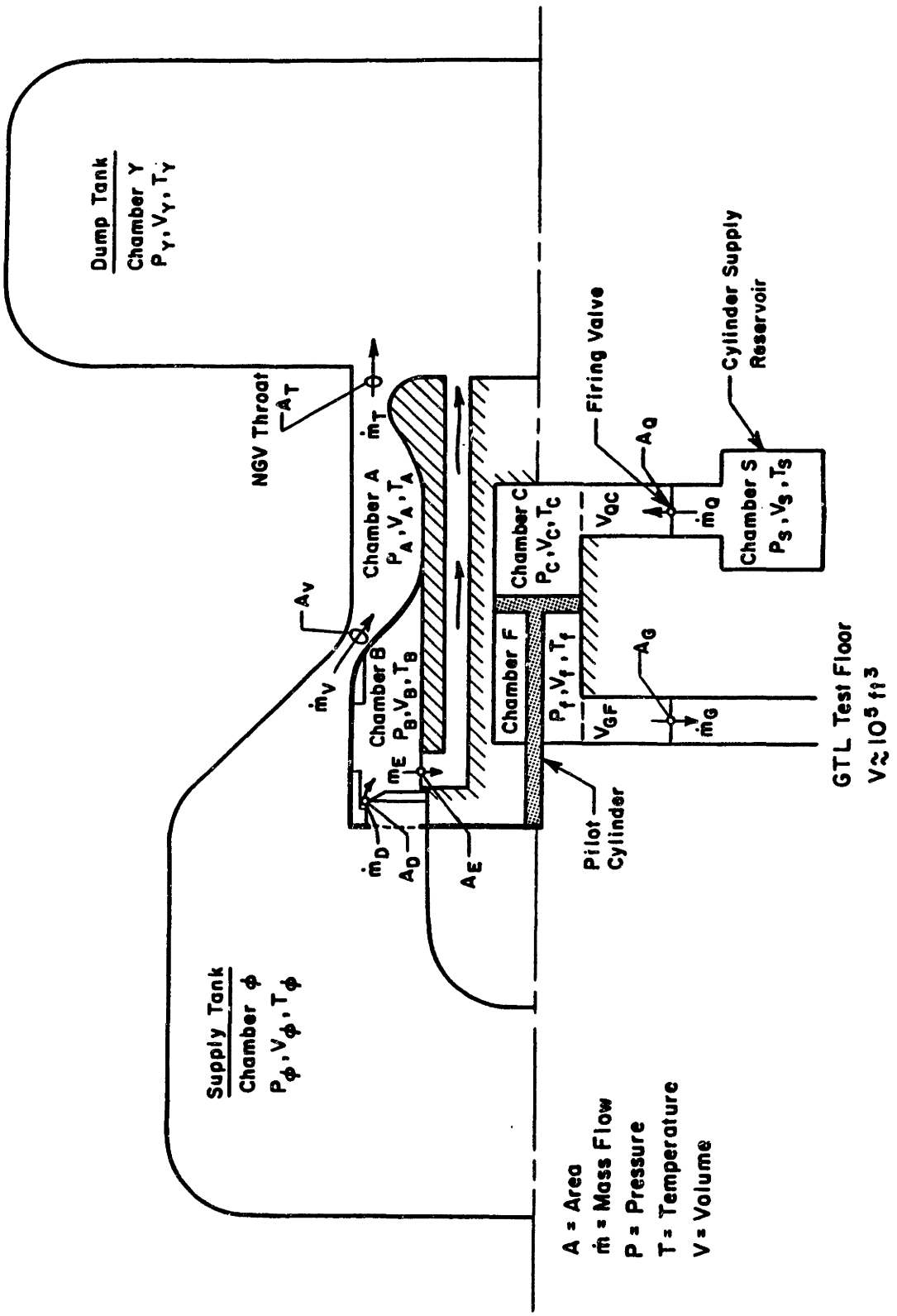

FIGURE 3.6: VALVE ANALYTICAL MODEL CONSTITUENTS

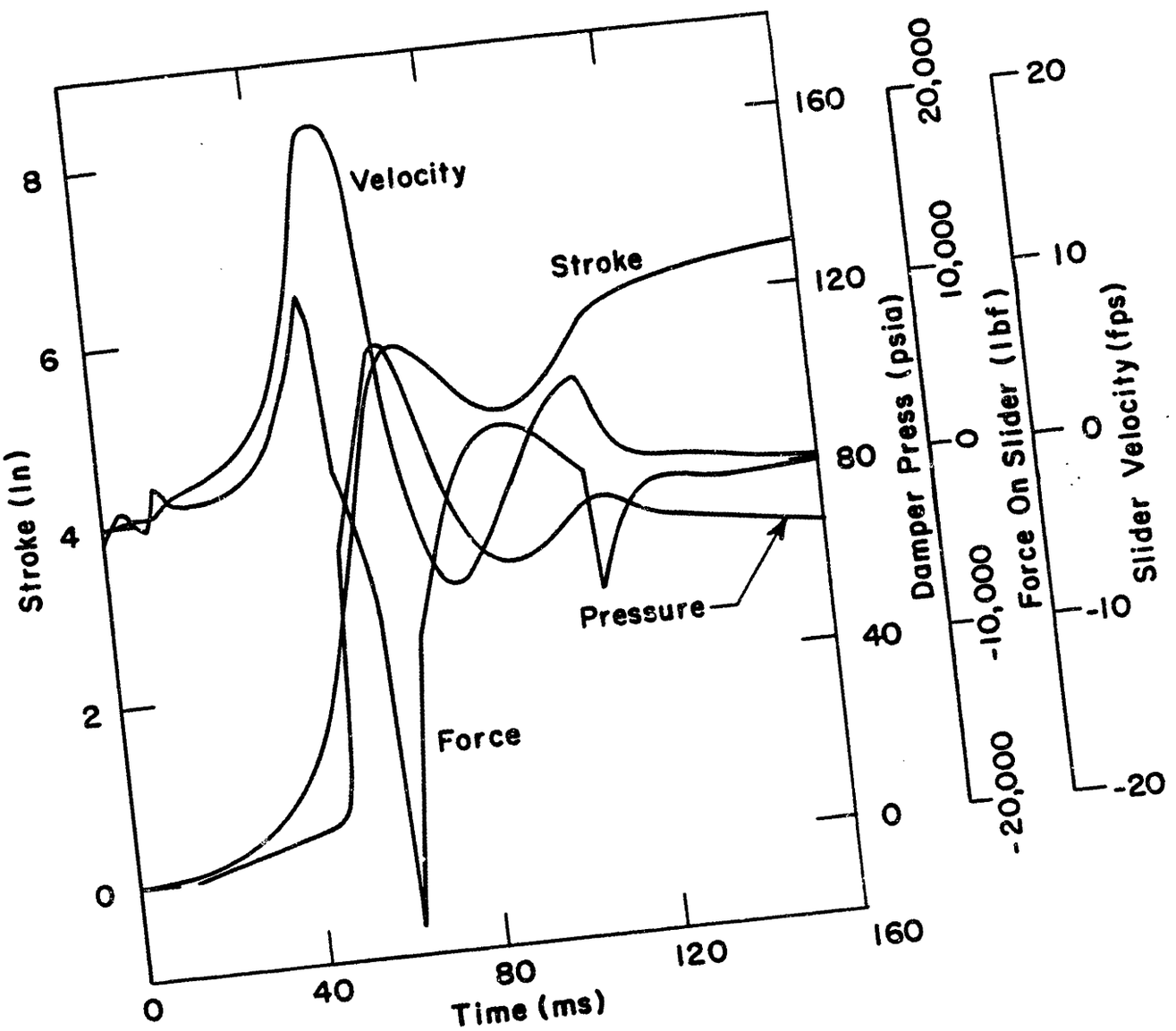

FIGURE 3.7: TYPICAL VALVE MODEL PREDICTION

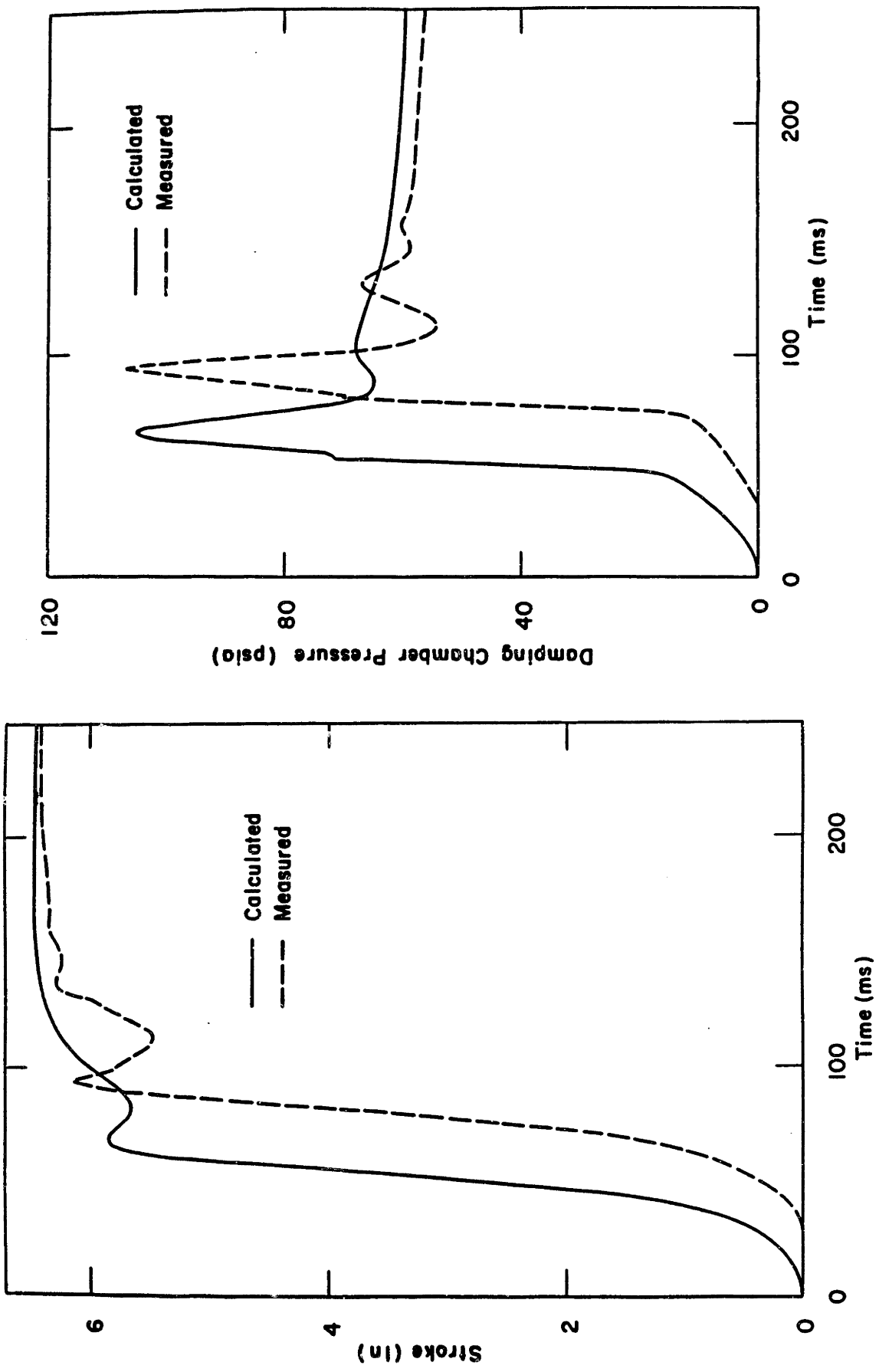

FIGURE 3.8: COMPARISON OF MEASURED VALVE BEHAVIOR WITH MODEL
(MEASURED PLOTS SHIFTED BY 30 MS)

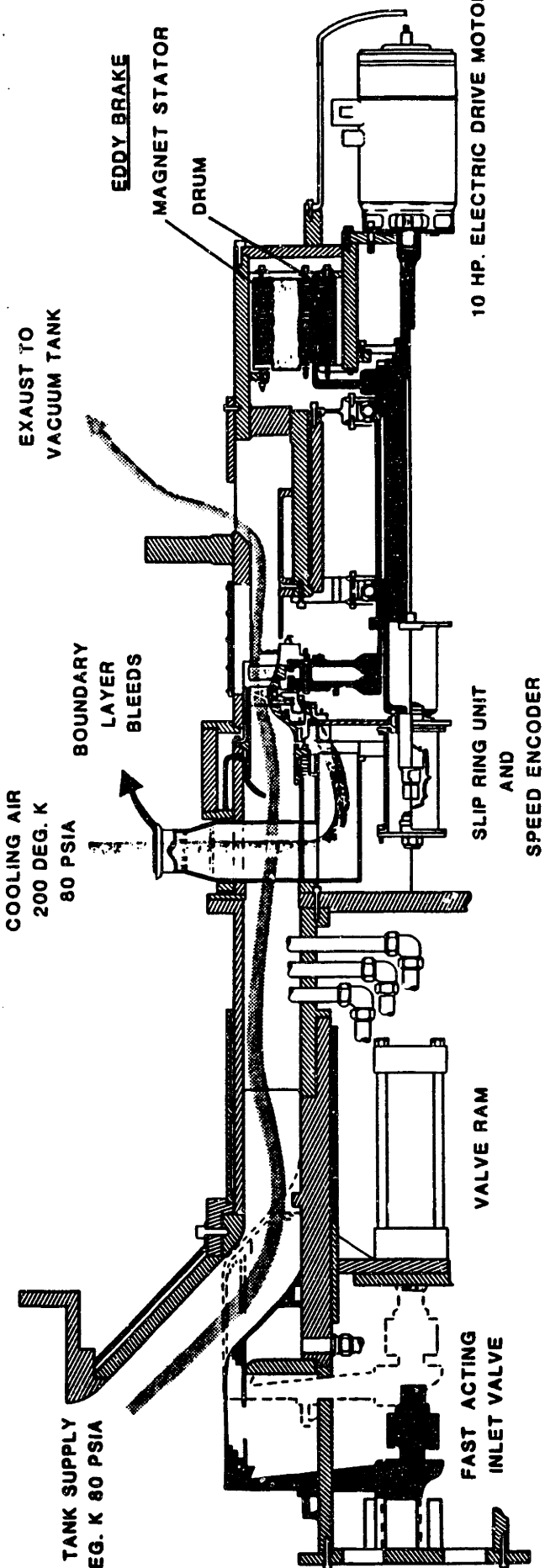

FIGURE 3.9: TURBINE FACILITY FLOW PATH

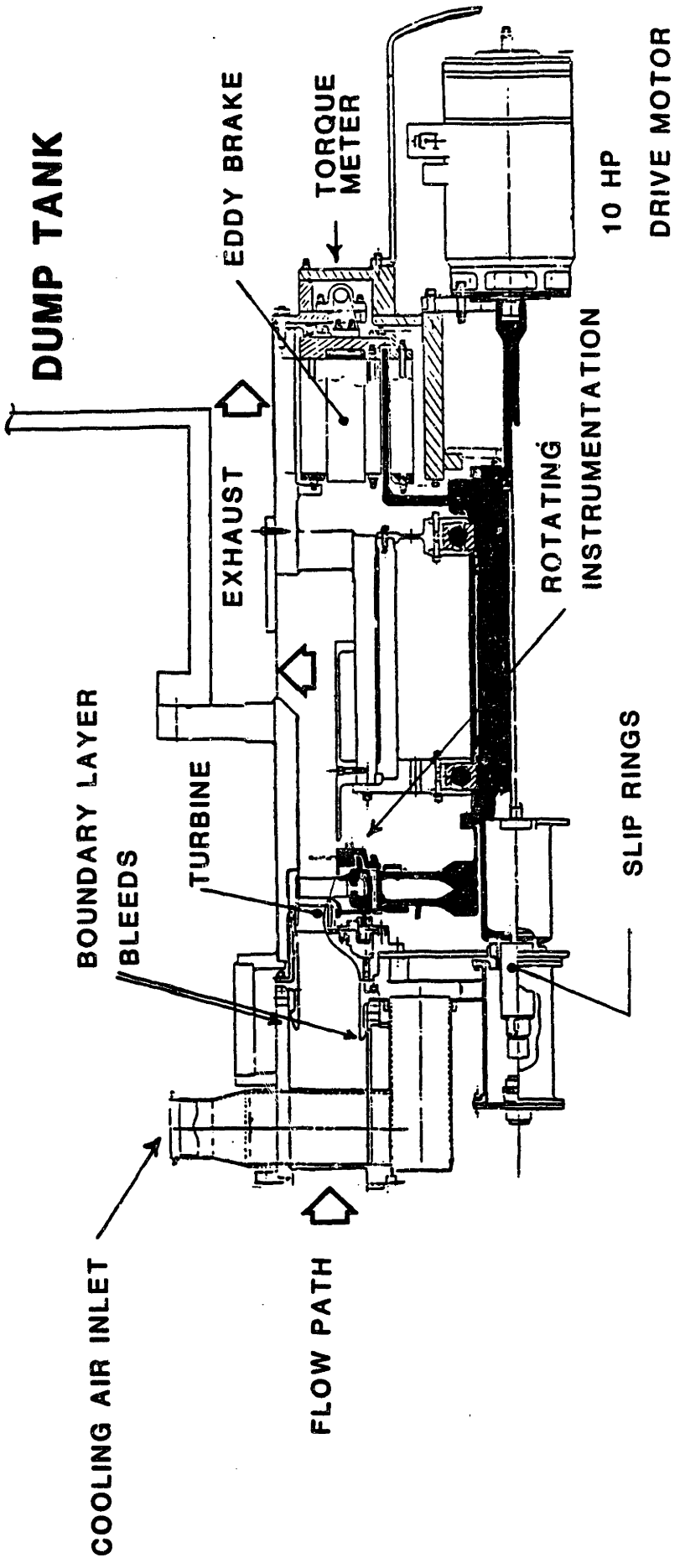

FIGURE 3.10: TEST SECTION DETAIL

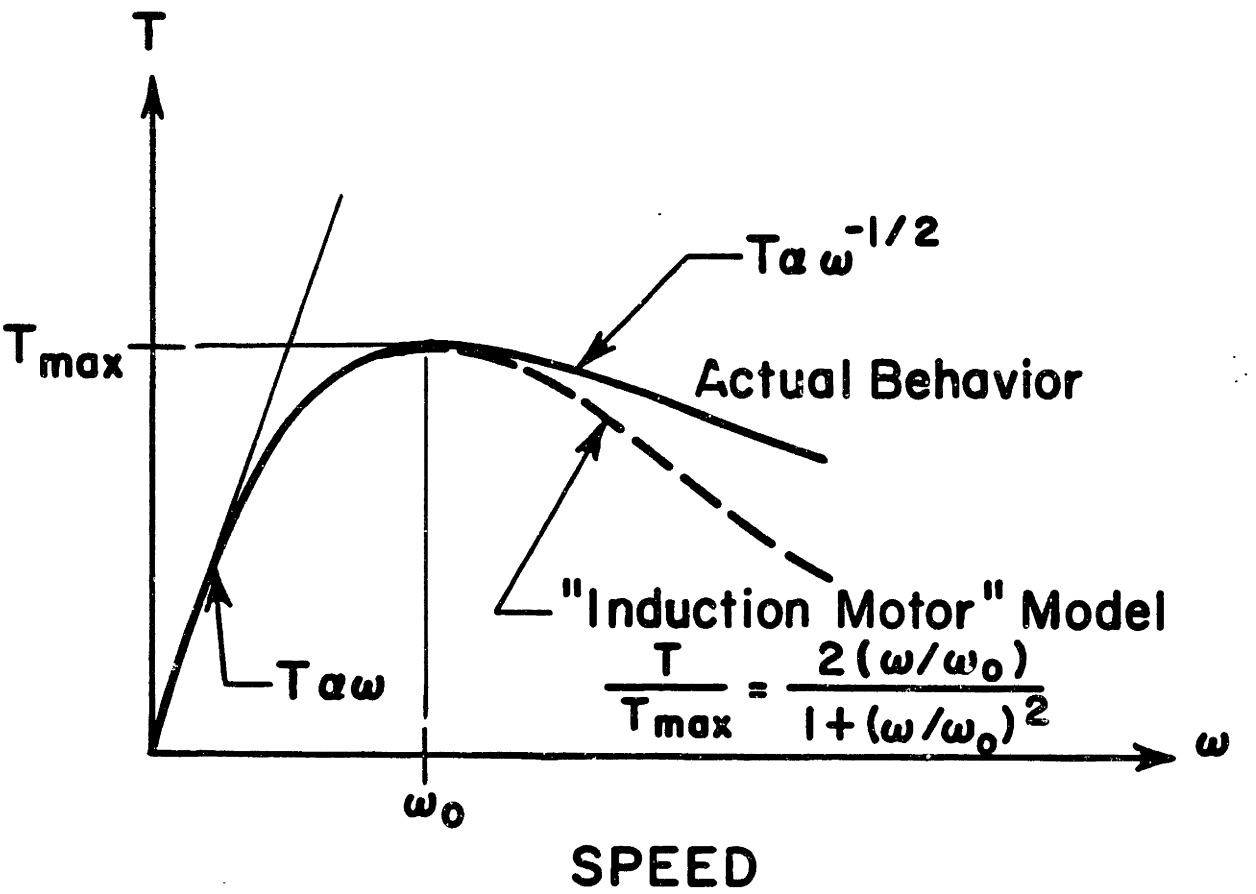

FIGURE 3.11: EDDY CURRENT BRAKE TORQUE VS. ROTATIONAL SPEED

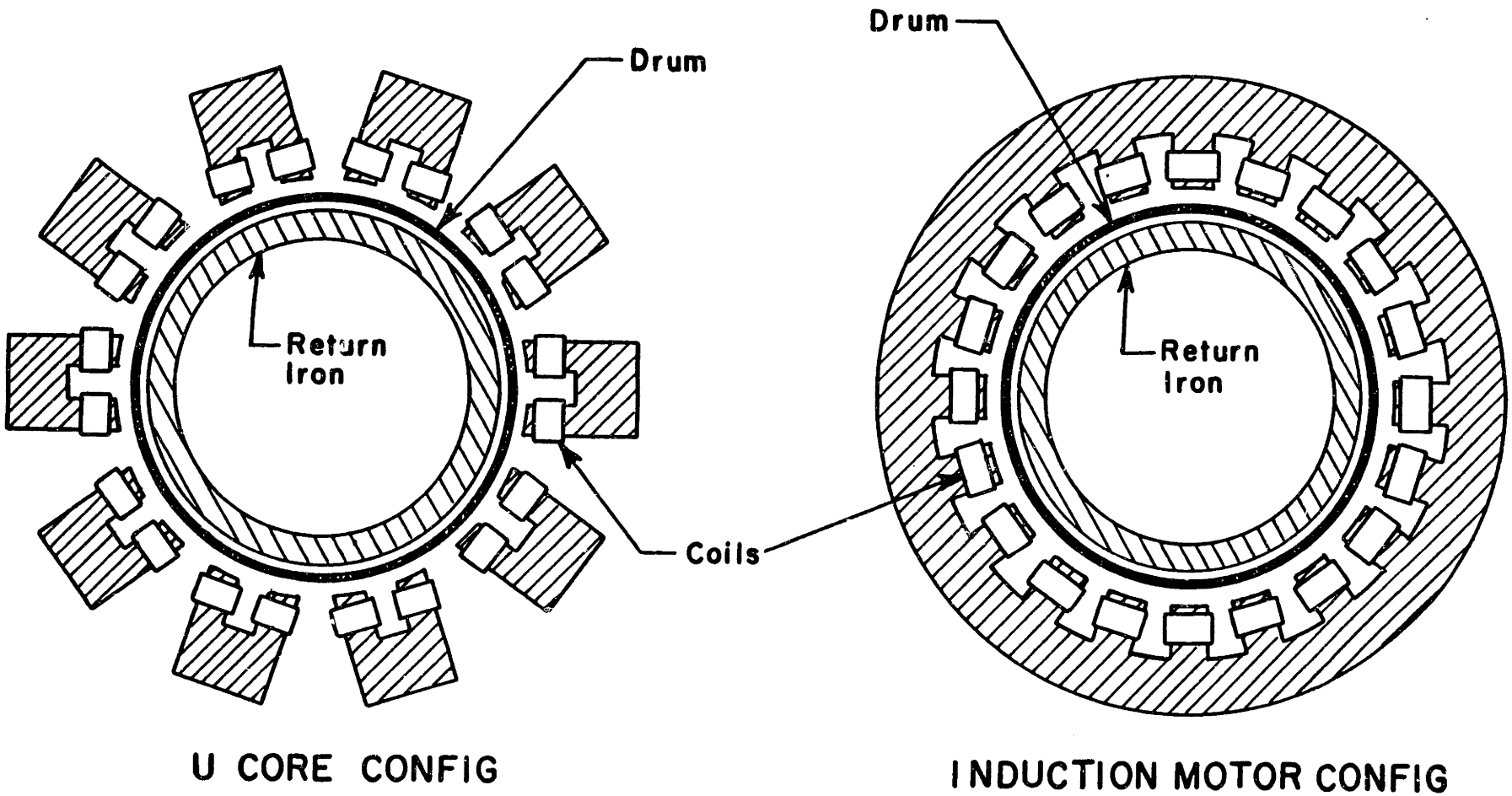

FIGURE 3.12: CANDIDATE EDDY BRAKE MAGNET CONFIGURATIONS

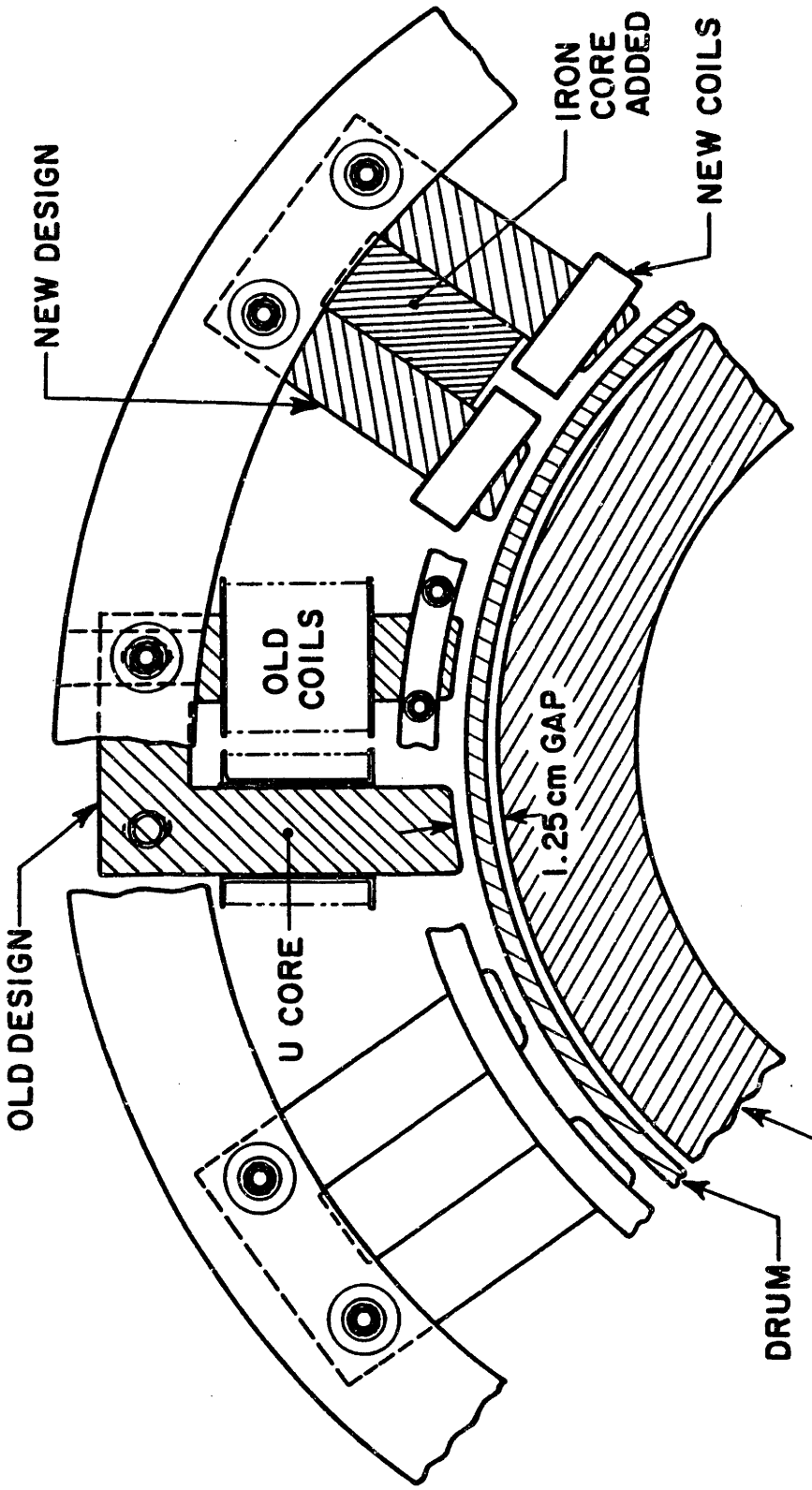

FIGURE 3.13: ORIGINAL AND MODIFIED BRAKE MAGNET DETAIL

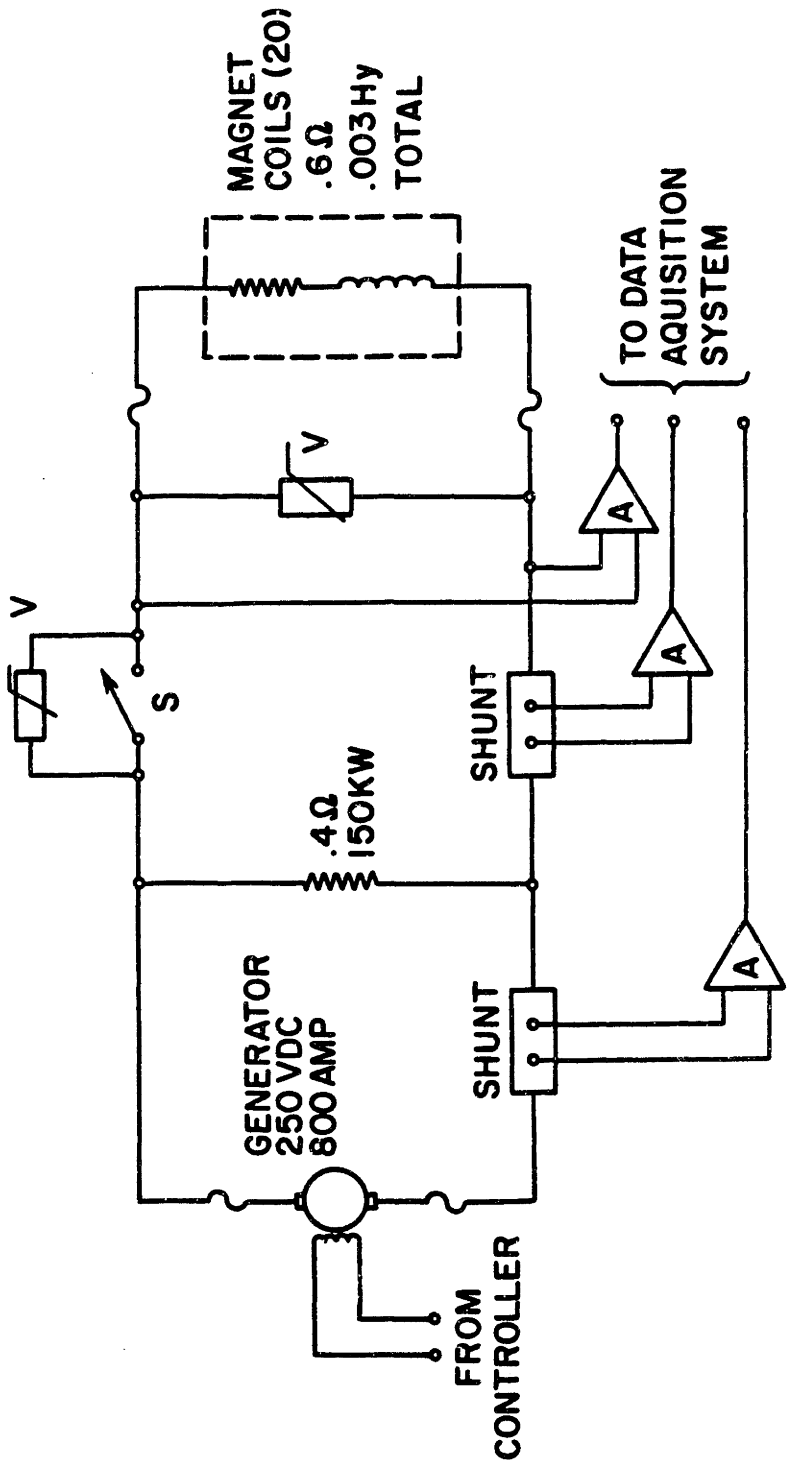

FIGURE 3.14: BRAKE MAGNET CURRENT SWITCHING CIRCUIT

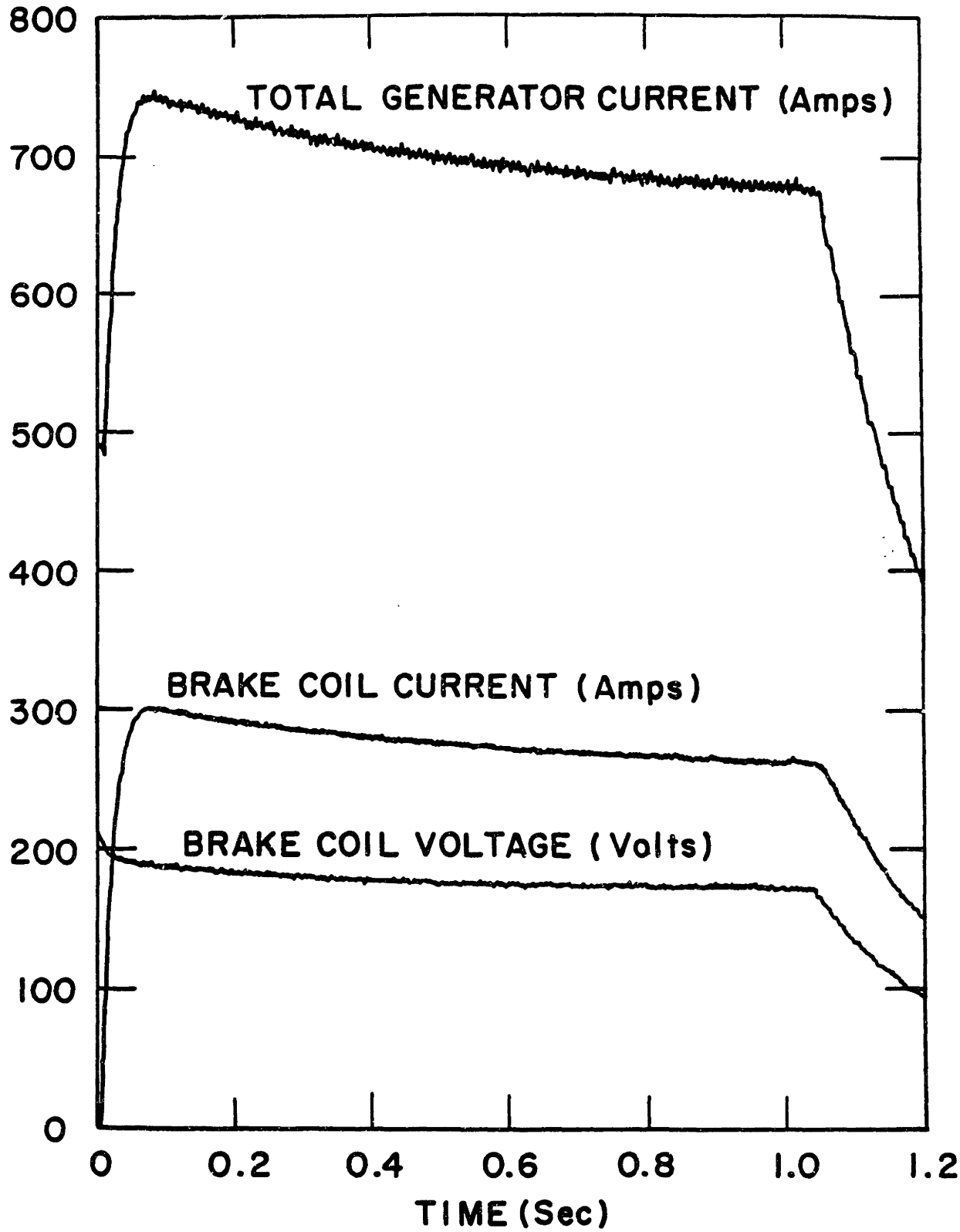

FIGURE 3.15: MAGNET SYSTEM ELECTRICAL PERFORMANCE

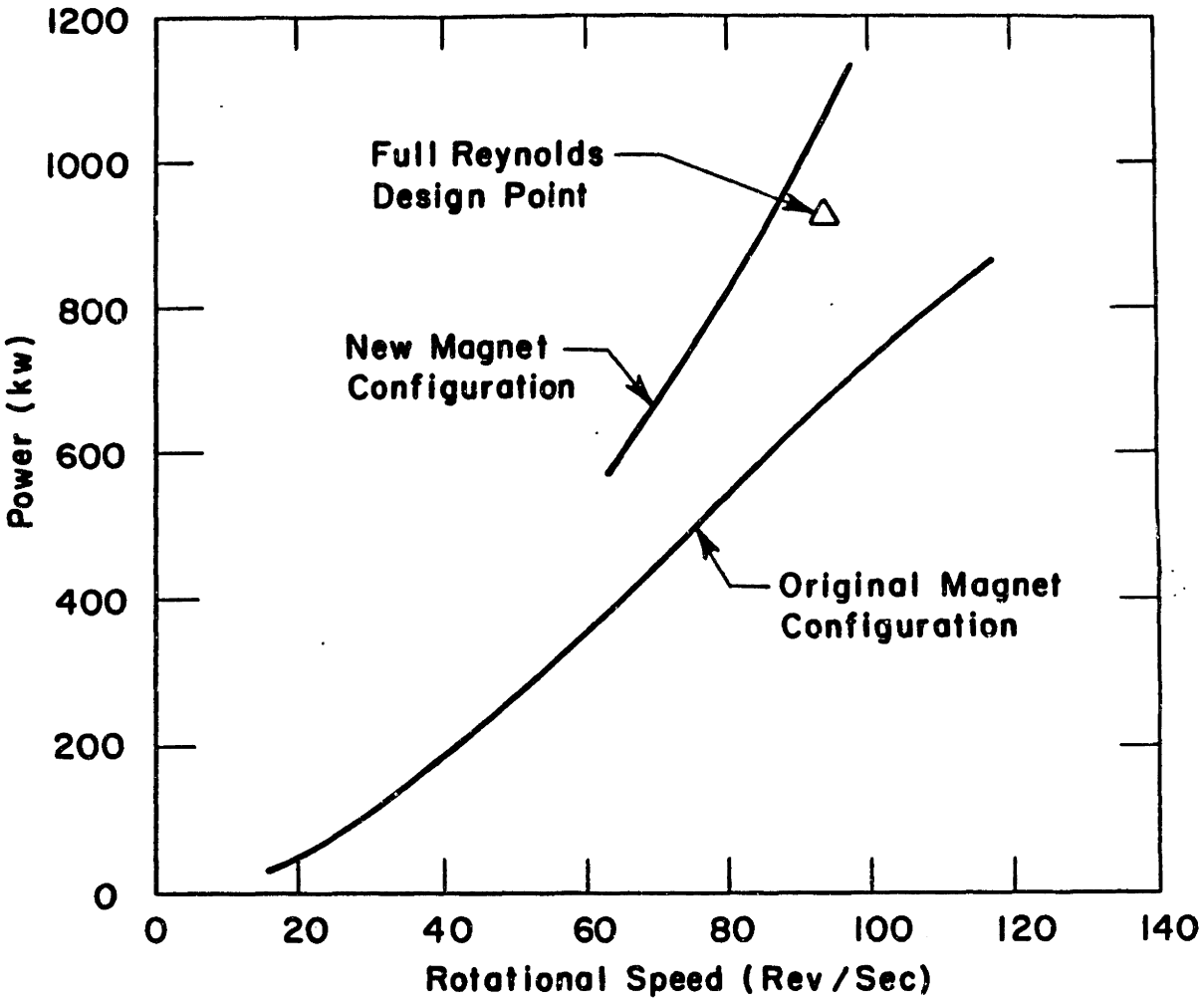

FIGURE 3.16: MEASURED BRAKE POWER ABSORPTION

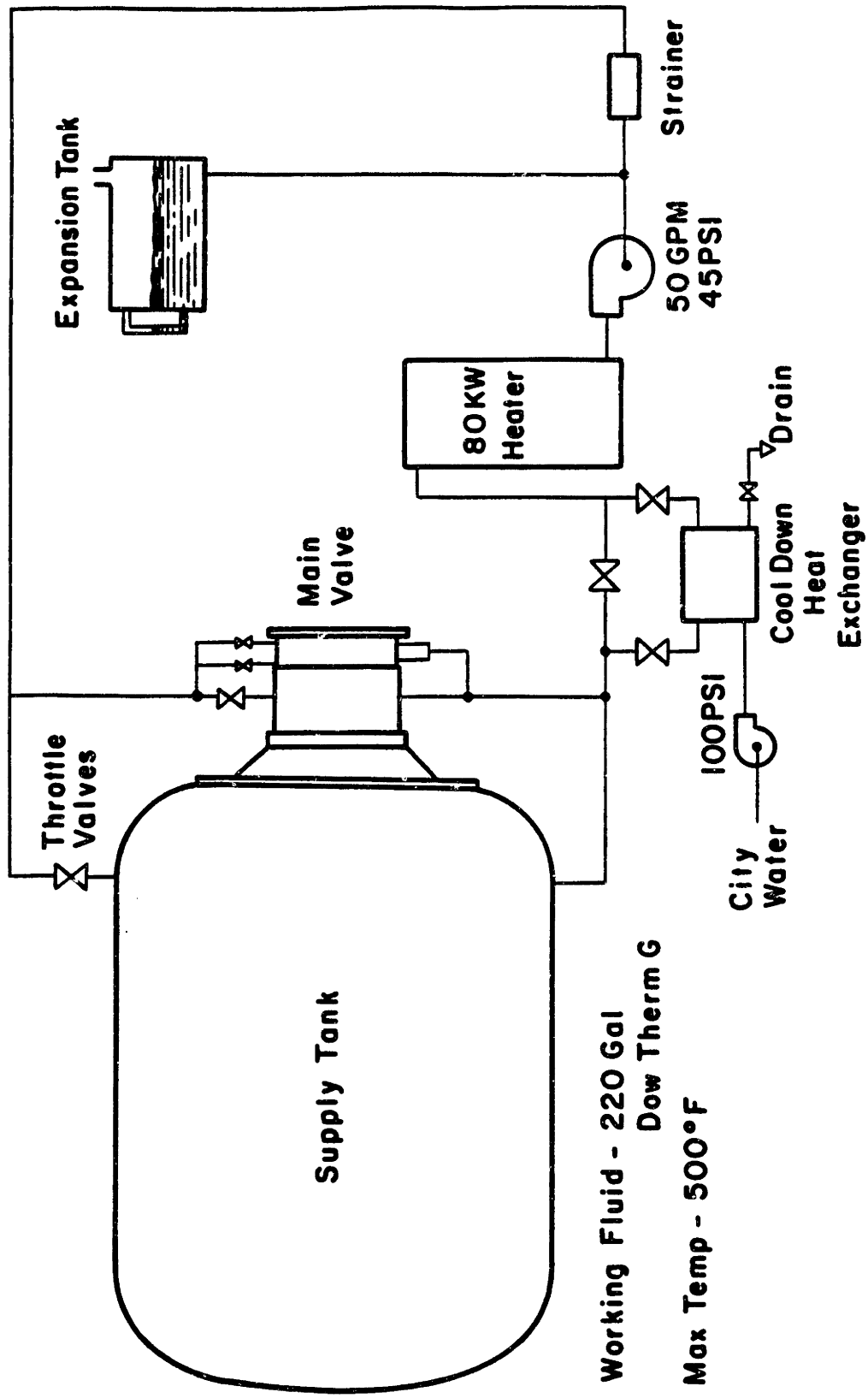

FIGURE 3.17: FACILITY OIL HEATING SYSTEM

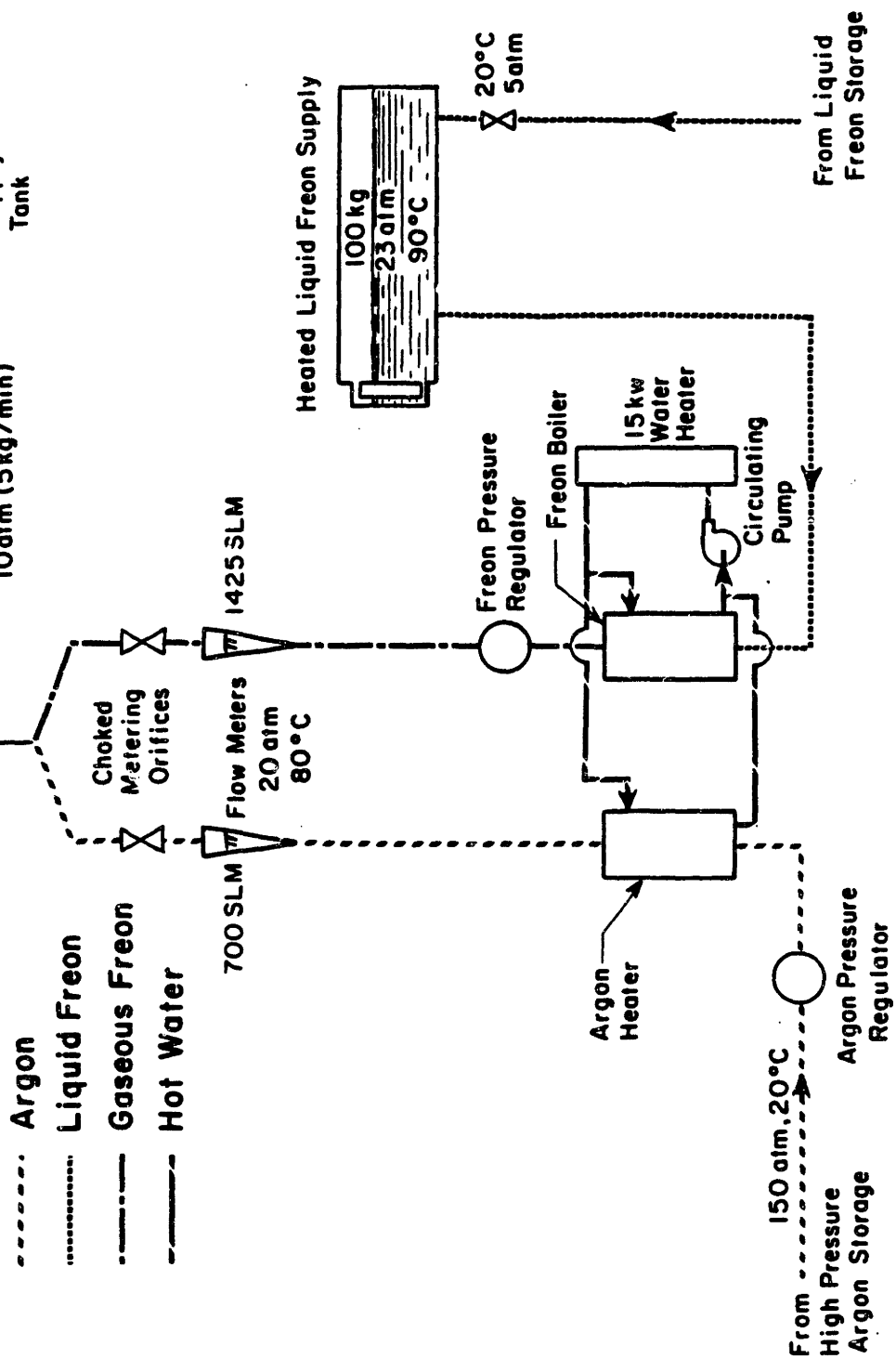

FIGURE 3.18: FACILITY GAS MIXING SYSTEM

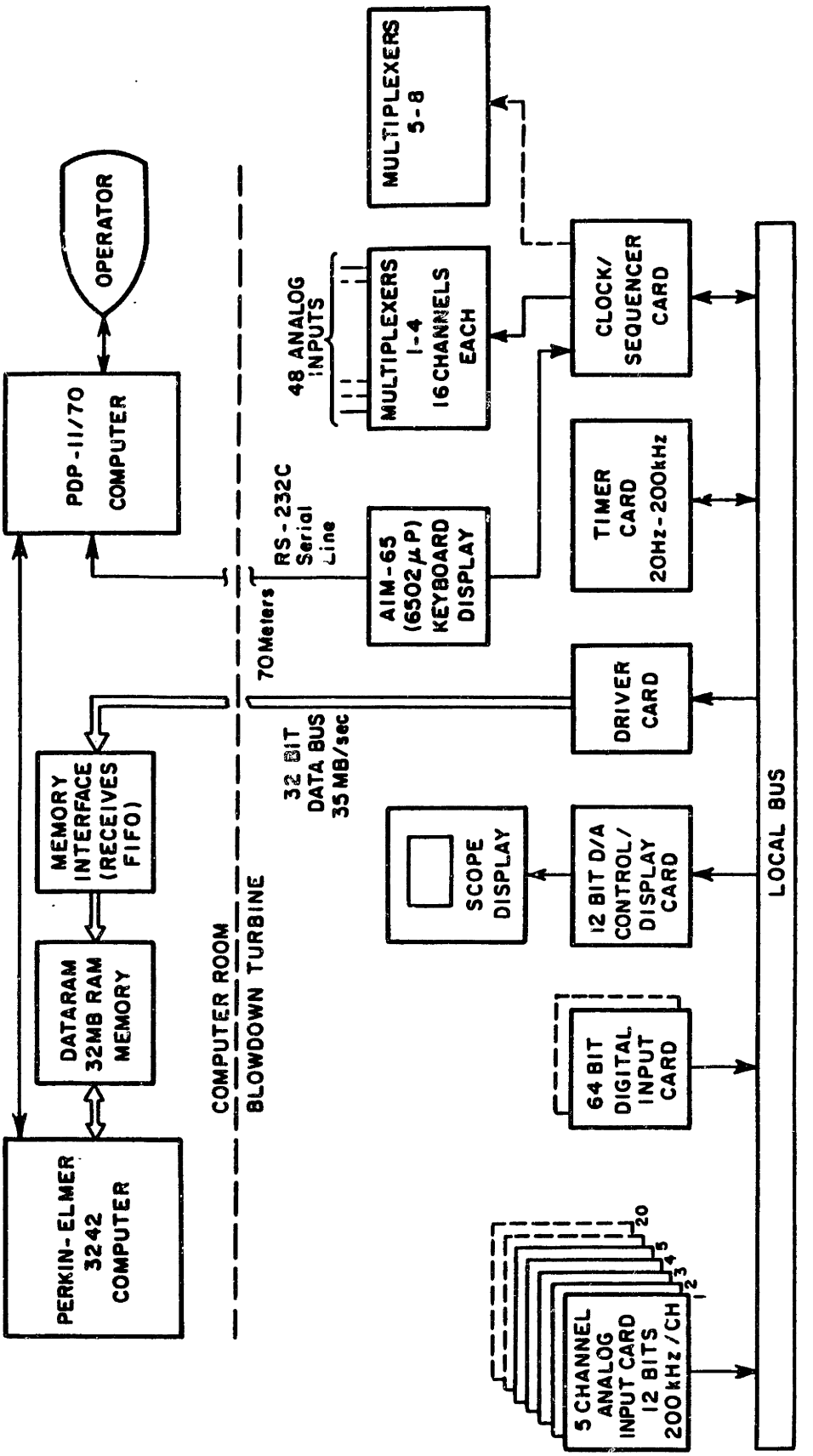

FIGURE 3.19: DATA ACQUISITION SYSTEM FUNCTIONAL LAYOUT

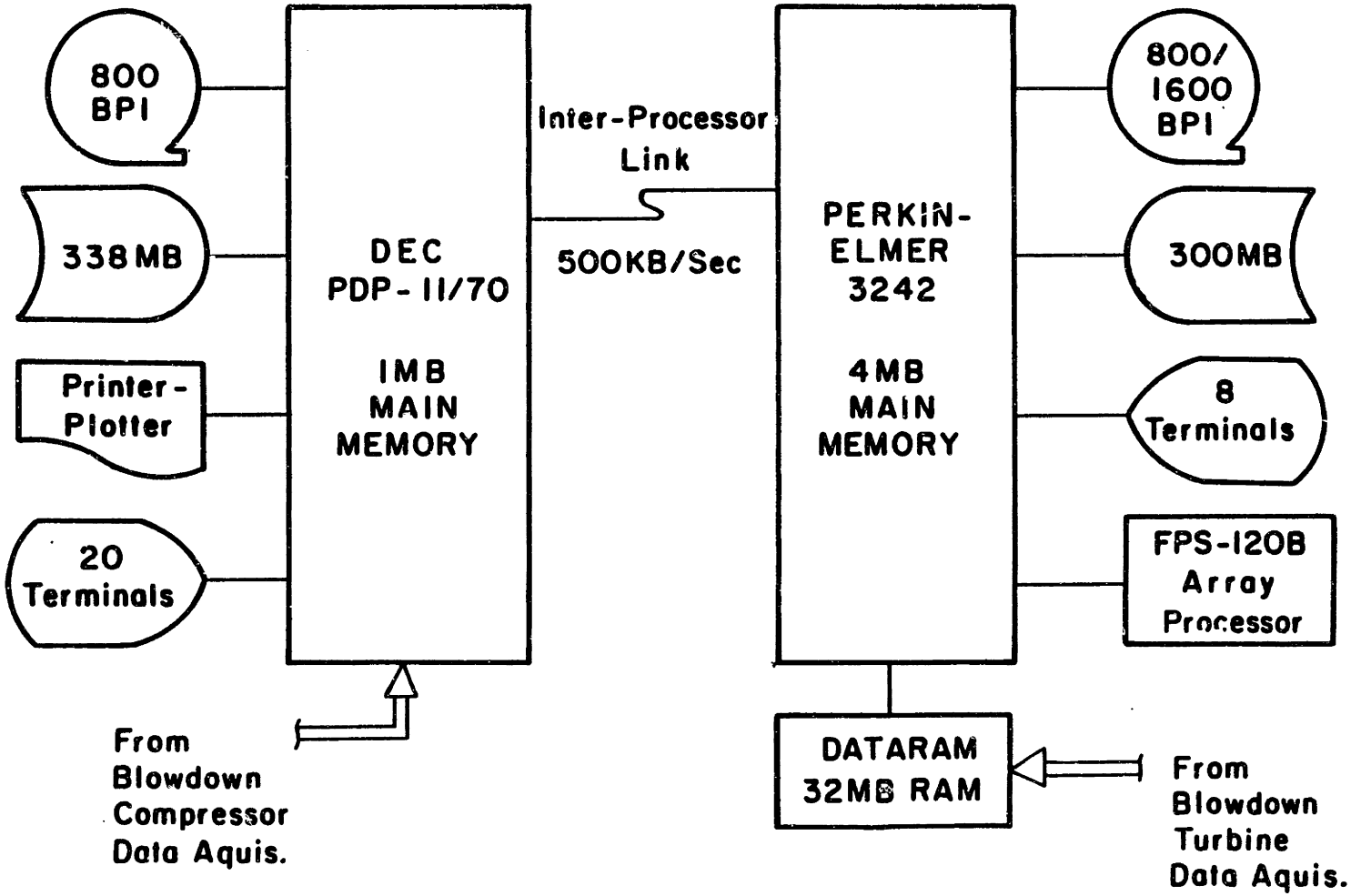

FIGURE 3.20: DATA ACQUISITION/ANALYSIS COMPUTER SYSTEMS

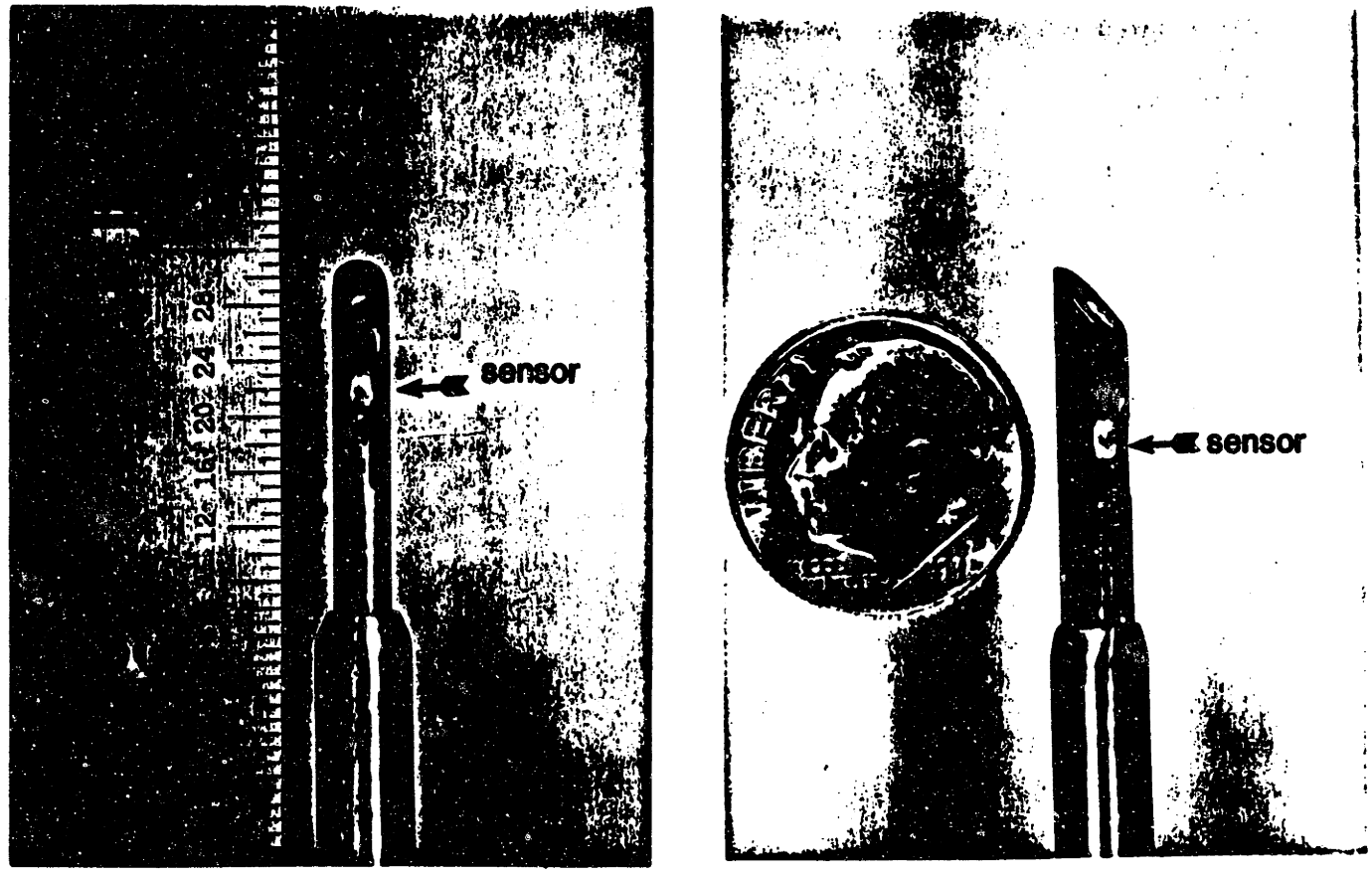

FIGURE 3.21: FOUR SENSOR CYLINDER PROBE MEASURES TOTAL AND STATIC PRESSURES AND TWO FLOW ANGLES. FREQUENCY RESPONSE IS D.C. TO 12 KHZ.

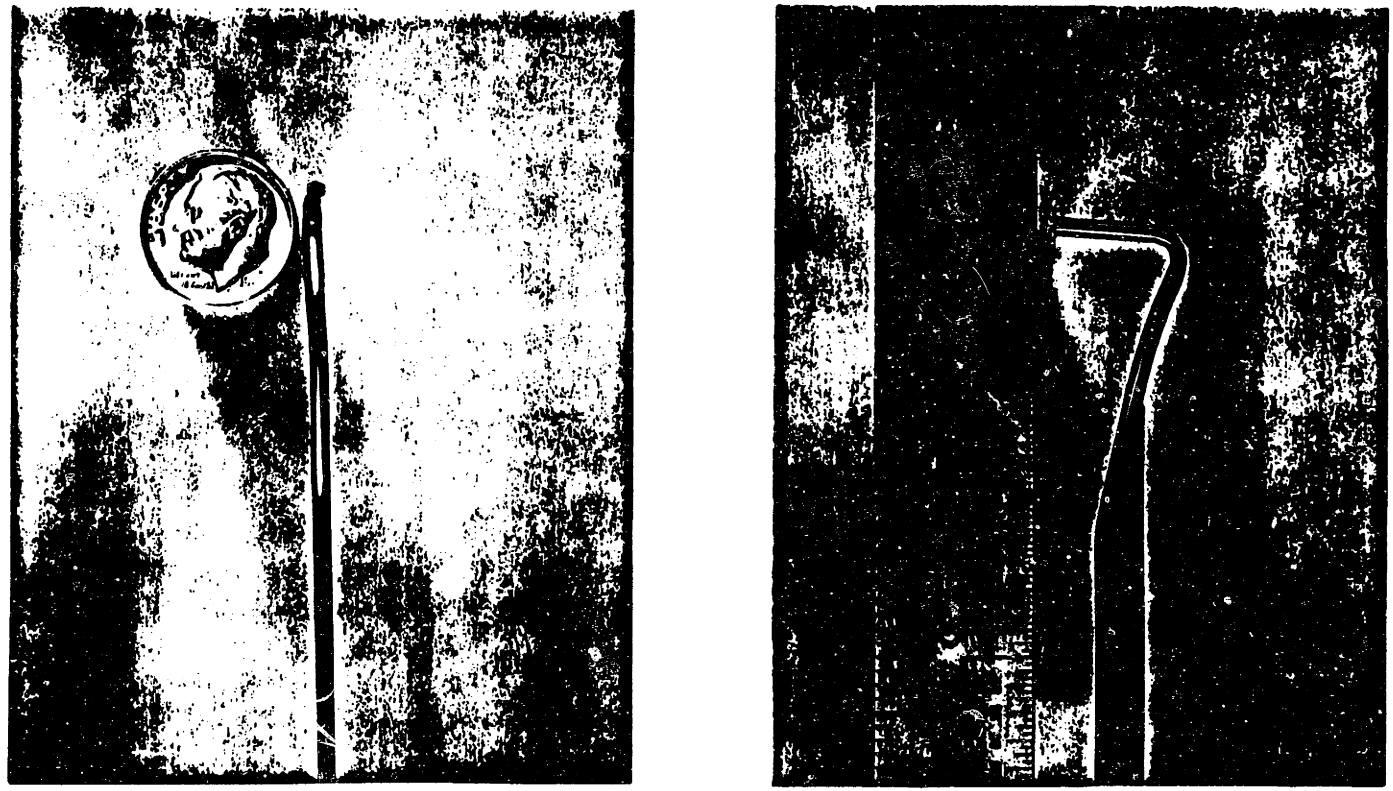

FIGURE 3.22: SINGLE SENSOR TOTAL PRESSURE PROBE, 1.2 MM O.D.

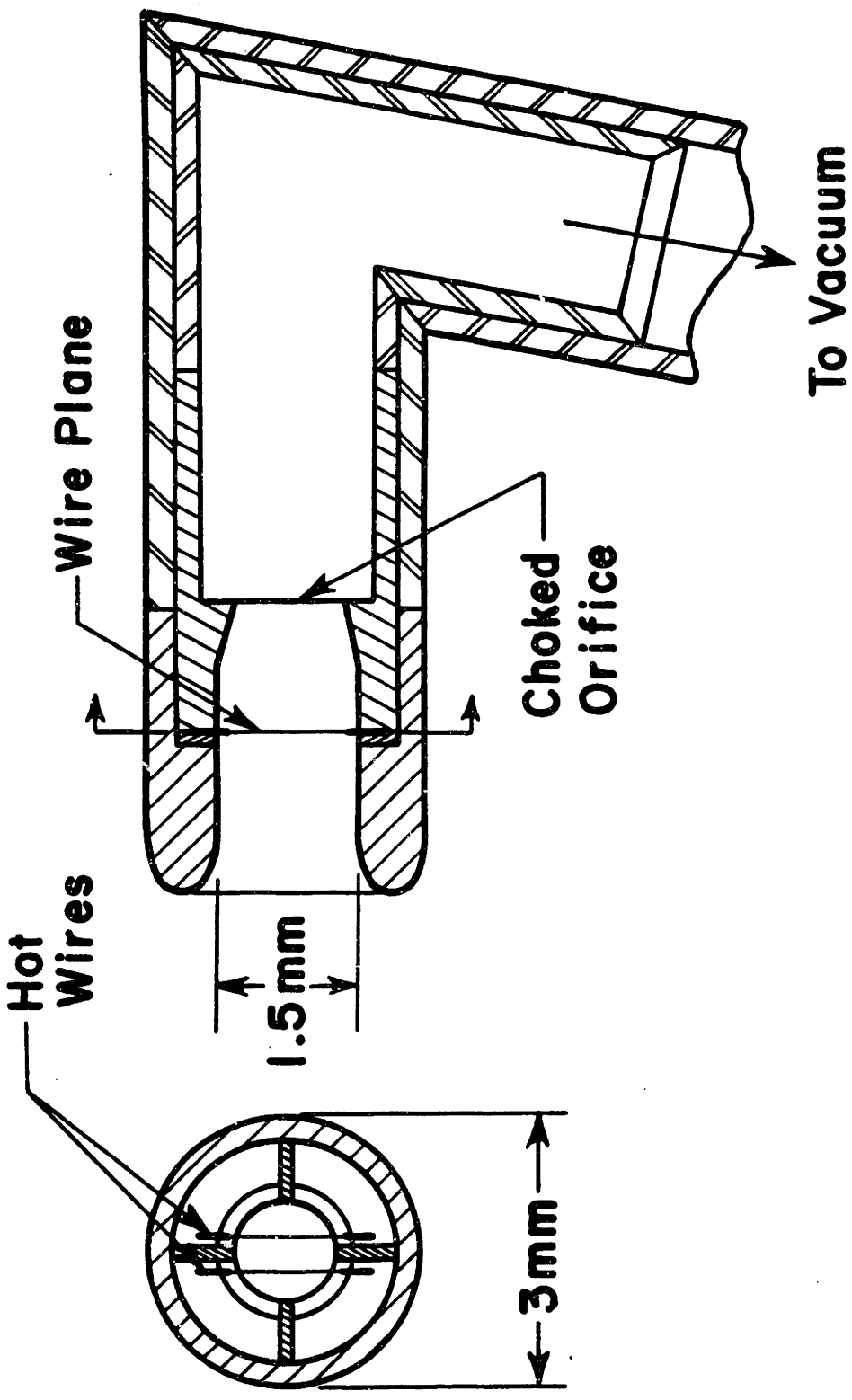

FIGURE 3.23: ASPIRATING PROBE MEASURES TOTAL TEMPERATURE AND PRESSURE. FREQUENCY RESPONSE IS D.C. TO 20 KHZ.

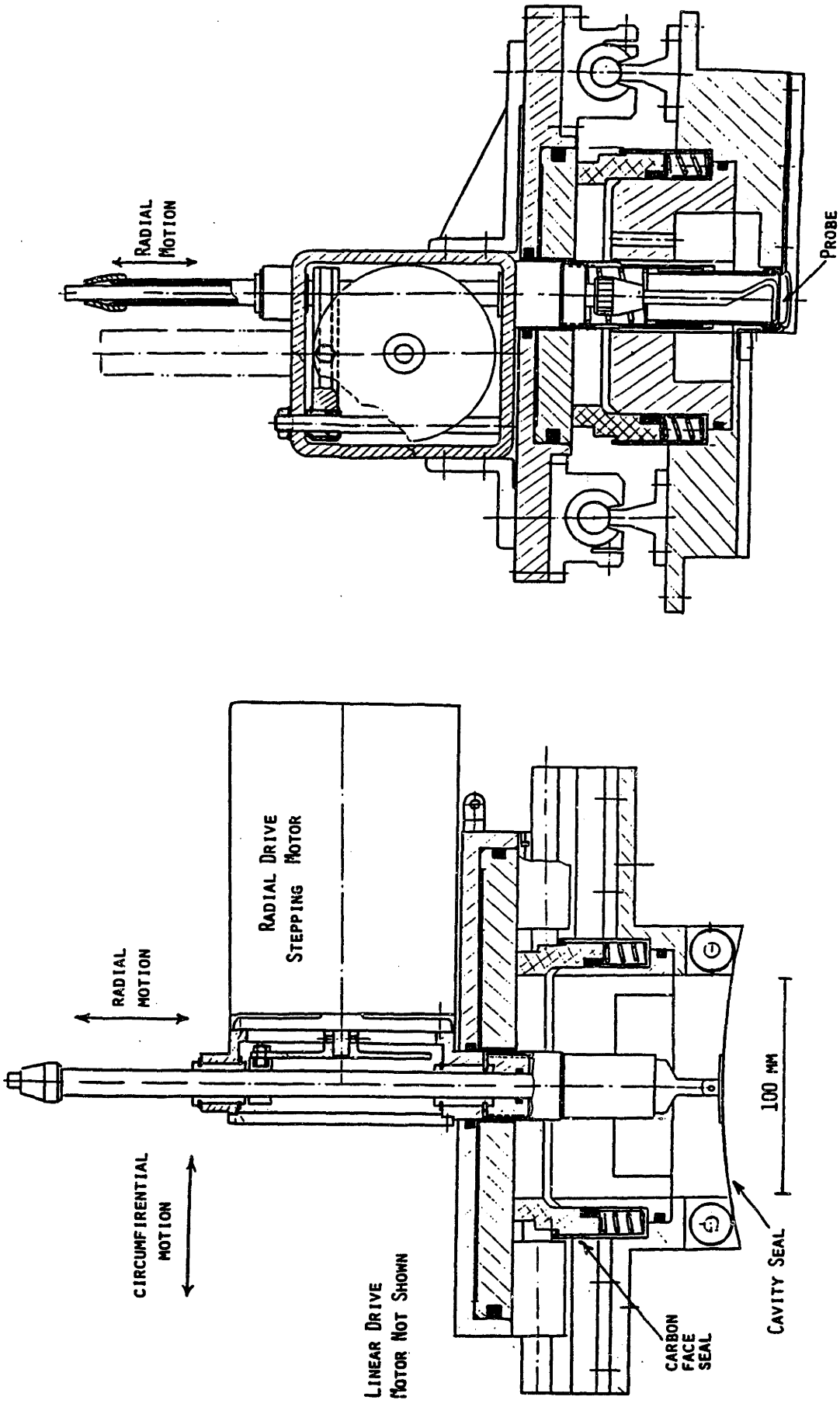

FIGURE 3.24: STATIONARY FRAME, RADIAL-CIRCUMFERENTIAL TRANSLATOR
A) DOWNSTREAM VIEW B) SIDE VIEW

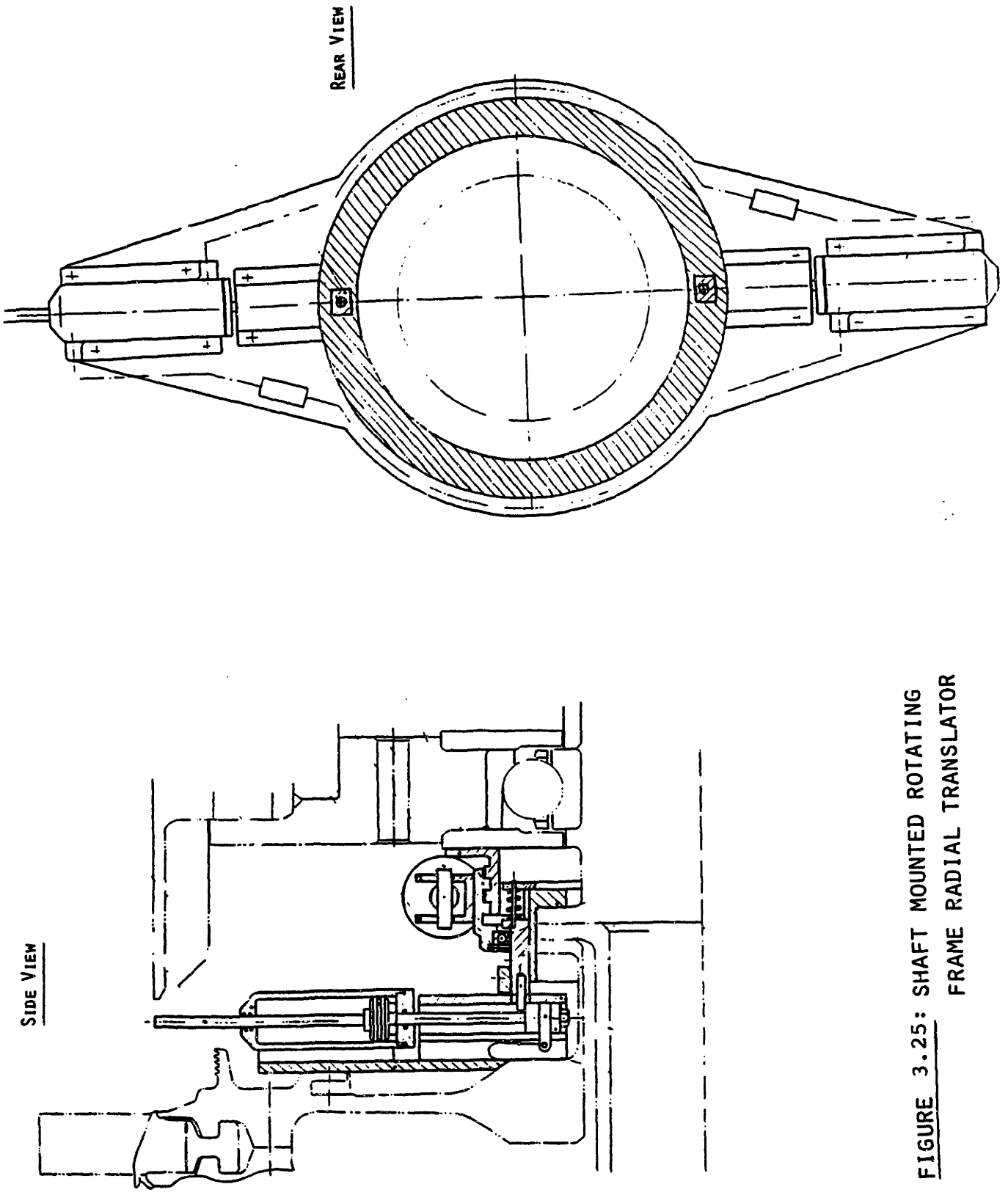

FIGURE 3.25: SHAFT MOUNTED ROTATING FRAME RADIAL TRANSLATOR

CHAPTER 4

INITIAL FACILITY EXPERIMENTS

A test in the Blowdown Turbine Facility consists of two parts: a manual preparation followed by an automatic sequence. The supply tank, test section, and dump tank are first evacuated to less than 0.1 mm Hg. For design point tests, the supply tank and valve are then heated. The main valve is closed and the supply tank filled with the test gas mixture. The turbine rotor is spun up past the chosen operating speed and the rotor drive is then shut down. As the rotor speed slowly decays past the operating speed, a preset digital tachometer initiates the automatic test sequence.

An overall view of the test sequence can be seen in Fig. 4.1, which shows the inlet (supply tank) total pressure, the turbine rotor exit total and static pressures, the valve position, rotor mechanical speed, and the brake current plotted as a function of time. As the valve opens, the supply tank pressure begins to drop and the rotor exit pressure rises. The eddy brake is switched off at approximately 1000 ms, terminating the test. The small ripples in the supply tank pressure are acoustic waves at the tank's longitudinal frequency. The slow rise in exit static pressure is transducer drift. The bounce evident in the valve position trace is not of concern since the motion does not carry the slider back past the full open position.

The corrected weight flow and corrected rotor speed are calculated from the measured rotor speed and change in the supply tank pressure. Figure 4.2 shows these to be constant to better than 1% over a 400 ms period. (The change in corrected flow reflects thermal drift in the supply tank pressure transducer, which has since been replaced.)

Because of the high swirl in the exit flow from this stage (40 degrees), the downstream flowfield is not totally decoupled from the back presure change in the dump tank. This increases the rotor back pressure earlier than would be expected for nonswirling, choked flow in the exit throttle. For these preliminary tests, the total pressure ratio changes 1% between 250 and 400 milliseconds (ms) from the start of the test and another 4% between 400 and 600 ms. Deswirl vanes are being installed at the exit of the rotor discharge duct in order to eliminate the coupling. This should extend the constant pressure ratio test time to 600-700 ms into the test.

The average stage quantities measured at two throttle settings are compared in Table 4.1 with a test of the same turbine in a conventional aerodynamic rig. The agreement is quite good. The difference reflects primarily transducer drift, which can be reduced through further data reduction and calibration.

TABLE 4.1
COMPARISON OF INITIAL TEST RESULTS

TEST IDENTIFICATION	T3	T4	S.S. RIG
Throttle Position	Full Open	Partial	N.A.
Mass Flow, $\dot{m}\sqrt{T/P}$ (lbs/sec $\sqrt{°K/PSIA}$)	8.85	8.89	8.95
Corrected Speed, $N/\sqrt{T}$ (°K)	408	412	421
Stage Total Pressure Ratio (P_{in}/P^*_{out})	4.38	3.65	4.33
$\frac{\text{Mid Span Total Pressure}^*}{\text{Tip Static Pressure}}$	1.33	1.23	1.28

* Measured 4 chords downstream of rotor

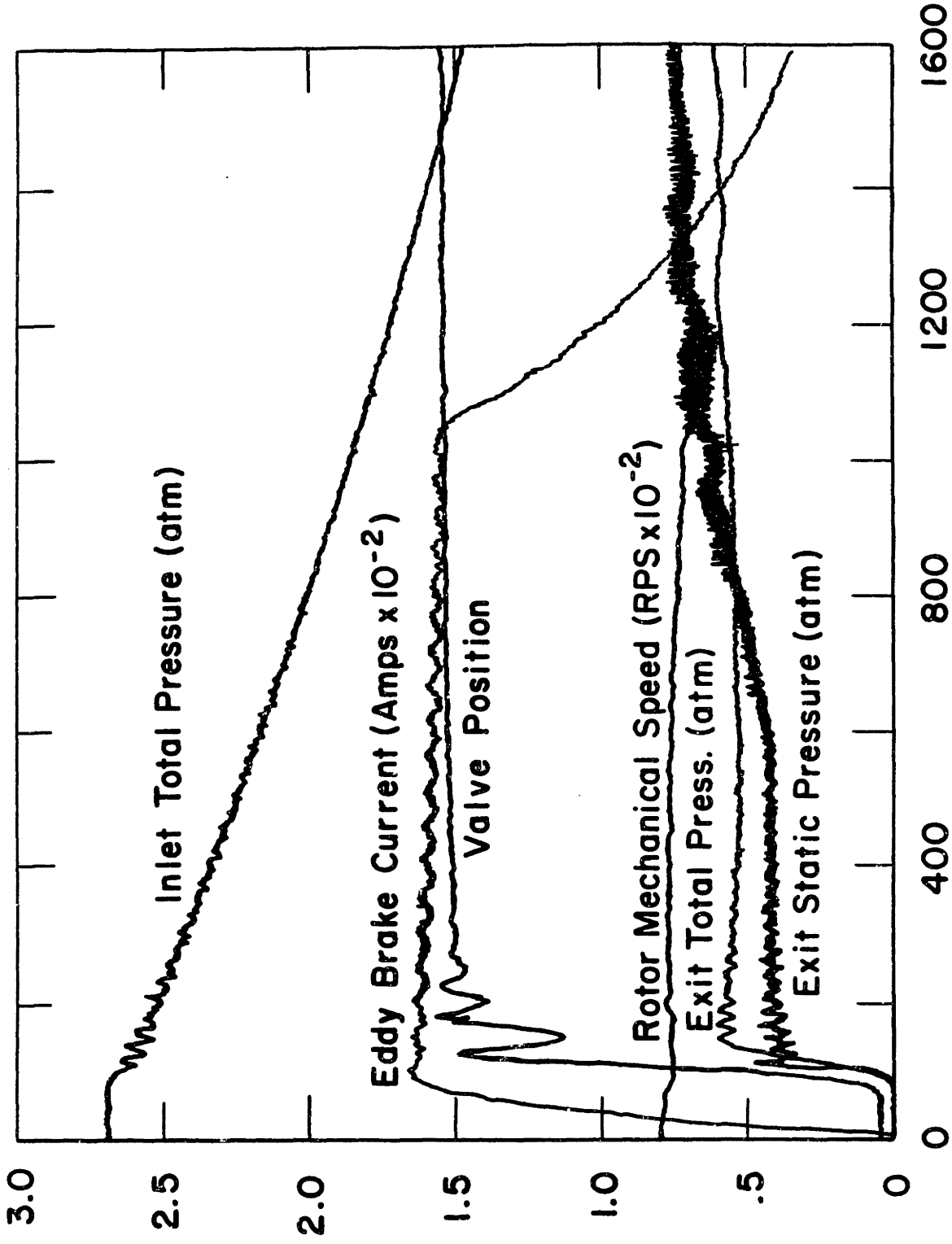

FIGURE 4.1: BLOWDOWN TURBINE FACILITY TEST RAW DATA. THE USEFUL TEST TIME EXTENDS FROM 250 MS TO 650 MS.

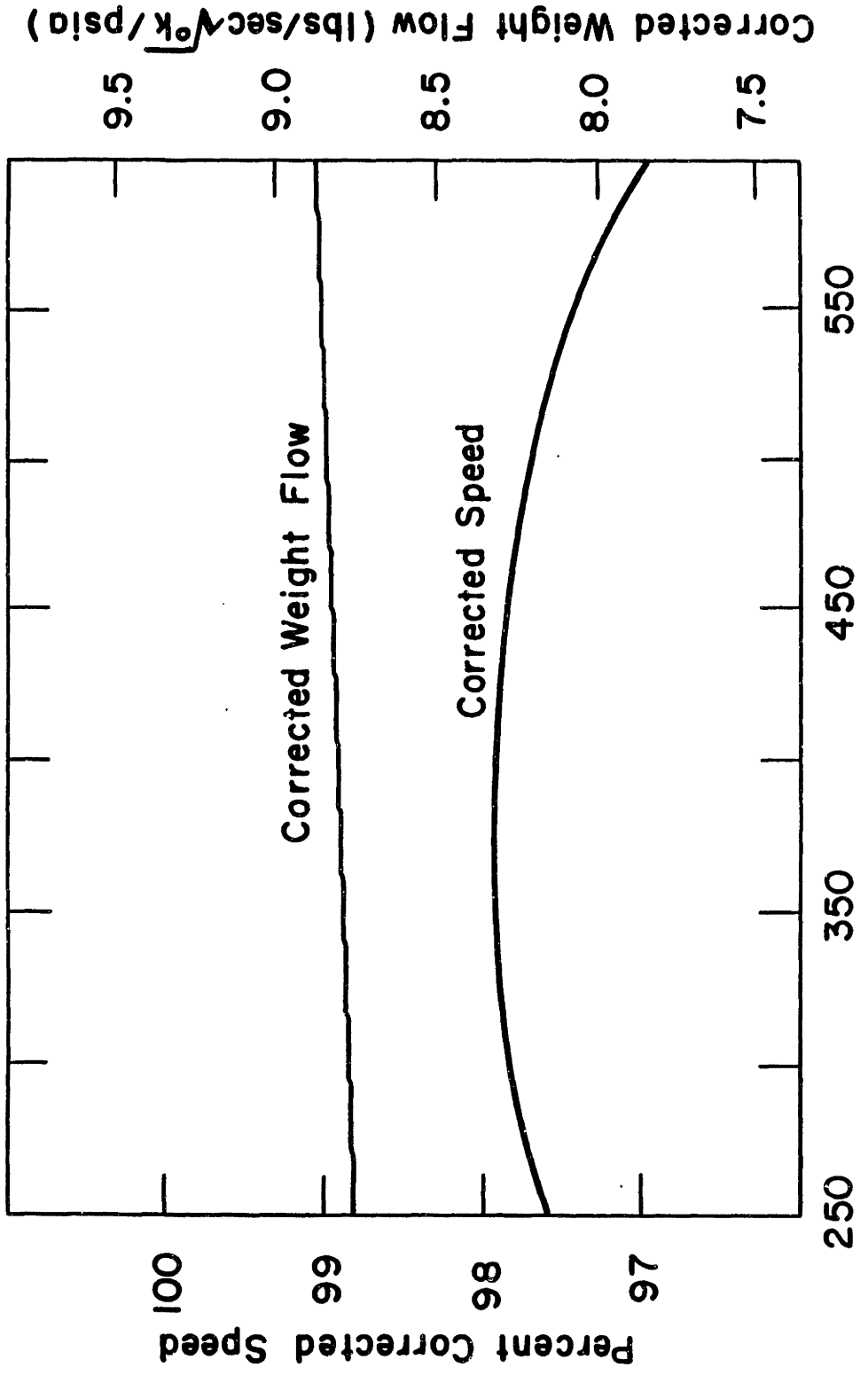

FIGURE 4.2: TYPICAL VARIATION OF CORRECT SPEED AND WEIGHT FLOW

CHAPTER 5

HIGH FREQUENCY RESPONSE HEAT FLUX GAUGE FOR METAL BLADING

5.1 Introduction

Accurate measurement of the heat transfer rate to turbine blading has long been recognized as a key to the improvement of high pressure turbine stages. The development of heat flux instrumentation for hot, warm, and cold machines has therefore been an active research area. In hot turbines, the harsh, oxidizing environment is a severely limiting constraint. Here, thermal gradient devices such as Gardon gauges are becoming increasingly practical for measurement of the time average heat flux level [Ref. 5.1].

The development of short duration turbine test facilities (30 to 700 ms test times) over the past decade has stimulated the development of heat flux instrumentation specifically optimized for the relatively benign environment (500-800°K gas temperatures) typical of these facilities [Refs. 5.2-5.5]. Calorimeter and thin film semi-infinite instruments have been extensively used in these applications [Ref. 5.6].

The goal of the work described herein was the development of a heat transfer gauge technology which would permit simultaneous measurement of both the steady state and time resolved heat flux distribution about the rotor blades in the MIT Blowdown Turbine facility [Ref. 5.5]. The specific requirements for this instrumentation are:

1) that it be compatible with the rig environment (500°K gas temperature, 290°K metal temperature, 200 KW/m^2 leading edge heat flux levels);
2) that it be capable of withstanding the high centrifugal stresses inherent to the rotor environment;
3) that it have frequency response extending from DC to 5 to 10 times blade passing frequency;

4) that it be usable in relatively large numbers per airfoil (10-20 per spanwise station);
5) that it require minimal modification to the blading; and
6) that it introduce the minimum disruption to, or interference with, the flow field and heat transfer.

Four candidate techniques were considered: calorimeter, blade temperature conduction models, thin film semi-infinite, and multilayer thin film gauges. All four techniques have been demonstrated, at least in stationary measurements, and are probably realizable in the rotating frame.

The calorimeter type gauges consist of insulated slugs of known thermal mass inset into the blade surface, the heat flux rate being deduced from the time rate of change of the slug temperature [Ref. 5.7]. A severe disadvantage to this type of instrument is the disruption of the thermal boundary layer due to the thermal discontinuities introduced by the sensor material [Ref. 5.8]. The blade temperature-conduction model technique can be considered an extension of the calorimeter approach into three dimensions with the entire blade acting as a calorimeter. Here, the temperature history is measured at a large number of points about the airfoil and the spatial distribution of heat transfer rate is inferred with the aid of time accurate, 3-D heat conduction calculation. This technique has the advantage of requiring a minimal modification to the blading and little flow disruption, but empirically requires a very large number of sensors (100 about the chord) and is very dependent upon the robustness of the 3-D calculational procedure [Ref. 5.9], thus reducing its attractiveness for rotor applications.

The thin film semi-infinite gauge consists of a thin film resistance thermometer mounted on an insulating substrate. Assuming that the

substrate appears infinitely thick to thermal disturbances propagating from the surface, the time dependent heat flux can be inferred using a one-dimensional heat conduction model. In practice, this technique has been brought to a high degree of perfection in stationary cascades by fabricating entire airfoils from ceramic material, thus eliminating flow disruption problems [Ref. 5.6]. Direct application of this technique would require fabrication of ceramic or plastic rotor airfoils, a formidable task. Alternatively, a metal airfoil might be coated with a suitable insulator, but this too is not simple in the rotor environment.

The technique selected was that of the multilayer heat flux gauge consisting of two temperature sensors on either side of a thin insulating substrate which is applied to the blade surface (Fig. 5.1). This is a thermal shunt. The temperature difference across the insulator is a direct measure of the heat flux to the surface. This direct proportionality between temperature difference and heat flux is valid only below a certain frequency. This frequency, however, increases as the insulator thickness is reduced. Conversely, above another frequency, the substrate appears semi-infinite to the upper sensor and a quasi-one-dimensional assumption can be used to infer the heat flux as with the semi-infinite gauges described above. In fact, the multilayer gauge could be considered an elaboration of the semi-infinite gauge in which a second sensor is placed within the substrate to eliminate the gauge performance dependence on the blade material properties. Alternatively, the gauges can be viewed as developments of the commercially available thermopile sensor, low frequency response gauges [Ref. 5.10], with the low response sensors replaced by high response resistance thermometers. For the 25 μm thick polyimide insulator chosen, the direct response [shunt] mode frequency response is DC

to 20 Hz, while the semi-infinite assumption is good above 1.5 kHz. In the MIT Blowdown Turbine tunnel, for which these gauges were designed, rotor blade passing frequency is 6 kHz. Furthermore, as will be shown, the response in the intermediate 20-1500 Hz region can be reconstructed through proper numerical signal processing.

The multilayer gauges are fabricated many to a sheet of insulating material, tested, and then glued to the blade or test article surface using standard strain gauge adhesive bonding techniques. The blade is completely covered by the polyimide. The specific advantages of this heat flux gauge technology include:

- frequency response from DC to tens of kilohertz,
- conventional metal blading may be used,
- no thermal or geometric discontinuities are introduced, and
- the gauges are fabricated and tested independently of the airfoil.

This chapter discusses the theory, fabrication, testing, and data reduction of these high frequency response multilayer heat flux gauges.

5.2 Gauge Model

A multilayer, time dependent, conduction model of the double sided heat flux gauge was formulated to assist in its design, calibration, and proper application. A cross-section of a mounted gauge is illustrated in Fig. 5.1. When mounted on a blade profile or test item, the gauge becomes part of a five-layered structure consisting of the upper thin film temperature sensor, the gauge insulating substrate, a second film thermometer, an adhesive layer, and finally the test article itself. In general, the thermal properties of each layer will differ and thus, to be fully rigorous, a five-layer model might be employed. In practice, however, the film thermometer sensors are sufficiently thin as to appear

thermally transparent to the applied heat flux, thereby permitting use of a three-layer model. Also, the sensors will be excited at power dissipation levels sufficiently low that their influence as sheet sources of heat can be neglected. The quantitative conditions required to meet these criteria will be derived later.

The model can be further simplified to two layers if it is assumed that the sensor substrate and adhesive have similar thermal properties with the temperature sensors embedded in the top layer. The model adhesive thickness represents not the exact physical thickness but an equivalent thickness including effects of uneveness and property variations. A similar assumption is made about any surface coating (protective or dirt) which may be on top of the upper gauge surface. The gauge adhesive, substrate and surface coating will therefore form Layer 1 of the model and the test article or blade will form Layer 2 (Fig. 5.2). The upper sensor lies below a surface coating of thickness $h=f_h d$ and the lower sensor lies above a glue layer of thickness $g=f_g d$, where d represents the sensor separation and f_g, f_h the glue and surface coating fractions respectively. Thus the positions of the upper and lower temperature sensors are, respectively, $x_u=f_h d$ and $x_\ell=(1+f_h)d$. The thickness of Layer 1 is given by $L = (1+f_h+f_g)d$.

The heat conduction equations are solved for the temperature distribution in a two layered, semi-infinite medium of unlimited lateral extent, subject to a spatially uniform surface heat flux, q(t). The flow of heat may therefore be considered to be one-dimensional. It is further assumed that the thermal properties within each layer are uniform and that the layers make perfect thermal contact. Thus, the temperature in each layer is governed by,

$$\text{Layer 1:} \qquad \frac{\partial T_1}{\partial t} = \kappa_1 \frac{\partial^2 T_1}{\partial x^2} \qquad 0 \leq x \leq L \tag{5.1}$$

$$\text{Layer 2:} \qquad \frac{\partial T_2}{\partial t} = \kappa_2 \frac{\partial^2 T_2}{\partial x^2} \qquad L \leq x \leq \infty \tag{5.2}$$

(where $\kappa = k/\rho c$ is the thermal diffusivity), subject to the interface conditions,

$$T_1(L,t) = T_2(L,t) \tag{5.3}$$

$$k_1 \left.\frac{\partial T_1}{\partial x}\right|_{x=L} = k_2 \left.\frac{\partial T_2}{\partial x}\right|_{x=L} \qquad -\infty < t < +\infty \tag{5.4}$$

and the semi-infinite condition,

$$T_2(\infty,t) = 0 \ . \tag{5.5}$$

To fully specify the problem, upper surface boundary conditions and initial conditions must be provided and these will depend upon the form of the driving surface heat flux to be investigated. We will consider two cases: 1) a steady sinusoid, and 2) a step in surface heat flux. The solution to these problems employs the standard techniques described in Ref. [5.11]. The results will be given in a form useful to the subsequent analysis and only the solution for the temperature in the layer containing the temperature sensors, $T_1(x,t)$, will be reported.

5.2.1 Response to a Steady Harmonic Variation in Surface Heat Flux

Initial conditions are not specified since the steady solution valid for all time is being sought. For the surface heat flux,

$$\dot{q}_s(t) = -k_1 \left.\frac{\partial T_1}{\partial x}\right|_{x=0} = Q_o \exp\{j\omega t\} \qquad -\infty < t < +\infty \tag{5.6}$$

the temperature distribution in Layer 1 is,

$$T_1(x,t) = (Q_o d/k_1)\, M \exp\{j(\omega t-\phi)\} \qquad 0 \leq x \leq L \tag{5.7}$$

where,

$$M \equiv \sqrt{2}\left(\frac{\omega}{\omega_c}\right)^{-1/2} \exp\left\{-\frac{1}{2}\left(\frac{\omega}{\omega_c}\right)^{1/2}\frac{x}{d}\right\}\left(\frac{A^2+B^2}{C^2+D^2}\right)^{1/2} \tag{5.8}$$

$$\phi \equiv \frac{1}{2}\left(\frac{\omega}{\omega_c}\right)^{1/2}\frac{x}{d} + \frac{\pi}{4} - \tan^{-1}\left\{\frac{BC-AD}{AC+BD}\right\} \tag{5.9}$$

A sensor characteristic frequency ω_c has been introduced based upon the sensor spacing d.

$$\omega_c = \frac{\kappa_1}{2d^2} \quad . \tag{5.10}$$

The other quantities are defined as follows:

$$A \equiv 1 - R \exp\left\{-\left(\frac{\omega}{\omega_c}\right)^{1/2}\left(\frac{L-x}{d}\right)\right\} \cos\left\{\left(\frac{\omega}{\omega_c}\right)^{1/2}\left(\frac{L-x}{d}\right)\right\} \tag{5.11a}$$

$$B \equiv R \exp\left\{-\left(\frac{\omega}{\omega_c}\right)^{1/2}\left(\frac{L-x}{d}\right)\right\} \sin\left\{\left(\frac{\omega}{\omega_c}\right)^{1/2}\left(\frac{L-x}{d}\right)\right\} \tag{5.11b}$$

$$C \equiv 1 + R \exp\left\{-\left(\frac{\omega}{\omega_c}\right)^{1/2}\left(\frac{L}{d}\right)\right\} \cos\left\{\left(\frac{\omega}{\omega_c}\right)^{1/2}\left(\frac{L}{d}\right)\right\} \tag{5.11c}$$

$$D \equiv -R \exp\left\{-\left(\frac{\omega}{\omega_c}\right)^{1/2}\left(\frac{L}{d}\right)\right\} \sin\left\{\left(\frac{\omega}{\omega_c}\right)^{1/2}\left(\frac{L}{d}\right)\right\} \tag{5.11d}$$

$$R \equiv \frac{r-1}{r+1} \tag{5.12}$$

$$r \equiv \frac{\sqrt{(\rho c k)_2}}{\sqrt{(\rho c k)_1}} \quad . \tag{5.13}$$

5.2.2 Response to a Step in Surface Heat Flux

Here, both the transient and steady solutions to the problem are of interest. The initial conditions are,

$$-\infty < t < 0 \quad \begin{cases} T_1(x,t)=0 & 0 \leq x \leq L \\ T_2(x,t)=0 & L \leq x < \infty \end{cases} \tag{5.14}$$

For the surface heat flux,

$$q_s(t) = -k_1 \frac{\partial T_1}{\partial x}\bigg|_{x=0} = \begin{cases} 0 & -\infty < t < 0 \\ Q_o & 0 \leq t < +\infty \end{cases} \tag{5.15}$$

the temperature distribution in Layer 1 is given by,

$$T_1(x,t) = (Q_o d/k_1)\sqrt{\frac{t}{\tau}} \sum_{n=0}^{\infty} (-R)^n (\text{ierfc } P_n - R \text{ ierfc } Q_n) \tag{5.16}$$

where

$$P_n \equiv \frac{(x/d)}{\sqrt{t/\tau}} + 2n \frac{(L/d)}{\sqrt{t/\tau}} \tag{5.17a}$$

$$Q_n \equiv - \frac{(x/d)}{\sqrt{t/\tau}} + 2(n+1) \frac{(L/d)}{\sqrt{t/\tau}} \tag{5.17b}$$

and ierfc() is the first integral of the complementary error function. A gauge time constant τ has been introduced, again based upon gauge thermal diffusivity and sensor spacing,

$$\tau \equiv \frac{d^2}{4\kappa} \quad . \tag{5.18}$$

The temperature is referenced to the quantity $(Q_o d/k_1)$ which represents the steady state temperature drop required to "drive" a heat flux Q_o across d, the distance between the temperature sensors.

The characteristic frequency ω_c and the time constant τ are defined

with respect to the gauge film spacing, and not the layer thickness L. Thus, the expressions for the solution may appear a little more cumbersome than necessary to describe the temperature distribution but they have the proper form for the subsequent analyses of the gauge response characteristics.

5.2.3 Gauge Model Discussion

The solutions for the temperature distribution in Layer 1, $T_1(x,t)$, depend intrinsically upon the properties of the gauge through $\sqrt{\rho ck}$ and k/d. These parameters form the basis for the normalization of the independent variables through the definitions of τ and ω_c. They are the fundamental parameters which characterize the gauge and which, therefore, must be known to interpret its output. Additional influence comes from the thickness fractions of the surface coating and adhesive (f_h and f_g respectively) and from the $\sqrt{\rho ck}$ of Layer 2 which enters through the parameter R, Eq. (5.12).

We will now use the gauge model to show that only the film thermometer scale factor, $\sqrt{\rho ck}$ and k/d need calibration. Variations in adhesive thickness and test article properties (f_h, f_g, R), although they influence the temperature levels, do not significantly affect the inferred heat flux level.

5.2.4 Gauge Model Response

The frequency and step response of the double sided gauge will now be derived, and will provide the basis not only for design and calibration but also for the verification of the data reduction method used in actual application. The parameters necessary to quantify the design trade of frequency response with measurement sensitivity are obtained from examination of the low frequency direct mode and high frequency semi-infinite mode

performance limits. These limiting solutions also provide the framework for the development of the gauge calibration methods.

In the direct or shunt mode, the surface heat flux is assumed to be proportional to the measured temperature drop across the gauge. While this is valid for static measurements, a uniform temperature gradient will not exist across the gauge if there are frequency components for which the thermal penetration depth is comparable to, or smaller than, the gauge thickness. The gauge is considered to be in the semi-infinite mode for those frequency components which are effectively damped by the gauge substrate. In this case, the heat flux may be obtained entirely from the upper film thermometer. It should be understood that 'direct' and 'semi-infinite' are terms used to describe limiting processes within the gauge substrate and are in no way exclusive of each other in actual operation of the gauge.

For steady harmonic excitation in the direct measurement mode, the upper and lower film temperatures are provided by Eq. (5.7),

$$T_u = T_1(x_u,t) = (Q_o d/k_1)\, M_u\, e^{j(\omega t-\phi_u)} \tag{5.19a}$$

$$T_\ell = T_1(x_\ell,t) = (Q_o d/k_1)\, M_\ell\, e^{j(\omega t-\phi_\ell)} \tag{5.19b}$$

where $M_u = M(x_u)$, etc.

The direct mode heat flux $\dot{q}_D$ indicated by an 'ideal' gauge, (i.e., error-free measurements of T_u and T_ℓ, and perfect knowledge of k_1/d), is

$$\dot{q}_D(t) = (k_1/d)(T_u - T_\ell) \tag{5.20}$$

Substituting for the temperatures using Eqs. (5.19), the ratio of the

measured to actual heat flux is,

$$\frac{\dot{q}_D(t)}{\dot{q}_S(t)} = M_u e^{-j\phi_u} - M_\ell e^{-j\phi_\ell} \tag{5.21}$$

This may be put into the more useful magnitude-phase form,

$$\frac{\dot{q}_D(t)}{\dot{q}_S(t)} = M_D e^{-j\phi_D} \tag{5.22}$$

where

$$M_D \equiv \{M_u^2 + M_\ell^2 - 2M_u M_\ell \cos(\phi_u - \phi_\ell)\}^{1/2} \tag{5.23}$$

and

$$\phi_D \equiv \tan^{-1}\{[M_u \sin\phi_u - M_\ell \sin\phi_\ell]/[M_u \cos\phi_u - M_\ell \cos\phi_\ell]\} \tag{5.24}$$

represent the magnitude M_D and phase ϕ_D response for direct mode.

These are plotted in Fig. 5.3 as a function of the normalized frequency ω/ω_c, for several values of glue fraction, f_g. The case shown is for a polyimide substrate mounted upon an aluminum test body, R=0.96. The results show that the direct temperature difference mode is valid, in this example, for frequencies up to the cutoff frequency ω_c, and that in this region the adhesive layer has negligible influence upon the performance of the gauge. Parametric studies show similar conclusions for the influence of R and f_h.

The results thus far show that, in the direct mode, the temperature rise per unit of surface heat flux can be approximated by,

$$\frac{\Delta T}{Q} = \frac{d}{k} \tag{5.25}$$

up to a cutoff frequency given by,

$$\omega_c = \frac{\kappa}{2d^2} = \frac{1}{2}\left(\frac{(k/d)}{\sqrt{\rho ck}}\right)^2 \tag{5.26}$$

If k/d is eliminated from these expressions, a constraint between the gauge sensitivity $\Delta T/Q$ and the response bandwidth f_c (in Hz) is obtained,

$$\frac{\Delta T}{Q} f_c^{1/2} = \frac{1}{2\sqrt{\pi}} \frac{1}{\sqrt{\rho ck}} \tag{5.27}$$

Thus, the overall tradeoff between signal strength and cutoff frequency depends only on the thermal property $\sqrt{\rho ck}$ of the gauge substrate. Both low thermal inertia ρc (more precisely high diffusivity), good for high f_c, and low thermal conductivity, good for high $\Delta T/Q$, are desirable.

The solution for steady harmonic excitation, Eq. (5.19b), shows that the response of the lower sensor is fully damped for frequencies above approximately 100 ω_c. In the case of the semi-infinite mode, the expression for the surface temperature, Eq. (5.19a), (for x=0) reduces to

$$T_u(t) = \frac{Q_o}{\sqrt{\rho ck}} \omega^{-1/2} e^{j(\omega t - \frac{\pi}{4})} \tag{5.28}$$

Thus, the condition for maximum high frequency temperature sensitivity is the same as for the direct measurement mode, low $\sqrt{\rho ck}$, except now it is seen that sensitivity also diminishes with frequency, as $\omega^{-1/2}$. This means that, for a fixed temperature measurement capability, low values of $\sqrt{\rho ck}$ will help to improve the upper frequency response limit of the semi-infinite mode.

In summary, this steady sinusoidal theory provides the basis for the selection of the substrate material and thickness, key aspects of the

overall gauge design. Low $\sqrt{\rho ck}$ is desirable for a high sensitivity-bandwidth product in the direct measurement mode, and for high sensitivity and frequency response in the semi-infinite mode. For a given $\sqrt{\rho ck}$, the trade between f_c and $\Delta T/Q$ is then set by the choice of substrate thickness, d, using Eqs. (5.25) and (5.26).

The semi-infinite mode step response is shown for the upper and lower thermometers in Fig. 5.4. The region in which the response of the upper thermometer is linearly proportional to $\sqrt{t}$ is that for which the semi-infinite assumption is valid. Here, the solution for x=0 is,

$$T_u(t) = \frac{2Q}{\sqrt{\pi}\ \sqrt{\rho ck}}\ t^{1/2} \tag{5.29}$$

This equation will provide the basis for the $\sqrt{\rho ck}$ calibration procedures discussed later. Note that, although increasing the adhesive fraction tends to extend the duration of the semi-infinite regime, it does not influence the performance of the gauge while in that regime. Similar conclusions follow for R and f_h.

The step response for the direct difference mode, obtained from Eqs. (16) and (20), is shown in Fig. 5.5. The effect of the glue layer is more evident from its influence upon the rise time of the measured response than from its effect upon the frequency response. Also shown is a discriminant, $(T_u-T_\ell)/T_u$, which can be used to estimate the effective thickness of the adhesive from test data.

These results clearly show the behavior of the semi-infinite ($t\leq\tau$) and steady state ($t>20\tau$) limits. The actual data is reduced with a numerical technique which reconstructs the entire frequency domain, as will be described in Sec. 5.5.

5.2.5 Design of the Thin Film Temperature Sensors

This section discusses the design of the thin film resistance thermometers used as temperature sensors in the multilayer heat flux gauge. These sensors are nothing more than metal film resistors whose resistance changes with temperature. For a change δT about a temperature T, the increment in film resistance may be expressed by a Taylor series expansion in powers of δT,

$$\delta R = R(T + \delta T) - R(T) = R(T)\,\alpha(T)\,\delta T + \text{higher order terms in } \delta T. \tag{5.30}$$

The temperature coefficient of resistivity $\alpha(T)$, a fundamental material property, represents the fractional change in resistance about a given temperature,

$$\alpha(T) = d(\ln R)/dT. \tag{5.31}$$

For the metals commonly employed in resistance thermometers, $\alpha(T)$ is usually a very weak function of temperature over ranges of practical interest. Thus, in many applications, a convenient form of Eq. (5.30) may be obtained by assuming α to be constant and neglecting the higher order terms,

$$\delta R = R\alpha\delta T. \tag{5.32}$$

(For the sensor here, this results in errors of order 0.1C over a 60C range.)

For a sensor excited at constant current, the change in voltage across the sensor, δV, is

$$\delta V = (V\alpha)\delta T, \tag{5.33}$$

where V represents the total voltage drop across the film. Thus, the sensitivity of the sensor is directly proportional to both its temperature coefficient and the excitation voltage. The excitation voltage is constrained, however, by the V^2/R heat dissipation in the film sensor,

$$Q_E = V^2/(R\ell w), \tag{5.34}$$

(where ℓ and w are the active length and width of the film). This heat dissipation must be kept small compared to the heat flux being measured.

To quantify this constraint, film resistance will be expressed in terms of film geometry and volume resistivity, ρ,

$$R = (\rho\ell)/(wt), \tag{5.35}$$

where t is the film thickness. Substituting into Eq. (5.34) yields

$$V = (\rho/t)^{1/2} \ell\, Q_E^{1/2} . \tag{5.36}$$

This expression sets the excitation voltage. Note that this result is independent of the width of the film. The level of Q_E can be adjusted for each measurement application. The film parameters (ρ/t, ℓ, w, t), however, must be selected beforehand by the design process. Substitution of Eq. (5.36) into Eq. (5.33) yields a form of the sensitivity equation useful for design,

$$\delta V/\delta T = (\rho/t)^{1/2}\, \alpha\ell\, Q_E^{1/2} . \tag{5.37}$$

This expression implies that long, thin films with high volume resistivity and temperature coefficient are best for high temperature measurement sensitivity. There are, however, many other conditions which must be considered to arrive at an overall optimum design of film resistance sensors for heat transfer gauges, some of which are discussed below.

The first two factors in Eq. (5.37), $(\rho/t)^{1/2}\alpha$, show the influence of film thickness and electrical properties on film sensitivity. Table 5.1 presents a ranking of some candidate film materials based upon the sensitivity parameter $\alpha\sqrt{\rho}$, derived using the bulk properties of the materials. Note, however, that these properties are a function of film

thickness in the region below 1 μm (where data is available for only a few substances [Ref. 5.12]). This table does provide some general guidance for maximizing temperature sensitivity, the final choice being also influenced by:

a) surface temperature changes resulting from the thermal resistance and capacity of the film,

b) abrasion resistance and substrate adhesion of the film,

c) residual stresses induced by the deposition process, and

d) changes in ρ and α from their known bulk property values.

TABLE 5.1
SENSITIVITY FACTORS FOR VARIOUS FILM THERMOMETER MATERIALS
(FOR EXCITATION AT CONSTANT HEAT FLUX) [Ref. 5.13]

Metal	T(°C)	Resistivity $\rho(\mu\Omega cm)$	Temp. Coeff. $\alpha x10^3(/°C)$	Sensitivity $\alpha\sqrt{\rho}$	Rank
Zirconium	20	40.0	4.4	27.8	1
Iron	20	9.71	6.51	20.2	2
Nickel	20	6.84	6.9	18.0	3
Tin	0	11.0	4.7	15.5	4
Tantalum	25	12.45	3.83	13.5	5
Platinum	20	10.6	3.927	12.7	6
Gold	20	2.24	8.3	12.4	7
Palladium	20	10.54	3.74	12.1	8
Cadmium	0	6.83	4.2	10.9	9
Chromium	0	12.9	3.0	10.7	10
Zinc	20	5.916	4.19	10.1	11
Copper	20	1.678	6.8	8.8	12
Aluminum	20	2.6548	4.29	6.9	13

Eq. (5.37) shows the influence of sensor surface geometry. The maximum length of the sensor, hence its sensitivity, will be determined by the spatial resolution requirements of the heat flux measurement. If this is characterized by a single length scale λ, for example, the film will be constrained to lie in a roughly square region, λ on a side. Since the

sensitivity has been shown to be independent of film width, a serpentine pattern may be employed to significantly increase the film sensitivity, if the minimum width that can be reliably deposited is much smaller than λ. For the film geometry chosen, $\ell \approx 14\lambda$. There are, however, several potential disadvantages to these thin, long and narrow film sensors. First, they will be more vulnerable to small scale nicks and scratches. Second, they may prove unsuitable for calibration of substrate physical properties by the electrical self-heating method, which requires that the film width be much larger than the thermal penetration depth over the required calibration time. Third, the sensitivity advantage of a long, thin, narrow film can be reduced by the reduction in its inherent signal to noise ratio which arises due to its increased resistance.

The signal to noise ratio of the thin film resistance thermometers will now be estimated. All resistors produce electrical noise as a result of the thermal motion of their electrons. The mean squared value of this thermal noise voltage is $\overline{V}_t^2 = 4kTBR$; where k is the Boltzmann constant, T the resistor absolute temperature, B the bandwidth over which this (white) noise voltage is measured, and R the resistance. A second contributor to resistor noise arises when the resistor 'feels' the flow of an externally applied current. All electrical currents have inherent fluctuations, arising from the fact that charge comes in discrete lumps (electrons). For a current of (average) magnitude I, the mean squared value of these fluctuations is $\overline{i}_s^2 = 2eIB$, where e is the electron charge. Passing through a resistor, these fluctuations appear as a voltage noise $\overline{V}_s^2 = \overline{i}_s^2 R^2 = 2eVRB$, commonly called shot noise. Since these sources are uncorrelated, the total resistor noise may be expressed as,

$$\bar{V}_n^2 = \bar{V}_t^2 + \bar{V}_s^2 = (4kT + 2eV)RB \ . \tag{5.38}$$

Note that $\bar{V}_n^2$, a measure of the noise power, is proportional to the product of the observation bandwidth and film resistance (and implicitly with the gain of the film sensor).

The mean squared signal power (obtained from Eq. (5.37)) is,

$$\delta\bar{V}^2 = (\rho/t)\alpha^2\ell^2 Q_E \delta T^2 \tag{5.39}$$

Forming the ratio of mean squared signal to noise powers yields the signal to noise ratio,

$$S/N = \frac{\alpha^2 Q_E(\ell w)(\delta T)^2}{(4kT + 2e\sqrt{Q_E(\rho/t)}\,\ell)B} \tag{5.40}$$

where Eqs. (5.35) and (5.36) have been used for R and V in Eq. (5.38).

The film noise will result in an indicated RMS temperature fluctuation, δT_n, which may be found from Eq. (5.40) by setting S/N=1,

$$\delta T_n = \delta T\Big|_{S/N=1} = \left\{\frac{4kTB}{Q_E l w \alpha^2}\left[1 + \frac{e\sqrt{Q_E(\rho/t)}\,\ell}{2kT}\right]\right\}^{1/2} \tag{5.41}$$

For the nominal operating conditions of the sensors designed here, this temperature is equal to 0.002°K, quite negligible. A more rigorous optimization of film design would include all the tradeoffs between the film, amplifier, and data acquisition system. This was not done in this case since this gauge noise level is less than the 0.08°K peak to peak equivalent noise of the amplification system used.

5.3 Fabrication and Mounting

Given the guidelines implicit in the gauge theory, the gauge design consisted of selection of the substrate material, the film resistor

material, and the sensor geometry. All three must be compatible with the fabrication technique selected. Vapor deposition and photolithography were chosen as being compatible with both large scale, low cost fabrication of these gauges and the fine sensor structure implied by the relatively high film sensor resistance desired.

Over fifty materials were studied as candidates for the gauge substrate. Polyimide (Kapton) was by far the most attractive material. It has the lowest $\sqrt{\rho ck}$ of any material studied (and thus the highest sensitivity bandwidth product), has excellent thermal and mechanical properties up to 600°K, has a well-developed adhesive technology (due to its wide use in strain gauges), is widely available, and is used in vapor deposition applications (for spacecraft). The substrate thickness, d, was selected as 25 μm to yield a direct mode response upper limit of 20 Hz and a semi-infinite mode lower limit of 1500 Hz.

The resistance thermometers are fabricated from 0.13 μm thick pure nickel. Nickel was chosen because of its relatively high net sensitivity (Table 5.1) and because of its very good adhesion characteristics in thin film applications. The sensor geometry selected (Fig. 5.6) was a square serpentine pattern to maximize the sensor length in an area compatible with the expected disturbance length in the flow field and thus maximize the signal to noise ratio as discussed earlier. The sensor resistance is approximately 500Ω. Low resistance gold leads or 'tags' 1 μm thick are deposited from the sensor to the edge of the polyimide sheet. Signals from the bottom sensor come through 0.5 mm diameter 'plated through' holes, laser drilled in the substrate before the deposition process. Twenty-six gauges are fabricated on a single polyimide sheet whose dimensions are compatible with a turbine airfoil surface area.

The vapor deposition is done by d.c. sputtering at a pressure of $5x10^{-4}$ torr of argon. The deposition rate of the nickel is 0.2 nm per second. The geometrical delineation is done using a liftoff process, the two gauge sides being done separately. The manufacturing yield and material properties are very strongly process variable dependent. The principal problem with the gauges is a high batch to batch variation in manufacturing yield which is not yet understood. The problem appears as a high level of intrinsic stress in the nickel, resulting in cracking of the sensors. Work is underway to solve this problem.

Originally, a silicon dioxide overcoat was applied to the bottom sensor surface to serve as an electrical insulator. This was discontinued in favor of anodizing the surface of the aluminum blading, a practice which has proven completely satisfactory.

The gauge sheets are simply cut to conform to the blade surface outline and then bonded to the surface using conventional strain gauge cement and mounting techniques. Thermal time response testing has indicated that the glue layer is 5 μm thick. Seventy-five micron diameter wires are soldered to the far ends of the gold tags to bring out the signals in a region far removed from the measurement area.

5.4 Calibration of the Heat Flux Gauges

5.4.1 Theory

As in most experimental techniques used to determine heat flux, temperature is the physical quantity measured, from which surface heat flux is inferred by one of several techniques: direct processing of the temperature signal by a physical RC analog network, numerical integration of the measurement with a kernal function, or processing of the measurement by a numerical analog of the gauge heat flow. These techniques are based

upon a model of the heat conduction process within both the gauge and, in most cases, the test article. The model not only provides the physical and mathematical framework for each approach but also the form of the fundamental parameters which govern the behavior of the gauge.

The multilayer gauge provides two temperature measurements: at the surface, and at a depth d below the surface. From the model derived earlier, it can be seen that two constants must be determined - $\sqrt{\rho ck}$ (the conventional parameter used with surface thermometry based upon the semi-infinite assumption), and k/d (representing the steady state heat flux per unit temperature drop across the gauge).

Careful calibration of these parameters is particularly important for this gauge since there is far less experience with Kapton as a substrate than with the more conventional quartz, Pyrex, or machineable ceramic materials. Significant deviations from the 'nominal' or advertised thermal and physical properties might occur within the manufacturing tolerances of the Kapton sheet. Furthermore, it is not yet known what influence, if any, the film thermometer deposition process might have upon these properties. Thus, given that the upper and lower film sensors have been calibrated as thermometers and that all the assumptions pertaining to the sensor model are satisfied, knowledge of $\sqrt{\rho ck}$ and (k/d) will fully characterize the operation of the heat flux sensor.

The temperature coefficient of resistivity of the thin film thermometers is conventionally calibrated by placing the gauges in a heated immersion bath and varying the bath temperature. All sensors on a test specimen are tested together. The accuracy of the calibration is limited by that of the reference thermometer to approximately 0.05°C.

Many calibration schemes for $\sqrt{\rho ck}$ and k/d place boundary conditions

on the gauge for which exact solutions of the heat conduction equation can be found. The calibration coefficients may then be inferred from a simple comparison of the experimental data with the theoretical solution. The overall accuracy of the result will be dependent upon both the quality of the various physical measurements required and the accuracy to which the assumed boundary conditions are realized. This latter condition is especially crucial since its validity may not necessarily be apparent from the test data alone. Thus, there is a practical virtue in making these boundary conditions as simple as possible, i.e., that the flow of heat be one-dimensional and that the gauge appear thermally semi-infinite. Given these conditions, simple analytical solutions can be found for the surface temperature response to a wide variety of surface heat flux time histories. For example, the top surface response to a step in surface heat flux, Q, is given by,

$$T(t) = \frac{2Q}{\sqrt{\pi}\sqrt{\rho ck}}\, t^{1/2} \tag{5.42}$$

Commonly, the step in surface heat flux is applied by pulsing current through the film, i.e., resistive dissipation in the sensor itself [Ref. 6.6]. This technique cannot be used with this gauge geometry, however, since the sensor width is on the order of the insulator thickness, violating the uniform heating assumption and introducing errors on the order of 100%. Instead, a calibration technique is used in which the gauge is radiantly heated by a laser pulse, simultaneously yielding $\sqrt{\rho ck}$ and k/d.

Conceptually, step radiant heating can be used as a direct calibration, i.e., a known heat rate is applied to the top gauge surface with $\sqrt{\rho ck}$ being inferred from the top sensor rise time and k/d simply

computed from the top and bottom sensor temperatures. In practice, this can be difficult to achieve since the measurement accuracy is directly proportional to the absolute accuracy to which the pulse power is known, dependent upon absorption characteristics of the surface, and is sensitive to the energy distribution in the laser beam. Rather than attempt to perform an accurate absolute measurement, a relative calibration technique was developed which depends upon ratios, not absolute values.

In the relative calibration, the step response is measured with the sensor both covered and uncovered by a reference fluid of known $\sqrt{\rho ck}$. The method is based upon the principle that the applied surface coating acts as a sheet source of heat at the interface of two semi-infinite substances. Theory shows that the ratio of heat entering each substance equals the ratio of their respective values of $\sqrt{\rho ck}$ (since both materials see the same interface temperature), and this fact may be exploited to measure this ratio [Ref. 6.6]. Since the method involves the comparison of measurements, absolute knowledge of the incident heat flux and film thermometer scale factor are not needed, being replaced instead only with the requirement that these quantities remain stable over the duration of the tests. However, any change in the total heat flux absorbed by the surface coating as a result of the application of the reference fluid (by mechanisms such as meniscus focusing, absorption by the fluid or by reflections from its surface) must either be negligible or quantifiable.

For the first set of tests, the sensor is placed in vacuum or still air. If Q_I represents the surface heating, the resulting temperature rise according to the theory is,

$$T_I(t) = \frac{2Q_I}{\sqrt{\pi}\sqrt{(\rho ck)_s}} t^{1/2} \tag{5.43}$$

For the second set of tests, the sensor is placed in good thermal contact with a material of known $\sqrt{\rho ck}$ by covering it with a fluid of high electrical resistivity. If Q_S represents the heat flux entering the sensor, and Q_F that entering the fluid, than at their common boundary the temperature rise is given by,

$$T_{II}(t) = \begin{cases} \dfrac{2Q_S}{\sqrt{\pi}\sqrt{(\rho ck)_S}} t^{1/2} \\ \\ \dfrac{2Q_F}{\sqrt{\pi}\sqrt{(\rho ck)_F}} t^{1/2} \end{cases} \tag{5.44}$$

from which it can be concluded that,

$$\frac{Q_S}{Q_F} = \frac{\sqrt{(\rho ck)_S}}{\sqrt{(\rho ck)_F}} \tag{5.45}$$

If the total heat flux absorbed by the coating for this second series of tests is Q_{II}, where $Q_{II} = Q_S + Q_F$, the flux into the sensor is found to be,

$$Q_S = \left[1 + \frac{\sqrt{(\rho ck)_F}}{\sqrt{(\rho ck)_S}}\right]^{-1} Q_{II} \tag{5.46}$$

and the temperature rise at the surface is therefore,

$$T_{II}(t) = \left[1 + \frac{\sqrt{(\rho ck)_F}}{\sqrt{(\rho ck)_S}}\right]^{-1} \frac{2Q_{II}}{\sqrt{\pi}\sqrt{(\rho ck)_S}} t^{1/2} \tag{5.47}$$

If m_I and m_{II} are the slopes of the linear region of sensor

temperature, versus the square root of time (i.e., from Eqs. (5.43) and (5.47)) for the two conditions, then

$$m_I = \frac{2Q_I}{\sqrt{\pi}\sqrt{(\rho ck)_S}} \tag{5.48}$$

$$m_{II} = \left\{ 1 + \frac{\sqrt{(\rho ck)_F}}{\sqrt{(\rho ck)_S}} \right\}^{-1} \frac{2Q_{II}}{\sqrt{\pi}\sqrt{(\rho ck)_S}} \tag{5.49}$$

and by forming their ratio,

$$\sqrt{(\rho ck)_S} = \left\{ \left(\frac{Q_{II}}{Q_I}\right)\left(\frac{m_I}{m_{II}}\right) - 1 \right\}^{-1} \sqrt{(\rho ck)_F} \tag{5.50}$$

If the total heat absorbed by the coating is the same in both tests (as has been verified in this case), this relation becomes,

$$\sqrt{(\rho ck)_S} = \left[\left(\frac{m_I}{m_{II}}\right) - 1 \right]^{-1} \sqrt{(\rho ck)_F} \tag{5.51}$$

and serves as the basic relative calibration formula. Note that only ratios of the quantities appear.

A simultaneous calibration of k/d may be obtained by extending the heating time to values very much larger than the characteristic time of the sensor, $\tau = d^2/4\kappa$. The lower sensor begins to respond to the surface heating at approximately time τ (τ = 1.6 ms for these gauges), with steady state conditions being achieved by $t = 20\tau$. For $t > 20\tau$, the steady state temperature difference, $(T_u - T_\ell)_{ss}$, between the upper and lower surfaces of the sensor becomes proportional to the applied heat flux, thus k/d may be found from,

$$\frac{k}{d} = \frac{Q}{(T_u - T_\ell)_{ss}} \tag{5.52}$$

given that Q is known.

The magnitude of Q could be obtained from an independent measurement of beam intensity and surface absorptivity (as would be required for an absolute calibration). However, when the k/d calibration is merged with the relative procedure, Q may be calculated directly be combining the initial step response data from the first set of tests, Eq.(5.48), with the value of $\sqrt{(\rho ck)}_s$ determined from the refrence fluid tests, Eq.(5.51). Substituting this result into Eq. (5.52) then yields the desired expression for k/d,

$$\frac{k}{d} = \left(\frac{\sqrt{\pi}}{2}\right)\left(\frac{m_I m_{II}}{m_I - m_{II}}\right)\frac{\sqrt{(\rho ck)_F}}{(T_u - T_\ell)_{ss}} \tag{5.53}$$

It should be pointed out that, unlike the $\sqrt{\rho ck}$ testing, this expression requires that the film thermometer temperature coefficients of resistivity be calibrated or, more precisely, that their scale factors, if unknown, at least be equal.

5.4.2 Calibration Results

An argon ion laser was used as the radiant heat source, providing an incident flux of approximately 30 kW/m^2 over an area slightly larger than the 1 mm square of the film thermometer. The laser output was modulated by an electro-optic modulator producing a light step with a 25 ns rise time. The surface of the sensor was blackened with a Staedtler Lumograph Model-316 non-permanent marking pen, commonly used for view-graph presentations. The coating has good opacity and low thermal inertia, as verified by comparing the measured temperature responses with the parametric theory

presented earlier, and its selection was the result of a large number of empirical tests. This coating has the advantage, unlike many of the other coating materials evaluated, of possessing both high electrical resistivity and poor solubility in the reference fluids.

The reference fluid chosen was dibutylphthalate, a commonly used heating bath medium with electrical equipment, because of its inert properties and high electrical resistivity. Its thermal properties were obtained from the manufacturer and checked against the properties of the more commonly employed glycerol using the electrical heating technique on a platimum-quartz film sensor. Its value of $\sqrt{\rho ck}$ is estimated to be 495 ±5%. Since it is much less viscous than glycerol, it does not produce measureable beam focusing effects, as did the latter fluid.

A sample calibration is shown in Fig. 6.7, from which it can be seen that the top sensor output is linear with the square root of time. The slopes m are then calculated from the least square fits to the data as illustrated by the lines. From these measurements, we conclude that $\sqrt{\rho ck}$ for this gauge is $575(W/m^2)(\sqrt{sec})/°K$ and k/d is 8086 $W/(M^2°K)$. This represents a 20% departure from nominal published data.

Since the gauges are intended for a highly stressed rotor environment, gauge sensitivity to strain must be considered. This was evaluated by pulling an aluminum specimen bearing a gauge in a tensile test machine. Strain sensitivity proved to be negligible, equivalent to 0.003°C at 2% strain.

5.5 Data Reduction - Numerical Analysis Technique

The heat flux gauges have been shown to be suitable for the evaluation of surface heat flux both at low and high frequencies where gauge characteristics can be simply defined. At low frequencies, the heat flux is

obtained directly from the measured temperature difference across the insulator and at high frequencies through the use of well established semi-infinite procedures. This section describes a data reduction method which expands the useable frequency range to include the regime between the DC and semi-infinite response modes.

The method employs a lumped parameter model of the gauge insulating substrate which is driven by the measured upper and lower temperature sensor outputs. The formulation of the model equations is based upon an extension of the work performed by Oldfield et al. [Ref. 5.14] for the design of physical R-C networks used in real time conversion of surface temperature measurements into heat flux data. Although concerned with the simulation of the semi-infinite heat conduction process, his results are readily adapted to the modeling of a finite length network by the addition of a terminating 'resistor' which is driven by the lower sensor output. The resulting set of coupled equations is solved by a fourth order Runge-Kutta method with the upper surface heat flux inferred from the calculated temperature drop across the first series resistance element of the model network.

The selection of the thermal properties of each of the lumped elements is set to satisfy the following conditions:

1) the finite thickness of the insulator must be mirrored in the total thermal impedance of the network;
2) ρck for each element must equal the physical value;
3) the 'length' of the first element is set by the required network bandwidth; and
4) the number of lumped elements to model the insulator sets the logarithmic spacing of all but the first element.

The performance of the lumped parameter model was established using the exact solutions presented in Sec. 5.2.1 and 5.2.2. By comparing the reconstructed surface heat flux response when driven by the exact solutions, the step response and sinusoidal magnitude-phase characteristics of the model were established as a function of the model parameters. Figure 5.8 presents the step response for a nine-stage network model over a range of model upper frequency limits, ie., first stage lengths. The results are excellent, displaying no overshoot or evidence of high frequency ringing. The frequency response, shown in Fig. 5.9 for a nine stage model with 100 kHz frequency limit, demonstrates the ability of the model to fully reconstruct the entire frequency domain, including the band between the low frequency and the semi-infinite modes.

5.6 Heat Flux Measurements

As an initial test of the gauge technology, the heat flux gauges were mounted on the stationary outer tip casing above the rotor of a transonic turbine in the MIT Blowdown Turbine Facility. A time history of the top and bottom temperature sensors of a gauge is shown in Fig. 5.10. At time equal to zero, the tunnel is in vacuum and the sensors are the same temperature. After the starting transient, the tunnel operation is then quasi-steady (from 250 ms). The metal substrate temperature remains constant while the inlet temperature slowly drops, reflecting the isentropic expansion from the supply tank. This is seen in the decrease in the top-bottom temperature difference and thus in heat flux over the test time. The thick line of the top sensor output is the envelope of the high frequency heat flux components.

The heat flux, as calculated by the numerical data reduction technique from these two signals starting at 300 ms, is shown in Fig. 5.11. The

blade passing frequency is approximately 6 kHz and the sampling frequency is 200 kHz. Note that the relatively small amplitude of the high frequency temperature fluctuation on the top sensor in Fig. 5.10 actually represents an ac heat flux modulation of 80%. The small ac temperature signal relative to the dc level reflects the $\omega^{1/2}$ rolloff in sensitivity discussed in the gauge theory.

5.7 Error Assessment

The primary sources of heat flux measurement error arise from film thermometer scale factor stability and substrate thermal property uncertainties. Secondary sources include initialization (bias) errors, uncompensated temperature coefficient non-linearity, film excitation heating, and substrate property stability and temperature dependence. Performance has been demonstrated to the following levels:

- Scale factor stability: 0.2 %
- Scale factor error: 0.002 °C/C
- Scale factor linearity: 0.1 °C over 50 °C
- Initialization error: 0.05 °C
- Absolute $\sqrt{\rho ck}$: 5 %
- Absolute k/d: 5 %
- $\sqrt{\rho ck}$, k/d stability: 1 %

The temperature scale factor, $\sqrt{\rho ck}$, and k/d stabilities were determined from a comprehensive set of calibrations performed before, during and after a major tunnel test series. Scale factor linearity was determined during the temperature bath calibration of the films. At these levels of stability and linearity the temperature difference measurement scale factor is governed by the quality of the calibration reference thermometers which are good to at least 0.1°C over 50°C.

The ρck uncertainty is the major contributor to heat flux measurement error and depends upon the assumptions employed in the relative calibration scheme discussed Section 5.4. The $\sqrt{\rho ck}$ uncertainty dominates temperature measurement errors in the determination of k/d. From data supplied by the polyimide substrate manufacturer, uncompensated errors resulting from the thermal property temperature dependence are estimated to be on the order of 2.5%. This dependence can be easily measured with the gauge calibration scheme discussed earlier and compensated by the data analysis technique presented in Section 5.5.

Substrate property uncertainties also dominate the temperature difference measurement errors for run time heat flux measurements over the working range of the gauge, 10-200 kW/m^2. Run time initialization errors arise from short term bias drifts, which are negligible in the system employed, and from data acquisitin system quantization. These contribute an additive heat flux error on the order of 0.2-0.5 kW/m^2.

As currently employed, a conservative assessment of the overall error may be placed at approximately 10% of the measured heat flux over the nominal working range of the gauge.

5.8 Conclusions

A multilayer heat flux gauge has been developed which successfully meets all of its design criteria. It is directly applicable to metal blading in large numbers, has frequency response extending from DC to 100 kHz, does not introduce flow disturbance, and is well suited to rotating frame applications. These gauges are now being extensively used in the turbine research program at MIT.

5.9 References

5.1 Atkinson, W.H., and Strange, R.R., "Development of Advanced High Temperature Heat Flux Sensors," NASA CR 165618, Sept. 1982.

5.2 Richards, B.E., "A Review of Heat Transfer Work in the VKI Hot Cascade Tunnel," AGARD Specialists Meeting on "Testing and Measurement Techniques in Heat Transfer and Combustion," Brussels, AGARD CP-281, May 1980.

5.3 Baines, N.C., Oldfield, M.L.G., Jones, T.V., Schultz, D.L., King, P.I., Daniels, L.C., "A Short-Duration Blowdown Tunnel for Aerodynamic Studies of Gas Turbine Blading," ASME 82-GT-312, 1982.

5.4 Dunn, M.G., Hause, A., "Measurement of Heat Flux and Pressure in a Turbine Stage, J. of Eng. for Power, 104, 1, January 1982.

5.5 Epstein, A.H., Guenette, G.R., Norton, R.J.G., "The Design of the MIT Blowdown Turbine Facility," ASME Paper 84-GT-116, 1984.

5.6 Schultz, D.C., and Jones, T.V., "Heat Transfer Measurements in Short Duration Hypersonic Facilities," AGARD AG-165, Feb. 1973.

5.7 Bachmann, R.C., Chambers, J.T., Giet, W.H., "Investigation of Surface Heat Flux Measurements with Calorimeters," ISA Trans, 4, 2, 1965.

5.8 Sprinks, T., "Influence of Calorimeter Heat Transfer Gauges on Aerodynamic Heating," AIAA J., 1, 2, 1963, p. 497.

5.9 Hylton, L.D., Mikelc, M.S., Turner, E.R., Nealy, D.A., York, R.E., "Analytical and Experimental Evaluation of Heat Transfer Distribution Over the Surfaces of Turbine Vanes," NASA CR 168015, 1983.

5.10 RDF Corp., Hudson, NH.

5.11 Carslow, H.S., and Jaeger, J.C., Conduction of Heat In Solids, 2nd Ed., Oxford University Press, Oxford, 1959.

5.12 Schwartz, N., and Berry, R.W., "Thin Film Components and Circuits," in Physics of Thin Films, Vol. 2, Hass and Thun, Eds., Academic Press, New York, 1967.

5.13 Weast, R., and Selby, S., Eds., Handbook of Chemistry and Physics, 63rd Ed., Chemical Rubber Co., Cleveland OH, p. F-133.

5.14 Oldfield, M.L.G., Burd, H.J. and Doe, N.G., "Design of Wide-Bandwidth Analogue Circuits for Heat Transfer Instrumentation in Transient Tunnels," Heat and Mass Transfer in Rotating Machinery, papers from the 16th Symposium of the International Center for Heat and Mass Transfer, held in Dubrovnik, September 1982, Hemisphere Publ. Corp., NY.

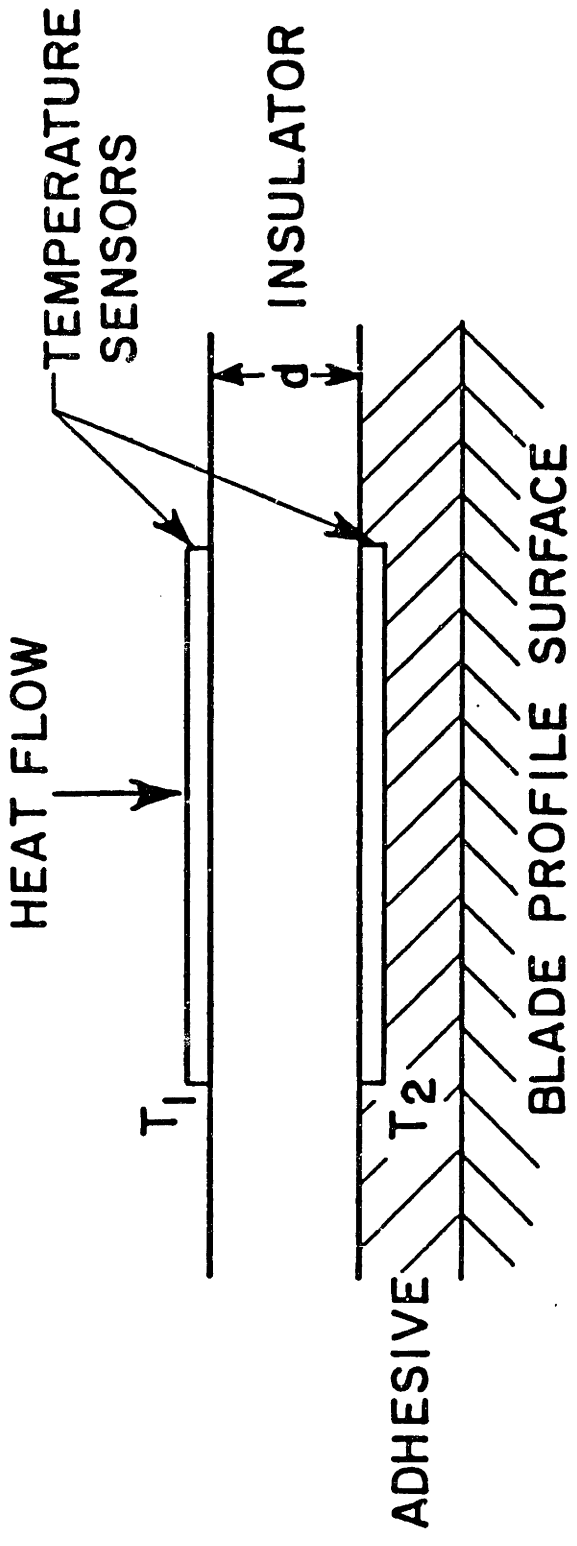

FIGURE 5.1: SCHEMATIC CROSS-SECTION OF MULTILAYER HEAT FLUX GAUGE

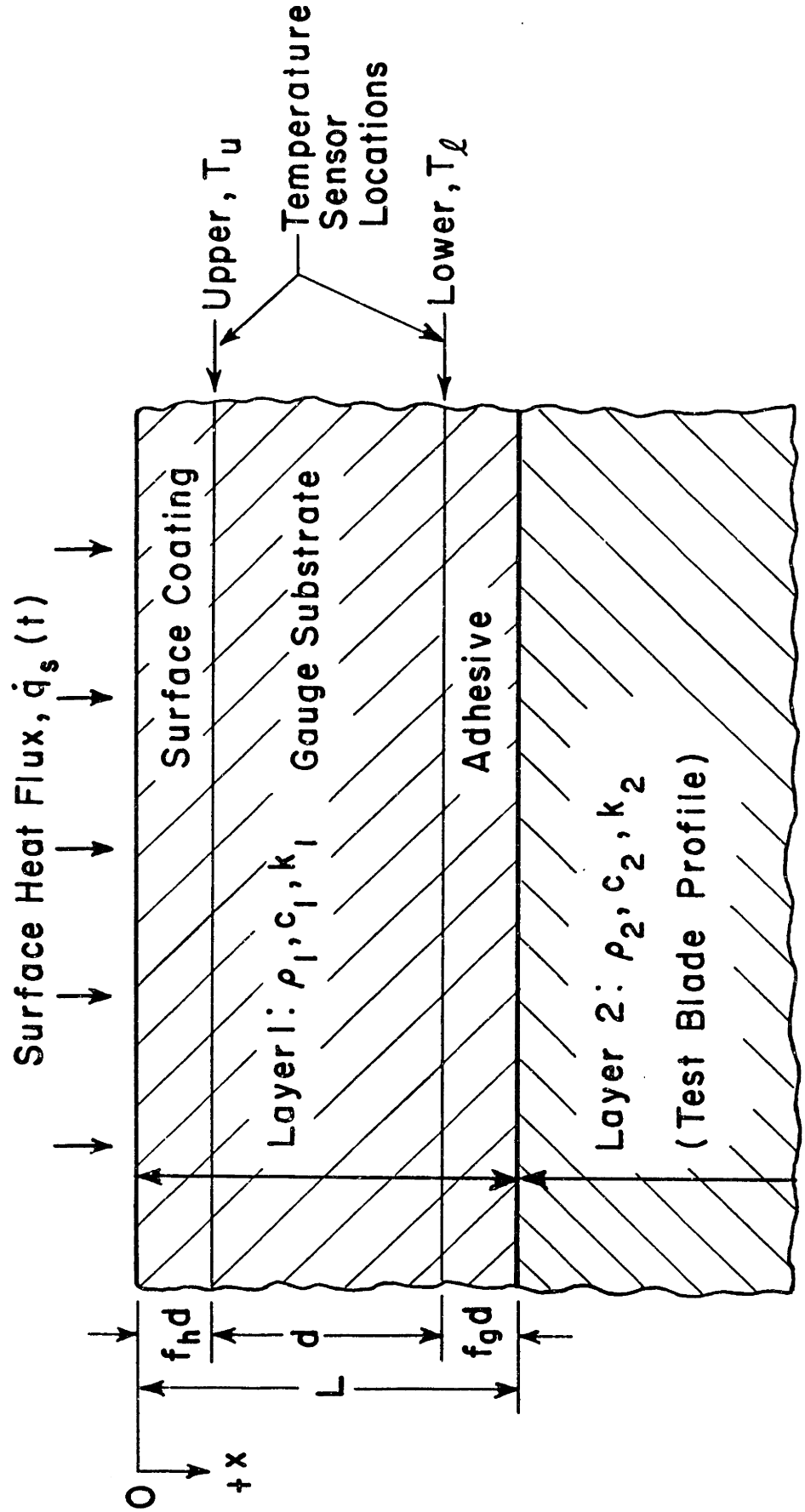

FIGURE 5.2: GEOMETRY OF GAUGE IN ANALYTICAL MODEL

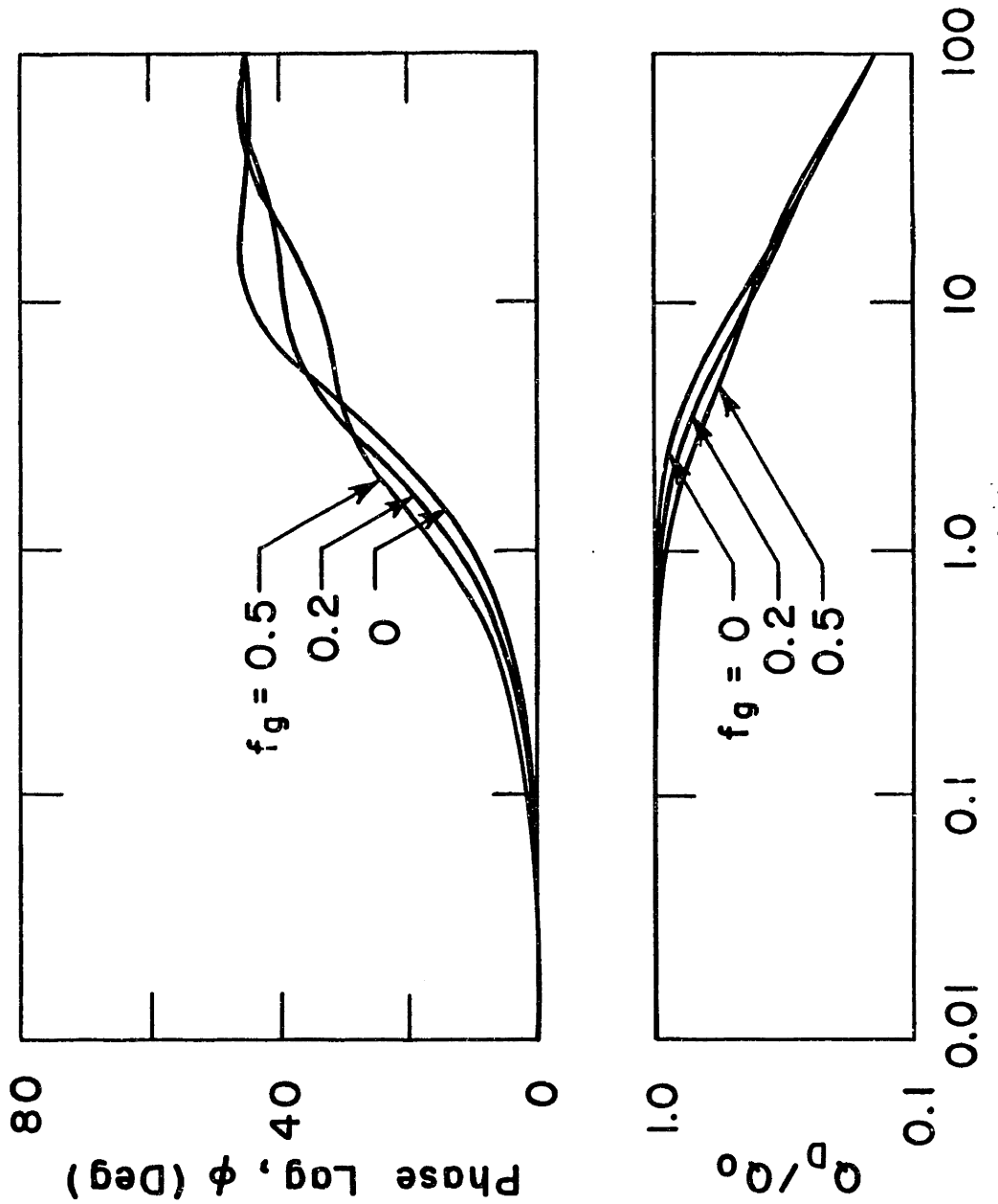

FIGURE 5.3: HARMONIC FREQUENCY RESPONSE OF GAUGE NORMALIZED TO THE DIRECT OR SHUNT MODE CUTOFF FREQUENCY, ω_c, AS A FUNCTION OF FRACTIONAL GLUE THICKNESS

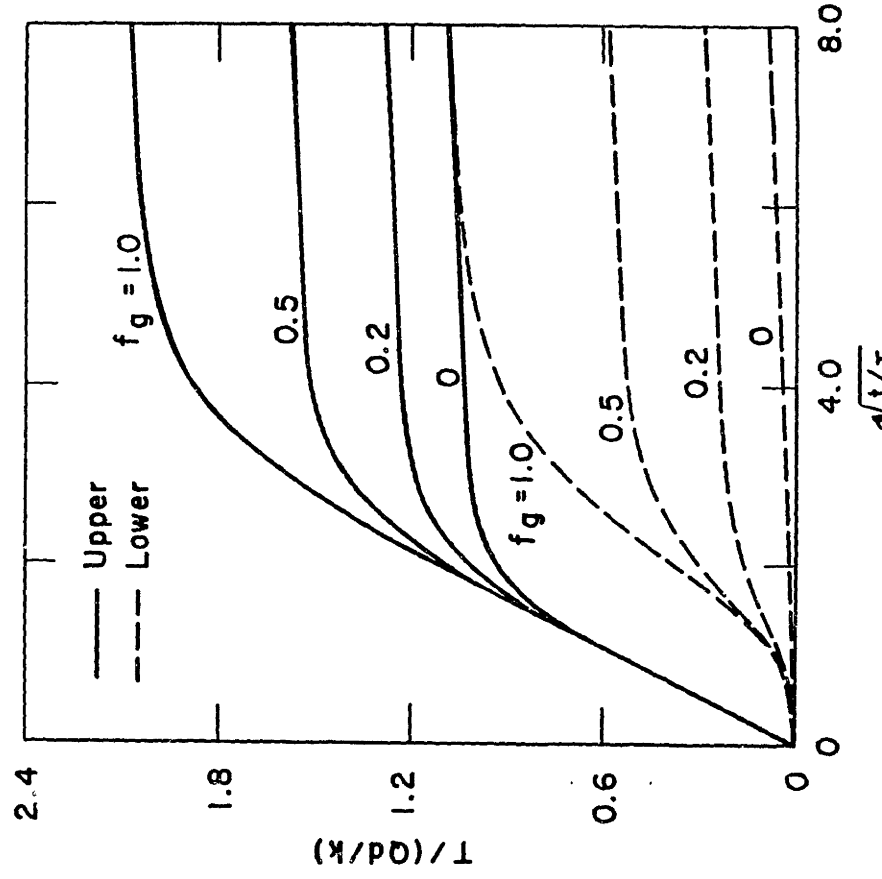

FIGURE 5.4: SEMI-INFINITE MODE NORMALIZED TIME RESPONSE OF UPPER AND LOWER SENSORS TO A STEP IN HEAT FLUX AS A FUNCTION OF FRACTIONAL GLUE THICKNESS

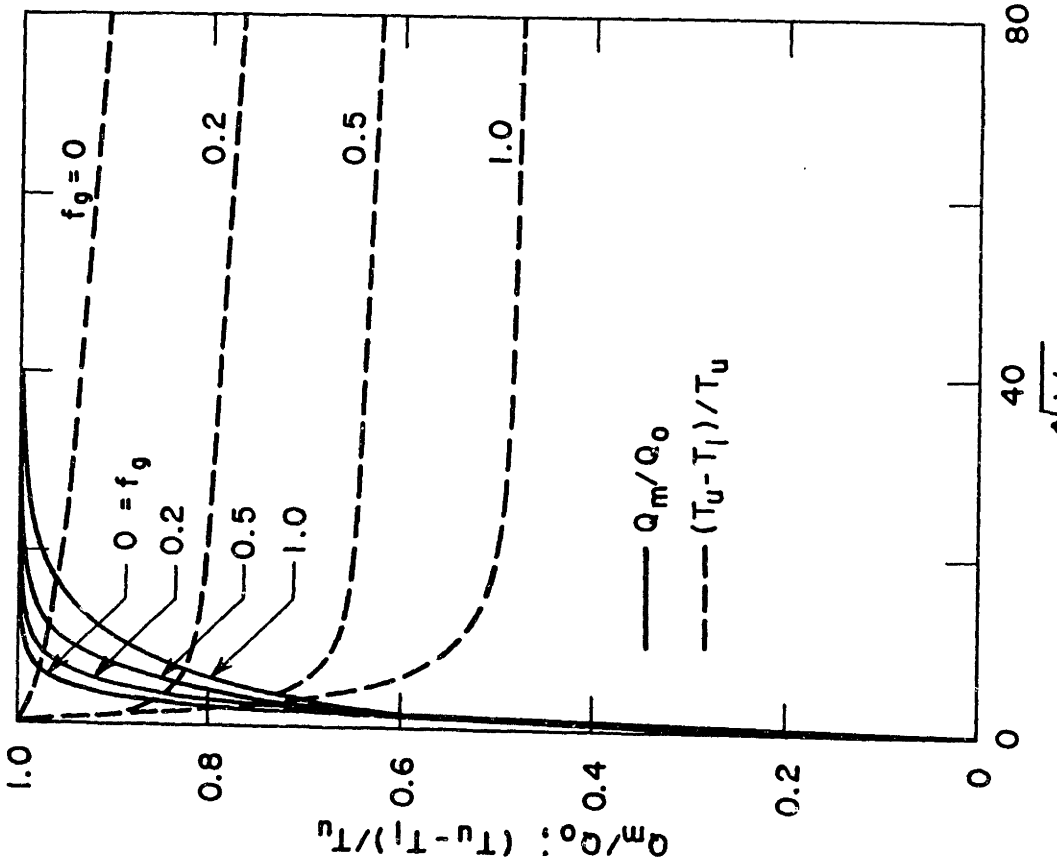

FIGURE 5.5: DIRECT MODE NORMALIZED RESPONSE TO A STEP INPUT OF HEAT FLUX AS A FUNCTION OF FRACTIONAL GLUE THICKNESS

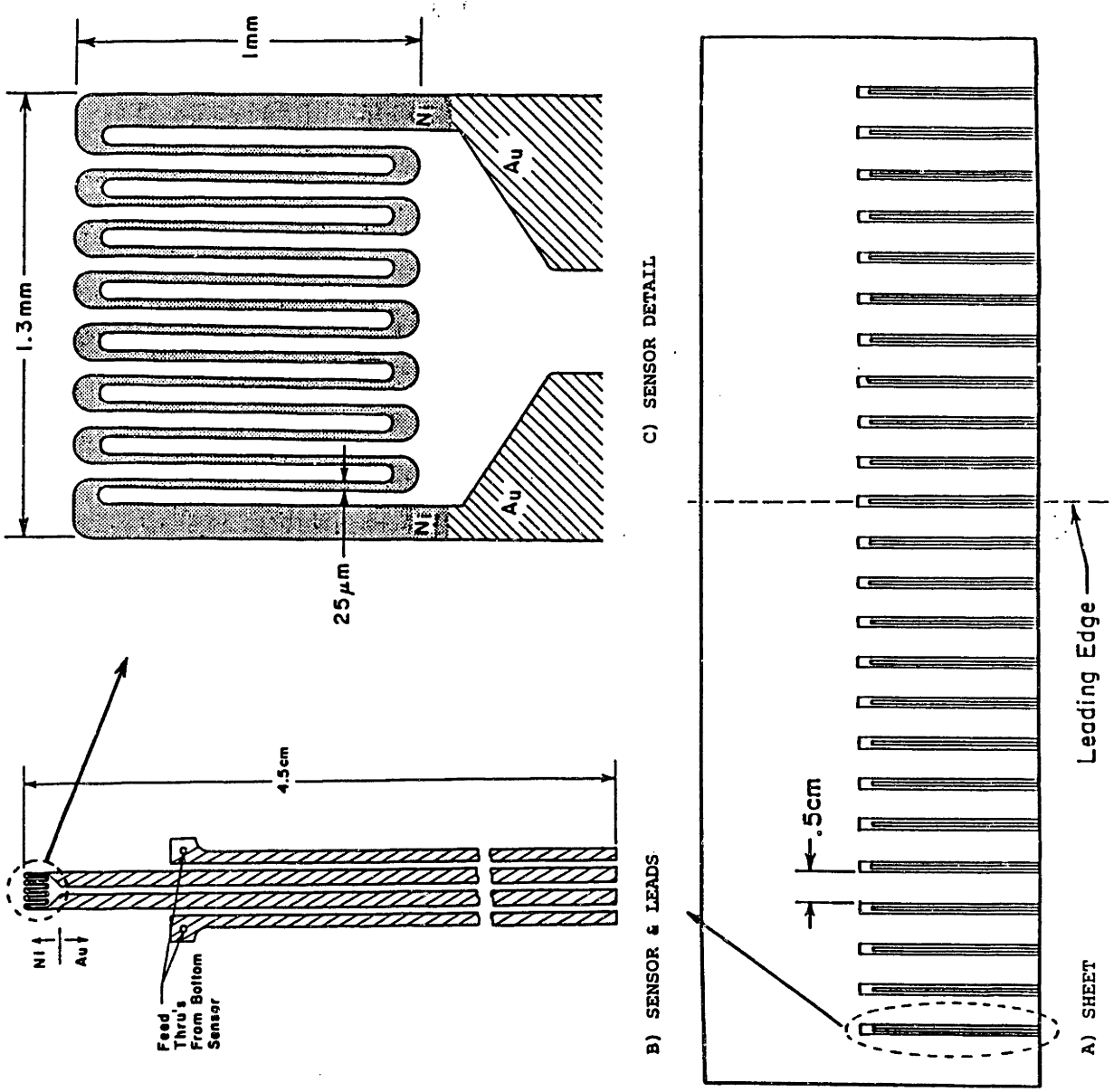

FIGURE 5.6: GAUGE GEOMETRY SHOWING SENSOR DETAIL, SENSOR AND LEADS, AND GAUGES ON MANUFACTURING SHEET

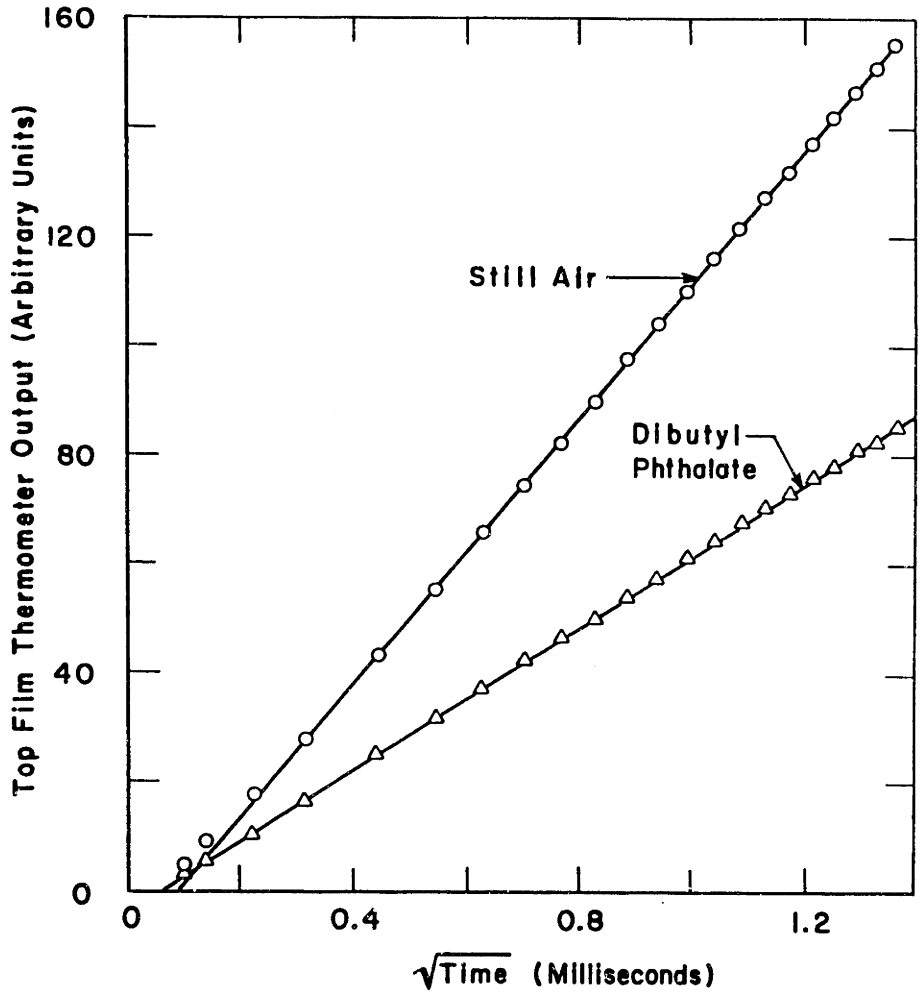

FIGURE 5.7: GAUGE THERMAL CALIBRATION DATA; $\sqrt{\rho ck}$ IS PROPORTIONAL TO THE RATIO IN SLOPE OF THE CURVES

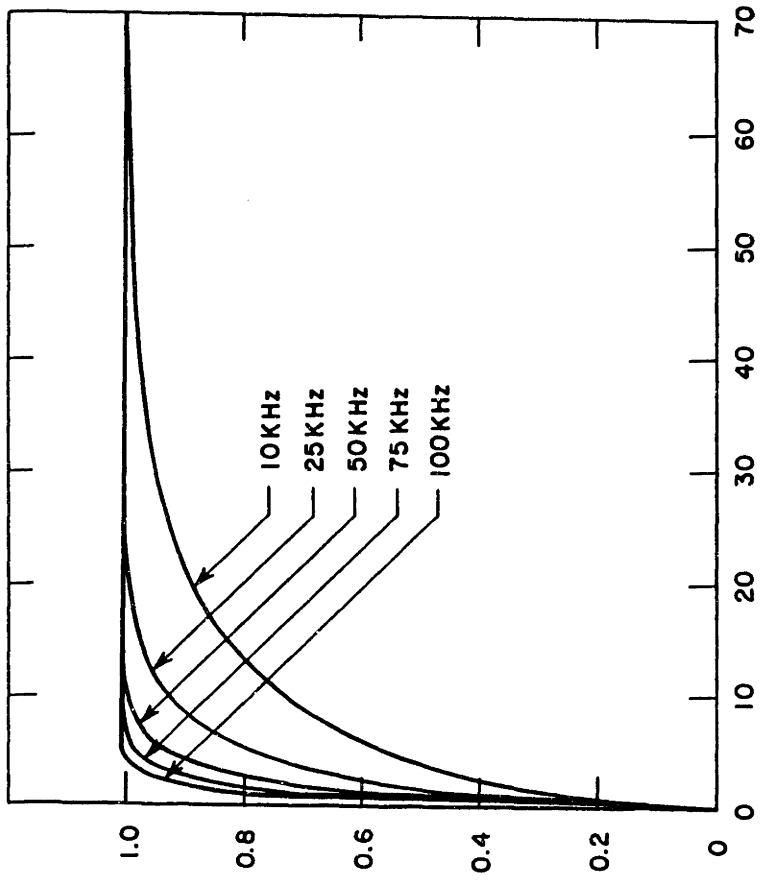

FIGURE 5.8: RISE TIME OF THE NUMERICAL DATA REDUCTION MODEL AS A FUNCTION OF MODEL BANDWIDTH

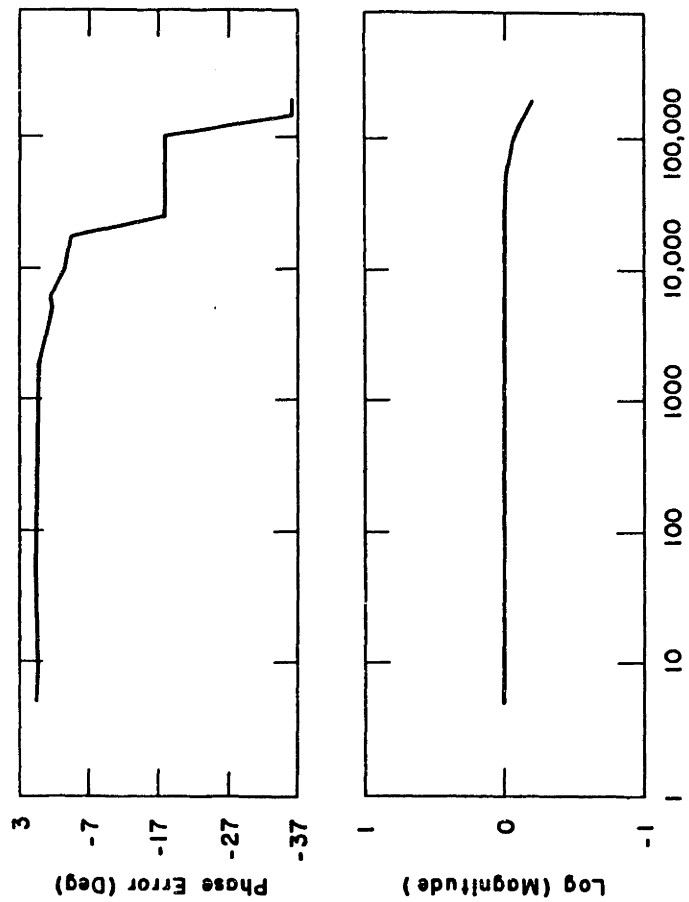

FIGURE 5.9: FREQUENCY RESPONSE OF THE 100 kHz BANDWIDTH DATA REDUCTION NUMERICAL SCHEME

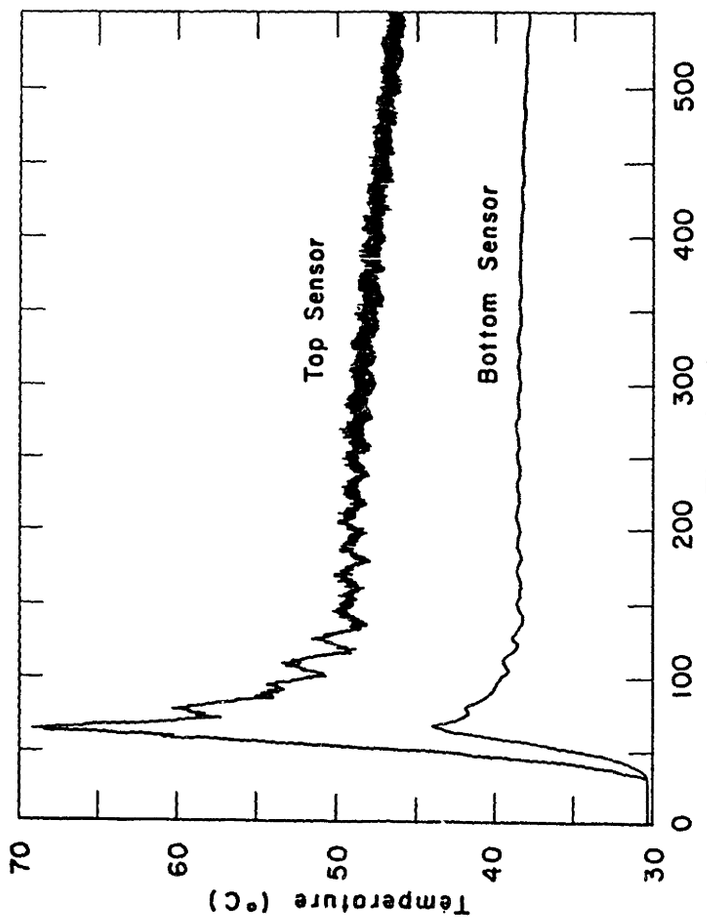

FIGURE 5.10: TIME HISTORY OF GAUGE SENSORS MOUNTED ON THE STATIONARY CASING ABOVE A TRANSONIC TURBINE ROTOR TIP

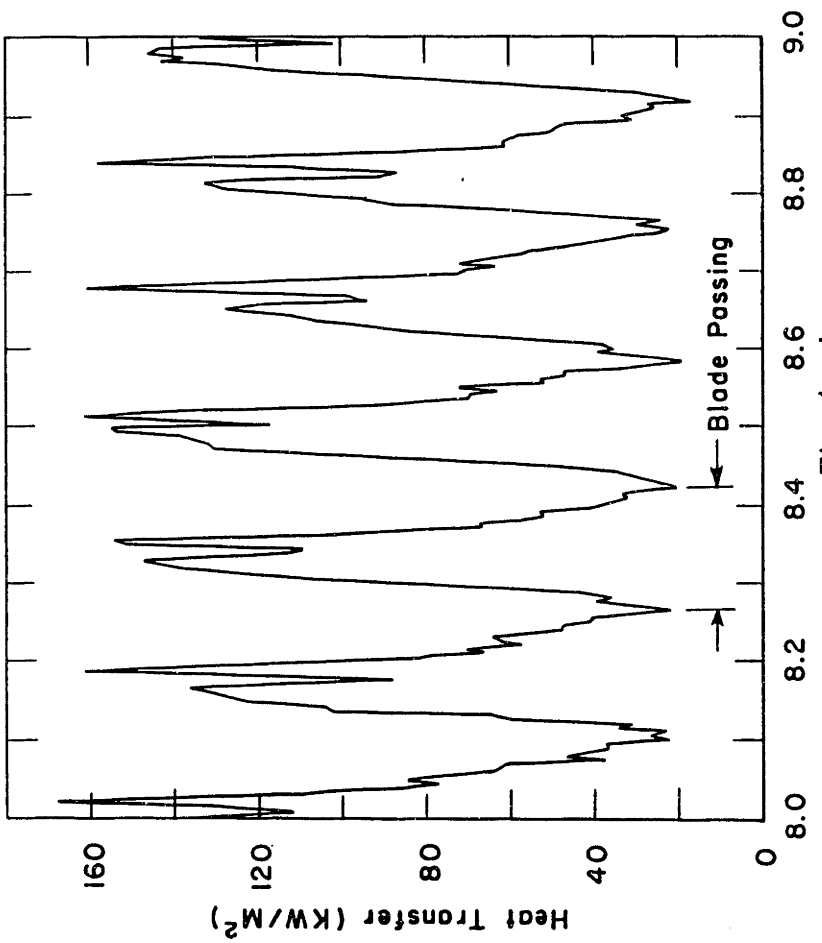

FIGURE 5.11: HEAT FLUX CALCULATED FROM THE DATA IN FIG. 10

CHAPTER 6

TIME RESOLVED MEASUREMENTS ON A TURBINE ROTOR TIP CASING

6.0 Summary

This chapter presents the results of the first detailed experimental investigation of both time resolved heat flux and static pressure distributions on the rotor tip casing of a transonic high pressure turbine. The test series reproduced all of the full scale, nondimensional turbine flow parameters. Measurements were made as a function of rotor corrected speed (rotor inlet incidence) and of Reynolds number. The pressure measurements suggest a strong under tip flow influenced by the airfoil loading distribution. The heat flux is highly unsteady with fluctuations in some cases being 80% of the mean level. Approximately 45% of the total heat load to the casing may be attributed to the tip leakage flow, and the axial distribution of time averaged heat flux reflects both the rotor enthalpy extraction and blade thickness distributions.

6.1 Introduction

As turbine pressure levels and loadings continue to rise, the heat transfer to the stationary casing surrounding the rotor tip (tip seal) of modern high pressure turbine stages is becoming increasingly important. The tip casing is now a complicated subsystem in itself, often containing mechanical abrasion material, film cooling, and external temperature regulation for active tip clearance control. The flow field on the casing surface is complex since it is an inherently unsteady, three-dimensional flow, strongly influenced by the close proximity of the passing rotor blades. Little quantitative data is available in the literature elucidating even the average casing flow and heat transfer, much less the unsteady distributions.

The unsteady character of this flow field makes it difficult to study in stationary cascades. Thus, data had been limited to that which could be derived from full scale engine tests. It is only recently that scaled, rotating facilities have been built which are well-suited to the casing heat transfer problem [Refs. 6.1 and 6.2].

Considerable work has been done on tip leakage aerodynamics in compressors and, to a lesser extent, in turbines [Refs. 6.3 and 6.4], but relatively little in regard to heat transfer. A simple steady state model has been used to study heat transfer to the rotor blade tip by treating the tip leakage as a simple couette duct flow, [Ref. 6.5]. Unlike the blade tip, the tip casing is subjected to an unsteady flowfield, so this model cannot be directly applied. Some time averaged casing heat flux data is available in the open literature [Refs. 6.1 and 6.6], but it does not shed much light on the structure of the flow in this region.

The study reported herein was undertaken to measure the time resolved heat transfer and pressure distributions on the tip casing of a high pressure turbine, in order to elucidate the flow phenomena in this region which are important to the casing heat transfer.

6.2 Instrumentation

For the tip casing tests, pressure and heat flux instrumentation were mounted on a removable aluminum plug which extended over four rotor blade spacings, as shown in Fig. (6.1). Wall static pressure was measured using five 1.5 mm diameter silicon wafer pressure transducers. These were mounted flush with the casing surface using a thin layer (25~50 μm) of silicon rubber cast over the diaphragm in order to conform to the wall curvature.

Time resolved heat flux to the casing wall was measured at seven axial

stations extending from just upstream to just downstream of the rotor, using the heat flux gauges described in Chapter 5. A single Kapton sheet containing the gauges was adhesively bonded to the tip casing insert, completely covering the flow passage area. Each gauge was calibrated using the pulsed laser technique both before and after the run series. The relative gauge calibrations were found to match to better than 1%. Absolute calibration accuracy is about 5%. A detailed discussion of the gauge theory, data reduction, and calibration may be found in Chapter 5 or in Ref. [6.7].

6.3 Experimental Observations

The time resolved heat flux and wall static pressure distributions were measured at three rotational speeds, two Reynolds numbers, and one gas to wall temperature ratio for a gap to span ratio of 0.8%. Test conditions are summarized in Table 6.1.

TABLE 6.1 - TIP CASING TEST SUMMARY

Test Designator	N^+	N^{DES}	N^-	Re^-
Corrected Speed [% Design]	125	101	81	98
Reynolds Number [% Design]	87	89	90	45
Gas to Wall Temperature Ratio, $T_{To}/\bar{T}_w$	1.43	1.41	1.39	1.45
Inlet Total Pressure, P_{To} [atm]	3.50	3.51	3.51	1.76
Inlet Total Temperature, T_{To} [°K]	469	461	459	462
Mean Casing Nusselt Number, $\bar{N}_u$	1007	971	1062	599

$$\bar{N}_u \equiv \frac{\bar{q}_w c_x}{k(T_w)[T_{To}-\bar{T}_w]}$$

The instantaneous casing surface heat flux for the N^+, N^{DES}, N^-, and

Re^- tests are shown in Figs. 6.2a to 6.5a respectively. The heat flux has been normalized by its mean level over the casing surface, $\bar{q}$, to show the relative magnitudes of the unsteadiness. Table 6.1 presents the mean heat flux as a Nusselt number based upon the difference between the inlet total, T_{To}, and the average wall temperatures, $\bar{T}_w$. The length scale is rotor axial chord and the gas thermal conductivity is based on mean wall temperature. Each time trace is identified by gauge normalized position, x/c, where x is the downstream axial coordinate centered at the rotor leading edge and c is the rotor tip axial chord. The shaded regions indicate the blade passing intervals over each sensor. Blade positions, derived from the shaft angle encoder, are accurate to about 3% of the blade to blade pitch.

Figures 6.2b to 6.5b present the corresponding time resolved wall static pressure measurements for the four test cases, normalized by the turbine inlet total pressure. The traces are identified by the pressure sensor axial positions.

The time traces may be replotted as contours to obtain a spatial representation of the instantaneous distribution over the casing surface. Figure 6.6 presents the normalized heat flux contours for the data in Figs. 6.2a - 6.5a. In drawing the contours, the horizontal (time) axis has been scaled by the blade passing period to keep the blade spacing constant, independent of rotor speed. The axial locations and relative size of the sensing elements are shown along the right edge of the plots. It is important to note that the information between axial sensor positions is derived by interpolation only. The corresponding contour plots of the normalized wall static pressure are shown in Fig. 6.7.

Both the static pressure contours and time traces reveal a very narrow

region of high (negative) pressure gradient at the pressure surface entrance into the tip gap extending forward from the aft (x/c=89%) sensor location. The contours indicate that the width of this region is about the same as the diameter of the pressure sensing elements, suggesting that the true gradient may in fact be larger than observed. Following this region, the contours show that the magnitudes of the spatial gradient within the gap are relatively low, matching the levels observed in the blade passage.

The extent of the high gradient region correlates with the wall pressure distribution observed in Fig. 6.7 at the instantaneous suction surface location. For the N^+ run, where the inlet incidence is low (i=-10°) and the suction surface pressure decrease near the leading edge relatively gradual, the high gradients are confined to locations aft of the 50% chord position. This region moves forward as the airfoil incidence and leading edge loading is increased, to cover most of the gap entrance for the N^-, i=+5° run.

Observe that the intersection of the 0.3 pressure contour with the suction surface remains relatively unchanged with run condition, the direction of the contours under the gap adjusting to match the pressure and suction distributions. (A 0.28 pressure ratio represents sonic conditions in the rotor relative frame.) Note also that the axial distribution of peak 'driving' pressure near the blade pressure surface (best observed from the time traces) as well as the blade passage distributions downstream of the 0.3 pressure ratio contour are relatively independent of the rotor inlet incidence. Thus, over most of the high gradient region, the net pressure drop is greater than a factor of two, implying sonic conditions at the gap entrance.

These measurements indicate, therefore, the existence of a strong,

sink-like leakage flow entering the gap from the pressure side controlled by the airfoil loading, with mass flow set by the pressure surface, and chordwise extent by the suction surface pressure distributions respectively. The influence of this flow on the instantaneous and averaged heat flux will now be examined.

The measured heat flux shows extremely large temporal and spatial variations. At a given chordwise location, the maximum heat flux under the rotor blade can be more than five times the value at midpassage. Peak levels are found along the regions of the high surface pressure gradient, Figs. 6.6 and 6.7, and have magnitudes comparable to those found on the nozzle guide vane leading edge. The relative influence of the tip leakage flow may be assessed by observing that approximately 45% of the total heat load to the end wall appears under the blade tips, even though this represents only 30% of the total end wall area.

The time traces, Figs. 6.2a to 6.5a, are characterized by maximum heat transfer rates at the pressure surface end of the gap followed by a drop moving through the gap to the suction surface. This drop continues into the blade passage, reaching a minimum within the passage generally near the suction surface. Moving axially downstream from the inlet, the magnitude of the fluctuations increases to about the mid-chord position. At this point, the average level of heat flux then begins to diminish significantly, while the relative magnitude of the fluctuations continues to remain high.

This very high modulation in heat flux is seen under all conditions, except in the region upstream of the sonic line for the N^+, low incidence run, Fig. 6.2a. The modulations aft of the sonic line are similar for all speeds. The heat flux measured at 52% chord (sensor 4) is compared in Fig.

6.8 for the three corrrected speeds to illustrate that, although average levels may be roughly the same at that location, the leakage flow field appears to significantly influence the magnitude of the fluctuations.

Time averages of the wall static to inlet total pressure ratio, surface heat flux, and surface temperature over a 50ms period are presented in Figs. 6.9 through 6.11, plotted as a function of the normalized axial position. This averaging period represents approximately five complete rotor revolutions, or 300 blade passings--long compared to blade passing or throughflow times, yet short compared to the tunnel operating time scales (Chapter 4).

The average static pressure (Fig. 6.9) drops by a factor of between 2 and 3 down the passage, depending on the run condition, reflecting the supersonic exit Mach number of the rotor blading. At design speed, a lowering of Reynolds number is seen to reduce the normalized pressures over most of the casing. At fixed Reynolds number, the overall pressure levels become higher as the speed is increased, reflecting the increase in rotor relative total pressure.

The time averaged heat flux is presented in Fig. 6.10 and the corresponding surface temperatures in Fig. 6.11. This data is non-dimensionalized in Fig. 6.12 as a Nusselt number N_q based on the inlet total to local wall temperature difference $[T_{To}-T_w(x)]$,

$$N_q = \frac{\bar{q}(x)\ c_x}{k(T_w)[T_{To}-T_w(x)]} \quad .$$

The normalized heat flux, N_q, exhibits a small rise over the forward half of the passage and then drops substantially toward the exit. Average heat loads over the forward half of the casing, however, are generally

higher for the high speed run (-10° incidence) and lower for the low speed run (+5° incidence), and may result from the differences in leading edge loading observed for these cases. Except near the rotor trailing edge region, N_q scales very closely with $Re^{0.8}$. Also observe that the data upstream of the rotor axial leading edge (x/c=-0.075) matches for the three speed runs.

6.4 Discussion

The overall reduction in heat flux down the passage is not surprising since enthalpy extraction by the rotor reduces the 'driving' temperature difference across the end wall boundary layer. The local free stream total temperature through the passage was estimated using loading data supplied for the rotor profile. The axial distribution thus calculated, $T_{T\ell}(x)$, represents a circumferentially averaged passage value which may also be used as a simple first estimate for the flow entrained by the tip gap sink along the pressure surface. The local driving temperature difference $[T_{T\ell}(x)-T_w(x)]$, normalized by its value at the upstream gauge location (x/c=-0.075), is plotted in Fig. 6.13 for the design speed run and shows a substantial reduction (by a factor of almost three) across the casing.

To separate rotor enthalpy extraction from boundary layer profile effects, the heat flux was renormalized using this local total to wall static temperature difference,

$$N_h = \frac{\dot{q}\, c_x}{k(T_w)[T_{T\ell}-T_w(x)]} \quad ,$$

In this form, N_h represents a dimensionless heat transfer coefficient. Its time averaged distribution is shown, along with the dimensionless heat flux, N_q, in Figure 6.14 for the design speed test. Figure 6.15 presents

the instantaneous distribution of N_h.

Having removed the influence of the changing driving temperature, the effect of the gap flow upon the overall end wall heat transfer coefficient may be clearly seen. The average heat transfer coefficient increases by a factor of two from the blade leading edge to the 0.75 axial location whereupon it drops abruptly to the passage exit. The time resolved data shows a remarkable symmetry along the pressure surface and indicates that the end wall boundary layer is dominated by the tip leakage flow in this region.

To further investigate this influence, the separate contributions of the passage and tip gap flows to the overall end wall heat load were determined. Using the profile data for the airfoil, the time resolved heat flux may be averaged over either the blade passage or tip passing time intervals. When expressed as the dimensionless heat transfer coefficient, N_h as defined above, this data shows the locally large influence of the gap flow, Fig. 6.16. This data, which still represents the heat transfer per unit area, may be multiplied by the relative circumferential gap and passage lengths (using the blade thickness distribution, Fig. 6.17) to obtain the individual contributions to the overall end wall heat load, Fig. 6.18. These contributions must sum to the total end wall distribution of N_h from Fig. 14, which is presented again for reference. Note that the passage distribution (except at the 0.75 chord location) shows a gradual reduction in heat transfer coefficient typical of a thickening boundary layer. The fractional contribution of the gap to the overall end wall load is shown in Fig. 6.19 which also shows the blade thickness to pitch distribution.

Given the observation that the very high heat flux levels to the shroud are a result of the underblade tip flow, it may be concluded that

the distribution in time averaged heat flux down the blade chord may be simply explained by two factors: the drop in flow total temperature due to the rotor enthalpy extraction, and the distributions of both the blade thickness and pressure loading driving the gap leakage.

This overall drop in heat flux is consistent with, although larger in magnitude than, data published by other experimenters [Ref. 6.6], reflecting the higher loading of this rotor. Full-scale engine data sometimes shows casing overheating over the rotor blade trailing edge; this is often explained in terms of migration of hotter fluid from a lower radius out to the tip. There is no evidence in these measurements to indicate this. It should be noted, however, that since the inflow temperature is uniform on this facility, radial convection would not change the temperature at the tip.

The time resolved pressure measurements imply that the flow under the blade tip is primarily inviscid core flow, essentially at the suction surface pressure. The large pressure drop at the blade pressure side entrance region establishes the mass flow rate. This is consistent with cascade experiments, Ref. [6.3].

It was observed earlier that the average heat flux over the forward half of the tip casing depends upon rotor incidence, (Figure 6.9). For the low incidence case (125% N), the average heat flux to this region is higher, but the magnitude of the fluctuations is considerably smaller (Figure 6.5) than for either the design point or positive incidence runs. As a result of the reduced forward loading, the high entrance pressure gradient does not extend into this forward region implying, therefore, a weaker tip leakage flow over the forward half. The reduced loading also implies a higher free stream total to wall temperature difference driving

the average heat flux. It is postulated that the combination of these two effects may account for the observed average and fluctuating heat flux behavior for the low incidence run.

6.5 Conclusions

The time resolved heat transfer and pressure distributions have been measured on the stationary casing above the tip of a transonic turbine rotor. These measurements show that:

- There is a strong sink flow along the blade pressure surface,
- This flow is a function of the airfoil loading distribution,
- Heat flux to the casing is primarily unsteady,
- Heat flux levels under the blade tip are 5 to 6 times those in the passage,
- Time averaged heat flux drops by a factor of 4-5 down the blade chord,
- Time averaged heat flux scales with $Re^{0.8}$,
- Chordwise variations in heat flux are due to changes in both heat transfer coefficient and temperature difference,
- The reduction in unsteady fluctuations for the high speed run appears be related to the reduced gap flow resulting from the unloading of the forward end of the airfoil, and
- The different levels in average heat flux to the forward half of the casing for the three corrected speeds correlate with the influence of blade loading upon the passage flow total temperature distribution.

It is concluded from consideration of these measurements that:

- The under-blade tip flow is driven primarily by the airfoil loading distribution, and
- The average heat flux distribution along the blade chord reflects both the rotor enthalpy extraction and the blade thickness and pressure loading distributions.

Efforts should be continued to model the measured flows described herein. Simple quasi-one-dimensional models following the approach of Ref. [6.5] should first be employed to gain a better and more quantitative

understanding of the relevant physical phenomena before attempting more complex analytical and/or numerical studies. Additional work could also be done studying effects of other turbine variables, such as tip clearance and radial temperature distortion. Flow visualization studies would unquestionably supply valued information and may be relatively easy due to easy access to the casing regions.

6.6 References

1) Dunn, M.G., and Hause, A., "Measurement of Heat Flux and Pressure in a Turbine Stage," ASME J. of Eng. for Power, 104, 1, January 1982, pp. 215-223.

2) Epstein, A.H., Guenette, G.R., and Norton, R.J.G., "The MIT Blowdown Turbine Facility," ASME Paper 84-GT-116, 1984.

3) Booth, T.C., Dodge, P.R., and Hepworth, H.K., "Rotor-Tip Leakage: Part I - Basic Methodology," J. Eng. for Power, 104, 1, January 1982, pp. 154-161.

4) Wadia, A.R., "Numerical Solution of Two and Three Dimensional Rotor Tip Leakage Models," AIAA Paper 83-1171, June 1983.

5) Mayle, R.E., and Metzger, D.E., "Heat Transfer at the Tip of an Unshrouded Turbine Blade," 7th International Conference on Heat Transfer, Munich, 1982.

6) Dunn, M.G., Rae, W.J., and Holt, J.L., "Measurement and Analysis of Heat Flux Data in a Turbine Stage: Part II - Discussion of Results and Comparison with Predictions," ASME Paper 83-GT-122, 1983.

7) Epstein, A.H., et al., "High Response Heat Flux Gauge for Metal Blading," presented at AGARD 65th Propulsion and Energetics Symposium, Bergen, May 1985.

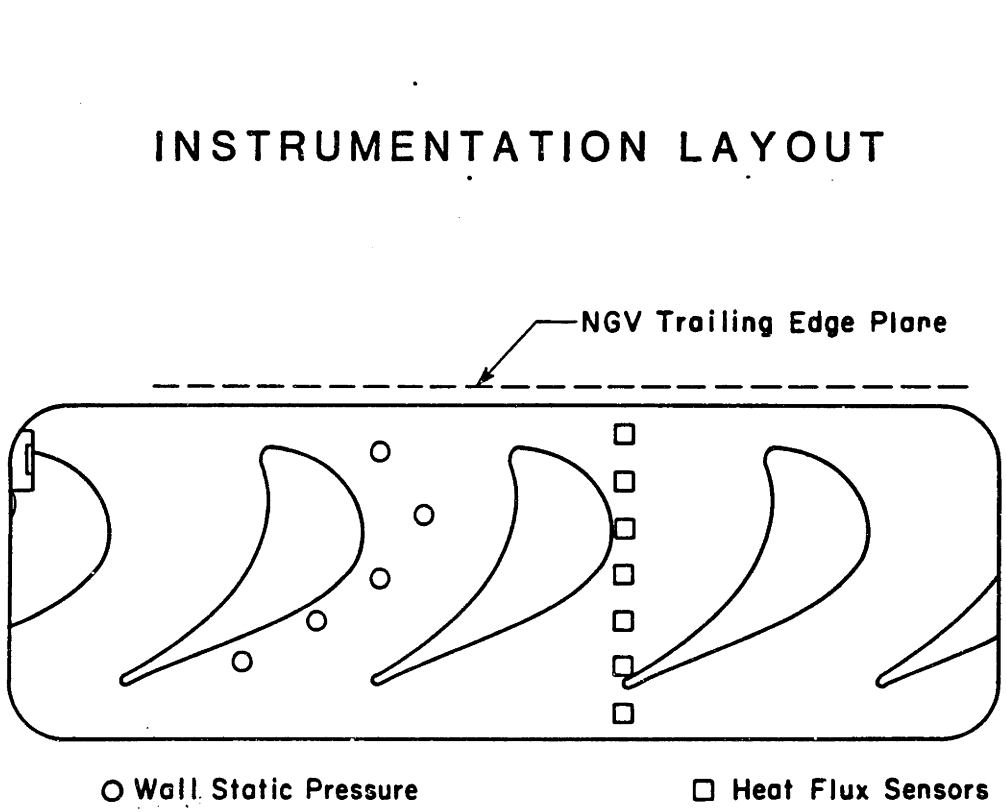

Figure 6.1: Layout of casing instrumentation

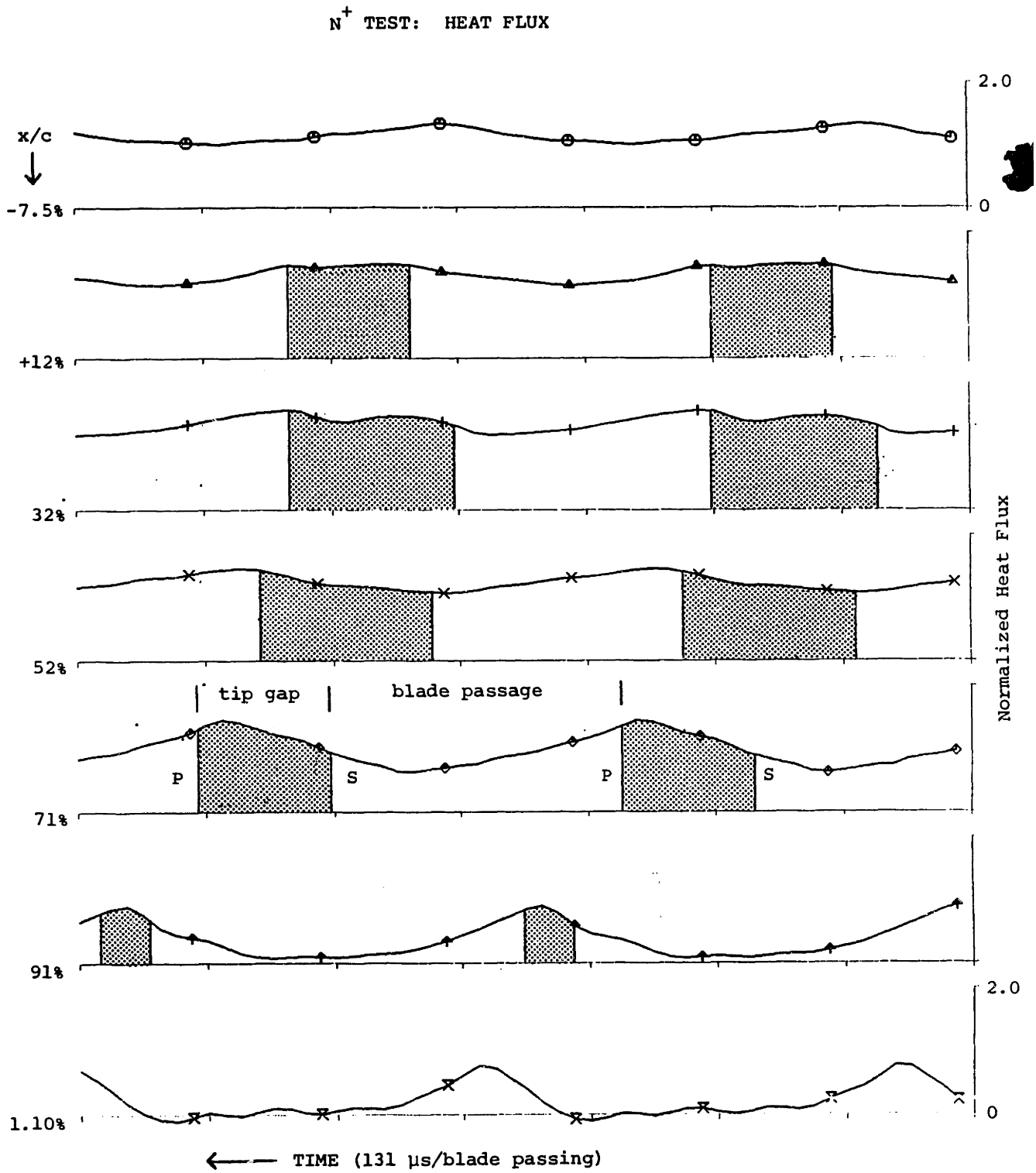

Figure 6.2a: Wall heat flux for the design speed test - relative to mean casing heat flux

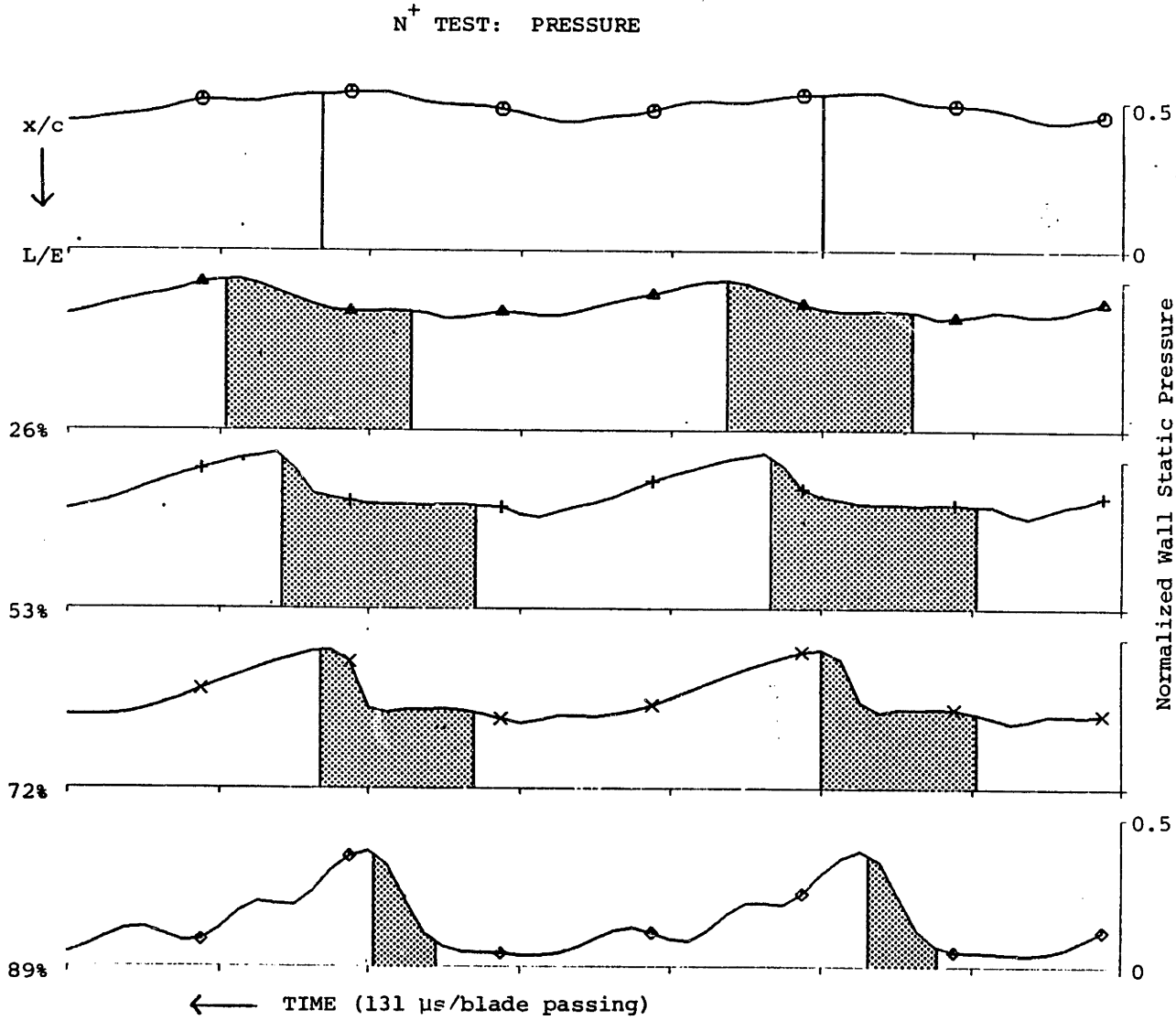

Figure 6.2b: Wall static pressure for high speed test - relative to inlet total pressure

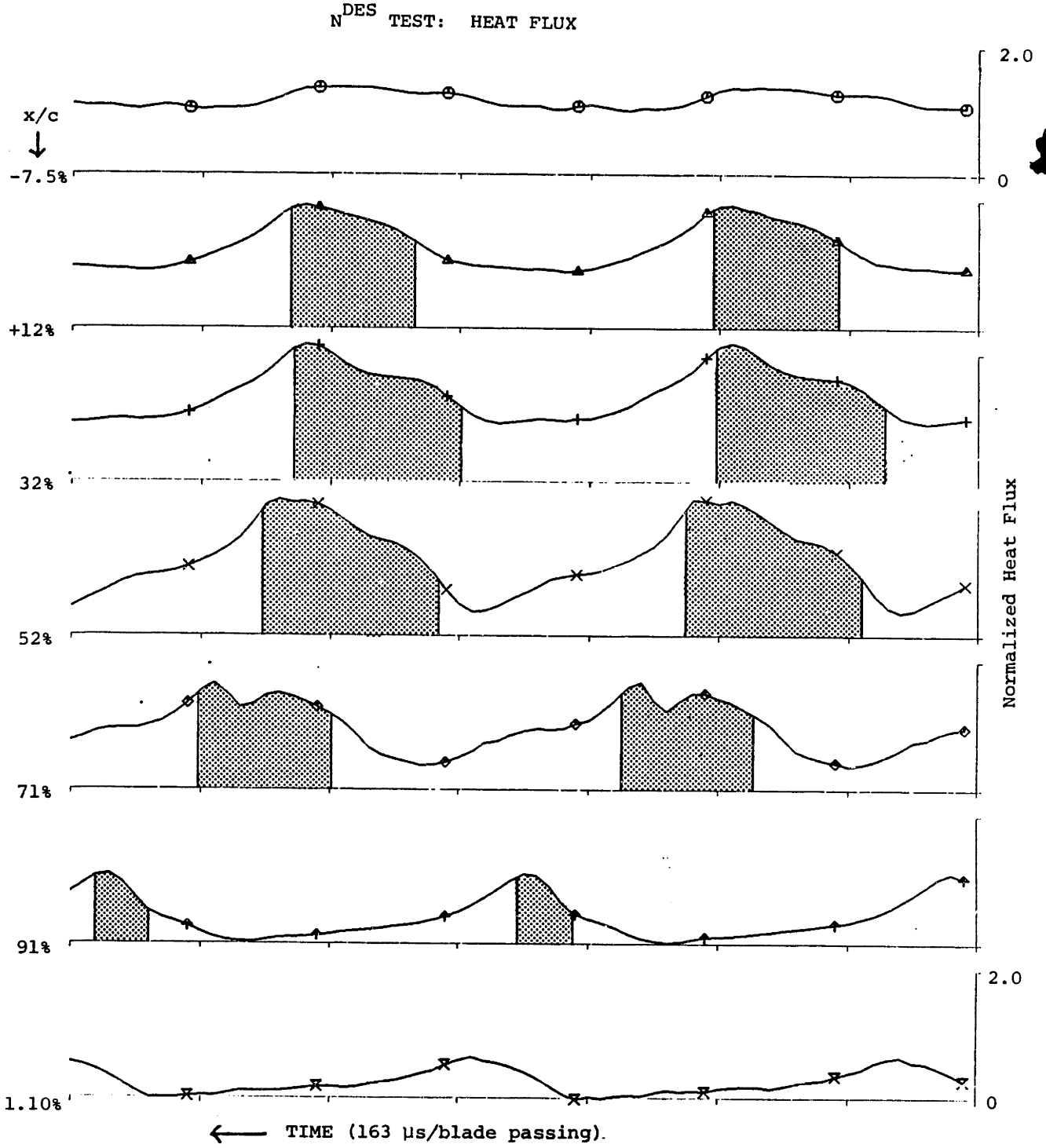

Figure 6.3a: Wall heat flux for the design speed test - relative to mean casing heat flux

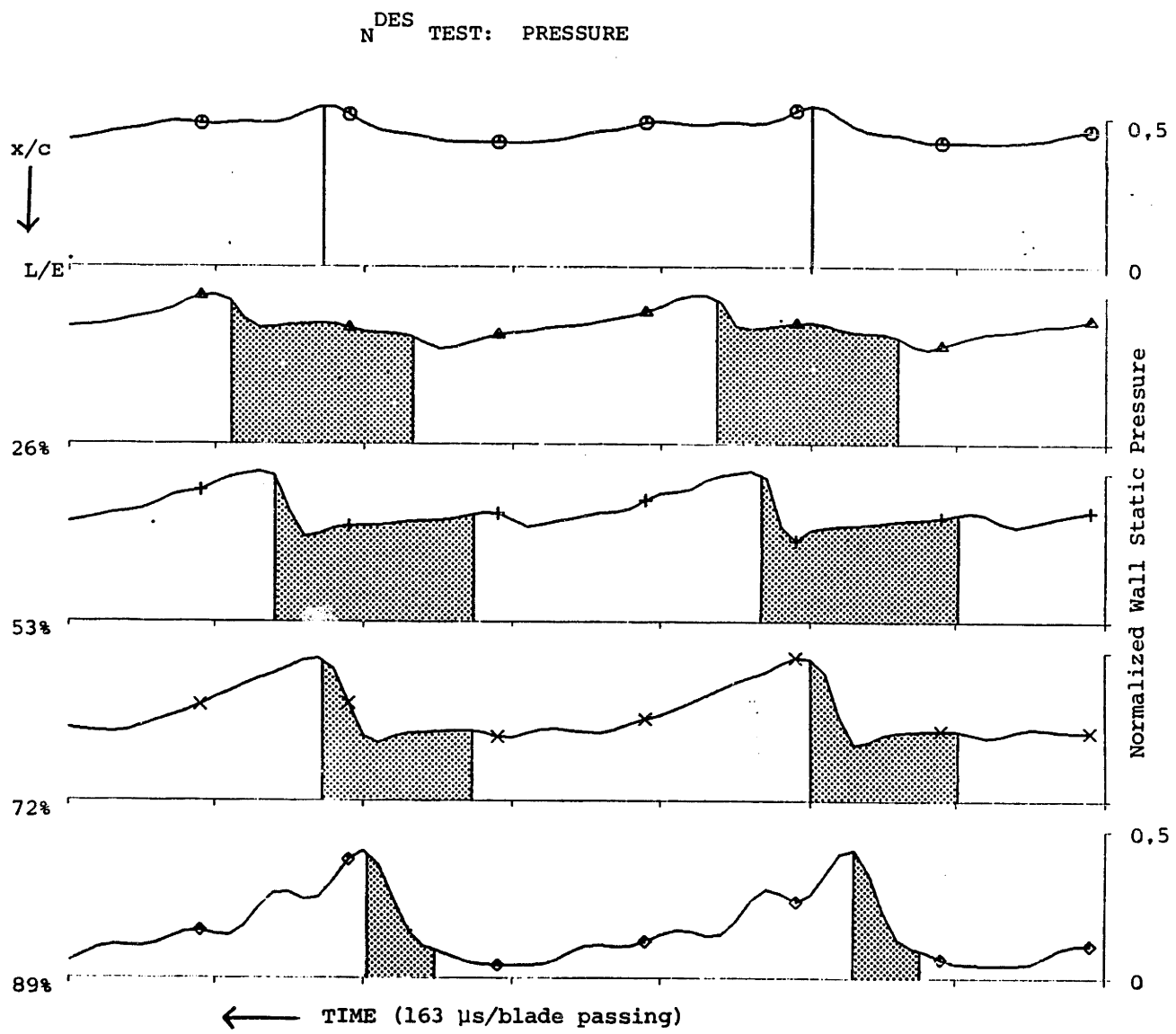

Figure 6.3b: Wall static pressure for design speed test - relative to inlet total pressure

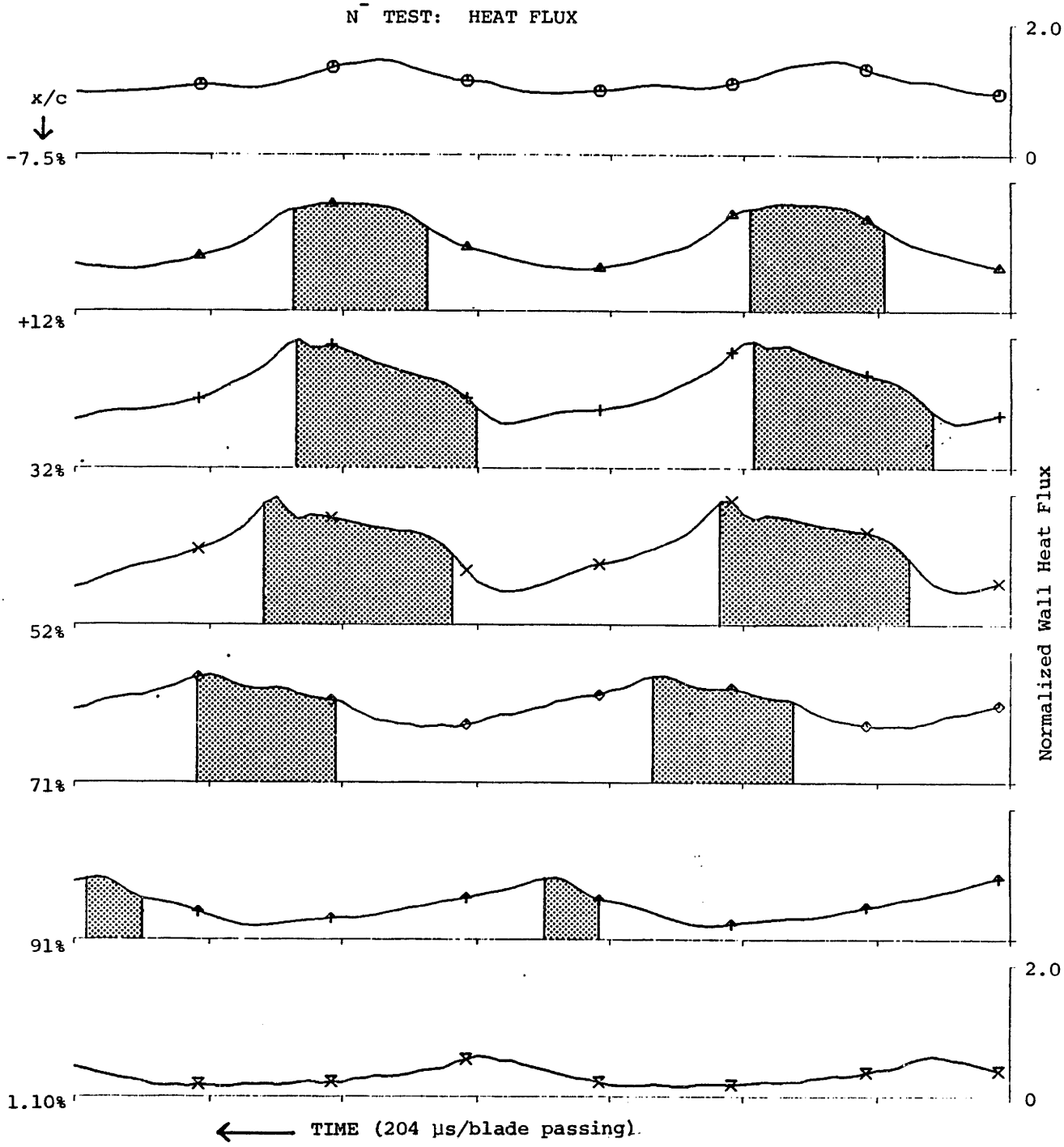

Figure 6.4a: Wall heat flux for the low speed test relative to mean casing heat flux

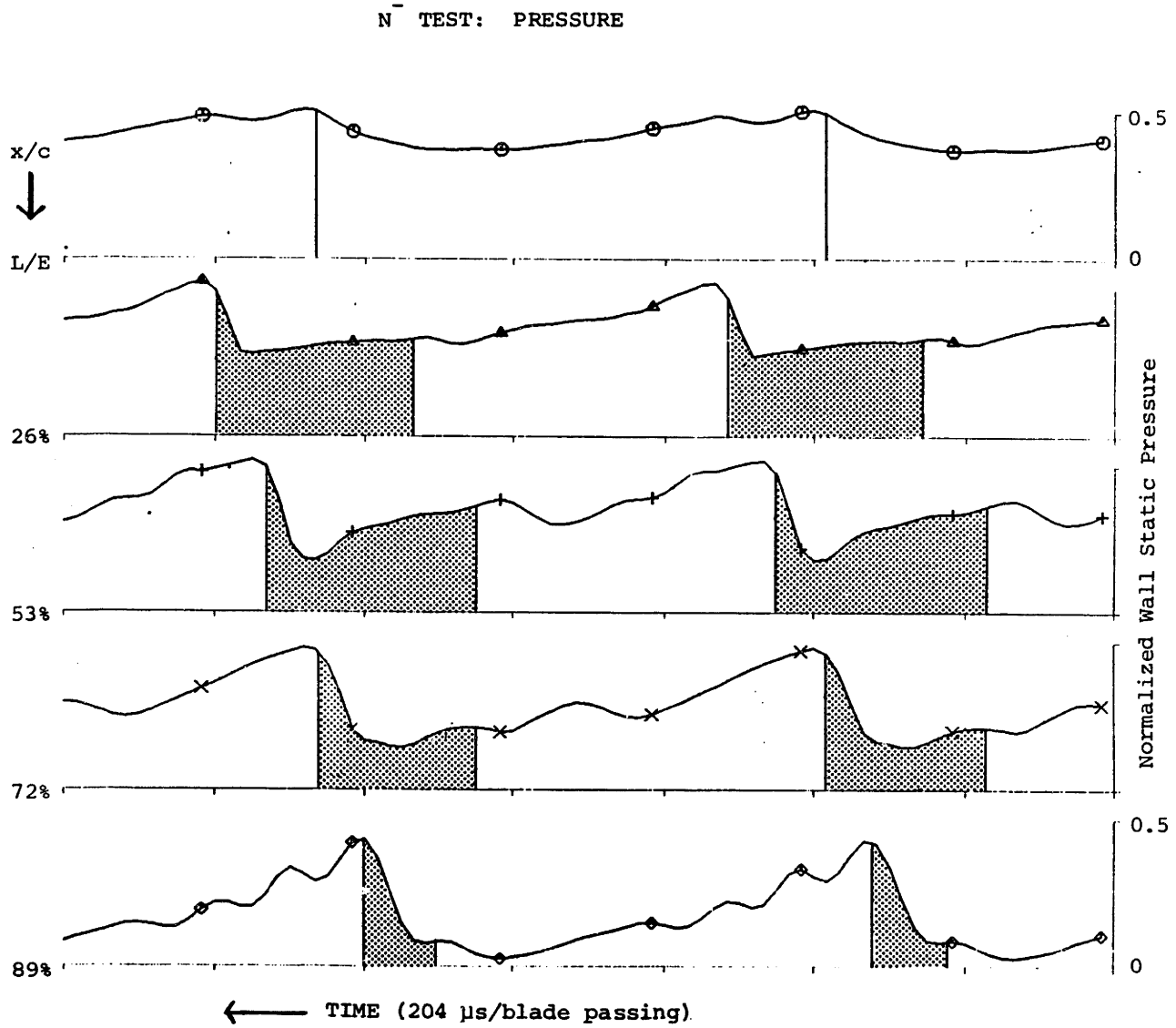

Figure 6.4b: Wall static pressures for the low speed test - relative to inlet total pressure

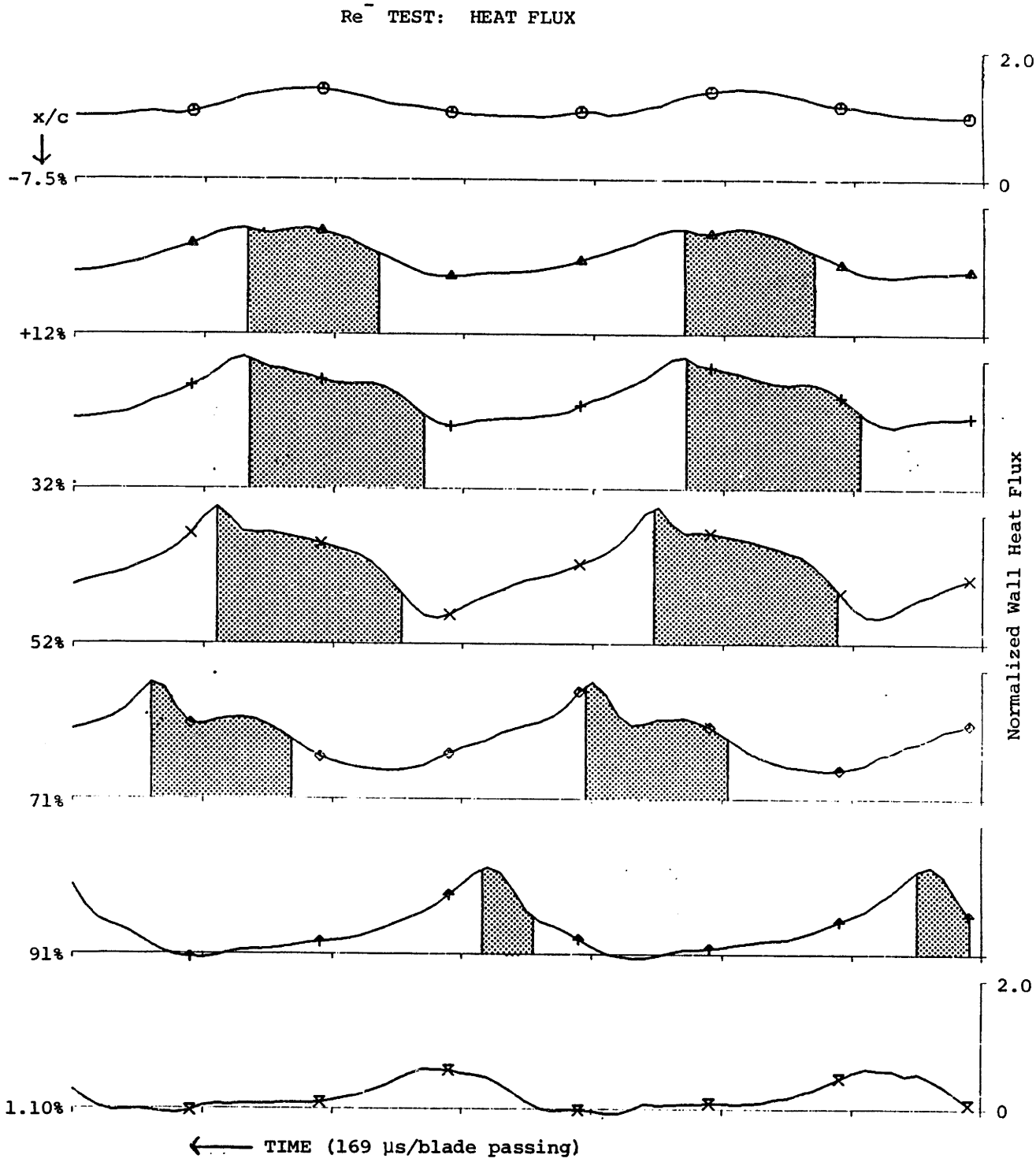

Figure 6.5a: Wall heat flux for the low Reynolds number test - relative to mean casing heat flux

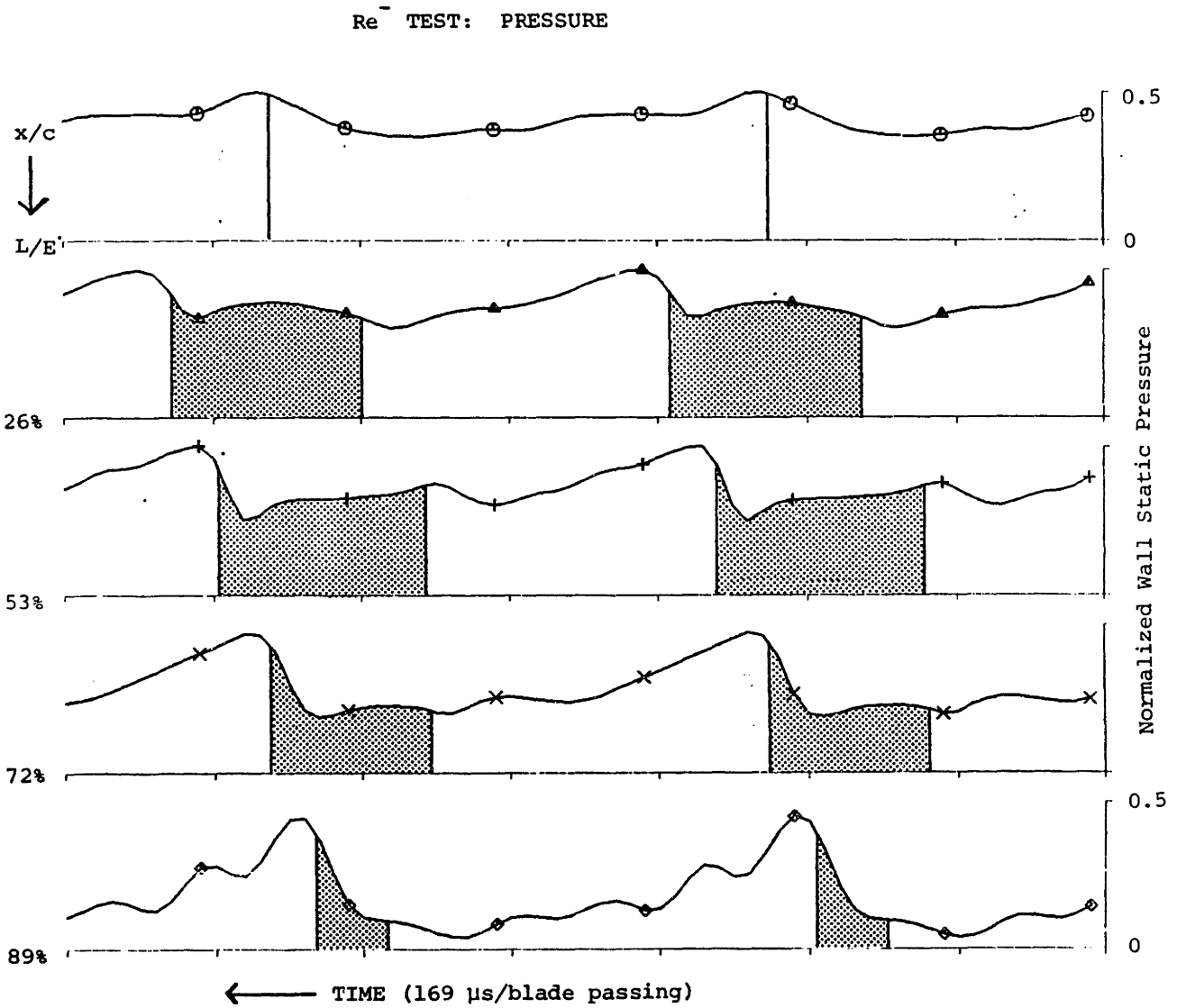

Figure 6.5b: Wall static pressure for the low Reynolds number test - relative to inlet total pressure

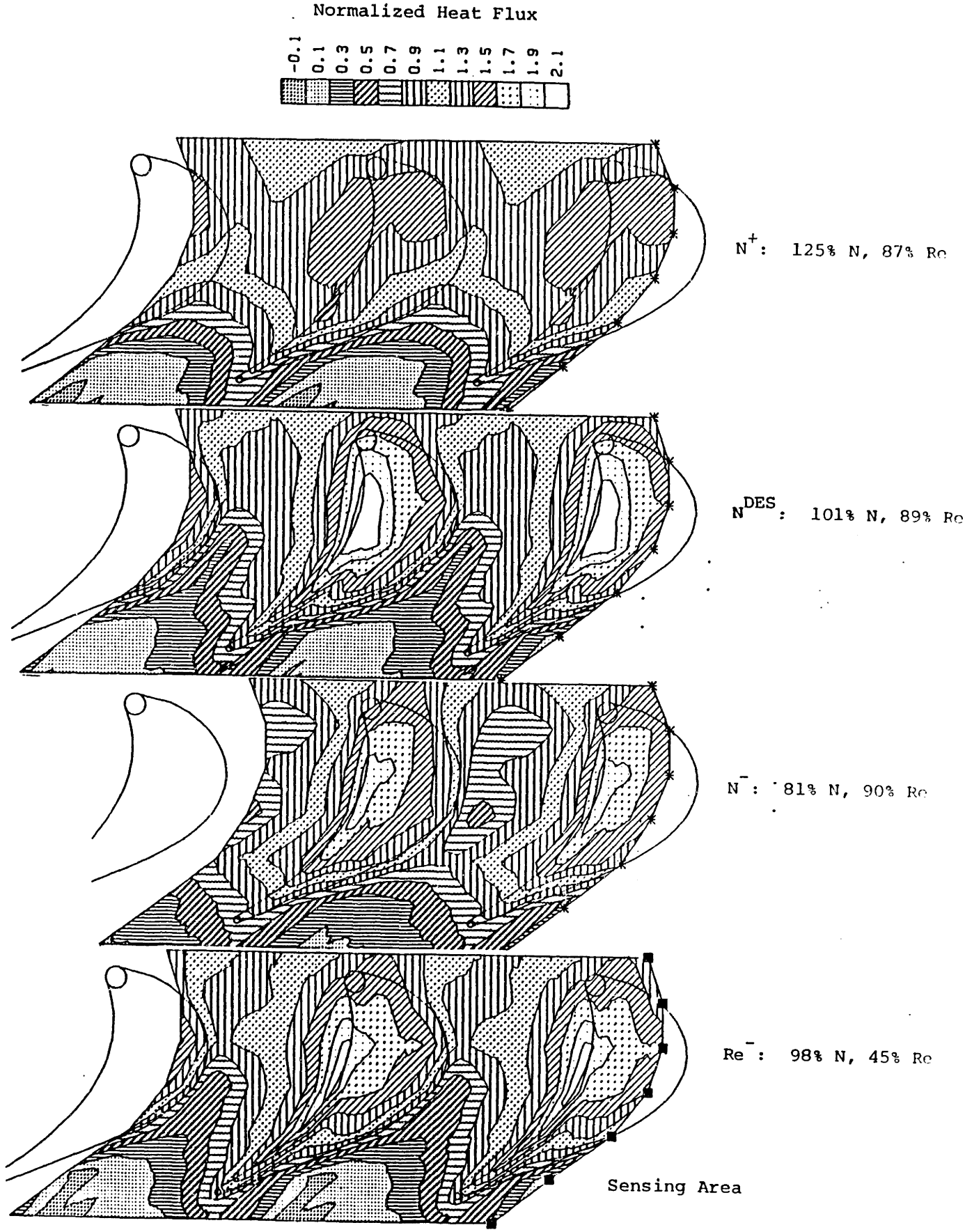

Figure 6.6: Wall heat flux contours for test series relative to mean casing heat flux of each test

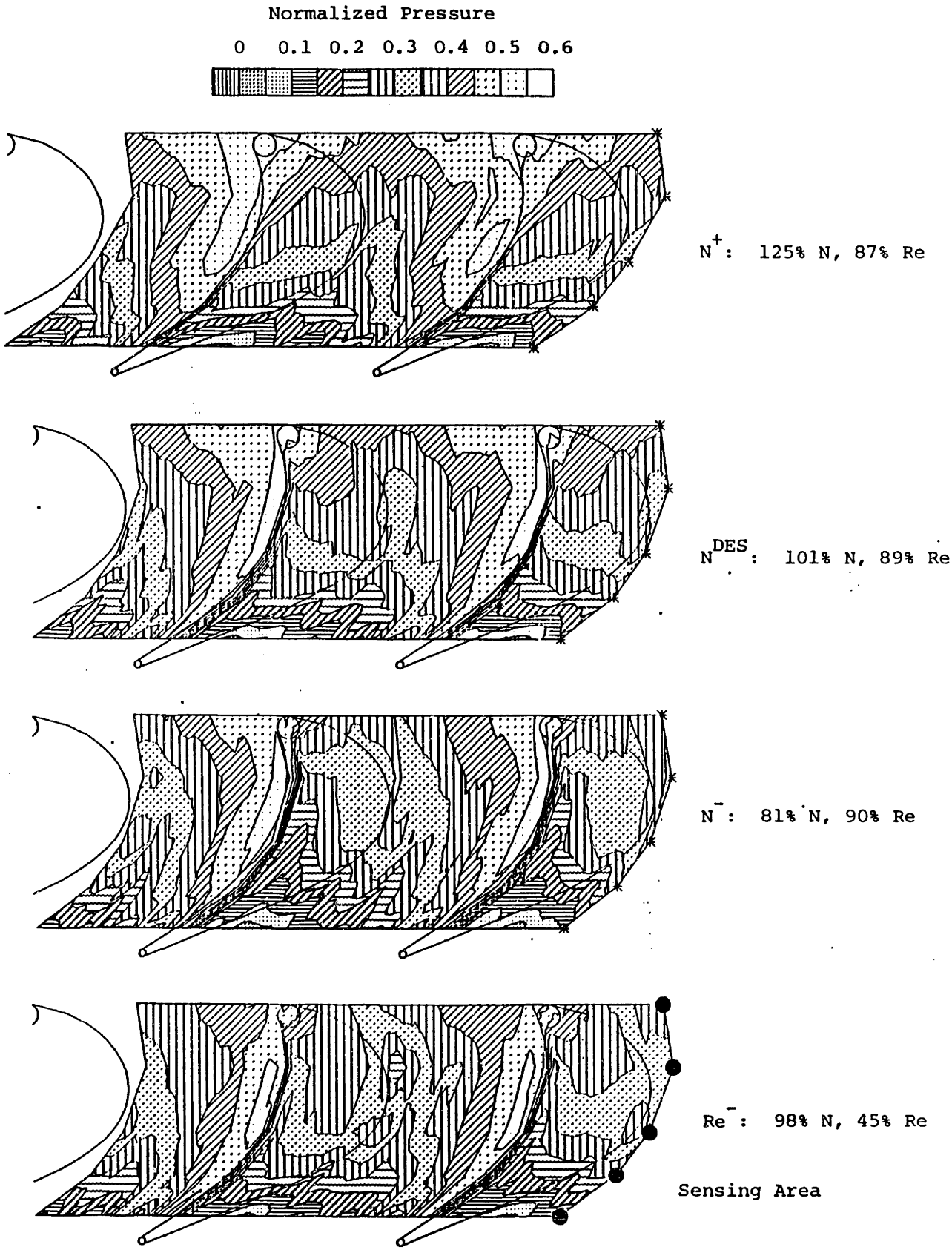

Figure 6.7: Wall static pressure contours for test series - relative to inlet total pressure of each test

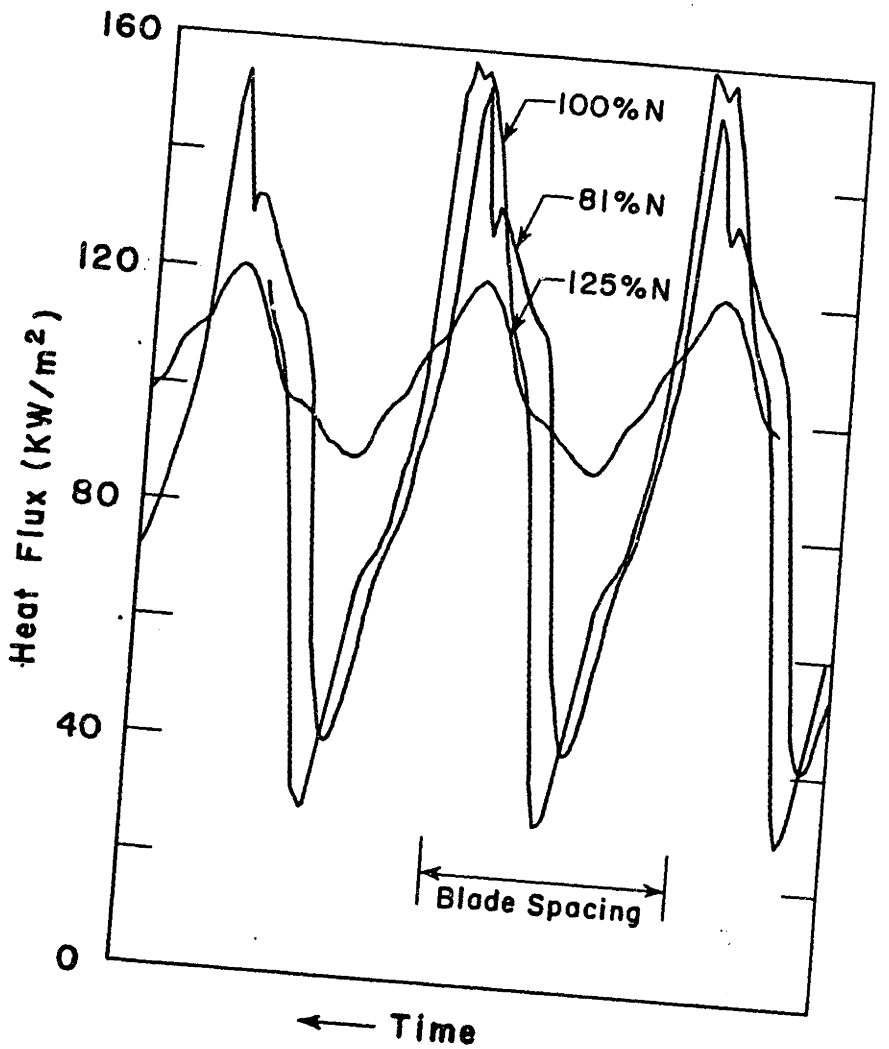

Figure 6.8: Comparison of instantaneous casing heat flux at 52% chord at three corrected speeds

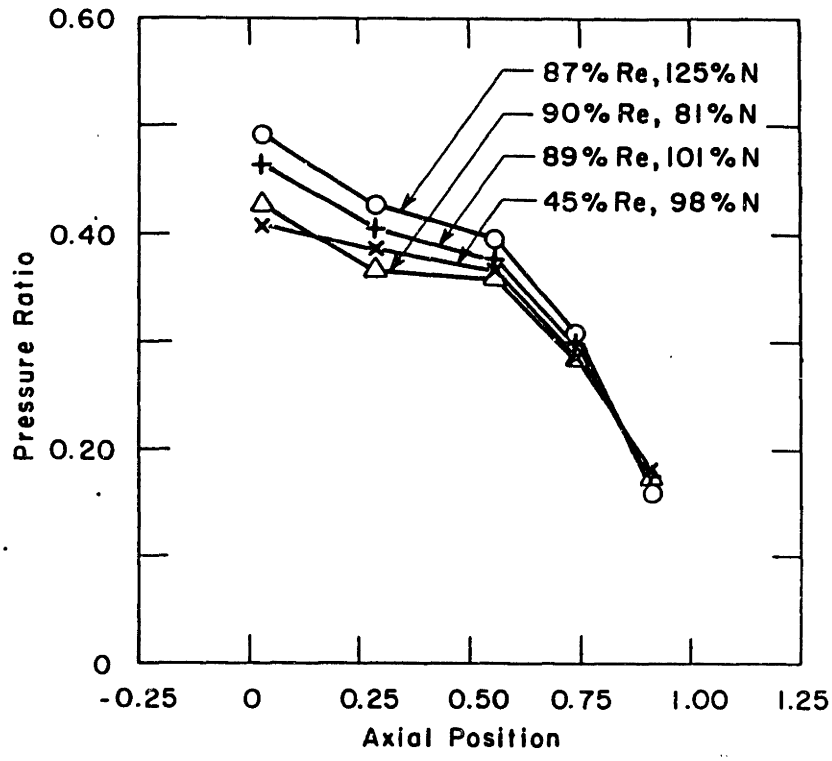

Figure 6.9: Time averaged wall static to inlet total pressure ratio

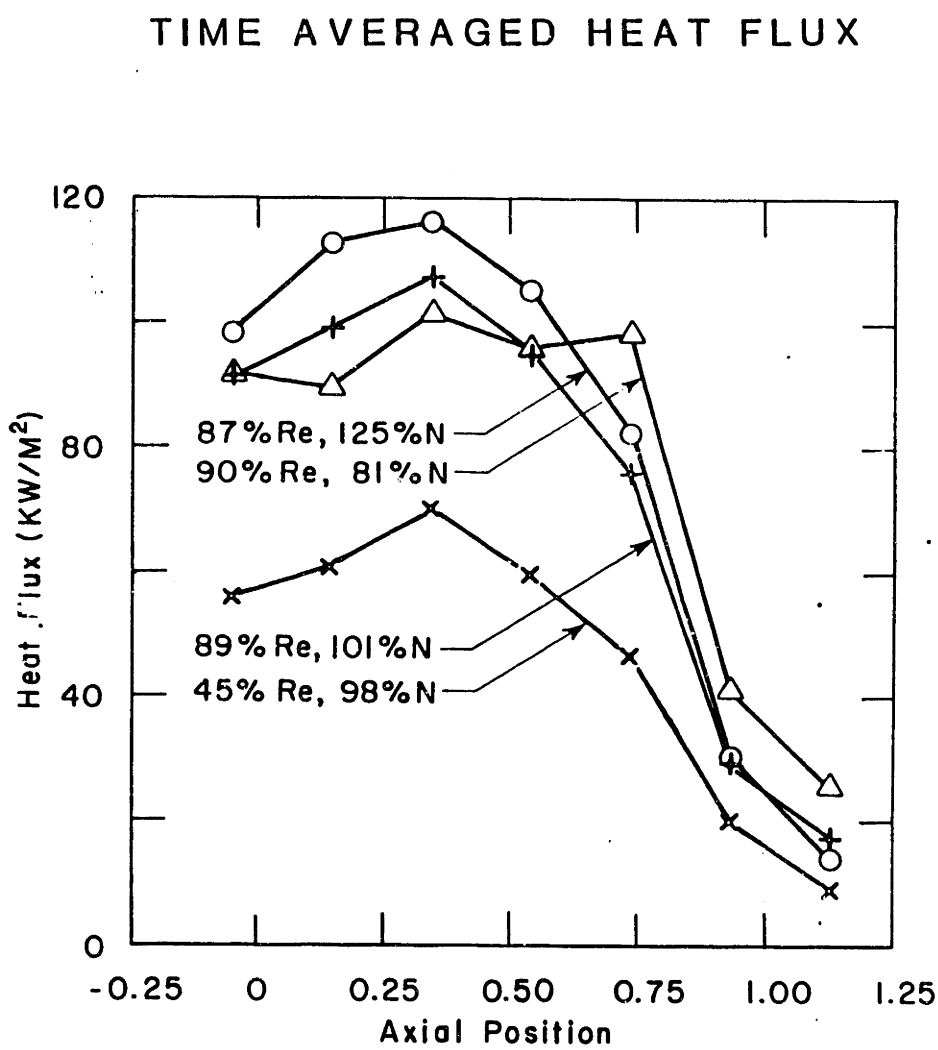
TIME AVERAGED HEAT FLUX
120
80
40
0
Heat Flux (KW/M²)
87% Re, 125% N
90% Re, 81% N
89% Re, 101% N
45% Re, 98% N
-0.25
0
0.25
0.50
0.75
1.00
1.25
Axial Position

Figure 6.10

TIME AVERAGED SURFACE TEMPERATURE

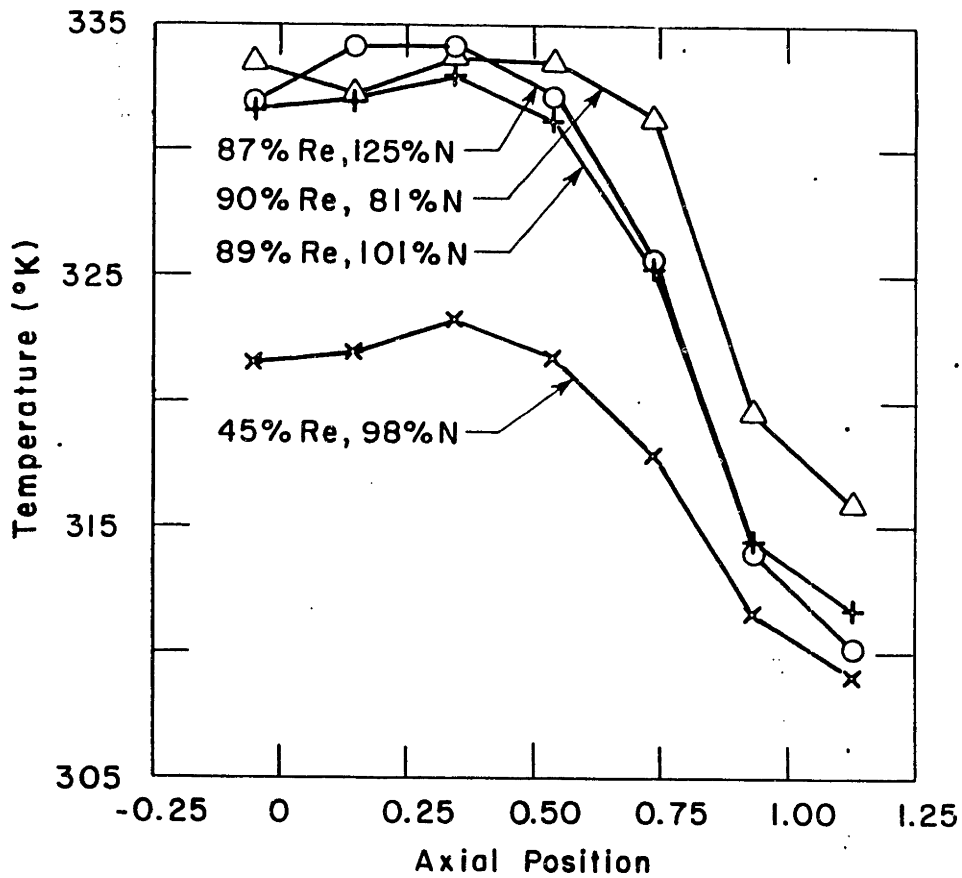

Figure 6.11

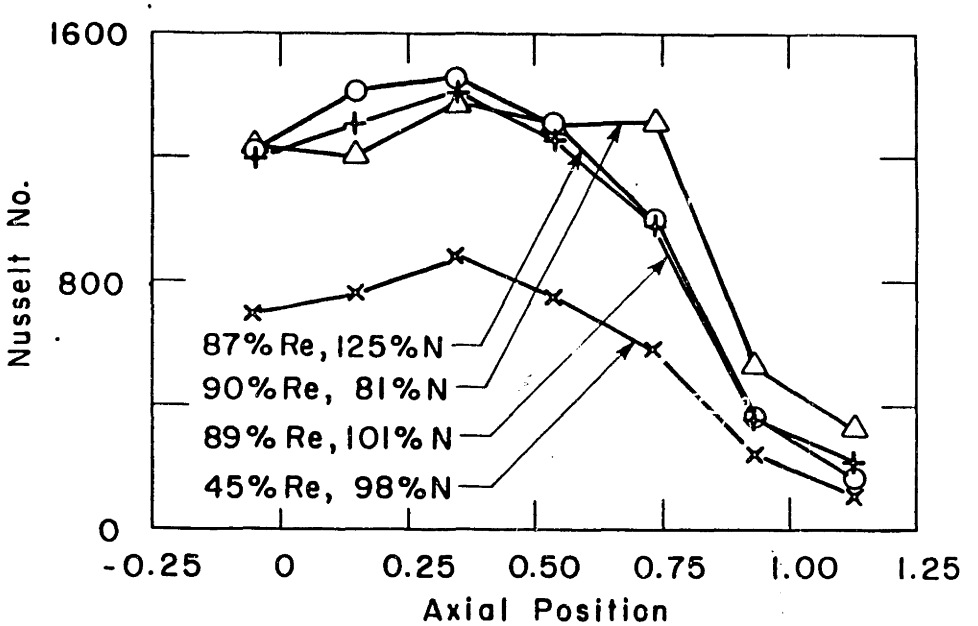

Figure 6.12: Time averaged Nusselt number, N_q, based on inlet total to wall static temperature difference

"DRIVING" TEMPERATURE DISTRIBUTION

$$\frac{[T_T - T_W]_{local}}{[T_T - T_W]_{inlet}}$$

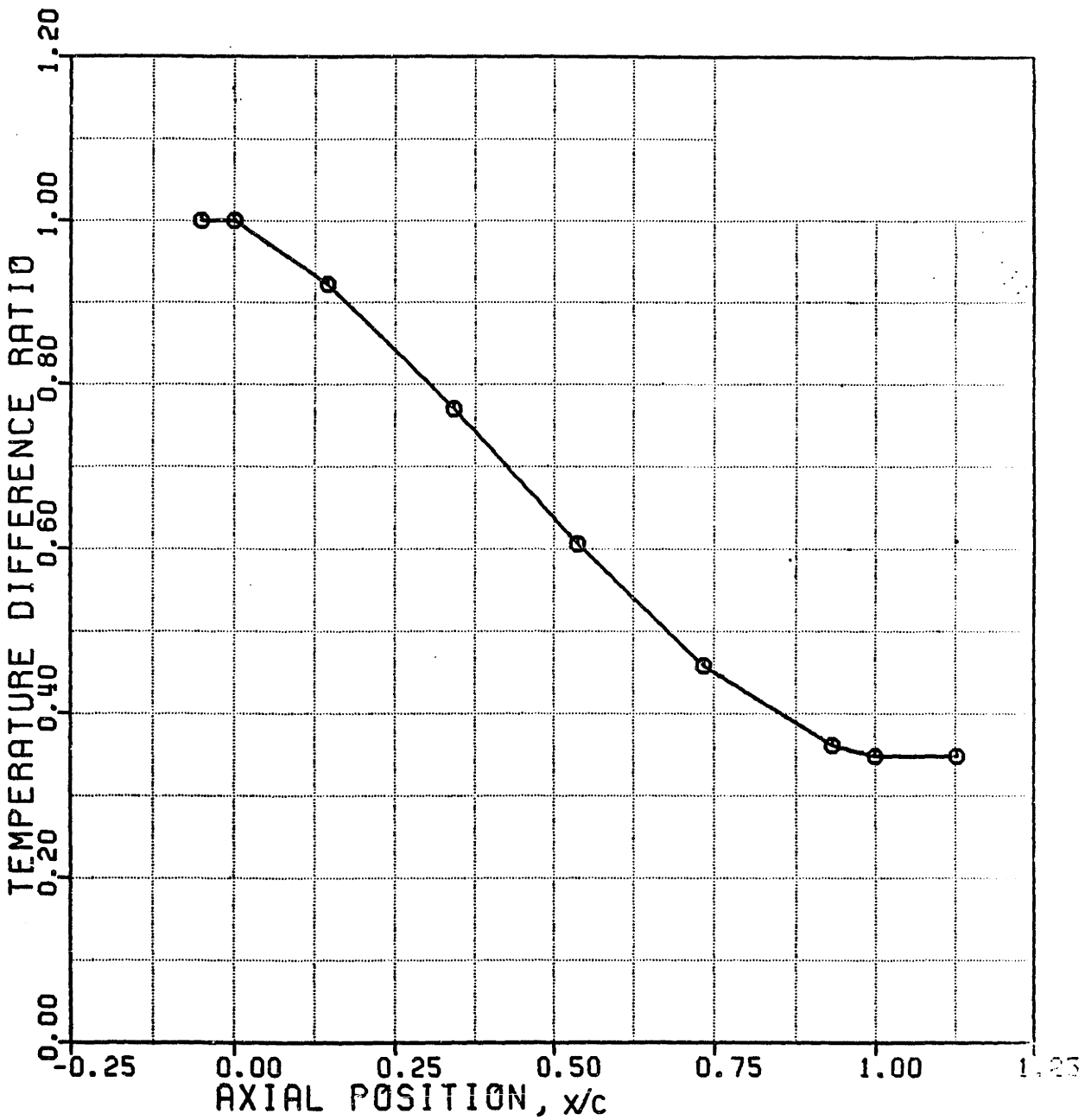

Figure 6.13: Local driving temperature difference $[T_{T\ell}(x)-T_w(x)]$ for N^{DES} test normalized by its value at the upstream sensor located at x/c = -0.075.

NORMALIZED HEAT TRANSFER COEFFICIENT, N_h.

N_h BASED ON LOCAL TOTAL TEMPERATURE.

N_q BASED ON UPSTREAM TEMPERATURE.

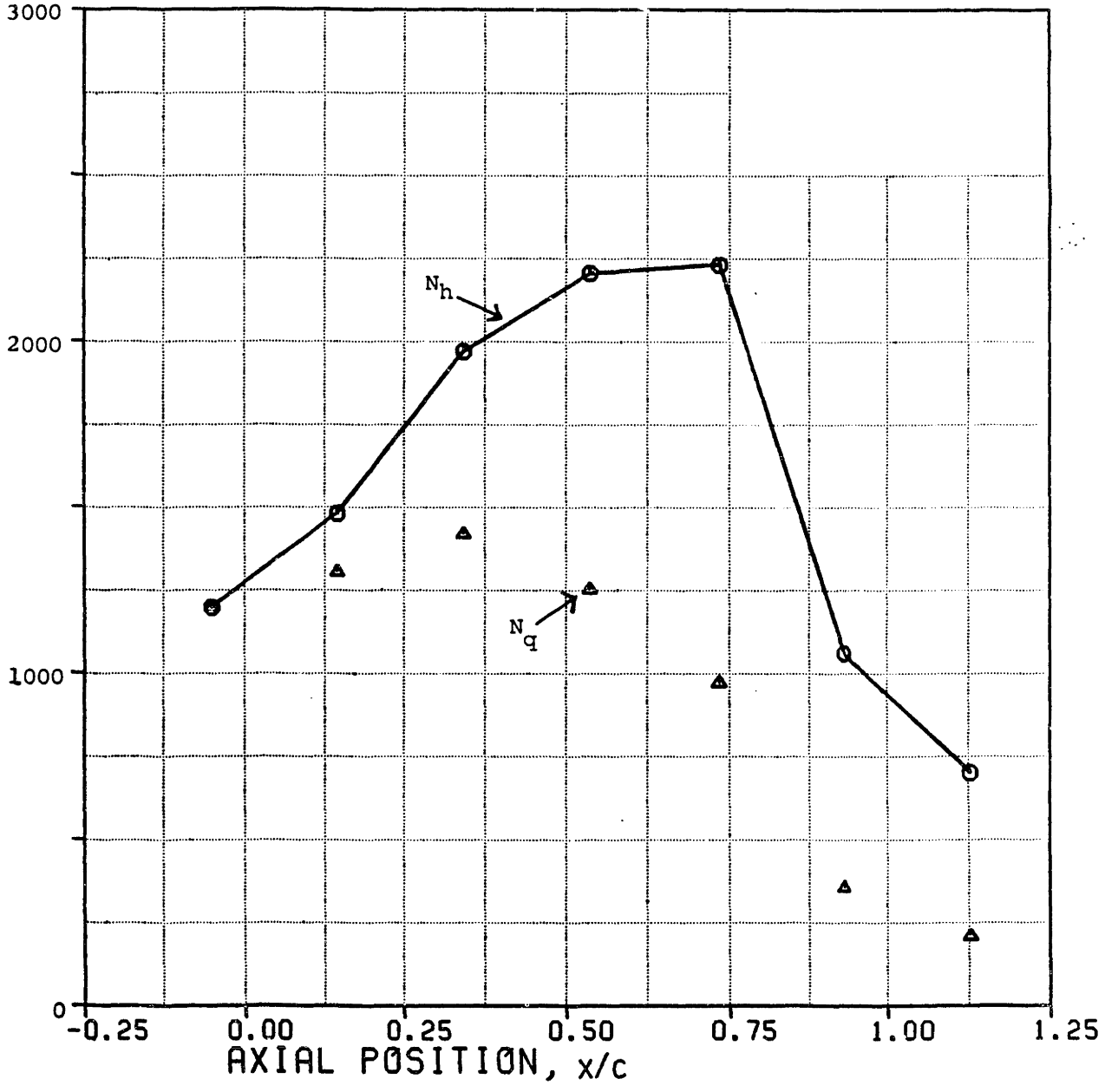

Figure 6.14: Normalized heat transfer coefficient, N_h, compared with normalized heat flux, N_q, to show the relative influence of the driving temperature decrease upon endwall heat transfer.

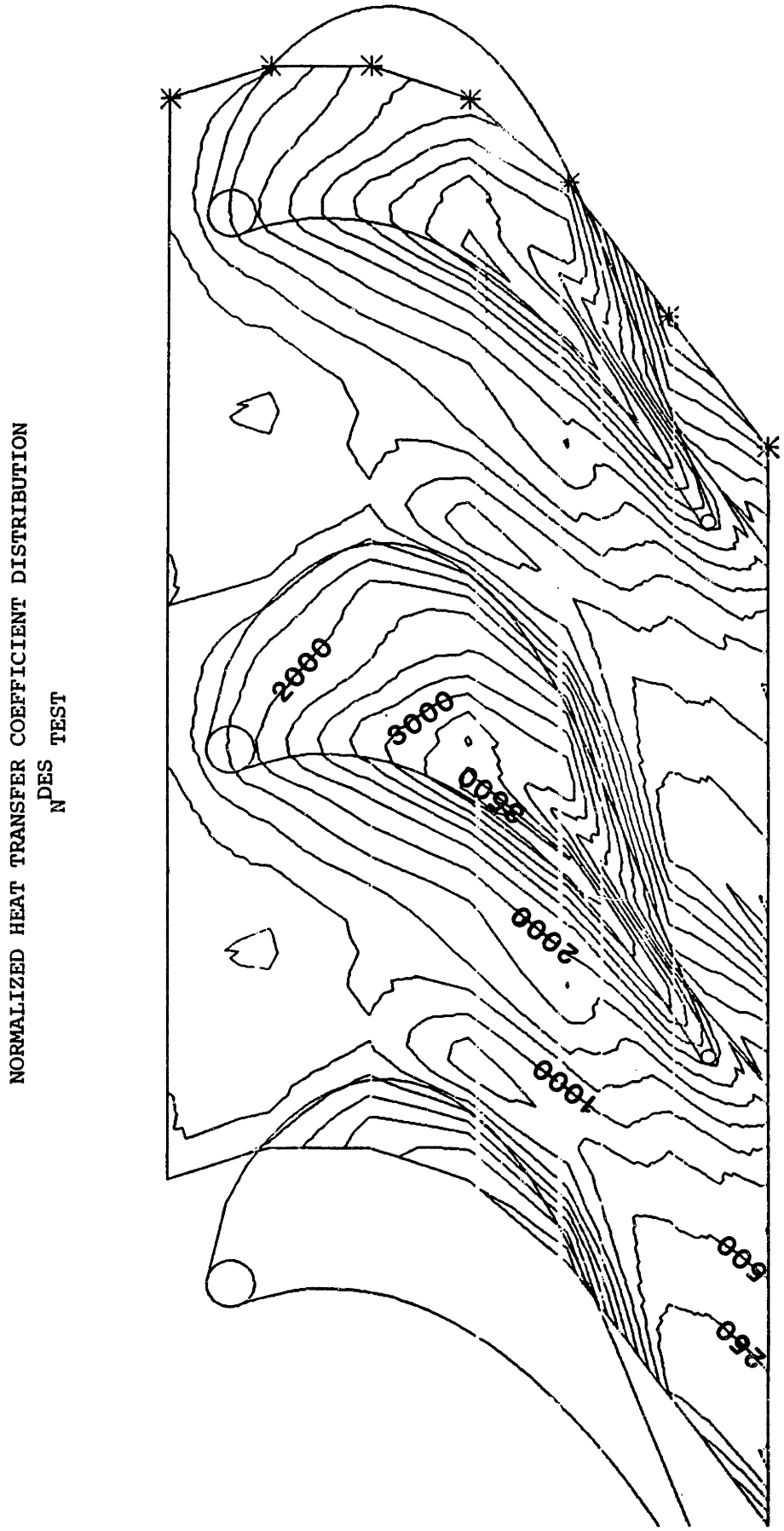

Figure 6.15: Contours of normalized heat transfer coefficient, N_h, for the design speed test

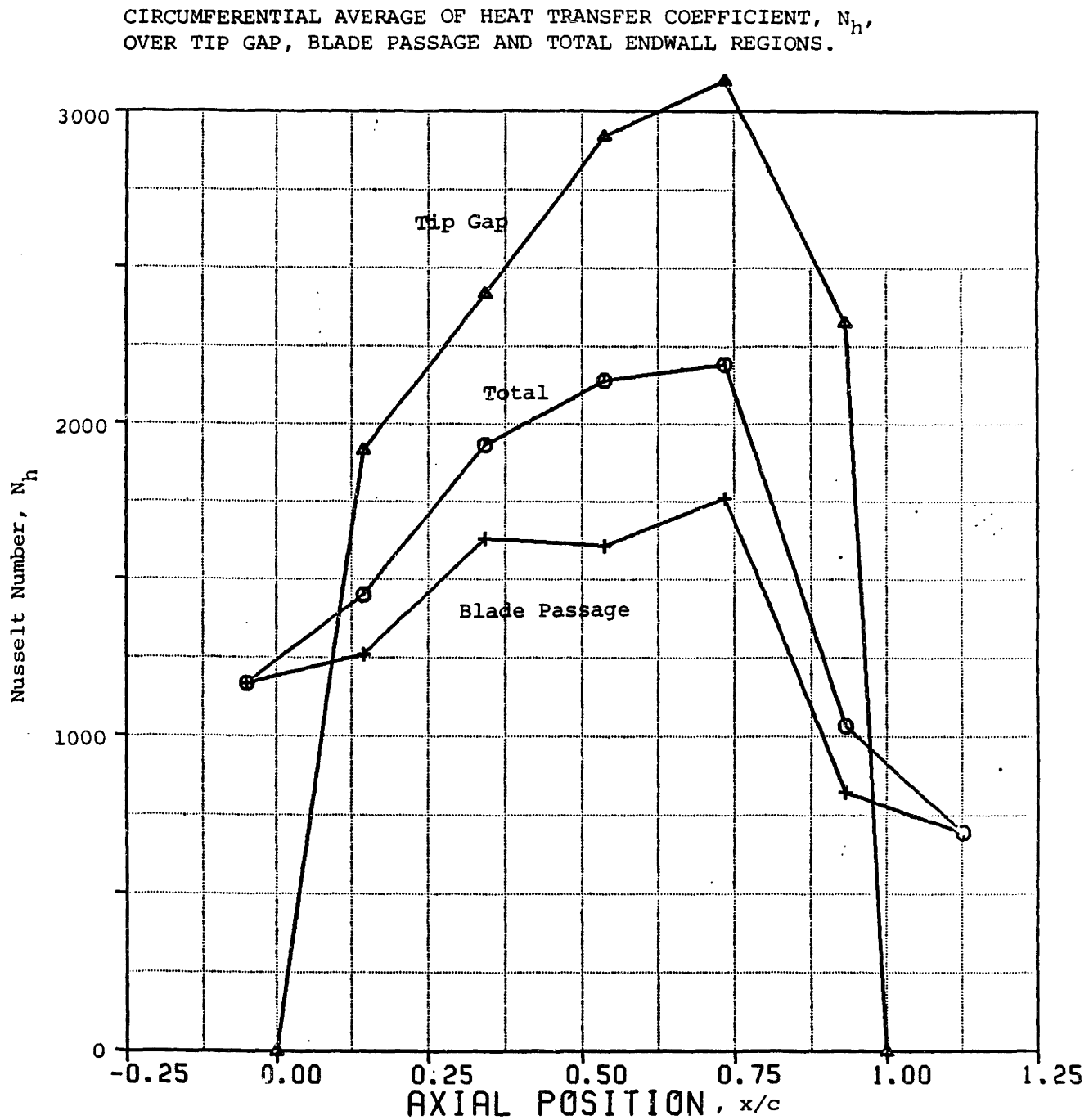

Figure 6.16: Normalized heat transfer coefficient distributions showing separate contributions for tip gap and blade passage regions compared with overall endwall distribution from Fig. 6.14.

ROTOR THICKNESS DISTRIBUTION

T - BLADE THICKNESS
S - BLADE SPACING (28.384 MM)
X - AXIAL POSITION (L/E = 0)
C - AXIAL CHORD (25.849 MM)

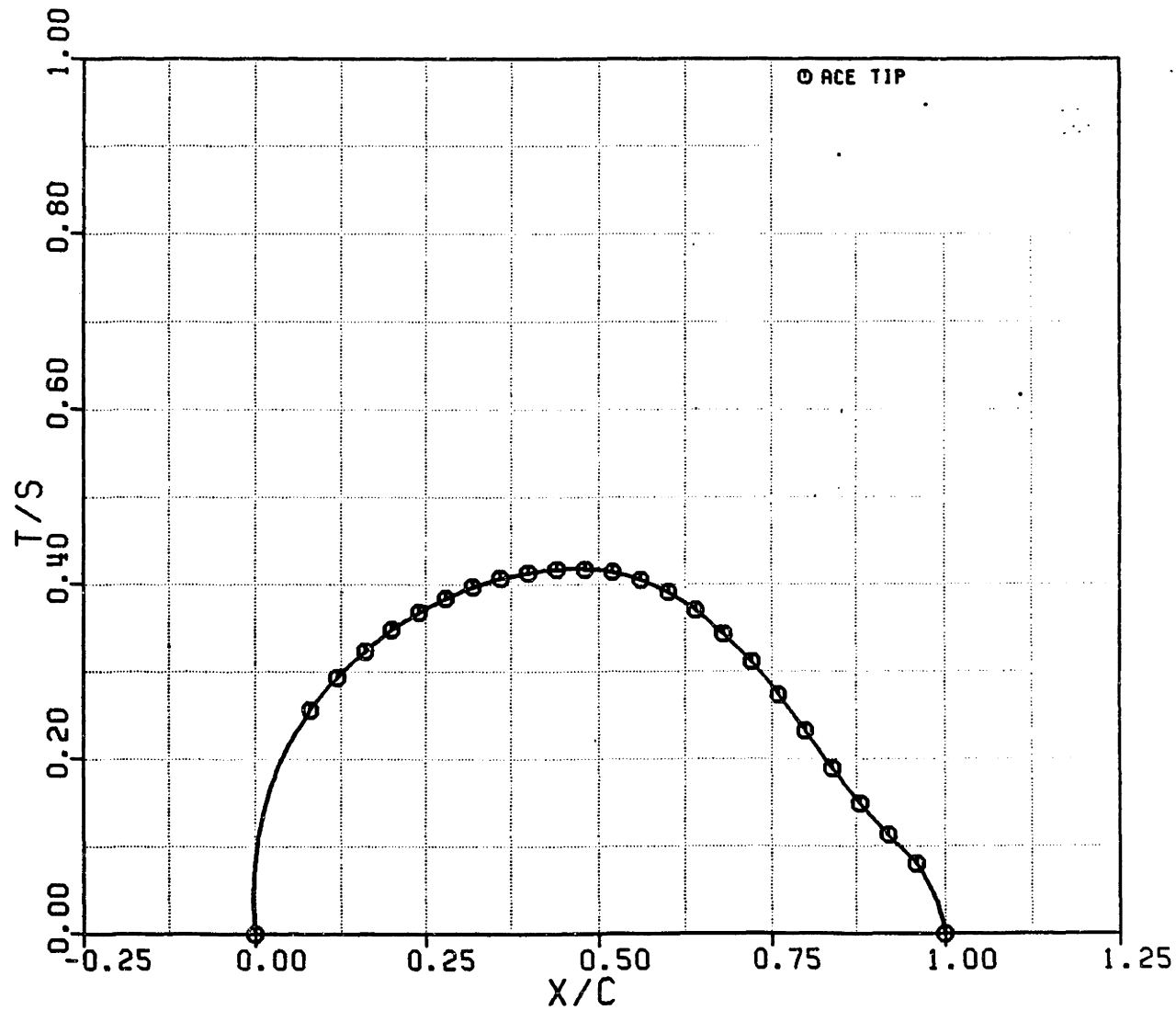

Figure 6.17: Blade thickness distribution

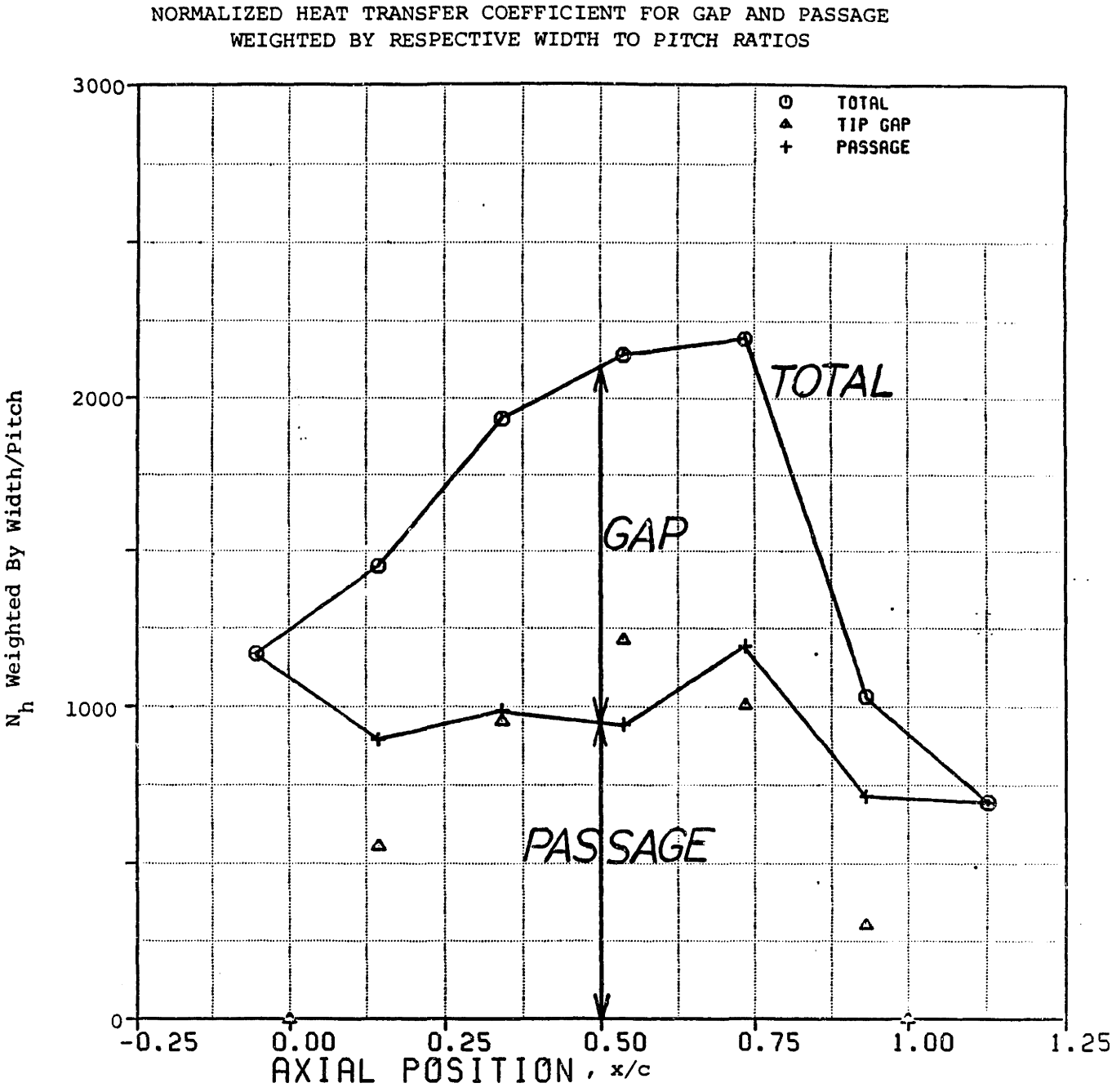

Figure 6.18: Individual contributions of gap and passage to overall endwall heat load.

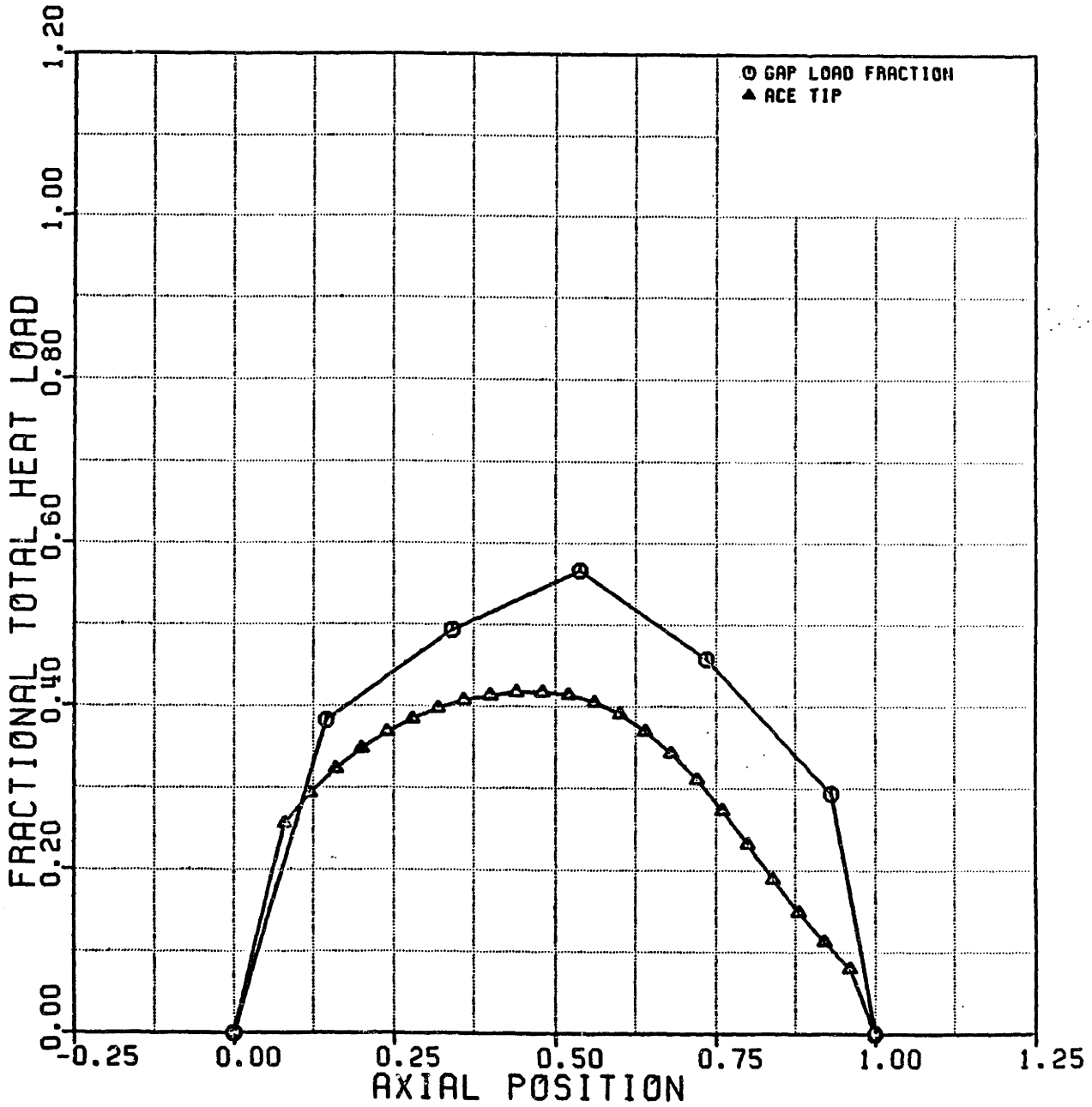

Figure 6.19: Contribution of tip gap region to overall end wall heat transfer coefficient.

CHAPTER 7

SUMMARY AND CONCLUSIONS

Experiments performed on a transonic high pressure turbine stage provided the first detailed, time resolved measurements of rotor tip casing static pressure and heat flux distributions. The tests were conducted under fully scaled conditions in a short duration facility specifically developed to provide rigorous simulation of the operational environment and covered a range of corrected speeds (inlet incidence angles) and Reynolds numbers. The results provide new insight into the factors which control the heat load distribution to the rotor end wall, including the influence of tip leakage flow and passage flow enthalpy extraction.

Specifically, the tip casing data reveals a region of very sharp pressure drop along the pressure surface entrance into the gap. The chordwise extent of this region depends upon inlet incidence and correlates with the changes in the time resolved end wall pressure distribution observed along the instantaneous profile surface. Pressure gradients within the gap are relatively low, with levels set primarily by the suction surface distribution. This data implies a strong potential leakage flow which is sonic over much of the entrance region and driven by the blade loading distribution.

Large peaks in the unsteady heat flux are found within the entrance along the regions of high gradient. The surface heat flux levels under the gap are 4 to 5 times higher than in the blade passage and when integrated over the gap area, are found to represent 45% of the overall end wall heat load. Starting from approximately the mid-chord positions, average heat flux levels drop significantly down the passage to the trailing edge as a result of the passage flow enthalpy extraction by the turbine.

The influence of enthalpy extraction was assessed by basing the dimensionless heat transfer coefficient upon an estimated local total to measured wall static temperature difference. The dimensionless heat transfer coefficient distribution was first calculated using the time averaged heat flux and surface temperature data. Average heat transfer coefficients were then separately computed for both the tip gap and blade passage regions, using the time resolved data. The results clearly show the large augmentation in heat transfer coefficient in the gap resulting from the tip leakage flow, while the distribution for the passage flow displays the gradual decrease down the passage typical of more conventional boundary layer flows.

It is concluded from these measurements that the tip leakage flow is driven primarily by the airfoil loading and is responsible for the high level of fluctuation in the time resolved heat flux. The average heat flux distribution reflects the influence of both the passage flow enthalpy extraction and the leakage flow.

These tests not only provided data on an important problem for which little full scale quantitative data existed but also demonstrated the unique capabilities of the new short duration test facility and heat flux instrumentation.

A major contribution of this work was the development of the blowdown turbine test facility, including instrumentation, to simulate and explore the operational turbine environment. Experiments are conducted on a full rotating stage under conditions which model all the relevant dimensionless flow parameters for durations sufficiently long (300 ms) to obtain comprehensive flow field surveys. By providing relatively benign, but nevertheless rigorously scaled, test conditions, it is now possible to

conduct detailed time resolved investigations upon critical flowfield phenomena which would otherwise be difficult and costly, if not impossible, to obtain.

It should be mentioned that a substantial portion of the facility engineering effort was devoted to the development of the fast acting valve and eddy current brake. Both were major contributors to the operational flexibility and technical simplicity of the facility, whose overall success, in fact, rested upon the performance realized by these initially high risk items. Apart from the facility, each is believed to represent a significant technical achievement.

A large part of this research effort also included the developement of instrumentation and data acquisition capabilities necessary to fully exploit the simulation capabilities of the facility. An important contribution was the invention of a heat flux gauge which directly measures surface heat flux from DC to over 60 kHz on warm turbine test rig components.

These gauges provide several unique advantages:

- their output can be interpreted without recourse to special models or assumptions regarding the flow of heat within the tested component,
- they induce minimal disturbance to the external flow, and
- they may be applied directly to the actual hardware including the thin walled regions near trailing edges or internal coolng passages.

Thus, they will greatly facilitate the future testing of cooled rotor components, where a combination of problems, including flowfield disturbance and high component stress levels, make testing with previously available gauges extremely difficult.

Combined with the instrumentation and data acquisition systems

concurrently developed, the blowdown turbine facility offers a unique and powerful experimental technique for the investigation of modern high pressure turbine flow. The feasibility of short duration experimentation upon high pressure gas turbines has been demonstrated, and important time resolved data has been obtained concerning end wall phenomena which could otherwise only have been obtained by a significantly greater investment.

Although the intent here has been to extend the fundamental understanding of unsteady aerodynamics and heat transfer, the advantages of such an approach for certain phases of component development by the engine industry should be evident. Given the enormous costs and risks attendant on the development of gas turbines and the ever increasing demands placed upon their levels of performance, the problem of obtaining the detailed, basic knowledge required to support their continued advance is becoming ever moer critical. In particular, this entire research effort including the facility and instrumentation development was conducted for less than one-half the nominal cost of a single developmental warm turbine build. The concepts and techniques developed by this work are therefore offered as an attractive approach.

APPENDIX A

BLOWDOWN DYNAMICS

In this section we develop an analytical expression for the blowdown of a fixed volume supply tank through a turbine coupled to an eddy brake.

A.1 Blowdown of Supply Tank

We assume an isentropic (adiabatic and reversible) expansion process in the supply tank and an isentropic flow through the inlet duct. The tank cross-sectional area is very much larger than the choking area A^* so that the tank may be considered a stagnation reservoir. During the expansion, all properties are assumed uniform throughout the tank. A fraction, α, of the test section mass flow is "by-passed" through the boundary layer bleeds. The mass flow at the tank exit (station 1) may be expressed in terms of the corrected flow at the test section inlet (station 2) as follows:

$$\dot{m}_1 = (1+\alpha)\dot{m}_2 \tag{A.1}$$

$$= (1+\alpha)\left\{\frac{\dot{m}_2\sqrt{\gamma RT_{T2}}}{P_{T2}A_2}\right\}\left(\frac{P_{T2}}{P_{T0}}\right)\left(\frac{T_{T0}}{T_{T2}}\right)^{\frac{1}{2}}\frac{P_{T0}A_2}{\sqrt{\gamma RT_{T0}}} \tag{A.2}$$

$$= (1+\alpha)\left\{\frac{\dot{m}_2\sqrt{\gamma RT_{T2}}}{P_{T2}A_2}\right\}\frac{P_{T0}A_2}{\sqrt{\gamma RT_{T0}}} \tag{A.3}$$

where the last equality follows from the isentropic flow assumption. The subscript T denotes stagnation quantities, while lack of the T denotes static quantities, and number subscripts denote flow stations. Thus, P_{T0} and T_{T0} represent the stagnation pressure and temperature within the supply tank (station 0), and A_2 is the test section inlet reference area.

Observing that $T_0 \simeq T_{T0}$ and $P_0 \simeq P_{T0}$, and using the perfect gas law, we have,

$$\dot{m}_1 = (1+\alpha)\left\{\frac{\dot{m}_2\sqrt{\gamma RT_{T2}}}{P_{T2}A_2}\right\}\frac{1}{\gamma}\,\rho_0\sqrt{\gamma RT_0}\,A_2 \tag{A.4}$$

For an isentropic expansion in the tank,

$$\frac{T(t)}{T(0)} = \left(\frac{\rho(t)}{\rho(0)}\right)^{\gamma-1}, \tag{A.5}$$

thus,

$$\dot{m}_1(t) = (1/\gamma)(1+\alpha)\rho_0(0)\sqrt{\gamma RT_0(0)}\,A_2\left\{\frac{\dot{m}_2\sqrt{\gamma RT_{T2}}}{P_{T2}A_2}\right\}\left(\frac{\rho_0(t)}{\rho_0(0)}\right)^{\frac{\gamma+1}{2}} \tag{A.6}$$

Conservation of mass requires,

$$\dot{m}_1 = -\rho_0(0)V\,\frac{d}{dt}\left(\frac{\rho_0(t)}{\rho_0(0)}\right) \tag{A.7}$$

where V is the supply tank volume. Therefore

$$\frac{d\bar{\rho}(t)}{dt} = \frac{(1+\alpha)A_2\sqrt{\gamma RT_0(0)}}{\gamma V}\left\{\frac{\dot{m}_2\sqrt{\gamma RT_{T2}}}{P_{T2}A_2}\right\}\left(\bar{\rho}(t)\right)^{\frac{\gamma+1}{2}} \tag{A.8}$$

where both $\bar{\rho}(t) \equiv \frac{\rho(t)}{\rho(0)}$ and the corrected mass flow are functions of time.

If the turbine is choked during the run, the corrected mass flow will be constant and a simple integral for $\rho(t)$ is obtained:

$$\bar{\rho}^{-(\frac{\gamma+1}{2})}\,d\bar{\rho} = -\left\{\frac{\dot{m}_2\sqrt{\gamma RT_{T2}}}{P_{T2}A_2}\right\}\frac{(1+\alpha)A_2\sqrt{\gamma RT_{T2}}}{\gamma V}\,dt\,, \tag{A.9}$$

$$(\frac{2}{1-\gamma})\bar{\rho}^{\frac{1-\gamma}{2}} = -\left\{\frac{\dot{m}_2\sqrt{\gamma RT_{T2}}}{P_{T2}A_2}\right\}\frac{(1+\alpha)A_2\sqrt{\gamma RT_{T2}}}{\gamma V}\,t + C\,. \tag{A.10}$$

Now $\bar{\rho}(t=0) = 1$, thus $C = 2/(1-\gamma)$, and,

$$\bar{\rho}(t) = \left[1 + \frac{(\gamma-1)}{\gamma} \frac{(1+\alpha)A_2\sqrt{\gamma RT_0(0)}}{2V} \left\{ \frac{\dot{m}_2\sqrt{\gamma RT_{T2}}}{P_{T2}A_2} \right\} t \right]^{-\frac{2}{(\gamma-1)}} . \quad (A.11)$$

Defining the blowdown time constant τ_g by,

$$\frac{1}{\tau_g} \equiv \frac{(\gamma-1)}{\gamma} \frac{(1+\alpha)A_2\sqrt{\gamma RT_0(0)}}{2V} \left\{ \frac{\dot{m}_2\sqrt{\gamma RT_{T2}}}{P_{T2}A_2} \right\} , \quad (A.12)$$

for the isentropic blowdown with constant corrected flow we have,

$$\rho_0(t) = \rho_0(0) \left[1 + \frac{t}{\tau_g} \right]^{-\frac{2}{\gamma-1}} \quad (A.13)$$

$$P_0(t) = P_0(0) \left[1 + \frac{t}{\tau_g} \right]^{-\frac{2\gamma}{\gamma-1}} \quad (A.14)$$

$$T_0(t) = T_0(0) \left[1 + \frac{t}{\tau_g} \right]^{-2} \quad (A.15)$$

A.2 Corrected Speed

We now summarize the derivation of the corrected speed equation.

A.2.1 Equation of Motion

The shaft mechanical speed $\omega(t)$ is governed by,

$$\frac{1}{2} I \frac{d\omega^2}{dt} = \Pi_t - \Pi_b \quad (A.16)$$

Where I is the moment of inertia of the rotating system,

$\omega(t)$ the shaft mechanical speed,

$\Pi_t(t)$ the turbine power output,

and $\Pi_b(t)$ the power absorbed by the brake.

Other contributions to the net power balance are neglected (e.g., bearing

friction).

A.2.2 Turbine Corrected Speed

Corrected shaft angular velocity is defined by,

$$\omega_{cor}(t) \equiv \frac{D\omega(t)}{\sqrt{\gamma R T_{T2}(t)}} \tag{A.17}$$

where D represents a reference diameter and $T_{T2}(t)$ the inlet total temperature. $\omega_{cor}(t)$ provides a measure of the turbine tip Mach number. We make the following manipulations to expresss $\omega(t)$ in terms of $\omega_{cor}(t)$:

$$\omega_{cor}(t) = \frac{D\omega(0)}{\sqrt{\gamma R T_{T2}(0)}} \left(\frac{T_{T2}(0)}{T_{T2}(t)} \right)^{\frac{1}{2}} \frac{\omega(t)}{\omega(0)} \tag{A.18}$$

We identify the quantity in braces as $\omega_{cor}(0)$, and defining,

$$\Omega(t) \equiv \frac{\omega_{cor(t)}}{\omega_{cor(0)}} \quad , \tag{A.19}$$

$$\Theta(t) \equiv \left(\frac{T_{T2}(t)}{T_{T2}(0)} \right)^{\frac{1}{2}} \quad , \tag{A.20}$$

we obtain $\omega(t)/\omega(0) = \Theta(t)\ \Omega(t)$. (A.21)

A.2.3 Turbine Power

The turbine shaft power, $\Pi_t(t)$, is given by,

$$\Pi_t(t) = P_{T2}(0)\ D^2 \sqrt{\gamma R T_{T2}(t)}\ \Pi_{cor}(t) \quad , \tag{A.22}$$

where $P_{T2}(t)$ and $T_{T2}(t)$ are the total pressure and temperature at the turbine inlet; D, a reference length; and $\Pi_{cor}(t)$ a turbine non-dimensional or "corrected" power, which is a function solely of the turbine

dimensionless operating conditions, themselves a function of time. Rearranging,

$$\Pi_t(t) = \left\{ P_{T2}(0) D^2 \sqrt{\gamma R T_{T2}(0)}\ \Pi_{cor}(0) \right\} \frac{P_{T2}(t)}{P_{T2}(0)} \left(\frac{T_{T2}(t)}{T_{T2}(0)} \right)^{\frac{1}{2}} \frac{\Pi_{cor}(t)}{\Pi_{cor}(0)} \qquad (A.23)$$

we identify the quantity in braces as $\Pi_t(0)$ and define,

$$\delta(t) \equiv \frac{P_{T2}(t)}{P_{T2}(0)} \quad , \qquad (A.24)$$

$$\theta(t) \equiv \left(\frac{T_{T2}(t)}{T_{T2}(0)} \right)^{\frac{1}{2}} , \qquad (A.25)$$

$$\Pi(t) \equiv \frac{\Pi_{cor}(t)}{\Pi_{cor}(0)} \quad , \qquad (A.26)$$

to obtain

$$\Pi_t(t) = \Pi_t(0)\ \delta(t)\ \theta(t)\ \Pi(t) \qquad (A.27)$$

A.2.4 Eddy Brake Power

Utilizing the "induction motor" model for brake power $\Pi_b(t)$,

$$\Pi_b(t) = 2\ \Pi_o(t)\ \frac{\left[\frac{\omega(t)}{\omega_o} \right]^2}{1 + \left[\frac{\omega(t)}{\omega_o} \right]^2} \quad , \qquad (A.28)$$

where Π_o is the maximum torque power and ω_o the maximum torque speed, we obtain,

$$\frac{\Pi_b(t)}{\Pi_b(0)} = E_b^2(t)\ \Theta^2(t)\ \Omega^2(t) \left[\frac{1 + \left[\frac{\omega(0)}{\omega_o}\right]^2}{1 + \left[\frac{\omega(0)}{\omega_o}\right]^2 \Theta^2(t)\ \Omega^2(t)} \right], \qquad (A.29)$$

where

$$E_b^2(t) = \frac{\Pi_o(t)}{\Pi_o(0)} \quad , \qquad (A.30)$$

and

$$\frac{\omega(t)}{\omega_o} = \frac{\omega(0)}{\omega_o}\ \Theta(t)\ \Omega(t). \qquad (A.31)$$

Rearranging, we obtain the form to be used in the corrected speed equation,

$$\frac{\Pi_b(t)}{\Pi_b(0)} = E_b^2(t)\ \Theta^2(t)\ \Omega^2(t) \left[1 + \frac{\left[\frac{\omega(0)}{\omega_o}\right]^2 \left[1 - \Theta^2(t)\ \Omega^2(t)\right]}{1 + \left[\frac{\omega(0)}{\omega_o}\right]^2 \Theta^2(t)\ \Omega^2(t)} \right]. \qquad (A.32)$$

When the excitation magnets are operating in their linear region, E_b represents the excitation current ratio $i_b(t)/i_b(0)$.

A.2.5 Corrected Speed Equation

Combining the above, we obtain the differential equation governing the corrected speed of the turbine,

$$\frac{1}{2}\ I\omega^2(0)\ \frac{d}{dt}\ \{\Theta^2(t)\Omega^2(t)\} = \Pi_t(0)\delta(t)\Theta(t)\Pi(t) - \Pi_b(0)E_b^2(t)\{\Theta^2(t)\Omega^2(t)\}$$

$$\left[1 + \frac{\left[\frac{\omega(0)}{\omega_o}\right]^2 \left[1 - \{\Theta^2(t)\Omega^2(t)\}\right]}{1 + \left[\frac{\omega(0)}{\omega_o}\right]^2 \{\Theta^2(t)\Omega^2(t)\}} \right] \qquad (A.33)$$

which can be solved for the corrected speed $\omega_{cor}(t) = \omega_{cor}(0)\ \Omega(t)$,

given the excitation history $E_b = E_b(t)$, and the initial values, $\Pi_t(0)$, $\omega(0)$ and $\Pi_b(0)$. At t=0, note that $\Omega(0)$, $\Theta(0)$, $\delta(0)$, $E_b(0)$ and $\Pi(0)$ are all unity. The time dependences of $\Theta(t)$ and $\delta(t)$ are a function of the blowdown dynamics, and relations have been derived for the constant corrected mass flow case. Also observe that, for fixed corrected operating point operation, $\Pi(t) = \Pi(0) = 1$.

The initial mechanical power $\Pi_t(0)$ and speed $\omega(0)$ are determined by the conditions of the particular test, and the initial value of braking power $\Pi_b(0)$ will govern the initial slope of the corrected speed response. For, at t=0,

$$\frac{1}{2} I\omega^2(0) \frac{d}{dt}\{\Theta^2(t)\Omega^2(t)\}\Big|_{t=0} = \Pi_t(0) - \Pi_t(0) \ , \tag{A.34}$$

from which we obtain,

$$\frac{d\Omega}{dt}\Big|_{t=0} = \frac{\Pi_t(0) - \Pi_b(0)}{I\omega^2(0)} - \frac{d\Theta}{dt}\Big|_{t=0} \ . \tag{A.35}$$

Blowdown Equations

For an isentropic blowdown at constant corrected flow, the inlet total temperature and pressure are given by,

$$\frac{T_{T2}(t)}{T_{T2}(0)} = \left[1 + \frac{t}{\tau_g}\right]^{-2} \tag{A.36}$$

$$\frac{P_{T2}(t)}{P_{T2}(0)} = \left[1 + \frac{t}{\tau_g}\right]^{\frac{2\gamma}{\gamma-1}} \tag{A.37}$$

where τ_g is the blowdown time constant. From our definitions of $\Theta(t)$ and $\delta(t)$, Eqs. (A.19) and (A.20), observe that

$$\theta(t) = \left[1 + \frac{t}{\tau_g}\right]^{-1} \tag{A.38}$$

$$\delta(t) = \theta(t)^{\frac{2\gamma}{\gamma-1}} \quad . \tag{A.39}$$

A.3 Conditions for Constant Corrected Speed

The corrected speed equation may now be used to find the eddy brake initial power $\Pi_b(0)$ and excitation history $E_b(t)$ which provides constant corrected test conditions. We assume that the turbine is choked so that Eqs. (A.38) and (A.39) apply for $\theta(t)$ and $\delta(t)$. Observing, therefore that,

$$\frac{d\theta}{dt} = -\frac{\theta^2(t)}{\tau_g} \quad , \tag{A.40}$$

and requiring

$$\left.\frac{d\Omega}{dt}\right|_{t=0} = 0 \quad , \tag{A.41}$$

Eq. (A.35) relating the initial condition yields,

$$\Pi_b(0) = \Pi_t(0) + \frac{I\omega^2(0)}{\tau_g} \quad . \tag{A.42}$$

Thus, to hold corrected speed constant as the test begins, the brake must initially absorb the full turbine power plus the additional amount necessary to slow the shaft speed to maintain a constant corrected speed. We see that this increment depends upon the initial rotational kinetic energy of the rotating assembly and the blowdown dynamics (τ_g).

We now use the corrected speed equation to find the required eddy brake excitation, $E_b(t)$. From Eqs. (A.38), (A.39), and (A.42), and observing that at constant corrected conditions,

$$\Omega(t) = \Omega(0) = 1 \tag{A.43}$$

$$\Pi(t) = \Pi(0) = 1 \ , \tag{A.44}$$

the differential Eq. (A.33) reduces to a simple algebraic expression which can be solved for $E_b(t)$. After a little manipulation we obtain,

$$E_b(t) = \left[1 + \frac{\left[\frac{\omega(0)}{\omega_o}\right]^2 \left[1 - \theta^2(t)\right]}{1 + \left[\frac{\omega(0)}{\omega_o}\right]^2 \theta^2(t)} \right]^{-\frac{1}{2}} \left[\frac{\theta^{\frac{\gamma+1}{\gamma-1}} + \frac{I\omega^2(0)}{\Pi_t(0)\tau_g}}{1 + \frac{I\omega^2(0)}{\Pi_t(0)\tau_g}} \right]^{+\frac{1}{2}} \ , \tag{A.45}$$

which is the sought after result. Recall that $E_b(t)$, for unsaturated eddy brake magnets, represents the excitation current $i_b(t)/i_b(0)$. A plot of $E_b(t)$ for a full Reynolds simulation in Argon/Freon-12 is shown in Fig. A.1.

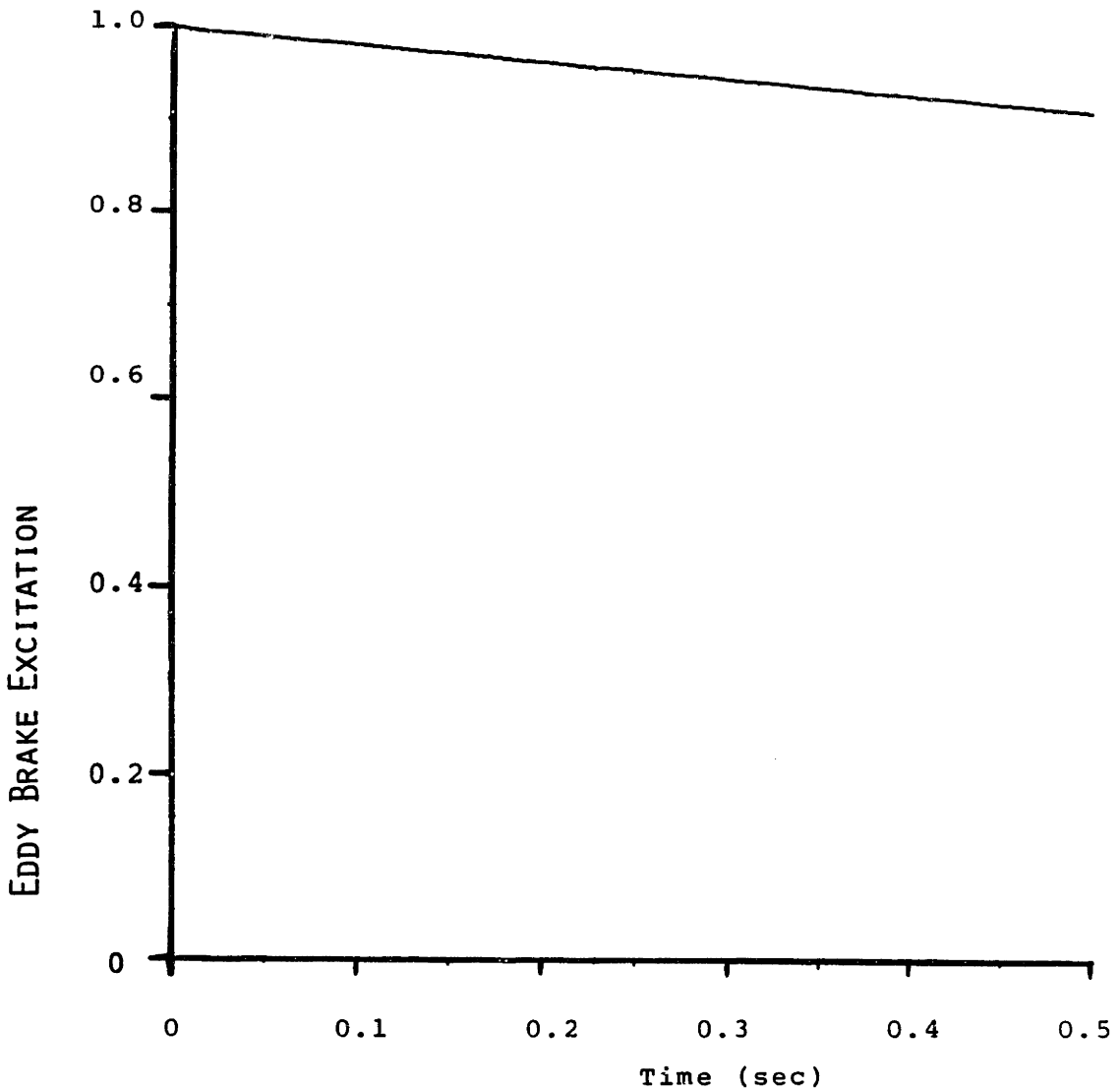

FIGURE A.1: EDDY BRAKE EXCITATION HISTORY REQUIRED FOR CONSTANT CORRECTED SPEED CONDITIONS

APPENDIX B

EDDY CURRENT BRAKE THEORY

B.1 Load Requirements

Even under the transient flow conditions of the blowdown facility, substantial power is produced by the test turbine. For a full-scale, design Reynolds number simulation in Argon/Freon-12, the test turbine generates approximately 1,078,000 Watts at 6190 RPM. Without a load, the "free-turbine" acceleration would be sufficiently large to preclude the simulation of steady-state operating conditions. In fact, for certain high Reynolds number tests, the mechanical speed might even increase beyond the turbine's safe operational limit. Furthermore, if the tests are to attain fluid dynamic similarity with actual operation, the turbine "corrected" speed, amoung several other parameters, must be held to within acceptable bounds over the 0.5 to 1.0 second test duration. Thus, the blowdown turbine must be coupled to a compatible power absorbing load which can match the power production of the test turbine at the desired testing speeds, control the test speed in accordance with the requirements of fluid dynamic similarity, and absorb the total energy generated during the run time.

The transient nature of the blowdown flow imposes additional requirements upon the turbine load. To conserve power and to establish the proper initial conditions for the tests, the turbine is brought up to operating speed in vacuum, whereupon the main flow is established as rapidly as possible; for the present facility, this is of the order of 50 milliseconds. To assure a smooth transition, the load must engage in a time compatible with the startup of the flow and hold the rotor speed "in-bounds" as the mass flow builds up, thereby allowing it to lock upon and maintain the desired corrected speed for the test.

Furthermore, as a result of the blowdown of a constant volume reservoir, both the turbine inlet temperature and pressure will decrease during the test. The "fixed operating point" turbine output power will consequently decrease, and if turbine corrected speed is to be maintained constant, the turbine mechanical speed must decrease in proportion to the corresponding drop in sound speed. Thus, both the power absorbed by the load and its mechanical speed must vary in a manner prescribed by the blowdown dynamics if constant corrected conditions are to be maintained during the test. Therefore, the load, in addition to matching the output of the turbine at a given test point, should have a power vs. speed characteristic compatible with the characteristics of the test turbine operating under blowdown conditions. It is highly desirable that this load characteristic track the turbine's in such a way that a passive "open loop" control can be achieved without the need to continually monitor the speed and actively control the load performance.

In summary, the blowdown turbine load should have the following capabilities:

1) The ability to match the power output and mechanical speed of the turbine over the desired range of test conditions,
2) A torque-speed characteristic which provides stable control of the corrected test conditions,
3) A turn-on response compatible with the blowdown start-up transient,
4) A total energy dissipation capacity to meet test duration and overspeed protection requirements in a physical package compatible with that of the blowdown facility.

B.2 Eddy Current Brake As Blowdown Turbine Load

The eddy current brake was chosen as the speed controlling load for

the blowdown facility because of its expected operating flexibility and mechanical simplicity. It can meet the load requirements in a physically compact package compatible with the size and layout of the facility, and its braking torque can be selected by a simple adjustment of its excitation current.

The torque vs. speed performance of the eddy brake is ideal for the desired "passive" control of turbine corrected speed, and, since the braking is purely electromagnetic with no physical contact or mechanically wearing parts, its performance should be stable and repeatable.

The eddy brake is excited electrically; it can be turned on and off at will with the proper high current switchgear. Its turn-on time constant, determined by the excitation coil/magnetic circuit configuration, can be configured to provide the transient performance required by the blowdown facility.

The total energy dissipated by the brake appears as an internal heating which must be stored within its structure. Although there are numerous design trade-offs with regard to performance vs. the size and configuration of the loss absorbing element, the eddy brake can be configured to meet the energy dissipation requirement while providing acceptable torque vs. speed performance.

Thus the eddy current brake can meet the criteria for the blowdown turbine load while also providing to the facility a flexibility, not only for a complete study of the present ACE turbine over a wide range of test conditions but also in providing the blowdown facility with the capability to match the load requirements of future test turbines.

B.3 Eddy Brake Configuration

The eddy current brake is illustrated in Fig. B.1. The principal

components of the brake are: 1) the cylindrical, electrically conducting, non-magnetic "loss" drum attached to the main shaft, and 2) the alternating array of d.c.-excited electromagnets surrounding the drum. Cirumferential motion of the drum through the alternating, radially oriented magnetic field induces an emf which drives an axial flow of electrical current within the drum. The eddy brake is fundamentally equivalent to the Faraday disc generator except that the current, instead of being "picked off", is allowed to flow in closed loops within the drum. As is the case for the generator, the electrical power production gives rise to an "armature" reaction; the rate at which electrical energy is produced must be balanced (under steady state contitions) by the rate at which mechanical energy is supplied to the rotating drum. Hence, a "braking" torque, opposing the rotation, is developed and the mechanical work supplied appears as an I^2R heating of the loss drum. The torque may also be viewed as the result of the Lorentz force which arises from the motion of a current carrying conductor through a magnetic field.

The magnitude of the braking torque depends upon both the strength of the applied magnetic field and the tangential speed of the drum. The analysis presented in the following section will show that the torque is proportional to the square of the applied magnetic field. We shall find, however, that the speed dependence is somewhat more complicated and, as we shall see, can be important to the overall performance of the eddy brake as a speed controlling load.

As the shaft speed increases from rest, the braking torque is initially proportional to speed. As the speed continues to rise, the torque peaks at a maximum value and then falls off with further speed increase. This behavior results from the influence of the "induced" magnetic field,

produced by the eddy currents, upon the applied field. At low speeds, the magnitude of the induced field is small compared to the applied field and exerts negligible influence upon the braking process. But with further increase in speed, it grows stronger, eventually attaining a magnitude comparable with that of the applied field. Furthermore, the induced field opposes the penetration of the applied field into the eddy brake drum. Thus, the applied field is "convected" away from the drum and is further weakened by the resultant stretching of its (solenoidal) field lines.

The torque-speed characteristic of the eddy current brake displays a torque maximum as a result of this back emf effect acting on its rotor. Typical torque and power performance curves for these "induced current" machines are shown in Fig. B.2, plotted against shaft speed. At speed ω_o, the torque reaches a maximum, T_{max}, and the corresponding absorbed power is $\Pi_o = \Pi(\omega_o) = T_{max}\omega_o$. Also indicated on the plots is the general shape of the curves at the limiting values of rotation speed.

The analysis will show that brake performance may be modeled by the induction motor torque-slip characteristic,

$$\frac{T}{T_{max}} = \frac{2(\omega/\omega_o)}{1 + (\omega/\omega_o)^2} \tag{B.1}$$

when the skin effect phenomenon can be neglected. (It will be shown that this is usually true when $\omega < \omega_o$.) The power absorbed is then,

$$\frac{\Pi}{\Pi_o} = \frac{T\omega}{T_{max}\omega_o} = \frac{2(\omega/\omega_o)^2}{1+(\omega/\omega_o)^2} \tag{B.2}$$

This model is useful for machine design and analysis because T_{max} and ω_o completely specify the model characteristic and can be simply related

to the machine configuration and excitation field strength. Thus, the operating line is completely specified by ω_o and either Π_o or T_{max}.

For each test condition, the eddy brake operating point must follow a time history prescribed by the blowdown dynamics if it is to hold turbine corrected speed constant during data acquisition. The magnitude of the applied field might be used to control operation of the brake as part of a feedback control system. However, active control of the very large total current (500-700 amps) required to excite the brake is difficult, therefore the corrected speed will be controlled "open loop" by proper matching of the brake characteristic and selection of its initial operating point. From a turbine-eddy brake load matching analysis, a set of operating point(s) on the normalized characteristic can be obtained which bound the required eddy brake excitation history to that which can be provided through adjustment of the passive ballast load resistor.

Rotating system stability is an important consideration in eddy brake design and operation, for although the brake may match the turbine at the desired operating point, the torque balance between the two must be stable. The relative slopes of the torque-speed characterisics of the two machines at the operating point will determine whether or not small perturbations will grow or decay. If the design speed is larger than the brake maximum torque speed, ω_o, turbine runaway becomes a possibility. In this case, a small increase in turbine speed, for example, could increase the turbine torque but would reduce the eddy brake torque resulting in an overall net acceleration torque.

As we have seen, the eddy brake operating characteristic is uniquely specified by its maximum torque conditions $\Pi_o(T_{max})$ and ω_o. For a given machine, Π_o may be varied by adjusting the magnitude of the applied

magnetic field (up to the saturation limit of its core material) and is thus an easily controlled variable for test to test adjustment. The maximum torque speed ω_o, as we shall see from our model, depends on the geometrical configuration of the drum and excitation magnets. For a given machine, it is possible to change its value by adjusting the magnet gaps or by reconfiguring the coil polarities. In practice, these adjustments are difficult and time consuming to accomplish on a test by test basis. Thus, it is important that the ω_o realized by the machine be suitable for the range of test conditions expected.

B.4 Excitation Magnets

The excitation field is supplied by conventional U-core electromagnets surrounding the outer surface of the loss drum. After passing across the air gap (including the non-magnetic drum), the magnetic flux loops through the annular return ring mounted inside the drum, thus completing the magnetic circuit. Both the U-cores and return ring are laminated to reduce eddy current losses and are constructed from standard transformer stock material with good hysteresis properties. This material saturates at approximately 20,000 Gauss which represents, therefore, the practical upper limit on core magnetic flux density.

The maximum torque and speed of the machine, hence its operating characteristic, depend in part upon the pole to pole spacing and air gap length of the magnets. However, these parameters also determine the strength of the magnetic field passing through the loss drum relative to its strength in the magnet cores (i.e., the amount of flux loss in the system), hence the maximum power absorbing capability of the machine.

The magnetic flux density in the loss drum will be less than that in the core, partly as a result of the lamination stacking losses but more

significantly as the result of magnetic flux path leakage and fringing. Both leakage and fringing depend critically upon the pole/gap geometry which, in the case of the eddy brake, is dictated by the performace requirements and design constraints of the machine. These state that the air gap be a significant fraction of both the pole face width and the pole-to-pole spacing (pole pitch), with the result that both leakage and fringing must be considered as possible sources of reduction of the loss plate field strength.

To minimize flux leakage, the coils are wound "squat" and are mounted close to the pole faces. This helps to reduce the pole-to-pole leakage path area, hence the total leakage flux. Predicting the exact level of the leakage is difficult due to the complex geometry of the configuration, however it can be bounded by a worst case estimate.

The U-cores, assembled from standard transformer stampings, present a constant area flux path around the "U". The total air gap flux, both leakage and "working", must loop the excitation coils. Hence, essentially all of the flux must enter and pass through that portion of the core surrounded by the coils. Since the magnetic flux is a divergence-free field, the flux density may be lowered significantly throughout most of the remainder of the core by filling the hole of the "U" behind the squat coils with ingot iron, thereby reducing both the reluctance of the core path and its susceptibility to saturation (see Fig. B.3).

Fringing is more difficult to reduce because it depends upon the air gap to pole width ratio, which is constrained by machine performance requirements. For the geometry of our brake, fringing and core stacking alone will limit the drum flux density to about 60% of that in the core pole faces. Therefore, before inclusion of the losses due to leakage, the

flux density available for braking would be limited by core saturation to about 12,000 Gauss. To conservatively account for leakage, the brake is designed for a maximum of 7500 Gauss applied to the drum.

B.5 The Loss Drum

The eddy current brake loss drum is a thin walled cylinder cantilevered from the end of the main turbine shaft. The excitation magnets are wrapped around its outer circumference and induce axially oriented current loops within the drum material. The I^2R power dissipation in the drum might be viewed as either the cause or the effect of the braking action.

Either way, the drum must have sufficient mass to absorb the total energy load requirements of the blowdown, which will typically be on the order of one to two megajoules. This requirement is dictated by the total turbine energy produced during the start-up and active test time of the experiment, plus that portion of the blowdown energy remaining after the test which would contribute to turbine overspeed.

Since it spins with the turbine, the drum must be capable of both high temperature and high stress operation. Since only the active portion of the drum under the magnets will see uniform heating, thermal stresses must also be considered. Each point on the drum will experience an N-pole per revolution excitation (and possibly lower harmonics if there are pole to pole magnetic field or loss drum nonuniformities), therefore the possibility exists for adverse structural drum dynamics.

The drum electrical resistivity is a significant parameter which affects not only the power dissipation per unit volume of the drum but also the maximum torque shaft speed. It is necessary that the resistivity be as high as possible for good brake performance. In order of increasing resistivity come copper, aluminum, carbon steel, non-magnetic stainless, and the

nickel superalloys. The stainless and nickel steels are the only ones that possess the magnetic, structural, and electrical properties suitable for the present application. Both were considered, but the increased structural and thermal load capability of the nickel superalloy resulted in its final selection.

B.6 Eddy Current Brake - Simplified Theory

Consider a non-magnetic, electrically conducting plate moving at velocity $\bar{v}$ through a magnetic field $\bar{B}$. An emf will be induced causing "eddy" currents to flow within the plate. From Faraday's and Ohm's laws, the induced current density is given by $\bar{j} = \sigma(\bar{v} \times \bar{B})$, where σ is the plate conductivity. The interaction of the current with the magnetic field results in a force opposing the motion, which per unit volume is given by $\bar{f} = \bar{j} \times \bar{B}$. Energy conservation requires that a force must arise, for mechanical work must be supplied to balance the rate at which power is dissipated in the plate due to the flow of current across its finite electrical resistance.

Now consider the linear eddy current brake configuration illustrated in Fig. B.3. The "loss" plate moves through the magnetic field produced by the array of alternately directed, rectangular poles of length 2a and width 2b. The applied field is assumed uniform under the poles, where it induces a current density σvB in the plate. Elsewhere, both the applied field and induced current are assumed zero. The current flowing in the plate element directly under each pole is $i = \Delta 2a\sigma vB$. The electrical resistance of this element, of cross-section $\Delta 2a$ and length 2b, is $2b/\sigma\Delta 2a$. The power dissipated per pole, Π, is therefore $\sigma\Delta 4abB^2v^2$, and must be supplied through the rate at which mechanical work is performed upon the moving plate. Thus, the force per pole acting upon the plate is

$$F = \Pi/v = \sigma\Delta A_p B^2 v \quad , \tag{B.3}$$

where A_p =(2a)(2b) is the magnetic pole area.

This simplified model provides a good estimate of the eddy braking force under the following conditions:

1) There is no fringing of the magnetic field, i.e., it is perpendicular to the plate and uniform under the poles,
2) The induced magnetic field produced by the eddy currents is small compared to the applied field,
3) The eddy current return paths contribute negligible power dissipation compared to the paths under the poles, and
4) The skin depth of the eddy currents is much larger than the plate thickness.

For the turbine braking application, item 2) will be responsible for the most deviation from this simple theory and will now be considered in more detail.

B.7 Magnetic Reynolds Number - Influence of Induced Field on Braking Force

Suppose a magnetic field of magnitude B_o is imposed perpendicular to the plate moving laterally at speed v. The induced current density, given by $\bar{j} = \sigma(\bar{E}+\bar{v}\times\bar{B})$, is therefore of order $\sigma v B_o$. From Ampere's law, curl $\bar{B} = \mu\bar{j}$, the magnitude of the induced field B_i will be of order $\Delta\mu j \tilde{=} \mu\sigma\Delta v B_o$. The ratio of induced field to applied field is therefore proportional to the quantity $\mu\sigma\Delta v$. This ratio is called the "magnetic" Reynolds number:

$$R_M = \mu\sigma\Delta v \tilde{=} B_i/B_o, \tag{B.4}$$

and it characterizes the ability of the applied field to penetrate the moving conductor. At low values of R_M (R_M<<1), the applied field passes

through the plate. At high values ($R_M \tilde{>} 1$), the applied field is convected along the moving plate with very little diffusion into the plate.

This phenomenon can strongly influence the braking force produced because it governs the penetration of the field, responsible for the flow of the power dissipating eddy currents into the moving conductor. The analysis which follows will show that its net effect is to place a limitation upon the force-producing capability of the device as the magnetic Reynolds number approaches unity. This represents a particularly important consideration for the turbine braking application where, as a result of the high power dissipation and shaft speed requirements, practical engineering designs will, of necessity, be required to operate in the unity Reynolds number regime.

B.8 Eddy Current Brake - Induction Motor Model

In modeling the eddy current brake, we follow the approach employed in Refs. [B.1-B.3]. The physical configuration illustrated in Fig. B.4 is replaced by the model configuration shown in Fig. B.5. To eliminate the dependence of the field quantities upon the transverse y-direction, we assume that the width of both the eddy plate w, and the magnetic poles 2b, is large compared to the pole pitch τ, and that all currents (both excitation and eddy) flow along the $\pm$ y-direction. An edge effect correction will be introduced later to account for the return path current loops in the eddy plate.

The excitation windings and salient poles of the physical machine are replaced in the model by two infinitely thin conducting sheets, parallel to the eddy plate and located at $\pm$ g. They are backed by a non-conducting material of infinite permeability. The gap magnetic field is generated in the model by surface currents assumed to flow on each of these "smoothed"

pole surfaces along the ± y-direction. The total current per unit length along the x-direction is specified by the linear current density K_y (x,t).

The physical airgap ℓ_g between the salient poles is replaced by an effective airgap 2g as determined by Carter's air gap coefficients, Ref. [B.4], to account for the interpole space and variable reluctance of the actual configuration.

The field equations will be solved for a harmonic current distribution, representing the fundamental component of the applied magnetic field. Solutions may then be superposed to find the results for arbitrary periodic excitations. The total current per unit length along the x-direction will therefore be modeled by the sinusoidal distribution of amplitude K_o, and (spatial) period 2τ:

$$K_y(x) = K_o \sin \frac{\pi x}{\tau} \tag{B.5}$$

representing the total current density from both sheets per unit length along the x-direction.

The average normal component of the gap magnetic field, B, may be found by applying Ampere's law to a rectangular loop of length τ and height 2g,

$$\oint \bar{H}_o \cdot \overline{d\ell} = i_{tot} \tag{B.6}$$

where i_{tot} is the net current crossing the surface of the loop. Observing that $\bar{H}$ must vanish in the regions behind the current sheets where $\mu = \infty$, and that as a result of the symmetry of the excitation:

$$H_z(x) = -H_z(x+\tau) \tag{B.7}$$

we have,

$$(2g)\ 2H_z(x) = \int_x^{x+\tau} K_o \sin \frac{\pi x}{\tau}\, dx \tag{B.8}$$

$$H_z(x) = \frac{K_o \tau}{\pi(2g)} \cos \frac{\pi x}{\tau} \tag{B.9}$$

Therefore, in the gap where $B = \mu H$, we obtain,

$$B(x) = B_o \cos \frac{\pi x}{\tau} \tag{B.10}$$

where

$$B_o = \frac{\mu_o K_o}{\pi(2g/\tau)} \tag{B.11}$$

The excitation poles are centered at the zeros of the distribution and in the model; each pole "face" occupies the entire region between alternate peaks of the sinusoid. The equivalent amp-turns per pole, I_e, for the sheet excitation is obtained by observing that each pole is composed of a pair of adjoining strips of equal width $\tau/2$, each carrying an equal but oppositely directed current of magnitude,

$$1/2 \int_0^{\tau/2} K_y(x)dx = K_o \tau/2\pi \tag{B.12}$$

per sheet. Assuming each pair to be connected at $y = \pm b$ to form a single turn loop, and noting that there are two such turns per pole, one from each sheet, we obtain,

$$I_e = K_o \tau/\pi. \tag{B.13}$$

The excitation current, as observed from a reference frame fixed to the current sheets, may be expressed in the form,

$$K(x) = K_o j \exp(-j\pi x/\tau) \tag{B.14}$$

where the real part of this, and the following complex expressions, are understood to represent the physical quantities. Assuming the plate moves at velocity v in the positive x-direction and that v<<c, the excitation as observed from the plate is:

$$K(x') = K_o j \exp(-j\ \pi/\tau(x'+vt)) \tag{B.15}$$

The field equations are then solved in the moving frame for a non-magnetic plate of permeability μ_o, see Ref. [B.3]. If the height 2g of the air gap is small compared to the pole pitch τ and skin depth δ_{skin}, the electric field induced in the gap (including the plate) is found to be essentially independent of z. Adapting the solution quoted in Ref. [B.3] to the geometry of our configuration, we obtain,

$$E_y(x') = E_{yo} \exp(-j\ \pi/\tau(x'+vt)) \tag{B.16}$$

where the complex amplitude

$$E_{yo} = -j\ \frac{\mu_o v K_o}{\mu_o \sigma \Delta v + j\pi\ 2g/\tau} \tag{B.17}$$

contains the magnitude and phase-shift information. Defining a magnetic Reynolds number R_M based upon the thickness of the non-magnetic plate,

$$R_M \equiv \mu_o \sigma \Delta v \tag{B.18}$$

and the ratio R,

$$R \equiv \frac{R_M}{\pi\ 2g/\tau}\ , \tag{B.19}$$

we express the complex amplitude E_{yo} (in magnitude phase form) by,

$$E_{yo} = -\frac{K_o}{\sigma\Delta}\ \frac{R}{\sqrt{1+R^2}}\ \exp(j\phi) \tag{B.20}$$

where,

$$\phi \equiv \tan^{-1} R \quad . \tag{B.21}$$

The induced gap field is therefore,

$$E_y = - \frac{K_o}{\sigma \Delta} \frac{R}{\sqrt{1+R^2}} \tag{B.22}$$

Applying Ohm's law in the moving frame, the induced current density in the plate is found to be,

$$j_y = - \frac{K_o}{\sigma \Delta} \frac{R}{\sqrt{1+R^2}} \left[\cos \frac{\pi}{\tau} (x' + vt) - \phi \right] \tag{B.23}$$

The power dissipated in an elemental plate filament of length 2b is then,

$$d\Pi = (j \, dx \, dy)^2 \frac{2b}{\sigma dx dz} \, , \tag{B.24}$$

Integrating over one pole pitch (having first transformed back to the stationary frame)

$$\Pi = \int_{x}^{(x+\tau)} \int_{-\Delta/2}^{+\Delta/2} \frac{2b}{\sigma} \frac{K_o^2}{\Delta^2} \frac{R^2}{1+R^2} \cos^2 \left(\frac{\pi x}{\tau} - \phi \right) dz dx \tag{B.25}$$

we obtain the power dissipation per pole,

$$\Pi = \frac{2b}{\sigma \Delta \tau} \frac{\tau^2 K_o^2}{4} \frac{2R^2}{1+R^2} \quad . \tag{B.26}$$

The first factor on the right is the total transverse resistance per pole of the loss plate. The second factor represents the squared magnitude of an "equivalent" uniform and uni-directional current yielding the same power dissipation per pole as the actual alternating induced distribution,

$$i_{eq}^2 = \frac{\tau^2 K_o^2}{4} \frac{2R^2}{1+R^2} \quad . \tag{B.27}$$

Given in terms of the amp-turns per pole of the applied excitation, I,

$$i_{eq}^2 = \frac{\pi^2 I^2}{4} \frac{2R^2}{1+R^2} \quad , \tag{B.28}$$

These expressions will be useful in characterizing the design and operation of the actual machine.

The braking force per pole, obtained from our power dissipation expression, is given by,

$$F = \frac{\Pi}{v} = \frac{2b}{\sigma\Delta\tau} \frac{\mu_o \sigma\Delta}{(\pi\ 2g/\tau)} \frac{\tau^2 K_o^2}{4} \frac{2R}{1+R^2} \quad . \tag{B.29}$$

This equation predicts a maximum force when R=1,

$$F_{max} = F(R=1) = \frac{2b}{\sigma\Delta\tau} \frac{\mu_o \sigma\Delta}{(\pi\ 2g/\tau)} \left[\frac{\tau K_o}{2}\right]^2 , \tag{B.30}$$

at a maximum force Reynolds number R_{Mo} of,

$$R_{Mo} = R_M(F_{max}) = \pi\ 2g/\tau \ . \tag{B.31}$$

The power dissipated at maximum force is,

$$\Pi_o = \Pi(R=1) = \frac{2b}{\sigma\Delta\tau} \left[\frac{\tau K_o}{2}\right]^2 , \tag{B.32}$$

where $\tau K_o/2$ is the equivalent induced loss plate current per pole.

We infer from the form of the force expression that R is the significant parameter characterizing the influence of the eddy current "back emf" and observe that it may be interpreted as a magnetic Reynold's number based upon the length scale ($\tau\Delta/\pi 2g$); its significance is made apparent from the solution of the field equations. If v_o is defined as the plate velocity

at maximum force,

$$v_o = v(R=1) = \frac{\pi\ 2g/\tau}{\mu_o \sigma \Delta} \quad , \tag{B.33}$$

it follows that R also represents the characteristic speed ratio,

$$R = \frac{\mu_o \sigma \Delta v}{\pi\ 2g/\tau} = \frac{v}{v_o} \quad . \tag{B.34}$$

In terms of the maximum force F_{max}, power at max force Π_o and speed ratio R, the power and force relations therefore become

$$\Pi = \Pi_o \frac{2(v/v_o)^2}{1 + (v/v_o)^2} \tag{B.35}$$

$$F = F_{max} \frac{2(v/v_o)}{1 + (v/v_o)^2} \tag{B.36}$$

and since $\Pi_o = F_{max}\ v_o$, we conclude that v_o and either Π_o or F_{max} completely specify the eddy brake performance characteristic within the assumptions of the thin plate limit. We also observe that, in this form, the force expression is identical to the normalized torque-slip relation of simple induction motors, Ref.[B.5], hence the term "induction motor model" is applied to these equations.

We should recall that the model is valid when,

a) the applied field is normal to the plate and varies harmonically with spatial period 2τ in the direction of plate motion,

b) the plate thickness is small compared to the skin depth δ, and the pole pitch τ,

c) the air gap is small compared to the pole pitch, and

d) the air gap permeability is uniform, hence the use of a nonmagnetic

plate.

The model developed for the linear machine may be applied directly to the rotating cylindrical configuration shown in Fig. B.1, where typically the machine radius will be much larger than the pole pitch and air gap spacing. The "loss plate" is a drum of radius r and axial length w, rotating at an angular velocity ω about its axis of symmetry. It is surrounded by N alternating electromagnets, with rectangular poles of circumferential length 2a and axial length 2b, spaced at a pitch τ along the circumference. Thus, $N\tau = 2\pi r$, with N an even integer.

The magnetic Reynolds number based on drum thickness Δ is,

$$R_M = \mu_o \sigma \Delta r \omega \tag{B.37}$$

From our "induction motor" characteristic Reynolds number,

$$R = \frac{\mu_o \sigma \Delta r \omega}{\pi(2g/\tau)} = \mu_o \sigma (\Delta\tau/\pi 2g) r\omega, \tag{B.38}$$

the maximum force condition (R=1) may be used to obtain the angular velocity at maximum torque,

$$\omega_o = \frac{\pi(2g/\tau)}{\mu_o \sigma \Delta r} = \frac{N(2g)}{2\mu_o \sigma \Delta r^2} \quad , \tag{B.39}$$

from which we obtain,

$$R = \omega/\omega_o \tag{B.40}$$

The total power at maximum torque for an N-pole machine is simply,

$$\Pi_o = N(2b/\sigma\Delta\tau)\ (\tau K_o/2)^2 \tag{B.41}$$

and, using the $N\tau = 2\pi r$ constraint for the cylindrical configuration, we obtain, in I^2R form,

$$\Pi_o = \frac{2b}{\sigma\Delta 2\pi r} (\pi r K_o)^2 \tag{B.42}$$

where we identify the first factor as the resistance of the active portion of the cylinder to an axial flow of current and the second as the square of the equivalent uniform current at maximum torque. Note that it is independent of N.

The total power and torque for the N-pole machine are given by,

$$\Pi = \Pi_o \frac{2(\omega/\omega_o)^2}{1+(\omega/\omega_o)^2} \tag{B.43}$$

$$T = T_{max} \frac{2(\omega/\omega_o)}{1+(\omega/\omega_o)^2} \tag{B.44}$$

where

$$\Pi_o = \frac{2b}{\sigma\Delta 2\pi r} (\pi r K_o)^2 \tag{B.45}$$

$$T_{max} = \Pi_o/\omega_o \tag{B.46}$$

and

$$\omega_o = \frac{\pi(2g/\tau)}{\mu_o \sigma \Delta r} \quad . \tag{B.47}$$

We must now remark that, so far, no account has been made for the "edge" effects of a finite width plate. It has been assumed that the induced current distribution is one-dimensional, alternating in sign in a direction perpendicular to the motion with a spatial period of 2τ. For the actual plate, the current distribution forms return loops at the ends of the loss drum. Thus, our force expressions are strictly valid for a plate where these loops face zero resistivity and therefore do not contribute to

the power dissipation.

To account for these return loops, a resistivity correction factor k is employed. It is computed by solving the field equations for the current distribution in the plate and is a function of plate and pole geometry and of the magnetic Reynold's number. An effective conductivity is then used in place of the physical conductivity in the eddy brake equations.

References

B.1 Singh, A., "Theory of Eddy-Current Brakes With Thick Rotating Disc," Proc. IEE, Vol. 124, (4), April 1977, pp. 373-376.

B.2 Jackson, W.D. and Pierson, E.S., "Operating Characteristics of the M.P.D. Induction Generator," IEE Conf. Rep. Ser. 4, 1962, pp. 38-42.

B.3 Bahler, W. and Van der Hoek, W., "An Eddy Current Coupling Employed as a Variable Speed Drive," Philips Tech. Rev., Vol. 27, 1966, pp. 15-21.

B.4 Nasar, S.A., "Electromagnetic Theory of Electrical Machines," Proc. IEE, Vol. III, (6), 1964, p. 1125.

B.5 Fitzgerald, A.E., Kingsley, Jr., C., and Kusko, A., Electric Machinery, 3rd edition, New York: McGraw-Hill, 1971.

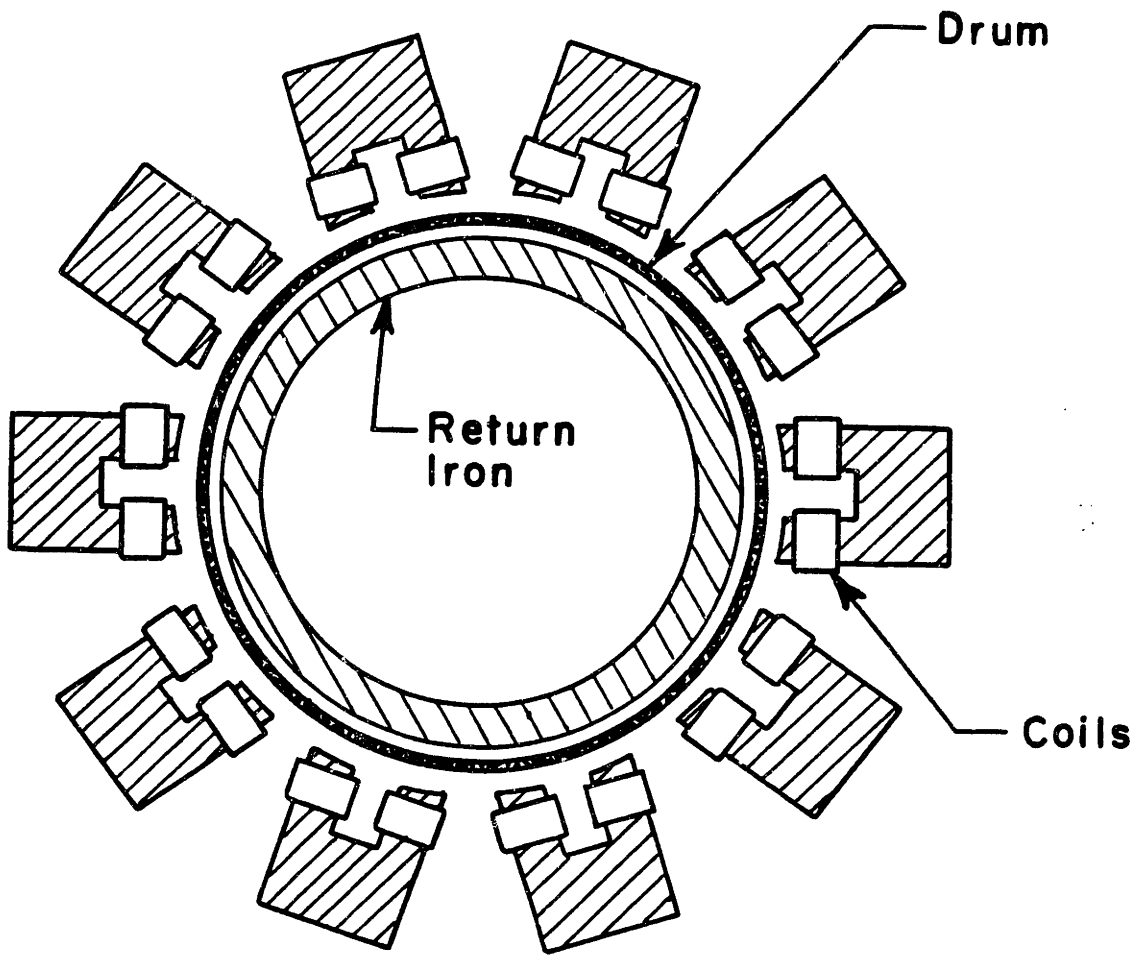

FIGURE B.1: EDDY CURRENT BRAKE GEOMETRY

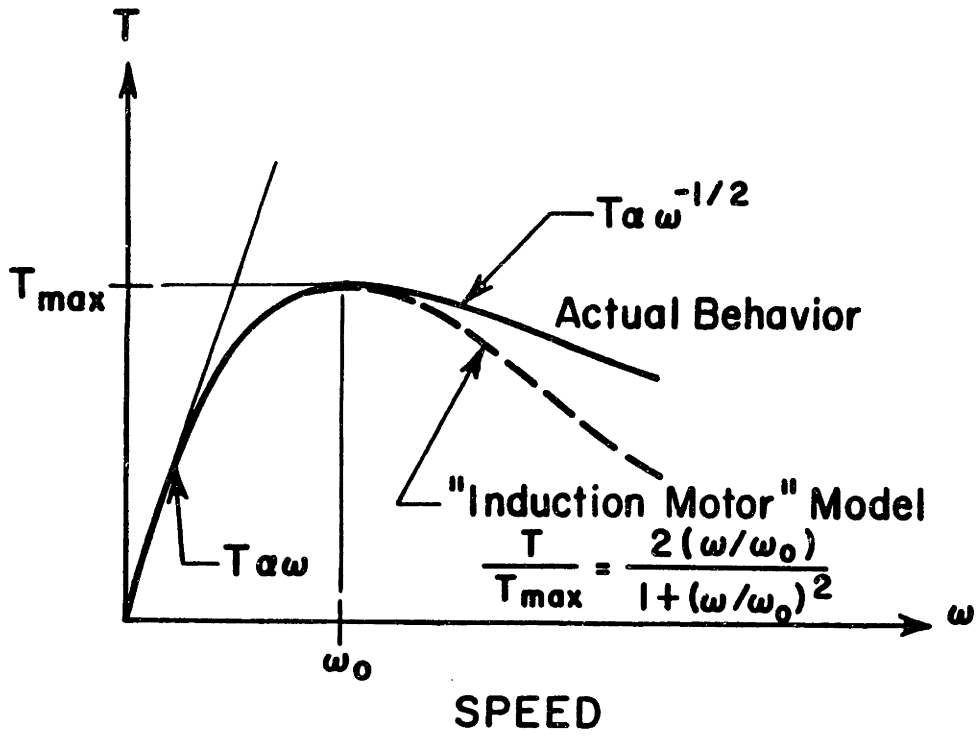

A) TORQUE VS. SPEED

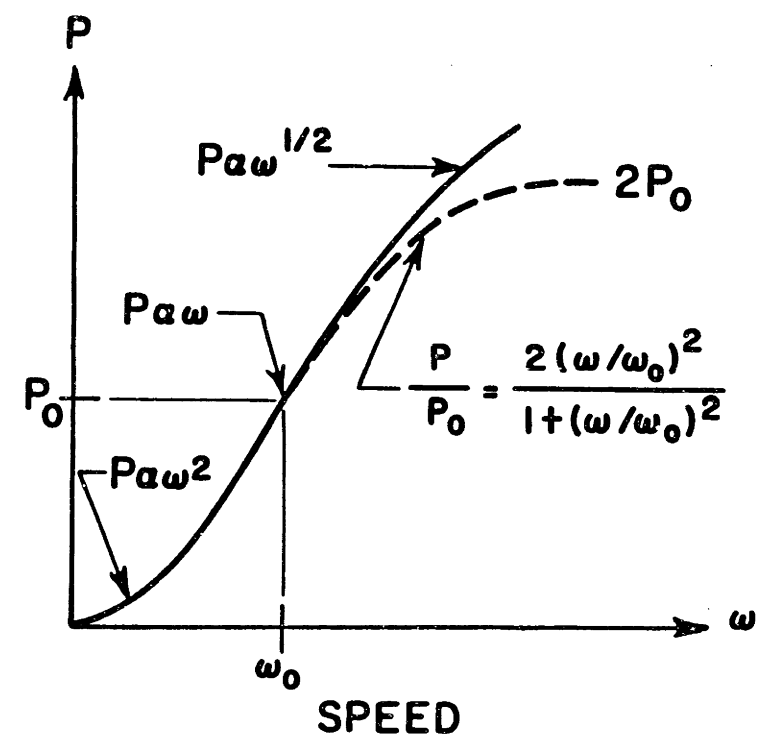

B) POWER VS. SPEED
(NOTE: THE P'S IN THIS FIGURE CORRESPOND WITH THE Π'S IN THE TEXT)

FIGURE B.2: EDDY BRAKE ROTATIONAL SPEED CHARACTERISTICS

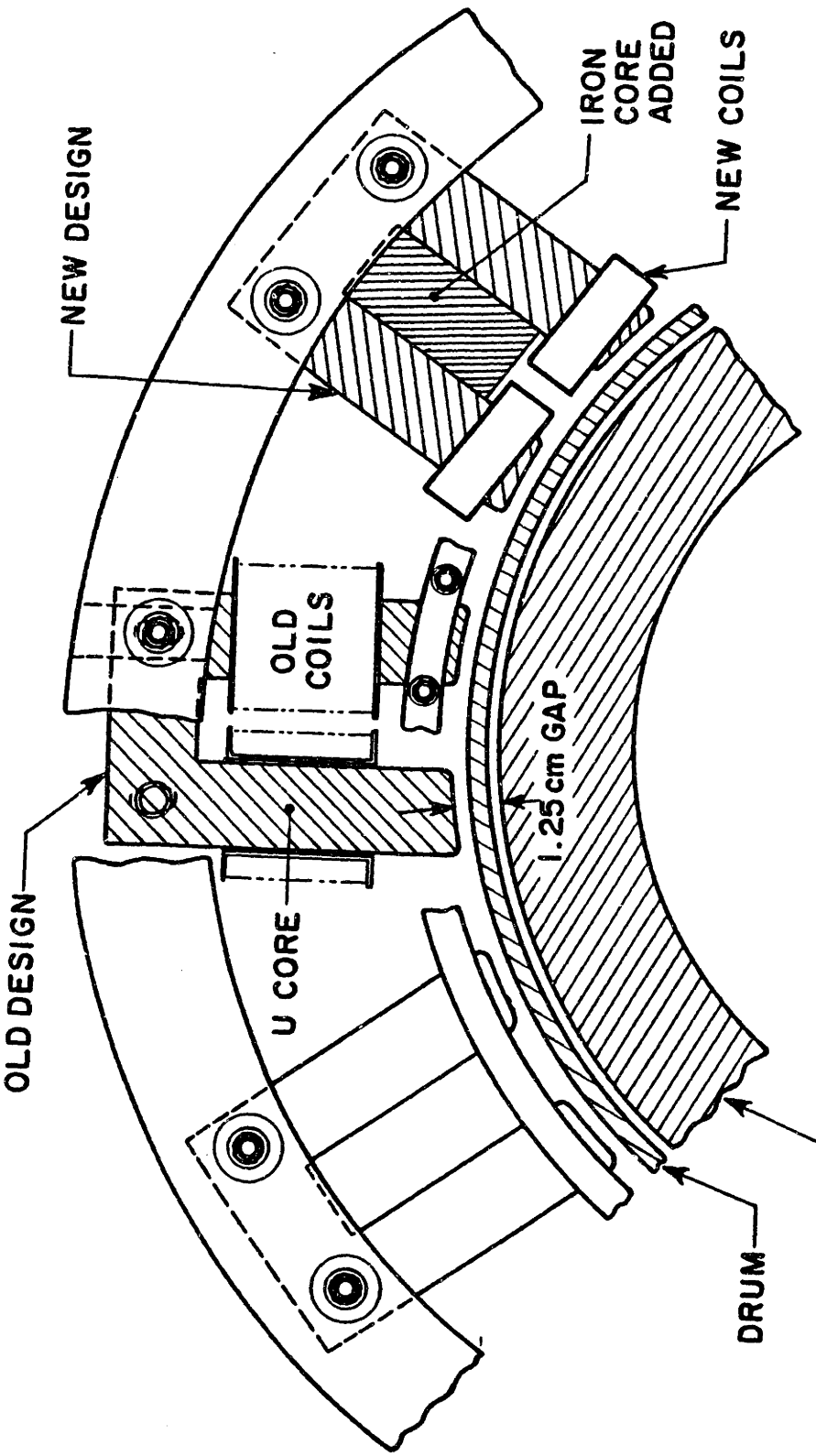

FIGURE B.3: MAGNET DETAIL

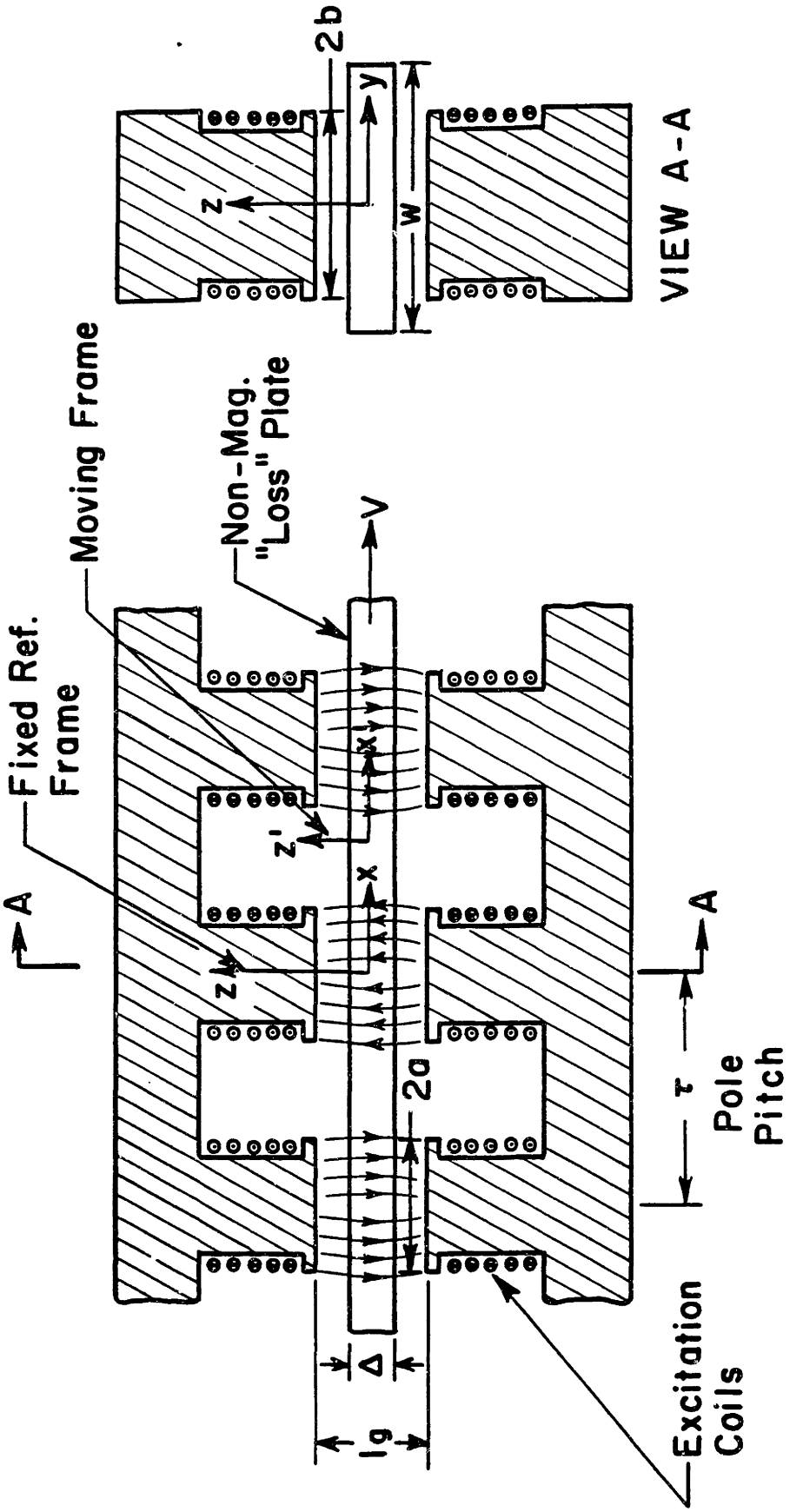

FIGURE B.4: LINEAR EDDY CURRENT BRAKE CONFIGURATION

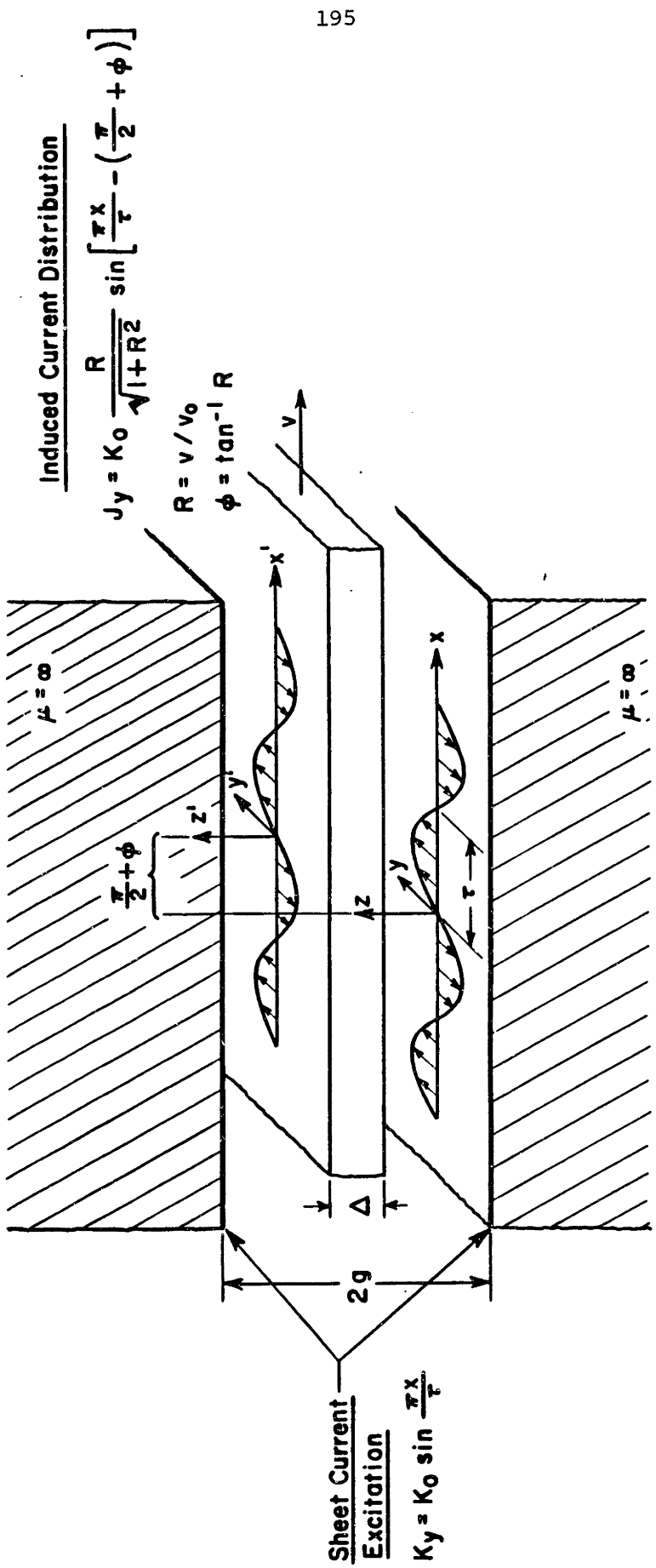

FIGURE B.5: INDUCED CURRENT NOMENCLATURE